UAB
Universitat Autònoma de Barcelona

Search for gamma-ray signals from dark matter annihilation or decay at the Draco dwarf galaxy and the Galactic halo with MAGIC

Daniele Ninci

Search for gamma-ray signals from dark matter annihilation or decay at the Draco dwarf galaxy and the Galactic halo with MAGIC

Daniele Ninci

Director: Dr. Javier Rico Castro

Tutor: Dr. Enriquez Fernández Sánchez

Departament de Física
Universitat Autònoma de Barcelona

A thesis submitted for the degree of
PhilosofiæDoctor

November 2020

Director:
Dr. F. Javier Rico Castro
IFAE
Edifici Cn, UAB
08193 Bellaterra (Barcelona) Spain
jrico@ifae.es

Tutor:
Dr. Enrique Fernández Sánchez
IFAE & UAB
Edifici Cn, UAB
08193 Bellaterra (Barcelona) Spain
enrique.fernandez@ifae.es

I herewith declare that I have produced this thesis without the prohibited assistance of third parties and without making use of aids other than those specified; notions taken over directly or indirectly from other sources have been identified as such. This paper has not previously been presented in identical or similar form to any other Spanish or foreign examination board.

The thesis work was conducted from October 2015 to November 2020 under the supervision of Javier Rico Castro at Barcelona.

Daniele Ninci
Barcelona, November 2020

Abstract

Astrophysical and cosmological observations affirm the existence of a non-baryonic and invisible form of matter, called Dark Matter, accounting for the 85Universe. Among the numerous models, the Weakly Interacting Massive Particle, a class of non-standard model(SM) particles, represents one of the best candidate as DM, as fit the characteristic request by the current cosmological model for DM: weakly interactive with ordinary matter, non-relativistic (cold DM), and stable at cosmological scale. WIMPs particles are supposed to have a mass between few GeV and hundreds of TeV, and to produce SM particles through annihilation or decay. Indirect search for DM signature in the astrophysical γ rays is very promising, since they point directly to the emitting source and γ-ray spectra from DM contains features that are related with no other astrophysical object except DM. Moreover, DM drove the historical evolution of the Universe, since baryonic matter accumulate in the DM over-densities, creating all the structures we see nowadays. Consequently, galaxies, satellite galaxies, and other structures, formed inside a DM halo, with a density peaked towards the center of the Galaxy and decreasing toward the outer region. Milky Way and its dwarf satellite galaxies represent the closest DM dominated objects. In this thesis I present the results from the observations of the Draco dwarf galaxy and the extended region of the Galactic DM halo. These targets have different characteristic: Draco is a moderate-extended source for MAGIC and can be treated with the standard analysis chain, while the halo region is very extended and the expected signal region goes far beyond the MAGIC field of view. The new approach I considered for observing successfully GH, consists in comparing pairs of observations performed at different angular distances from the Galactic Center, selected in such a way that all the diffuse components cancel out, except for those coming from the DM. In order to keep the systematic uncertainty of this novel background estimation method down to a minimum, the observation pairs have been acquired during the same nights, follow exactly the same azimuth and zenith paths with excellent weather conditions. A 20% of the data was used to determine the systematic level, while the rest is used to constraint the DM thermally averaged cross-section and/or the lifetime. For both searches, a binned maximum-likelihood analysis optimized for exploiting the spectra feature of DM annihilation and decay, is applied on both data sets. No hints of DM have been found in both data sample, constraining the

thermally averaged cross-section down to $\sim 10^{-23}$ cm^3/s and the DM lifetime up to $\sim 10^{26}$ s.

Contents

List of Figures

List of Tables

Chapter 1

What is Dark Matter?

Nowadays there are compelling experimental evidence for a large non-baryonic component of the matter in the Universe, observed in all the astrophysical scales, such as galaxies, galaxy clusters and cosmic background radiation. This matter is called Dark Matter (DM), since is not visible though the usual cosmic radiation (electromagnetic radiation, cosmic rays, or neutrinos), and it accounts for about 23% of the energy budget of the Universe and represents almost the 85% of its matter content. The discovery of such matter and its deep nature is one of the most important challenges of modern science.

1.1 Observational Evidences

The concept of *Dark Matter* (DM) has been introduced in 1933 after the work of Zwicky [36], who through the observation of individual galaxies in the coma cluster concluded that the their radial velocity was too high to be gravitationally stable, unless there was a dominant and invisible *mass* keeping them together. This work came after the ones of Öpik [37] and Oort [38] that already pointed that the luminous component of the galaxies was not sufficiently massive to explain their dynamics.

In the following decades, many observational evidence supports the existence of a dark component of the matter, at all scales. The next sections describe the most relevant evidence collected so far.

1.1.1 Dynamic of the galaxies

The first direct evidence for the existence of DM are the galaxies' rotation curves, i.e. the circular velocities of the visible stars and gas given as a function of their radial distances from the galaxy center.

For a stable bound system with a spherical distribution of mass (stars, galaxies, etc) the virial theorem establish a relation between the kinetic and the potential energy, so that we can derive the velocity distribution of an element of the system as $v(r) \propto (M(r)/r)^{1/2}$, where r is the distance from the center and $M(r)$ is the mass within a radius r. In the innermost region of the galaxies, the mass distribution can be considered spherical with constant density, so that $v(r) \propto r$. Moving outward, the matter is very spread apart and thus $M(r)$ is approximately constant, so that $v(r)$ is expected to follow $r^{-1/2}$. However, the measurements of the rotation curves, obtained combining observations of neutral Hydrogen 21cm-line with optical surface photometry, show a velocity that does not decrease with the distance, but remains flat, also for distances from the galaxy center beyond the edge of the luminous disk (see Fig. 1.1).

This discrepancy is solved with the hypothesis of the existence of a dominant DM halo embedding the galaxies. Commonly, for an astrophysics system, the amount of DM is quantify through the *mass-to-light ratio* M/L, normally given in solar unit ($M_\odot/L_\odot$). The total mass is usually estimated studying the dynamic of the system, and, when it is possible, the strong gravitational lensing effects (explained in the section), while the total luminosity is measured from photometric observations. The mass to light ratio changes a lot depending on the target considered (i.e. a spiral galaxy has a $M/L \sim$10, while the dwarf galaxies, the most DM dominated objects, can reach $M/L \sim 10^3$).

1.1.2 Gravitational lensing evidences

In the general relativity contest, space-time is distorted and curved under the influence of matter and energy. The light travelling from distant sources is consequently bended when passing around foreground mass-energy concentrations, causing the background object to look distorted to the observer. This effect is known as *gravitational lensing*, and it is very useful also to ascertain the presence of mass even when it emits no light and, furthermore, even probe its nature to certain extent [39]. Many observations indicate that the reconstructed mass producing this effect is greater (from a few to hundreds times) than the visible mass of the object, indicating that DM must be present (see Fig. 1.2).

The lensing technique can also be applied to galaxy-cluster collisions, as happens in the spectacular case of the Bullet cluster. Here two clusters of galaxies collided passing each one through the other, as shown in Fig. 1.3. The regions where the gas forming both clusters are located is shown (red) and measured through X-ray measurements, while through the lensing effect can be estimated the positions of the center of mass. For both clusters, the center of mass does not coincide with the one of the baryonic mass distribution, but appears separated into separated regions near the visible galaxy (blue). This provides support for the idea that

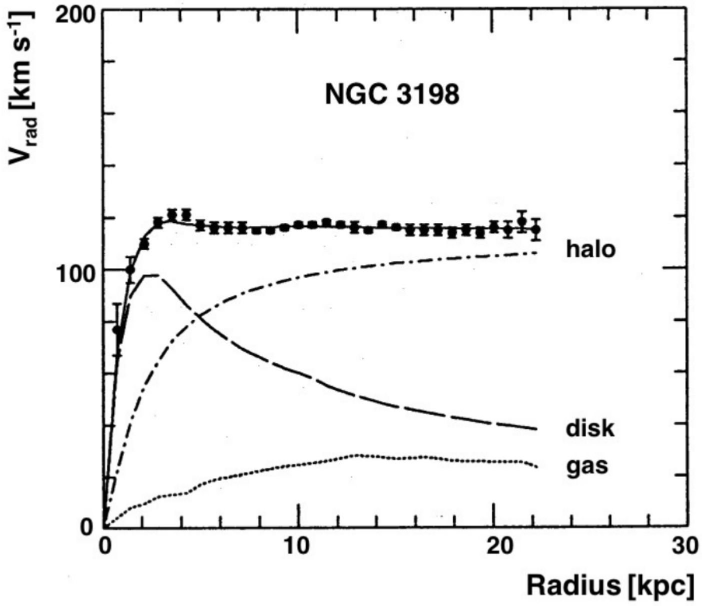

Figure 1.1 Rotation curve of NGC 3198 star-members as a function of the distance to the center of the galaxy. The Figure also shows the contribution of the velocity due to visible baryonic matter (gas (dotted) and disk (dashed)) and to the DM halo (dot-dashed). Fig adapted form [1].

Figure 1.2 The massive foreground cluster (Abell2218) distorting the images of background galaxies and forming arcs due to strong gravitational lensing. The arcs align in a way that their ellipticity is oriented tangent to the direction of the foreground mass, in this case the galaxy cluster center. Image credit NASA/ESA.

most of the mass in the cluster pair is in the form of two regions of DM, which bypassed the gas regions during the collision.

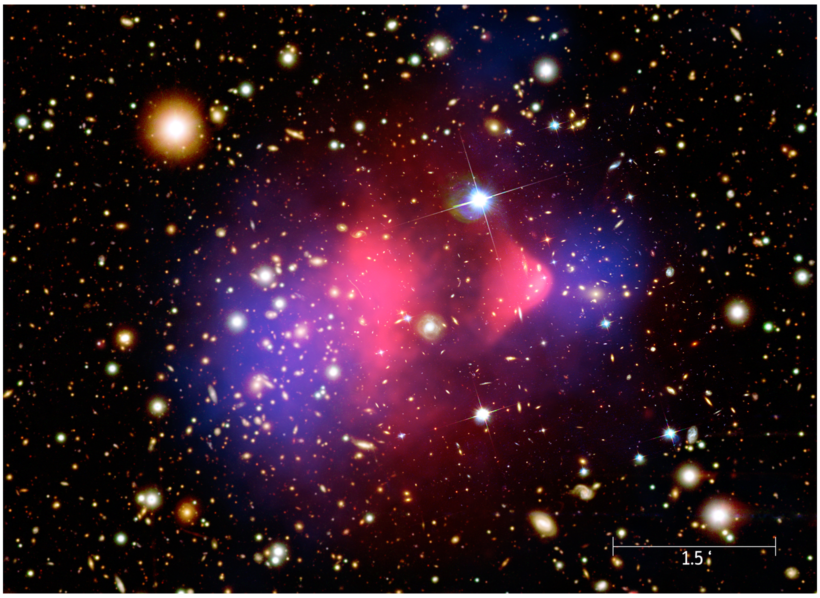

Figure 1.3 The Bullet cluster to cluster collision. In Blue is mapped the gravitational potential extracted from weak lensing and in red the radio emission.

1.2 Λ Cold Dark Matter model

The measurements provide hints that a DM exists in the universe, but a cosmological theoretical framework is needed to incorporate the DM in the evolution and in the current stage of the Universe. The most valid and elegant explanation so far is provided by the Λ *Cold Dark Matter* (ΛCDM) model (see [40] for a complete review). The framework provided by this model is sustained by two main pillars:

- General relativity (GR) equations;
- the Universe, at large scales, is homogeneous and isotropic (*Cosmological Principle*).

The *big bang theory* is one of the pillar of the ΛCDM which asserts that extrapolating backwards in time the measurements of the energy content of the Universe today, a singularity is found at 10^{10} years (age of the universe), the so-called *big bang*.

The evolution of the Universe in its first stage is still a matter of debate, while from 10^{-10} s the history is established with more precision. What is sure is that the Universe went through an inflationary epoch lasted from 10^{-36} s to sometime between 10^{-33} and 10^{-32} s after the Big Bang singularity. This represents a period of accelerated expansion during which the size of the Universe increases at least by a factor 10^{26}, due to the inflation field that decayed into *Standard Model* (SM) particles after the end of the inflation. Inflationary period offers support to the validity of the cosmological principle.

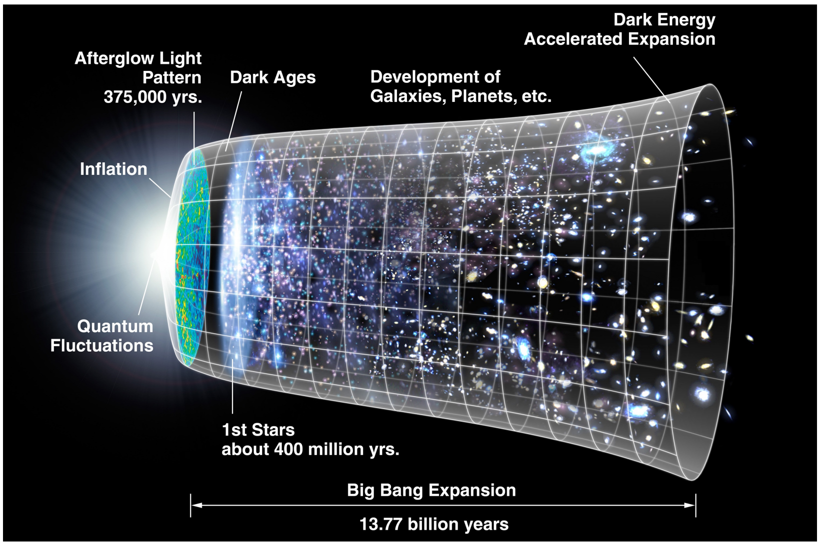

Figure 1.4 A schematic view of the Universe's history. Time evolution goes in the right direction. On the left side, the first singularity is shown the Big Bang, where radiation, matter and cosmological constant epochs go after (in this order).

The Universe went through different epochs during its expansion (see Fig. 1.4). A large number of independent observables converges into a single image in which the Universe was a very hot plasma of particles (mainly electrons, protons and neutrons) in expansion. In this first stage, known as the *radiation dominated era*, high energetic photon radiation prevented the formation of complex structures As the Universe expanded and cooled, the energy of photons decreased down under the energy need for hydrogen atoms ionization, and consequently, the Universe became *transparent* to photons. From this point, a *matter dominated era* took place, in which the large structures (galaxies and clusters of galaxies) starts to form under the gravity force, following a hierarchical merging of smaller structures into larger ones. The expansion rate of the Universe slowed down during this epoch, for increasing again after 10^9 years after the big bang. The accelerated expansion is due to a negative pressure from an unknown form of energy, *Dark Energy* (DE). The density of DE ($\sim 7 \times 10^{-30}\ g/cm^3$) is very low, much less than the density of ordinary matter or DM within galaxies. However, it dominates the mass-energy of the Universe because it is uniform across space.

The terms Λ in the ΛCDM model represents the cosmological constant introduced to explain the accelerated expansion phase we are nowadays, and accounts for the DE contribution. The dynamic of the Universe is then described in the context of the GR by the Friedman equations

$$H^2 \equiv \left(\frac{\dot{a}}{a}\right)^2 = \frac{8\pi G\rho}{3} - \frac{kc^2}{a} \tag{1.1}$$

and

$$\left(\frac{\dot{a}}{a}\right) = -\frac{4\pi G}{3c^2}(\rho + 3p) \tag{1.2}$$

where a is the cosmic scale factor, k is the spatial constant curvature, ρ the total energy density, p the relativistic pressure, H the Hubble parameter, defined as the expansion velocity of the Universe. In this view, the Universe is composed of DE (ρ_Λ), matter (baryonic matter and DM, $\rho_m = \rho_b + \rho_{DM}$), radiation ($\rho_r$) and extra component which account for the curvature of the Universe. So the total ρ is

$$\rho = \rho_r + \rho_m + \rho_\Lambda. \tag{1.3}$$

In the case of a spatial flat metric ($k = 0$), we obtained the *critical density* ρ_c from Eq. 1.1 as:

$$\rho_c = \frac{3}{8\pi G}H_0^2 \tag{1.4}$$

where H_0^2 is the Hubble parameter nowadays ($67.3pm1.2$ kms^{-1}Mpc^{-1}). Normalizing Eq. 1.3 to ρ_c we obtains the *density parameter* Ω:

$$\Omega \equiv \frac{\rho}{\rho_c} = \Omega_m + \Omega_r + \Omega_\Lambda + \Omega_k = 1 \tag{1.5}$$

Current best fits values of the density parameters are ([3]):

$$\Omega_b = 0.0486 \pm 0.002 \tag{1.6}$$

$$\Omega_{DM} = 0.2647 \pm 0.015 \tag{1.7}$$

$$\Omega_\Lambda = 0.6850^{+0.017}_{-0.016}. \tag{1.8}$$

This means that baryonic matter and DM account for $\sim$ 5% and 25% of the total energy content of the Universe, respectively.

1.2.1 Cosmic microwave background

The success of the ΛCDM lies mainly in both the prediction of structures formation and the fluctuation in the *Cosmic Micorwave Background* (CMB).

CMB represents a remnant radiation, composed by photons frozen-out at the mass-radiation decoupling era and cooled down by the expansion of the Universe, predicted by the Big Bang theory. The CMB is the most precise black-body spectrum in nature (T=2.725 K), with anisotropies corresponding to the *Doppler effect* caused by the movement of the Milky Way (MW) with respect to (w.r.t.) the CMB reference rest frame. represents an evidence for

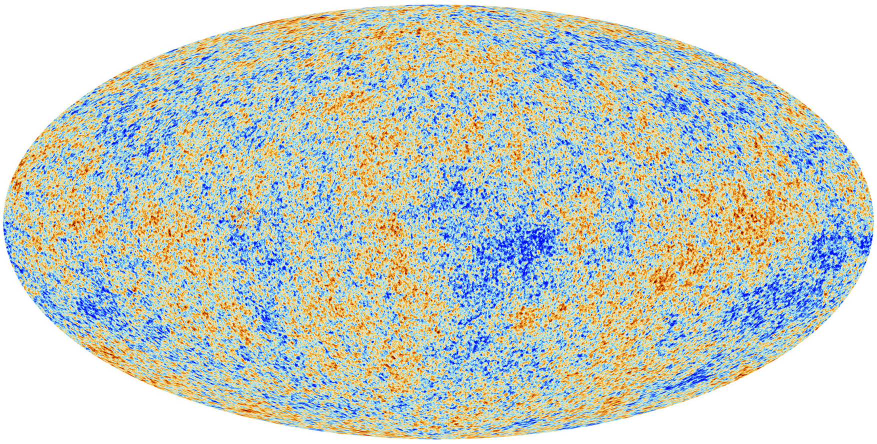

Figure 1.5 The anisotropies map from the 15.5 months of measurements with the Planck space telescope, showing the temperature fluctuation in the early Universe. The covered temperature range is ±500 μK. Image taken from [2].

the validity of the Big Bang theory. Recently, the predicted temperature anisotropies (10^{-5} K) have been measured by Planck space telescope (see Fig. 1.5, as a further evidence of the correctness of the ΛCDM. Moreover, the CMB is expected to provide information on the Universe during the epoch of the recombination[1]. The coupled photon-baryon plasma in the early Universe created acoustic oscillation as the result of the conflict between the photon pressure and the baryonic gravitational potential, which froze when photons decoupled. At the present epoch, those fluctuations should be seen as a series of peaks in the observed angular power spectrum, whose positions and amplitude can be used to constrain a variety of cosmological parameters (see Fig. 1.6). In particular, the position of the first peak probes the overall energy content of the Universe, while the relative heights of the peaks constraint the baryonic density Ω_b.

For a more complete review of the whole cosmological parameters and their implications on our universe, refer to [3].

1.2.2 Large Structure formation

ΛCDM model predicts the formation of large scale structures in the Universe, which has been confirmed from the measurement from the redshift survey.

Structures formation in the ΛCDM context, are triggered from primordial perturbations in gravitational potential field, probably created by quantum fluctuation derived from the inflation era. During the evolution of the Universe, overdensity regions were able to grow, till

---

[1] At $\sim 4\times 10^5$ year after the Big Bang, at T$\sim$ 10^3 K, electrons combined with nuclei into electrically neutral atoms. The photons decoupled, forming the CMB, so that the universe became transparent to the light.

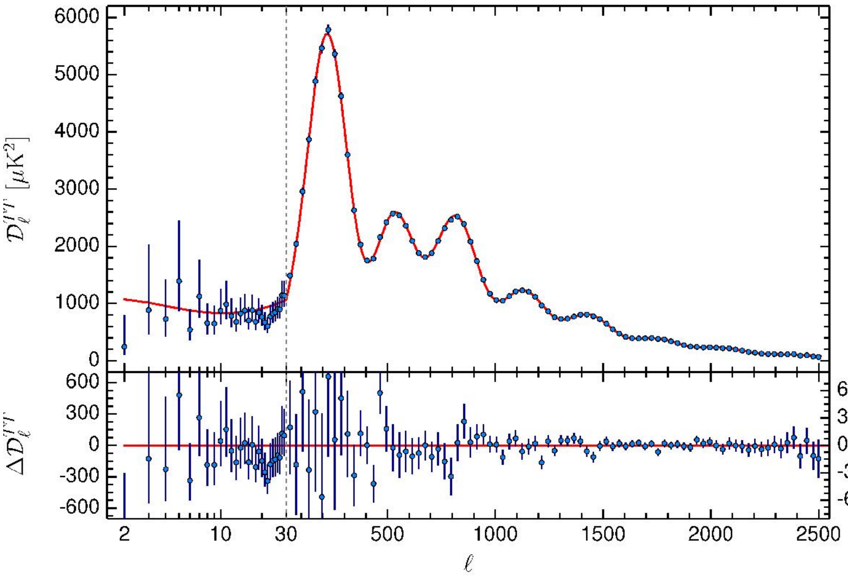

Figure 1.6 The temperature angular power spectrum of the primary CMB from the Planck telescope, showing the precise measurement of the seven acoustic peaks, that are well fitted by the ΛCDM theoretical model (full line). Image taken from [3].

when, during the matter-dominated epoch, the fluctuations entered in the non-linear regime, collapsed and triggered the formation of the gravitationally bound structures [41].

The temperature fluctuation of CMB points that the fluctuations of the baryonic matter at the recombination epoch, had a magnitude of 10^{-5}, that grew to 10^{-2} during the matter domination. This value is still too low for allowing the formation of the structures observed nowadays. A simple solution consists in adding as an extra ingredient the existence of DM: DM decoupled when fermions and baryons were still in thermal equilibrium and strongly interacting. That way, the density fluctuations in DM began growing earlier than in the baryonic matter. Thus, when baryonic structures collapsed, they fell into the already existing potential wells created by the DM over-densities. Given the overwhelming fraction of DM in the total mass budget of the universe, DM components actually drive the structure formation in the Universe.

The properties of DM have a direct impact on how the structures form. So far, three possible types of DM has been identified:

- *Hot* DM is expected to freeze-out while is still in a relativistic fase, thus with a very large free-streaming length. This implies that density fluctuations below the Mpc scales would be cancelled out. The supercluster-scale structures would have to form first and then fragment into smaller objects. This scenario is very disfavoured by the observations at high redshift [42].

- *Cold* DM would freeze-out as non-relativistic particles, thus with small free-streaming length. This supports the herircal formation from smaller structures that merge into larger ones. Cold DM hypothesis is favoured by the excellent agreement between the observational data and simulation [43].
- *Warm* DM particles are the intermediate solution between hot and cold DM [44]. Their free-streaming lengths are of galaxy-size, suggesting bottom-up formation at large scales and top-down scenario at smaller ones.

Cosmological models can be tested and validated through the N-body simulations. These studies attempt to reproduce the current image of the Universe at large scale, making evolving a dynamic system a particle under the influence of gravity. So far, ΛCDM model provides the best agreement between simulations and measurements, considering the existence of a cold and weakly interacting DM (see Fig. 1.7).

1.2.3 Challenge to ΛCDM

ΛCDM provides the best agreements between model predictions and cosmological data. However, still some observational results cannot be properly justified by this model.

DM halos DM dominated halos of galaxies are predicted by ΛCDM and mapped out by the rotation curves. However, the measurements show a velocity almost linear with the radius, that can indicate a central core in the DM distribution ($\rho_{DM} \sim r$, where ρ_{DM} is the DM density and r the distance from the center of the galaxy). Indeed, the high density of stars and of baryonic matter in general can dominate the dynamic of the galaxy, like the MW, without a larger contribution of DM. Here the models use the assumption that the stars move in a circular trajectory. In the outer region the DM dominates the dynamic, with the effect of an increase of the rotational speed.

The N-body simulations, where a non-interacting CDM uniformly distributed in the space is perturbed and naturally evolves, show that where galaxies have formed the DM has a cuspy profile in the inner part of the galaxy ($\rho_{DM} \sim r^{-1}$). The simulation improvement can investigate at radii each time smaller, but the results still point to a steep DM profile.

This discrepancy is known as the *cusp-core problem*. During the years different solutions have been proposed. From one side the observations can suffered by systematic effects not taken into account, dealing with the circular motion of the stars in the galaxy and the existence of a small offset between the center of the galaxy and the center of the dynamic motion. On the other hand, the N-body simulations usually do not take into account interaction with

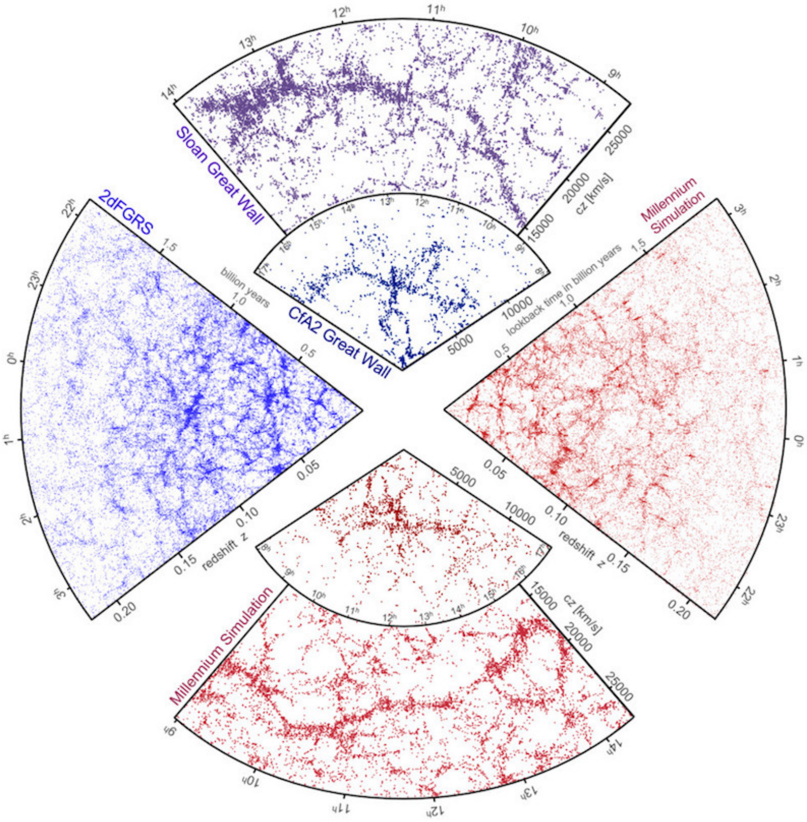

Figure 1.7 The large scale structure of the Universe mapped by the 2dF Galaxy Redshift Survey [4], the Sloan Digital Sky Survey [5] and the CfA Redshift Survey [6]. Each point represents a galaxy as a function of the right ascension and redshift. The corresponding Millennium simulations [7] of the ΛCDM structure formation are shown. Credit to VIRGO/Millennium Simulation project.

baryonic matter, or possible self-interaction, that would flatten the DM profiles. Which is the right solution is still under debate (see [45] for a detailed review of the problem).

The missing satellite problem N-body simulations predict that DM halos are created clumpy, and the substructures persist during the successive merging. One of the consequences is that a large population of satellite galaxies increases in abundance with decreasing mass. This prediction is not supported by the observations, as the number of the detected satellite galaxies is one order of magnitude lower than what is expected from simulations [46]. One possible solution to the problem is that the smaller DM halos do exist, but are simply not massive enough to have attracted sufficient baryonic matter to become visible. Another possible explanation is that the smaller dwarf galaxies may tend to merge into the galaxy they orbit after the star formations, or be tidally stripped by larger galaxies [47]. However, in the last decade a number of ultra-faint dwarfs have been discovered, with a $M/L \sim$1000. Newer galaxies may be found with the new photometric surveys.

Among other challenging discrepancies are the Tully-Fisher relation [48], the large scale velocity flow, the low multipoles in the CMB, the quasar optical alignment and the imperfect rotation curves. However, these problems are not sufficient for abandoning the ΛCDM concept.

1.2.4 Alternative cosmology

ΛCDM is not the unique model that provides an explanation of the evolution of the Universe. Alternatively cosmological models have been proposed, based on the assumption that DM is not cold either weakly interacting, or event it does not exist. However, this model only provides solutions to singular problems and adds new inconsistencies. At the moment, only ΛCDM offers a complete evolutionary image of the Universe. However, for the sake of argument, the best-justified of these alternatives are briefly described.

Modified Newtonian Dynamics (MOND) claims that the law of gravity deviates from the Newtonian one, thus eliminating the need for existence of DM [49]. According to MOND, below a certain gravity scale the effects of the gravitational force are magnified. This would explain the observed flattening of the rotation curves, as well as the Tully-Fisher relation. However, MOND fails to explain the dynamics of large objects like CGs, as well as the gravitational lensing effects without adding an additional component of matter. Moreover, MOND cannot account for any relativistic phenomena, and overall, does not provide a satisfactory cosmology.

Tensor-Vector-Scalar (TeVeS) gravity is developed as the relativistic generalization of MOND [50]. TeVeS works in the weak-field limit and possesses all good qualities of the MOND the- ory. In addition, TeVeS can explain gravitational lensing effects, although in a way non- consistent with the galaxy rotation curves. Major drawbacks of the TeVeS gravity model are the incompatibility with stellar evolution theory and the inability to explain the Bullet cluster phenomena (Fig. 1.3).

1.3 Dark Matter candidates

The existence of DM is well motivated by numerous observations, but still its nature remains unknown. However, astrophysical and cosmological observations can significantly constraint the properties of the DM. In a ΛCDM contest, DM should Despite the strong evidence for the existence of DM, the nature of its constituent is still unknown. However, significant constraints on the DM properties can be inferred from the astrophysical and cosmological observations. In the context of the ΛCDM, the DM particles should:

- be neutral – otherwise, it could couple with photons and therefore would not be dark;
- match the DM relic density (Ω_{DM});
- be stable at cosmological scales, so that it was present in the early Universe and is still around today;
- interact only weakly and gravitationally: the couplings with electromagnetic sector, as well as strong interactions are highly suppressed by the observations;
- play a leading role in the structure formation in the Universe, as the fluctuations in the DM density are dominating the evolution of the perturbations in the matter dominated era;
- DM density are dominating the evolution of the perturbations in the matter-dominated era;
- not affect the stellar evolution;
- be experimentally verifiable and consistent with the constraints derived by different methods of DM searches.

This section presents some of the theoretically best-motivated dark matter particle candidates.

1.3.1 The Weakly Interacting Massive Particle (WIMP) miracle

The class of Weakly Interacting Massive Particles, or WIMPs, have been the most studied DM candidate so far. WIMPs are postulated to be non-baryonic, stable and weakly interacting particles. Their success due to the fact that they naturally reproduce the correct relic density (what is commonly referred as the WIMP miracle), and can be detected in many ways, making WIMP a testable theory [51].

As for the others particles, WIMPs were in thermal equilibrium with the primordial plasma; when temperature dropped below the WIMP mass m_χ, WIMPs decoupled with rest of the particles, their production ended and consequently their density started to drop exponentially (Fig. 1.8). As the Universe kept expanding, their density became not sufficient to annihilate and at that point, WIMPs density froze-out, and the total number of WIMPs

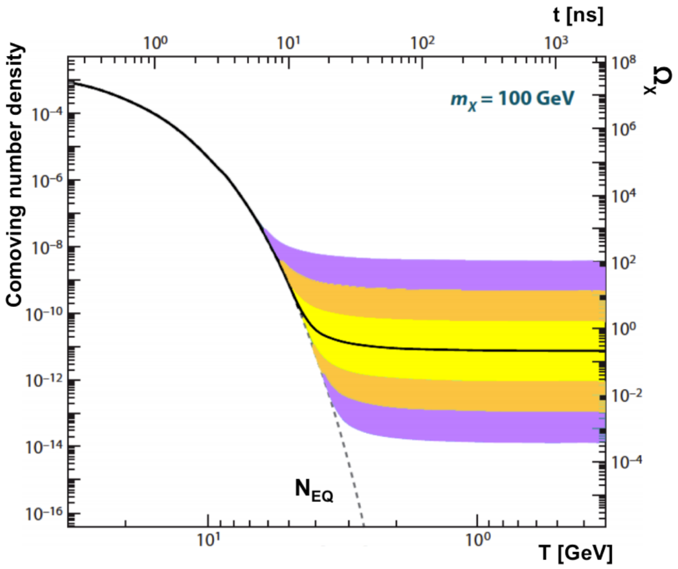

Figure 1.8 The comoving number density (left) and the thermal relic density (right) of a 100 GeV annihilating WIMP as a function of the inverse temperature of the Universe (bottom) and time (up). The solid black line corresponds to the annihilation cross section that yields the correct relic density, the yellow, orange and violet regions are for cross sections that differ for a factor 10, 100, 1000 (respectively) from this value. Finally, the dashed gray line is the number density of a particle that remains in thermal equilibrium. Image adapted from [8].

asymptotically reached a constant value, the so-called thermal relic density. The relic DM density today is:

$$\Omega_\chi h^2 = \frac{10^{-27} cm^3 s^{-1}}{< \sigma v >} \tag{1.9}$$

where Ω_χ is the WIMP density parameter, h is the scaled Hubble constant and $< \sigma v >$ refers to the thermally averaged product of the annihilation cross section and velocity. This value is naturally produced by a thermal relic with a mass and interaction cross section on the weak scale. For WIMPs, the freeze-out occurred at $T \approx m_\chi/20$, which sets the m_χ value in a GeV$\div$TeV range. Therefore, these particles were non-relativistic when the decoupling occurred, and thus, are suitable candidates for the role of cold DM.

However, WIMPs like particles do not exist within the Standard Model (SM) framework, and hence, new theories should be produced to have these particles included in a consistent theoretical framework. A class of models, describing the physics beyond the SM, includes in their development possible candidates for WIMP.

SM particles/fields		**SUSY partners**			
		Interaction eigenstates		Mass eigenstates	
quark	q	squark	$\tilde{q}_{\mathrm{L}}, \tilde{q}_{\mathrm{R}}$	squark	$\tilde{q}_1, \tilde{q}_2$
lepton	l	slepton	$\tilde{l}_{\mathrm{L}}, \tilde{l}_{\mathrm{R}}$	slepton	$\tilde{l}_1, \tilde{l}_2$
neutrino	ν	sneutrino	$\tilde{\nu}$	sneutrino	$\tilde{\nu}$
gluon	g	gluino	$\tilde{g}$	gluino	$\tilde{g}$
W-boson	$W^{\pm}$	wino	$\widetilde{W}^{\pm}$	chargino	$\tilde{\chi}^{\pm}_{1,2}$
Higgs boson	$H^{\pm}$	higgsino	$\widetilde{H}^{\pm}_{1,2}$		
B-field	B	bino	$\widetilde{B}$	neutralino	$\tilde{\chi}^{0}_{1,2,3,4}$
Higgs boson	$H^{0}_{1,2,3}$	higgsino	$\widetilde{H}^{0}_{1,2}$		
W^3-field	W^3	wino	$\widetilde{W}^{3}$		

Figure 1.9 Standard model particles and their superpartners in the MSSM model.

1.3.1.1 Supersymmetric Dark Matter

According to SUperSYmmetry (SUSY) theory, to every SM particle is associated with a new partner particle with the same set of quantum number and gauge interactions, with a spin increased by 1/2. At the moment no evidence for these new particles are found.

The theoretical framework of SUSY gives an unified image of the whole zoo of particles, and, more important, indicates possible solutions to some of the major SM problems:

- hierarchy problem. SUSY would solve this problem by removing the divergences in the radiative corrections to the Higgs boson mass [52];
- unification of the gauge couplings of the SM became possible whether the SUSY particle (sparticle) are included in the renormalization group equations [53];
- the lightest SUSY particle (LSP) is expected to be heavy, neutral and stable, hence fits perfectly the ΛCDM prediction on DM nature [54].

SUSY contains a large number of unknown free parameters. Typically specific models in which simplify assumptions unify many parameters are considered. One of the most important is the Minimal Supersymmetric Standard Model (MSSM) [55], representing the minimal extension to the SM in sense that contains the smallest possible field content necessary to give rise to all the fields of the SM. The MSSM requires two times the SM degree of freedom, plus two complex Higgs doublet, plus the complete set of SUSY partners (Tab. 1.9).

Since no sparticle with the same mass as its SM partner has been seen by the accelerator experiments, SUSY has to be broken. Breaking of the symmetry, produces some critical effects on the proton lifetime, shortening it down to values lower than the age of the Universe, which contradicts the observations. Thus, in MSSM, an *ad hoc* discrete symmetry, called *R-parity*, is introduced. R-parity is defined as $R \equiv (-1)^{3B+2L+2s}$, where B, L and s stand for the baryon, lepton and the spin numbers, respectively. SM particles have R-parity of +1, and their SUSY partners of -1. If R- parity is conserved, the sparticles can only be produced/annihilated in pairs, so that the LSP is stable and a viable DM candidate.

Despite the MSSM is “minimal” it has the drawback to have still 120 free parameters. The usual approach is to assume a specific framework, where further well motivated assumptions are introduced [56] [57] [58].

SUSY dark matter candidates

The best candidates for DM, among the whole candidates introduced by SUSY, have to be searched between the electrically neutral ones with weak interactions. In this contest, the spin 3/2 fermion gravitino (G), the spin 1/2 fermions called neutralinos and the spin 0 scalars sneutrinos are the most suitable candidates.

Sneutrinos have large cross section for scattering off nucleons, and thus have to be detected from direct detection experiments, for all masses near m_{weak}. The missing detection excluded this particle as a DM candidates.

In some SUSY scenarios, *Gravitinos* (G) is identified as DM candidates, being the lightest stable particles. Although theoretically well-motivated, G interacts only gravitationally, which makes their detection very difficult.

Neutralinos are by far the most favoured DM constituents. MSSM predict four neutralinos $\tilde{chi}_{1,2,3,4}$, resulting by the superimpositions of the neutral, spin 1/2 fermions: bino ($\tilde{B}$), wino ($\tilde{W}_3$) and two higgsinos ($\tilde{H}_1^0$ and $\tilde{H}_2^0$ [54]. With R-parity conserved, the neutralino is the lightest SUSY particle and thus a natural DM candidate, with a relic density compatible with current one, a mass at the GeV-TeV scale, and a typical cross section of the order of weak interactions. As a Majorana fermion (fermions that are their own antiparticle), the neutralino can self-annihilate into (detectable) SM particles, such as Fermions, Photons, Gauge bosons and Higgs boson.

1.3.2 Non-WIMP Dark Matter

Despite the enormous success of the WIMP theory, a vast collection of DM candidates is present nowadays (see Fig. 1.10). In the following I am going to present some of these other candidates (see [59] for a complete review).

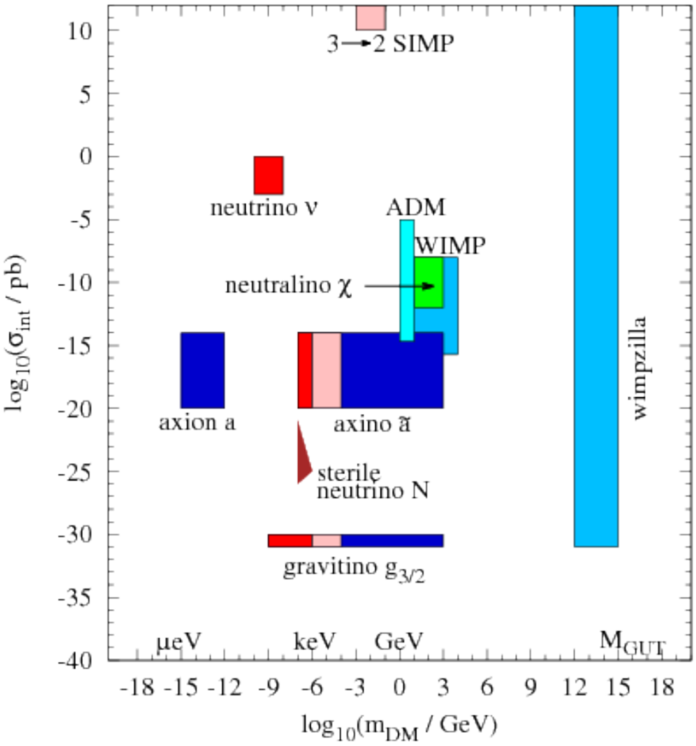

Figure 1.10 Schematic representation of some well-motivated DM candidate particles. σ_{int} represents a typical order of magnitude of the interaction strength with ordinary matter. The box marked as ”WIMP“ stands for several possible candidates. Image taken to [9].

Sterile Neutrino

Physics beyond the SM is supported by other experimental evidence, as the non-zero mass of the neutrinos. As for other SM particles, the mechanisms that generate neutrino masses request the existence of a right-handed neutrino, called *sterile* neutrino. This particle is classified as a weakly-interacting *Majorana fermions*. The lightest of sterile neutrinos, with mass predicted to be in the keV range, is compatible with warm DM, but could also be considered cold candidate, depending on the production mechanism. Additionally, sterile neutrinos may provide a solution for the baryon asymmetry [60] and, in the warm DM scenario, the missing satellites problem [61]. Sterile neutrinos are supposed to be unstable particles, with a lifetime of 10^{17} years, and decay into SM neutrinos or in $\gamma\nu$. While the first decay mode is extremely difficult to detect, given the low energy of the resulting neutrinos, the second could produce a detectable X-ray flux line in the KeV energy range.

SuperWIMP

Many BSM scenarios describe the possibility that WIMPs particles freeze-out in the early Universe, but lately decay into very weakly interacting particles, called *superWIMPs* [62]. They naturally inherit the relic density to the WIMPs, maintaining their miracle valid. Being very low interacting, they cannot be detected in the conventional direct and indirect DM searches, but may have an impact on cosmological measurements, as the CMB spectrum, small-scale structure, and diffuse photon spectrum. The gravitino is the prototypical example of superWIMP.

Axions

The axion particle was initially proposed as a solution to the strong CP problem of the SM [63]. Being light, neutral and weakly interacting, spin 0 boson it represents also a natural DM candidate. However, axion can be produced thermally being candidates for hot DM. However, in this scenario axion mass is constrained to be ~ 80 GeV, in order to reproduce the current relic density.

As an alternative, the non-thermal production of axions is possible through the spontaneous Peccei-Quinn (PQ), with a mass in the $10^{-6} \div 10^{-2}$ eV range. In the presence of electromagnetic fields, axions are predicted to couple with photons, leading to the so-called photon-axion oscillations. This effect may imprint a distinctive signature in the observed spectra of distant γ-ray sources.

In both scenarios, the axions cannot be the dominant component of the DM, due to their low mass.

Chapter 2

Dark Matter search

During the last years, many experiments have been devised to the search for DM signals, however, no evidence has been claimed, so far. Considering a DM mainly composed by WIMPs, three main detection techniques can be distinguished (Fig. 2.1): production of DM in particle accelerators, direct detection through DM scattering off ordinary matter, and indirect detection of primary or secondary SM particles produced in DM annihilation or decay.

2.1 Production at particle colliders

Possible detection of new physics in particle collider experiments may shed some light on the nature of DM. WIMPs could be created in a collider, in the case the luminosity and center-of-mass energy are sufficiently large for reaching the WIMP mass. Its presence in a collision event can be identified indirectly, by the missing transverse energy in the detector (see, e.g. [51], and references within). It refers to the energy carried away by a body leaving the detector unseen and reconstructed from the momentum conservation law: the momenta of incoming projectiles in the direction orthogonal to the beam is zero, so the final products of the collision must balance their momenta in the transverse plain. If in the final state an unbalanced contribution is found, the production of DM can result as a possible explanation.

WIMPs can be produced at colliders following different mechanism. In the specific case of SUSY, the best detection prospects would arise from the creation of heavier superparticles that in turn decay into quark and gluon jets and pair(s) of neutralinos. The detector ATLAS and CMS at LHC should have the capability to detect such events. However, no evidence for DM has been found so far, putting serious constraints on the simplified SUSY models (see Fig.2.2).

Pairs of WIMPs can be also produced accompanied by emission of a photon or a jet from the initial state. Such mono-photon and mono-jet events, respectively, together with the

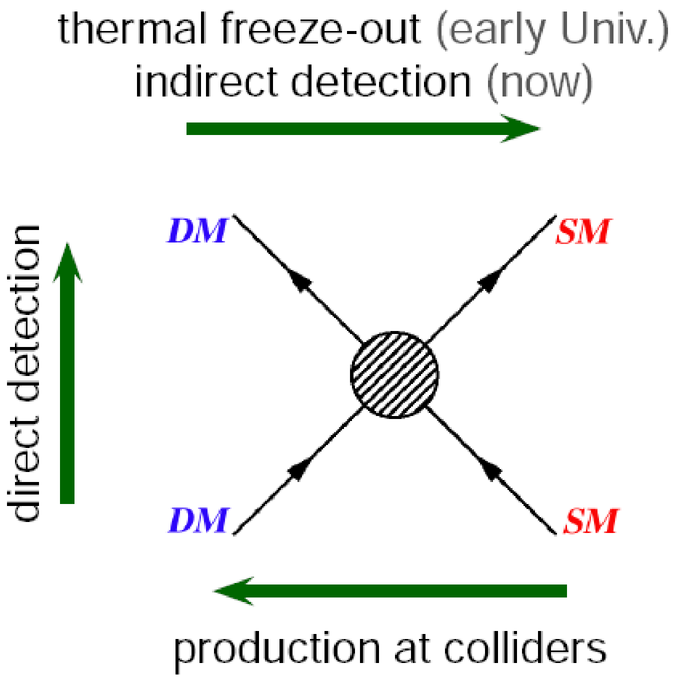

Figure 2.1 WIMP interaction diagram with SM particles. Depending on the path followed, different type of processes involving DM are shown: production at colliders (right to left), direct search (bottom to top), indirect search (left to right).

missing transversal energy carried away by the WIMPs, would represent striking signatures of DM presence. Lepton colliders have better possibility to disentangle such signals from the background compared to hadron collider. In the former, the energy of the lepton colliding can be controlled with high precision, whereas in the latter the gluons and the quarks that constitute the hadrons, are the particles that collide, at the LHC energy. The energy states of such constituents inside the hadron is unknown and can be defined only through a probabilistic way. Consequently, in LHC, mono-jet and mono-photon signals are highly obscured by the background. Still, limits for such events can be derived, and they are directly comparable to the constraints of direct search experiments.

The detection of a DM particle in colliders would reveal significant information, like its mass, annihilation and direct detection cross section, as well as the value of its thermal relic density. Nevertheless, both direct and indirect detection experiments would have to independently confirmed the discoveries of a particle with such characteristics before identifying the new particle as DM.

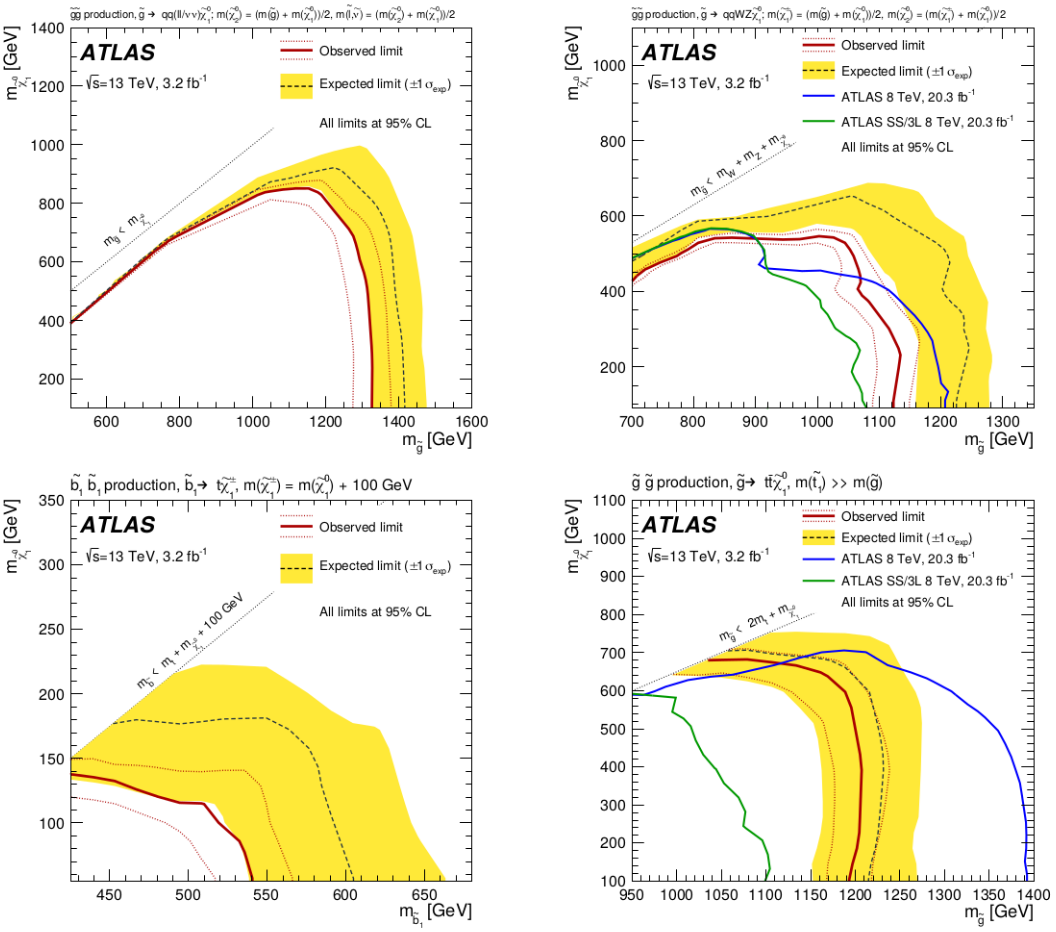

Figure 2.2 Observed and expected exclusion limits on the $\tilde{g}$, $\tilde{b}_1$ and $\tilde{\chi}_1^0$ masses in the context of SUSY scenarios with simplified mass spectra featuring $\tilde{g}\tilde{g}$ or $\tilde{b}_1\tilde{b}_1^*$ pair production with exclusive decay modes. The signal region used to obtain the limits is specified for each scenario. The contours of the band around the expected limit are the $\pm 1\sigma$ results, including all uncertainties except theoretical uncertainties on the signal cross-section. The dotted lines around the observed limit illustrate the change in the observed limit as the nominal signal cross-section is scaled up and down by the theoretical uncertainty. All limits are computed at 95% CL. The diagonal lines indicate the kinematic limit for the decays in each specified scenario. Image taken from [10].

2.2 Direct detection

The motion of the Earth inside the Milky Way produces a incident flux of WIMPs that lie in the Galactic halo. The expected WIMP flux on Earth is of the order of 10^5 cm^{-2}s^{-1} for a particle of m$_\chi$ = 100 GeV [51]. This flux is sufficiently large to have a small, but potentially detectable fraction of WIMPs interact with ordinary matter. In direct detection experiments, DM is searched through the nuclear recoils caused by the elastic scattering of the WIMPs on the baryonic matter, composing the target. The recoil for a GeV-mass WIMP to a heavy nucleus on the Earth, is typically of the order of tens keV. The nucleus recoiled can deposit its energy in the detector through ionization, scintillation or heat (phonon) production. All the information about DM microscopic properties is codified into the differential elastic scattering cross section, generally separated into spin-independent and spin-dependent contributions. The spin-independent term comes from scalar and vector couplings to quarks, and its value basically scales as the square number of nucleons. On the other hand, the spin-dependent term comes from axial-vector couplings to quarks, and it is dependent on the nuclear angular momentum. For different DM models the relation between these two contributions may differ, and although both have to be taken into account, the scalar component dominates for heavy targets, which is the case for most direct detection experiments. Since the expected elastic cross section is of order of $\sigma \sim 10^{-43}$ cm^2, the rate of nuclear interactions is extremely low (less than 1 event per kg per day). That makes the background characterization and control the greatest challenges of direct detection experiments. Better performance is ensured by choosing a large detection target, composed of extremely radiopure elements; the same philosophy steers the selection of the rest of the detector parts. Furthermore, the target material is often surrounded by a high-density metal shielding, and special care is taken to minimize the electronic noise. In order to suppress the unwanted background originating from cosmic rays (mainly muons), the installations of the experiments are typically located deep under ground. During the last decade, hints of direct detection of DM have been reported by experiments like DAMA/Nai [64] and DAMA/LIBRA [65], and CoGeNT [66]; however, neither was conclusive enough on its own and could not be reproduced by other experiments. Moreover, the most stringent limits over the spin-independent interaction cross section, measured by the XENON1T experiment (XENONT1T) and of order $\sim 10^{-46}$ cm^2 [11], already exclude both the DAMA/LIBRA and the CoGeNT favoured regions (Fig 2.3). Current best sensitivity for the spin-dependent cross section is obtained by LUX that provides 90% CL upper limits to the WIMP-neutron (WIMPproton) cross section of $\sigma_n = 1.6 \cdot 10^{-41}$ cm^2 ($\sigma_p = 5 \cdot 10^{-40}$ cm^2) at 35 GeVc^{-2} [67].

More recently, XNENON1T announced the observation of excess events around $2-3$ keV, reported in Fig. 2.4. Different scenario can provide possible explanation to the excesses

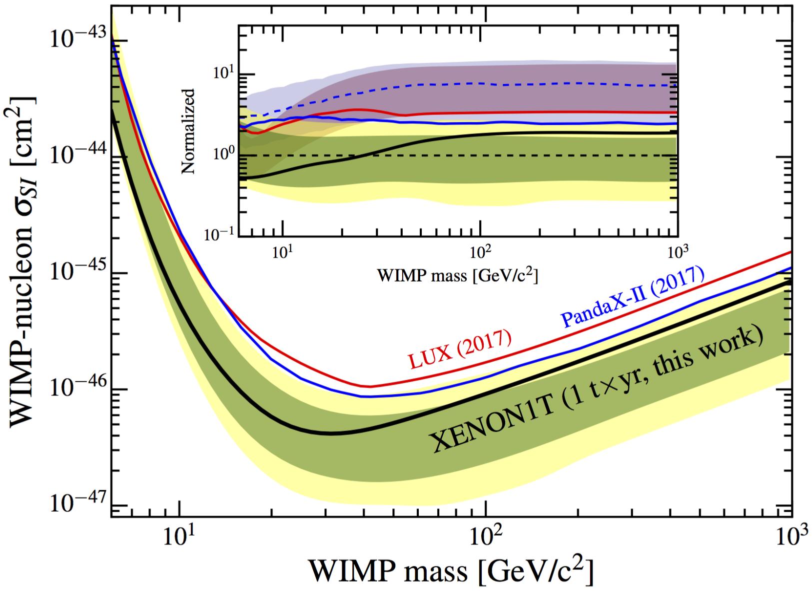

Figure 2.3 The spin-independent WIMP-nucleon cross section limits as a function of WIMP mass at 90% confidence level (black) for XENON1T [11]. In green and yellow are the 1 and 2 σ sensitivity bands. Results from Large Underground Xenon (LUX) [12] (red), PandaX-II [13] (brown), and XENON100 [14] (gray) are shown for reference.

observed: a solar axion flux model fit the data with a significance of 3.5σ over the background, while an anomalous magnetic moment of neutrino is favoured for 3.2σ. Another possible explanation concerns the presence of residual quantities of tritium in the water tank of the detector, which can create spurius signals through β decay. The concentration of tritium can be neither confirmed nor excluded with current knowledge of production and reduction mechanisms. The significances of the solar axion and neutrino magnetic moment hypotheses decrease to 2.1σ and 0.9σ, respectively, if an unconstrained tritium component is included in background model (see [15] for further details).

The future of the direct detection instruments goes along the line of increasing the mass of the target materials above one ton, lowering the ambient temperature down to few mK, and measuring the signals from ionization, scintillation and heat production within the same detector. Efforts on several of such future experiments, like EURECA [68], DARWIN [69] and DarkSide-20k [70], are already under way. For more information on direct detection searches, see e.g. [51] and references within.

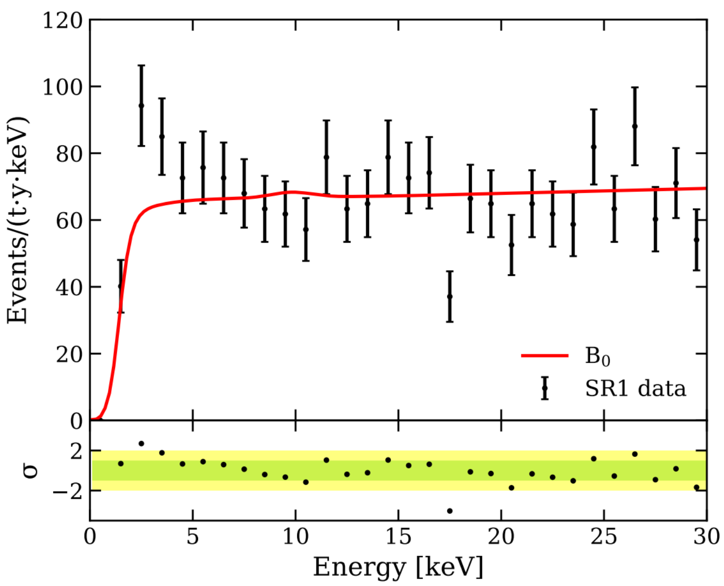

Figure 2.4 The XNENON1T analysis of the data collected during the period February 2017-February 2018 (SR1) shows an event excess for energy of 2−3 keV. Figure taken from [15].

2.3 Indirect detection

Indirect detection searches exploit the possibility that DM particles can annihilate or decay, producing SM particles detectable through a variety of modern ground and space-based observatories. The resulting SM products are expected to carry valuable information on the properties of DM particles. Moreover, the indirect approach can probe the astrophysical distribution of DM, which is not possible with direct neither with collider searches. The main obstacle to this search method is the overwhelming abundance of astrophysical background, which makes the disentanglement of SM particles that have DM origin a complex task. The annihilation and decay rates of a DM particle should be low enough to guarantee stability on cosmological scales, i.e. their lifetime is longer the age of the Universe, and not reduce significantly the total DM budget. Indirect detection approaches search for signatures of DM through in the final and stable SM products: photons, neutrinos, electrons, protons and their corresponding antiparticles. The expected signal depends DM properties and on the annihilation/decay channel considered.

2.3.1 Messengers for indirect DM searches

Photons are particularly interesting products of DM annihilation or decay, as they travel in straight lines from the emitting source and are almost unabsorbed in the local Universe. Because they point back to the place of their creation, astrophysical foregrounds can be

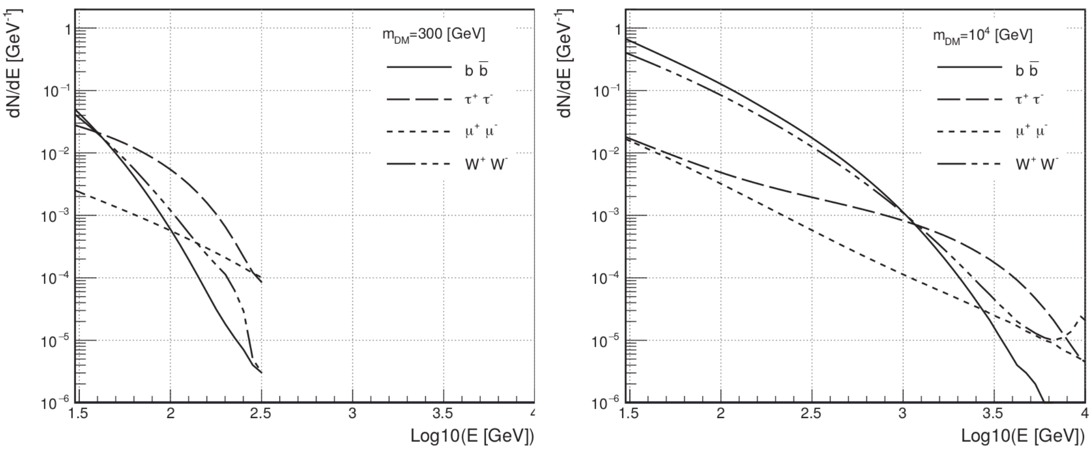

Figure 2.5 γ-ray spectra due to prompt emission from different DM annihilation/decay SM pairs. m_{DM} is the mass of the DM particle annihilating ($2m_\chi$ for the case of decay.

significantly reduced by looking for signals in regions with high DM density. Furthermore, the resulting photon spectrum should reveal characteristic features (Fig. 2.5), unique and universal for DM. The detection of such features would represent a clear detection of DM. A WIMP is expected to emit photons in the γ-ray energy range. More details on the γ-ray-based searches are provided in the following sections.

Neutrinos, like photons, are neutral particle and thus, not deflected by magnetic fields. As consequence, they can be traced back to the source that emits them. Neutrinos interact with matter via weak force, with a very low cross-section. Large size detectors are usually adopted for increasing the probability of making a neutrino interact with the material of the target. The larger astrophysical neutrinos observatories are build deep in the sea (Astronomy with a Neutrino Telescope and Abyss environmental RESearch ANTARES [71]) or in ice (IceCube [72]). DM annihilation or decay are expected to produce a large amounts of neutrinos, as final state. If the primary products are heavy leptons, they decay into lighter ones producing the corresponding neutrinos. Primary states of gauge bosons, produced neutrinos in leptonic decay. Moreover, Z boson can decay into quark pairs and neutrinos, or directly into a neutrinos pair.

Neutrinos are expected to be produced in large amounts in DM annihilation or decay. If primary products from these processes are heavy leptons, their consequent decay into lighter ones will be accompanied by neutrino emission. If the primary products are gauge bosons, neutrinos are also produced in their decay into lepton (for $W^{\pm}$, Z) and quark pairs (for Z). In addition, if Z boson is among the primaries, it can decay directly into a pair of neutrinos. Direct annihilation into a neutrino pair is possible as well. The currently best limits on DM annihilation cross section from neutrino searches come from IceCube observation of the Galactic Center [73]: $< \sigma v >$ for direct annihilation into neutrinos is constrained to $18{\cdot}10^{-23}$ cm^{3}s^{-1}, while the lower limit on the lifetime of the DM particle is $\tau_\chi \sim 10^{22}$ [74], for m$_\chi$ $\sim$ 100 GeV.

Charged cosmic rays interact with galactic magnetic fields, and diffuse in the Galaxy from their production site to the Solar System, so, unlike photons and neutrinos, they can not be traced back to their production region. Therefore, it is cleaver to search for DM for DM signal as an anomalous component in the isotropic cosmic ray spectrum than in specific target. DM processes are expected to create the same amount of matter and antimatter products. On the "standard" matter side, the (DArk Matter Particle Explorer DAMPE) has recently provided a direct measurement of the all-electron spectrum with unprecedentedly high energy resolution revealing a spectral break at about 0.9 TeV [75], confirming the evidence found by previous indirect measurements [76] [77]. On the "anti-"mater side[1], distributions of positrons and antiprotons are very promising places to look for deviations from conventional fluxes expected from astrophysical processes. In the last years, there have been reported a considerable number of unusual features in the electron-positron spectrum at high energies. The Payload for Antimatter Matter Exploration and Light-nuclei Astrophysics (PAMELA) found an interesting rise in the positron fraction, computed as $e^+ /(e^+ + e^-)$, at energies up to 100 GeV [78].This behavior is in contradiction to the expected decline predicted by traditional models of DM propagation [79]. This result was corroborated by measurements by Fermi-LAT [80] for energies up to 200 GeV [81]. The latest news on this subject come from the high-precision results of Alpha Magnetic Spectrometer-02 (AMS-02) that extend up to 350 GeV [82]: these measurements confirm the rise for energies up to $\sim$ 250 GeV, above which there is a hint of spectrum flattening. There are number out proposed theories involving DM [83] that can justify the observed excess, however, they are not fully supported by the experimental measurements (for instance, the positron excess should be accompanied by photon excesses at other wavelengths, which is not the case). On the other hand, a more conventional explanation, with particles being accelerated by the nearby pulsars [84], is much more plausible. Another stable product from DM annihilation or decay are the antiprotons. Antiprotons may also be created from decay of primary products; however, current measurements of the antiproton flux show no deviation from the predictions for local astrophysical sources [85].

---

[1] The "anti"-products are extremely attractive for indirect searches, since their astrophysical background is much lower compared to standard matter.

2.3.2 Photon flux from DM

DM can annihilates or decays into SM particle, expecting to produce γ-ray signals with some characteristic observational features that can be used to obtain information about its nature and its spatial distribution. Moreover, such signatures would help in rejecting the astrophysical background from possible DM signal, and possibly, identify with no ambiguity the DM particle.

Assuming the WIMP model, the general formula of the expected DM flux can be written as:

$$\frac{d\Phi(\Delta\Omega)}{dE} = \frac{d\Phi^{\mathrm{pp}}}{dE} \cdot J(\Omega), \tag{2.1}$$

where the flux is the product of two terms. The particle physics terms ($d\Phi^{\mathrm{pp}}/dE$) is determine by the choose of the DM theoretical framework, and it is the same for every source. The astrophysical term, $J(\Delta\Omega)$ (named J-factor) on the other hand depends on the observed source, the DM distribution at the source region and the property of the instrument.

DM annihilation In the annihilation case, the particle physics term takes the form:

$$\frac{d\Phi^{pp}}{dE} = \frac{1}{4\pi} \frac{< \sigma_{ann} v >}{2m_\chi^2} \frac{dN}{dE}, \tag{2.2}$$

where $< \sigma_{ann} >$ is the thermally averaged annihilation velocity cross-section, dN/dE is the differential γ-ray spectra per annihilation, summed over all the n possible channels that product photons, given its particularly branching ratio Br:

$$\frac{dN}{dE} = \sum_{i=1}^{n} \mathrm{Br_i} \frac{dN_i}{dE}. \tag{2.3}$$

This terms contains the spectral information of the DM process. The astrophysical term for annihilation process is computed as follow:

$$J_{ann}(\Delta\Omega) = \int_{\Delta\Omega} \int_{los} \rho^2(l,\Omega) dl d\Omega, \tag{2.4}$$

where ρ is the DM density profile, l the line of sight and $\Delta\Omega$ the solid angle. Finally the integrated flux for DM annihilation above a certain energy E_0 is:

$$\Phi(E > E_0) = \frac{1}{4\pi} \frac{< \sigma_{ann} v >}{2m_\chi^2} \int_{E_0}^{m_\chi} \frac{dN}{dE} dE \int_{\Delta\Omega} \int_{los} \rho^2(l,\Omega) dl d\Omega. \tag{2.5}$$

DM decay Assuming that a DM particle is not completely stable, i.e. breaking the R-parity, hence a small fraction of them can decay into detectable final state. This is a plausible scenario, since DM is expected to be stable at cosmological scale. The expected DM flux has the same form shown in Eq 2.1, however the singular terms are different. The particle physics term depends on the DM lifetime τ_χ as:

$$\frac{d\Phi^{pp}}{dE} = \frac{1}{4\pi}\frac{1}{m_\chi \tau_\chi},\frac{dN}{dE}, \tag{2.6}$$

while the astrophysical term scale linearly with the DM density:

$$J_{dec}(\Delta\Omega) = \int_{\Delta\Omega}\int_{los} \rho(l,\Omega) dl d\Omega, \tag{2.7}$$

Finally, the total integrated flux above a certain energy is computed as in Eq 2.5.

2.3.2.1 DM density profile

The main uncertainty in the DM flux formula arises from the DM density profile ρ_{DM}. These distributions cannot be directly measured and can only be constrained by N-body simulations from one hand and stellar and gas kinematic measurements from the other one.

The N-body simulations are performed studying the dynamic of a system of particles under the effect of gravity force. They aim to recreate the hierarchical formation of the CDM halos, and have shown that spherical-averaged DM halo distribution is well described by an universal profile. Navarro, Frank and White [86] (NFW) have made a fit on this profile ρ_{NFW}, applicable to over 20 decades of mass range. The NFW profile is characterized by a center power-law cusp with $\rho_{\{mathrmNFW} \sim r^{-1}$, which is in contradiction with the evidences from astrophysics observations.

The recent high-resolution simulations have shown that the asymptotic slope in the center of the halo converge to a finite not divergent cusp. As results, the Einasto profile ρ_{Ein} [87], provides a better fit to the simulation. The slope of Einasto fit asymptotically approaches to 0 toward the center, producing a finite density at $r = 0$.

However, as explained in Sec. 1.2.3, the central cusp is not a common features for many galaxies, that tends preferibly to a cored profile. The Isothermal profile ρ_{ISO} [88], characterized by a constant velocity dispersion, provides a model with a central cored density distribution, in contrast with the NFW and Einasto profiles.

Below, the expressions of the three different DM profiles mentioned are presented:

$$\rho_{\mathrm{NFW}}(r) = \frac{\rho_0}{(r/r_s)[1+(r/r_s)]^2}, \tag{2.8}$$

$$\rho_{\mathrm{Ein}}(r) = \rho_0 \cdot \exp\left[-\frac{2}{\alpha}\left(\frac{r}{r_s}\right)^{\alpha}\right], \tag{2.9}$$

$$\rho_{\mathrm{ISO}}(r) = \frac{\rho_0}{1+r^2/r_s^2}, \tag{2.10}$$

where r is the radial distance from the center of the halo, r_s and ρ_0 are the scale radius and the overall normalization factor. Tab 2.1 shows the value of the parameters for each considered profile for the MW case, as example. In the whole scenario, ρ_0 is chosen in order to reproduce the local dark matter density $\rho_{\odot} \approx 0.4\ \mathrm{GeV/cm^3}$ for a $r_{\odot} = 8.33$ kpc [89] [51] .

	α	r_s [kpc]	ρ_0 [GeV/cm^3]
NFW	–	24.42	0.184
Einasto	0.17	28.44	0.033
Isothermal	–	4.38	1.387

Table 2.1 Summary of the parameter values for the three DM profile considered for the MW case.

The choice of the DM profile influences the expected photon flux, in particular in the case of DM annihilation (Eq 2.4): as J depends on the density squared, the cored profile will yield lower flux than the cusped one. This effect is less evident for DM decay, as in this case the dependence on the density is linear.

2.3.2.2 Annihilation cross section and decay lifetime

The expected DM flux goes through the evaluation of the Φ^{pp} term, which accounts for the nature and the properties of the DM particle. Interaction operators can be constructed starting from the hypothesis that DM is a scalar particle or a fermion. This leads to the calculation of the annihilation cross section or decay lifetime.

The natural value of reference for $< \sigma_{ann} v > \simeq 3 \cdot 10^{-26}\ \mathrm{cm^3 s^{-1}}$, that is determined by the requirement to produce the observed DM relic abundance during the DM freeze-out process in the early Universe [90].

Regarding the decay lifetime, no physical arguments lead to an expected value, that depends on the considered model and DM particle properties. As DM have to be stable at cosmological scale, it has to be longer than the current age of the Universe ($\sim 4 \cdot 10^{17}$ s).

For example, in SUSY extension of the SM with a small R-parity violation and gravitino as lightest SUSY particle, decay lifetime into photon and neutrino is calculated to be $\tau_{\chi\to\gamma\nu} \simeq 3.8 \cdot 10^{27}$ s [91].

2.3.3 Review of the observational targets

When choosing the best target for the indirect DM searches, the selection criteria should go in the direction to maximize the astrophysical J-factor. Therefore, following the Eq. 2.4 and 2.7, the suitable targets should have a high DM density, while the distance from the observer should be a small as possible. The M/L of the system should be taken into account either, since a large baryonic content may can major drawback. Baryonic matter disrupt the DM profile smoothing the central high DM density, and hence reducing the expected flux. Furthermore, baryons can act as strong background to the DM signals, as they can produce photons via conventional astrophysical process in a far more abundant number than the annihilation or decay can.

The Galactic Center and Galactic Halo The *Galactic Center* (GC) is the closest known region dominated by DM ($\sim$ 8.5 Kpc). Theoretical arguments and numerical simulations foreseen a central DM cusp, that would strongly enhance the annihilation signal. However, the GC is highly populated region, with large background present at all wavelength coming from conventional sources. Furthermore, the large baryonic content in the center and the presence of a black hole leads to a modification of the DM profile, making the density distribution highly uncertain [92].

Observations of the GC at *very high energy* (VHE) range, where WIMP signals are expected, have already carried out by Cherenkov telescopes and satellite telescopes. A non-variable signal was confirmed with hard power-law spectrum extending up to 20 TeV, which disfavours its DM origin. In addition, the spatial extension does not agree with the DM profile and the detected signal is several order of magnitude above the prediction for pure DM emission. A more likely origin is the radiation from the conventional counterparts in the vicinity of the GC (the super-massive black hole SgrA*, the supernova remnant SgrA* East and the pulsar with nebula G359.09-004), which completely hide the potential DM signal [93] [94].

A way to overcome the background contamination is to search for DM in the region outside the Galactic Plane, less contaminated by astrophysical background, but still quite close to the GC to profit from the high DM density. Still, this search in influenced by the uncertainty related to the DM profiles considered (NFW or Isothermal). This approach has been applied by H.E.S.S, and provides the currently most stringent limit for the $< \sigma v >$

value in the given energy range considering a NFW profile [35], while the method would not work with an Isothermal profile, since both signal and background FoVs would have the same J-factor.

On the other hand, DM decay searches should be more effective if carried out at larger galactic latitude [91]. The decay J-factor does not decrease drastically with the distance from the center, because of the linear dependence with ρ_{DM}. This guarantee the possibility to achieve similar results as for the observation close to the central region of the galaxy, with a considerable less background level and almost no uncertainty concerning the DM profiles. This approach has been used in this thesis for measuring the DM lifetime in observations of the *Galactic Halo* (GH), at galactic latitude larger then 10°. All the details concerning the measurement will be discuss in Chapter 5.

DM subhalos According to N-body simulations, the DM evolves by creating hierarchical clusters, that results in formation of DM clumps within halos at all scales. The larger clumps may attract enough matter to trigger stars formation, while the smaller ones does not have enough gravitational attraction and remain completely dark. Those small halos are invisible in the context of the conventional mechanism, but should may shine in the energy windows where DM signal is expected, so becoming γ-ray emitter. The lack of any astrophysical background makes the subhalos excellent target for indirect search, but with the drawback that their location is unknown. However they can appear in γ-ray sky survey.

Fermi-LAT has detected so far hundreds of the so-called Unidentified Fermi Objects (UFOs), sources that emits at very high energy but does not have any counterpart at other wavelength. Some of this UFO are potential candidates for DM subhalos, if their emission is not variable. Moreover, most of these objects lie outside the Galactic Plane.

Complementary observations of the UFOs have been performed by Cherenkov telescopes, but no detection has been reported so far [95].

Dwarf satellite galaxies Dwarf sheroidal Milky Way satellite galaxies (dSphs) are among the most dominated DM objects known so far [96]. Those objects have M/L ratio is between $100 \div 1000\ M_{\odot}/L_{\odot}$ and are relative close (up to $\sim$ 250 Kpc) to the Earth. Moreover, the absence of gas and the presence of old star population, provide an negligible γ-ray background. These statements make dSphs excellent targets for indirect DM search.

Currently the most constraining limits are set by the joint analysis of the observation of 10 dwarf by Fermi-LAT and the Segue 1 result by MAGIC [23]. Nowadays, many dwarfs have been observed by different ground based telescopes, which trigger the different collaborations in performing a joint analysis of their best results (achieved by combining the observations of the single dwarf). In this contest, in Chapter 4 will be presented the results of the analysis of Draco dwarf galaxy, as part of a combined analysis of 4 dSphs promoted by MAGIC.

Galaxy clusters Galaxy clusters are the largest known gravitational bound systems, with radii of several Mpc and masses of $\sim (10^{14} \div 10^{16})\ M_{\odot}$. These objects represents the top stage of the hierarchical formation of the large scale structures. Galaxy cluster are among the most DM dominated objects, with more than 80% of dark matter content. The high DM content makes them attractive objects for indirect DM search. However, the potentiality as DM target is weakened by the huge astrophysical background of astrophysical origin, dominantly form the active galactic nuclei galaxy population, as well as by the secondary component of cosmic-ray induced radiation.

So far, γ-ray observations of Virgo, Perseus, Coma and Fornax galaxy clusters do not return any evidences for DM signals, as well for other wavelength observations [97] [98] [28].

Chapter 3

The MAGIC Imaging Atmospheric Cherenkov Telescopes

In the indirect search for DM signals, photons have a particular interest, as they result unabsorbed by the local universe and travel in straight line from the emitting point. Because of this, the astrophysical foreground can be significantly reduced. Moreover, the resulting photon spectrum should show some characteristic features unique for DM annihilation or decay, whose detection would represent a clear signature in the indirect search.

3.1 Cherenkov radiation

The name γ-rays is referred to the highest radiation in the Electromagnetic (EM) spectra, which covers 20 energy decades between radio and γ range (see Fig 3.1). The EM radiation can travel across the atmosphere, but the atmosphere usually prevents the most energetic radiation from penetrating and reaching us. In order to detect these photons, the experiment has to be taken outside the atmosphere. The satellite detectors, like Fermi-LAT, can directly detect γ-rays using the pair conversion of the photon into the detectors layers. Those detectors can benefit for a large duty cycle (almost 100%), very large *Field of View* (FoV) and a good energy calibration, since they are tested with real particle beam before being launched. As a drawback, the weight and the size are limited for this experiment, so that they cannot provide results for energy above hundreds of GeV, where γ-ray flux is typical of the order of $\sim m^{-2}y^{-1}$.

Above those energy, the γs can be detected indirectly from the ground, where the telescopes have a collection area larger than the satellite telescopes one. Ths indirect detection method foreseen to use the atmosphere as a giant calorimeter for astroparticles.

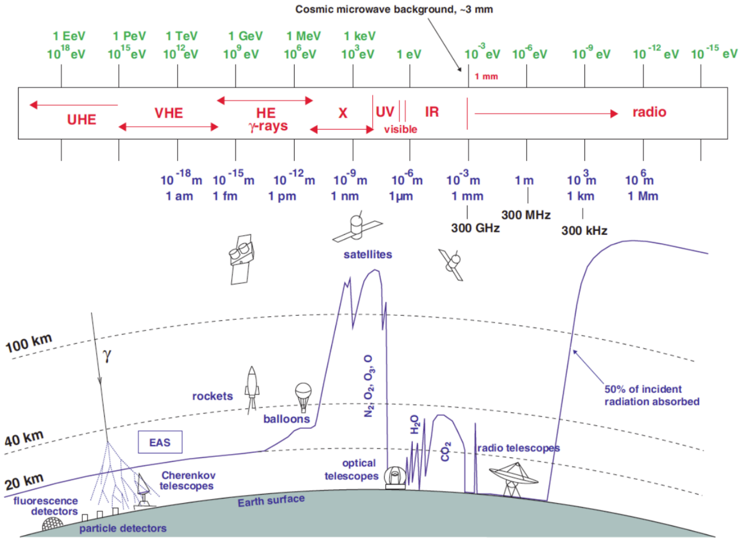

Figure 3.1 Above: observable edges of the EM spectra. Below: the instruments in use to detect the EM spectra at different frequency and the altitude where the photon are fully absorbed in the atmosphere. Credit to [16].

When a γ ray (or a *cosmic ray*, CR) enters the atmosphere, it interacts with atmospheric molecules and nuclei initiating a particle cascade, usually named *Extended Air Shower* (EAS). The charged particles created in the EAS disrupts the local electromagnetic field, and polarized the medium. If the particles travel slow, the perturbation is relaxed back to the equilibrium as the particle pass. However, if the particles speed is larger than the speed of light in the atmosphere, the perturbation remains in the wake of the particle and the energy contained in this disturbance radiates as a coherent shock-wave, generating a bluish radiation light, called *Cherenkov light*. The existence of this type of radiation was proposed by Pavel Alekseyevich Cherenkov [99], who received the Nobel prize along with Igor Tamm and Ilya Frank for the discovery and interpretation of the Cherenkov effect.

The Cherenkov light usually appears as a bluish radiation. In fact the spectra peaks at ~320 nm in the UV band. However, the emission and the observation cherenkov specta can differ due to the interaction with the atmospheric layer (see Fig 3.2). The main sources of attenuation are:

- *Rayleigh scattering*: scattering off air molecules, with a wavelength dependency of λ^{-4}. It affects mostly UV radiation;
- *Mie scattering*: scattering off aerosols, dust and droplets ater. It does not show any strong wavelength dependency;

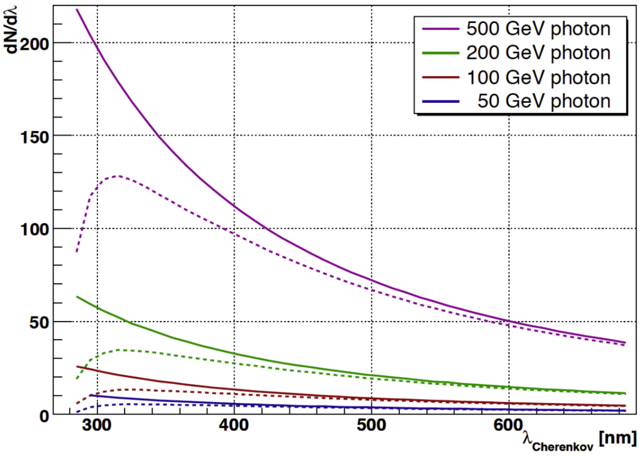

Figure 3.2 Spectra of Cherenkov radiation produced by vertical EAS initiated by γ rays at different energies. The solid line corresponds to the unabsorbed spectra at 10 km altitude, while the dashed line are the observed spectra attenuated by Rayleigh and Mie scattering.

- *Ozone molecules*: these molecules are responsible for the strong absorption of hard UV photons (< 300 nm);
- *H_2O and CO_2 molecules*: they produce absorption in the infra-red band.

The attenuation of the EAS depends also by the zenith angle. In fact, at large zenith angle the cascades develop in the highest layer of the atmosphere and the radiation has to travel a larger path for reaching the observer. Consequently, the probability of being attenuate from the above mentioned processes increases and the, only the EAS initiated by the most energetic particles are significantly detected by the telescopes at large zenith distance.

The Cherenkov radiation is emitted along a conic surface with an aperture angle Θ with respect to the flight direction of the charged particle (see Fig. 3.3a), given by:

$$cos(\Theta) = \frac{c'}{v} = \frac{c}{vn(\lambda)},$$

where $c' = c/n$ is the speed of light in the medium and $n(\lambda)$ is the refractive index of the medium, which value depends by the wavelength λ of the Cherenkov light and v is the velocity of the particle. A Cherenkov cone has an mean aperture of $\sim 1^\circ$ in the air. At a given time, an ultrarelativistic particle travelling vertically through the atmosphere produces Cherenkov light in a ring that propagates downwards with an angle Θ w.r.t. the direction of the particle. The contribution of the whole particles involved in a EAS that emit Cherenkov radiation leads to a full circle on the ground, the so-called Cherenkov light pool (see Fig. 3.3b). In the case of a vertical EAS initiated by a γ ray, the Cherenkov pool extends for a radius

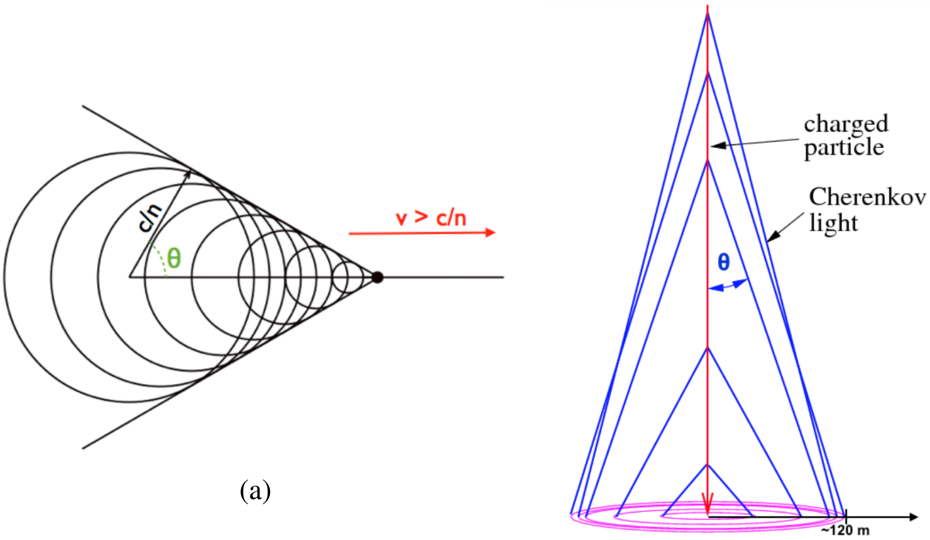

(a)

(b)

Figure 3.3 Left: Schematic view of the Cherenkov radiation emitted by a charged particle moving through a dielectric medium with a velocity v. Right: the superimposition of the Cherenkov light rings produces a circle in the ground, the so called Cherenkov light-pool

of $\sim$120 m, where the Cherenkov photon density can be considered approximately uniform. This is an approximation since the density slightly increases moving in the outer part of the pool, whose origin arises from the increasing of Θ due to the changing in the refraction index while the particle penetrates the atmosphere. The density of Cherenkov photons is proportional to the energy of the primary particle when this is a γ ray, which is not true when the EAS is initiated by a different particle (see Fig. 3.4). Therefore, this relation is taken into account to estimate the energy of the incident γ ray.

Although the major interest is for EASs intiated by γ rays, cascades induced by hadrons (mainly protons) are much more numerous. Even for strong γ-ray sources, like the Crab Nebula, the ratio between the hadron induced and γ-ray induced cascades is considerably high, around 1000 hadronic cascades for each electromagnetic shower above 100 GeV. Therefore, hadronic cascades represents the major source of background during ground based Cherenkov telescopes observation. Thus, a good background rejection power is necessary for getting rid of the background that embedded our observation. For this task, is necessary to understand the characteristics of the both types of showers.

3.1.1 Electromagnetic showers

Above a certain energy threshold ($\gtrsim$ 20 MeV) γ rays can initiate particle cascades through the pair creation process on air nuclei. The electrons and the positrons created out of this

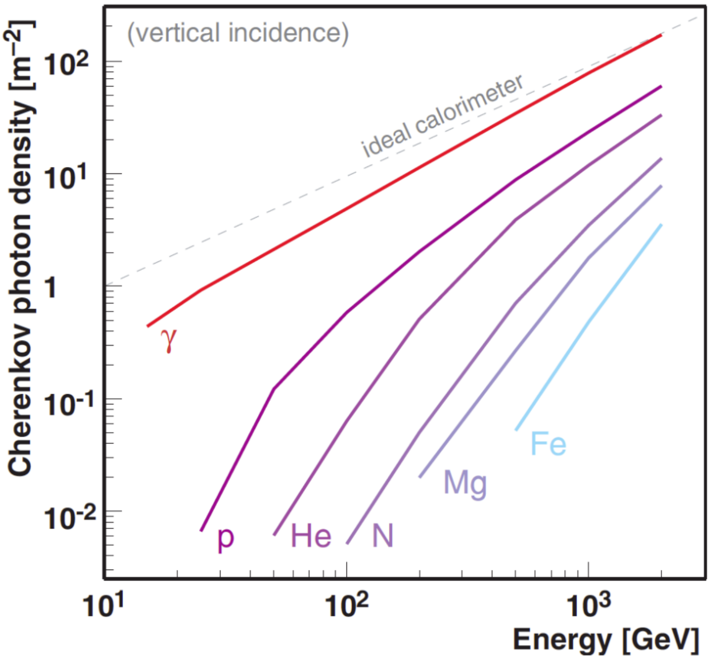

Figure 3.4 Cherenkov photon density within a radius of 125 m from the core shower as a function of photon energy for different primary particles. Credit to [17].

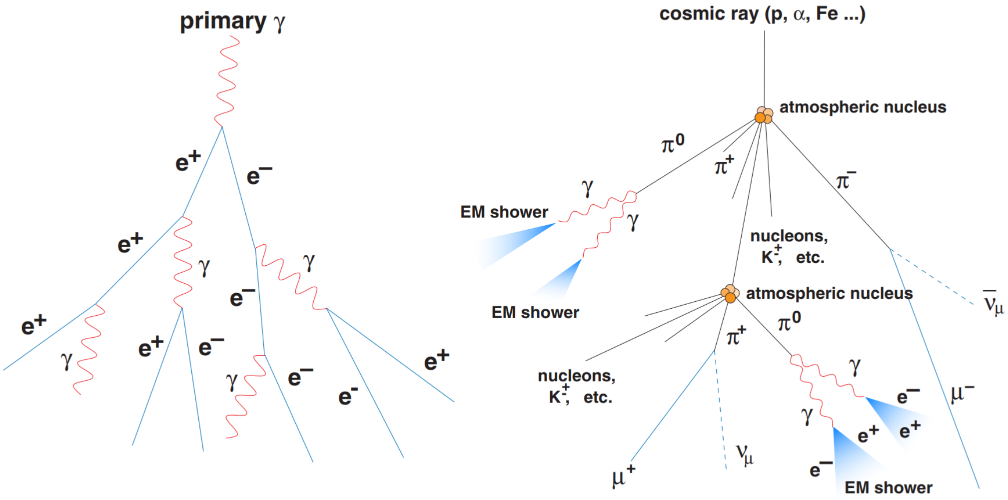

Figure 3.5 Schemes of an EM (left) and hadronig (right) showers. image taken from to [17].

interaction, emit in turn γ rays via bremsstrahlung process. If photons emitted though bremsstrahlung have enough energy, they undergo pair creation as well, leading to a EM cascade (see Fig. 3.5).

The bremsstrahlung *radiation length* (χ_0^e) for electrons and positrons in air and the γ ray *mean free path* χ_0^γ (average distance travelled between collisions) due to pair creation are

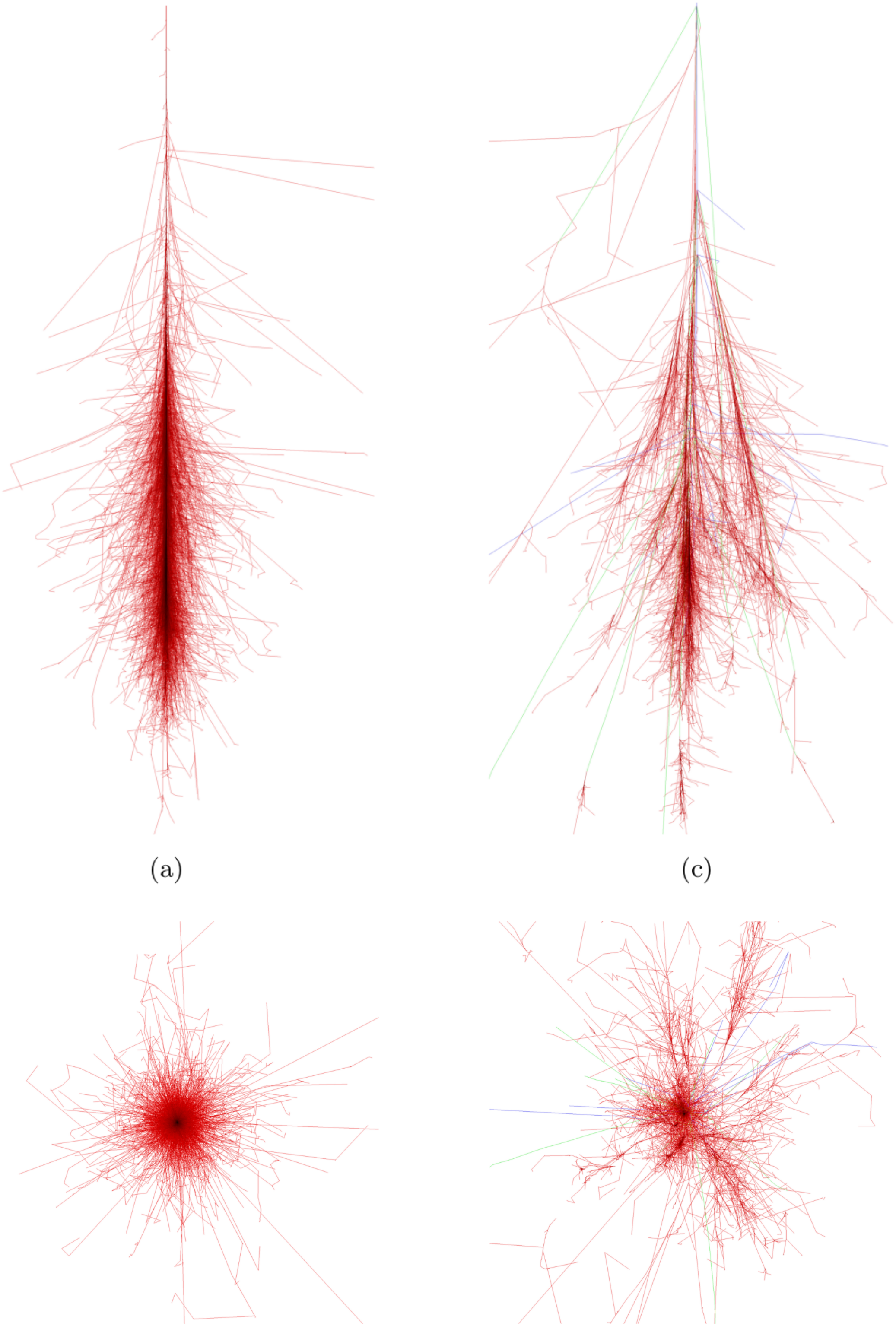

(a) (c)

(b) (d)

Figure 3.6 On the left: MC simulation of an EM cascade initiated by a γ ray of 100 GeV. On the right: MC simulation of an EM cascade initiated by a proton of 100 GeV. Red lines show the γ ray, electron and positron tracks, green lines are used for muons and blue ones for hadrons. The upper plots represent the vertical trajectory, while the lower plots represent the transversal planes.

quite small and comparable ($\chi_0^\gamma = 7/9\chi_0^e$). Consequently, the particles composing a EM shower do not scatter to much from the shower axis, leading to a quite symmetric cascade (see left side of Fig. 3.6). The cross-section for th interaction of γ ray with the atmospheric nuclei is weakly dependent on the photon energy, and therefore the height of the collision of the primary γ ray is similar for different energies, being located at $\sim$ 20-30 km above the sea level (a.s.l.). In each step of the shower, the number of particle is doubled, while the particle energy halves, until reaching a critical energy of $E_C = 86$ MeV where the ionizing energy loss dominates over the bremsstrahlung. At this moment the number of particles reaches its maximum. The altitude at which this conditions is fulfilled is called *height of the shower maximum*, $H_{max} \propto 1\ln(E)$, where E is the energy of the primary γ ray.

3.1.2 Hadronic showers

Hadronic cascades are those produced by interaction between cosmic rays and atmospheric nuclei. Normally, the primary particle of this interaction is a proton which gives rise mostly (90%) to pions (approximately in the same proportion π^+, π^- and π^0). Beside pions these collisions produce kaons and nuclei (see Fig. 3.5). The cascade stopped when the energy per nucloen is less than $\sim$ 1 GeV, the minimum energy needed for pion production. Different components can be distinguished in the hadronic showers:

- **Hadronic component:** composed by nuclei and mesons (like pions). Both of them are heavy particles and therefore, the transerred transcersal momentum in each collision is high;

- **EM component:** composed by secondary photons, electrons and positrons mostly produced by the decay of π^0 meson. If these EM subcascades are deteced, the distinction between them and a γ ray-induced shower is almost impossible;

- **Muonic component:** muons and neutrinos are produced by the decay of charged pions. Neutrinos cannot be detected by Cherenkov telescopes as they cannot produced Cherenkov radiation due to the lack of charge. On the other hand, muon can create Cherenkov light and thus, be detected.

In general, hadronic showers are wider than the EM ones because of the large transversal momentum the kaons and pions receive. Furthermore, this type of cascade undergoes more subshowers leading to a not only wider but also asymmetric EAS. In Fig. 3.6 MC simulations of *gamma* ray- and hadronic-induced cascades are presented, where the shape difference is evident. Moreover, the EM showers develop faster (3 ns) than the hadronic ones (10 ns).

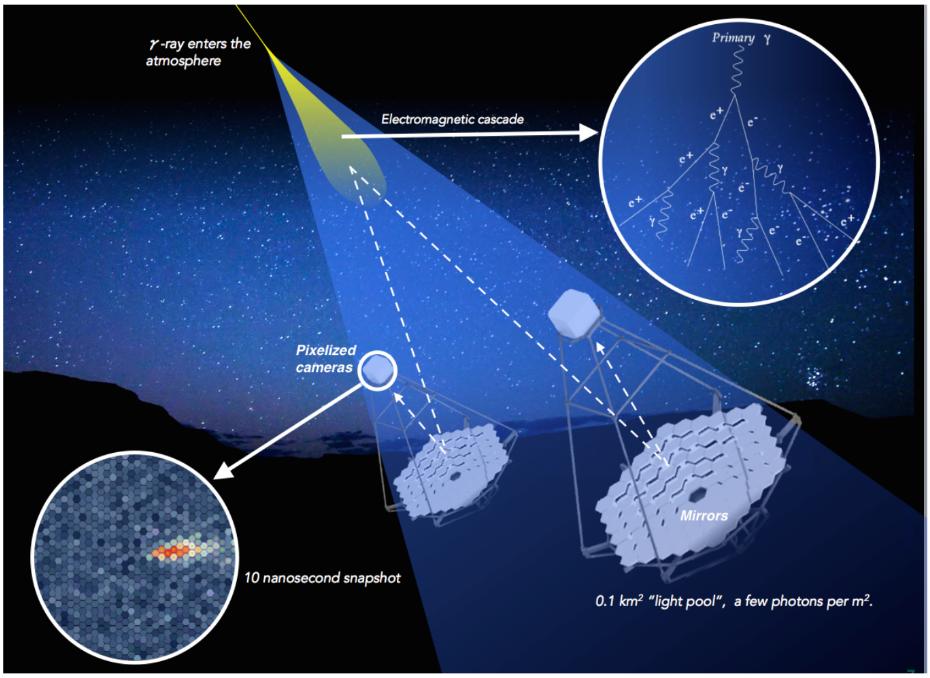

Figure 3.7 Sketch of the IACT technique. The cherenkov light from the cascade is reflected by the mirrors and collected in the camera. Modified image from www.cta-observatory.org.

Thus, among the image feature left on the telescopes, the development timing can be used as a parameter to distinguish between these type of showers.

3.2 Imaging atmospheric Cherenkov technique

The *Imaging Atmoshperic Cherenkov Technique* bases its study of γ rays on the observation of the Cherenkov radiation produced in EAS. Fig. 3.7 shows how ground based cherenkov telescopes work: if the telescopes are inside the Cherenkov light pool, part of the Cherenkov light is reflected in the mirrors and collected in their fast pixelized cameras. The images created are projection of the EASs, from which spatial and timing information is obtained. The Cherenkov light density at ground level is used to reconstruct properties of the initial particle colliding the atmosphere as:

- the initial incoming direction of the particle;
- the arrival energy at which the interaction took place;
- the nature of the interacting particle, being the events classified into γ-like (hadron-like) showers.

Figure 3.8 Picture of the MAGIC telescopes at el Roque de los Muchachos. Image taken from https://magic.mpp.mpg.de/.

Cherenkov flashes are very fast ($\sim$ 3 ns), for which precise and very efficient detectors are needed. Photomultiplier tubes (PMTs) are commonly used in *imaging atmoshperic Cherenkov Telescopes* (IACTs) as they have proven to fulfil these requirements. These detectors can multiply the photoelectron produced by the incident light by a factor 10^9, in multiple dynode amplification stages, enabling individual photon detection. A fast response time is also important to reduce the collection of undesirable photons from the light of the night sky. This is the so-called Night Sky Background (NSB) that is formed by the stars' light, airglow, polar and zodiacal light and artificial lights. Typically, IACTs are built in arrays of telescopes, performing stereoscopic observations. Such operation mode will both improve the angular resolution of the instrument and improve the rejection of the NSB, since EAS events would leave a trace in the telescopes that NSB is unlikely to reproduce.

Nowadays, the Silicon Photomultiplier (SiPM) tubes are becoming very popular in the field[1], being much more robust than PMTs. However their small size (area $\lesssim$ cm^2) makes covering the usual IACT camera ($\sim$ m^2) still challenging.

3.3 The MAGIC telescopes

The *Florian Goebel Major Atmospheric Gamma-ray Imaging Cherenkov Telescopes* (MAGIC) is a stereoscopic system consisting of two 17 m diameter imaging atmospheric Cherenkov

---

[1] http://www.astri.inaf.it/

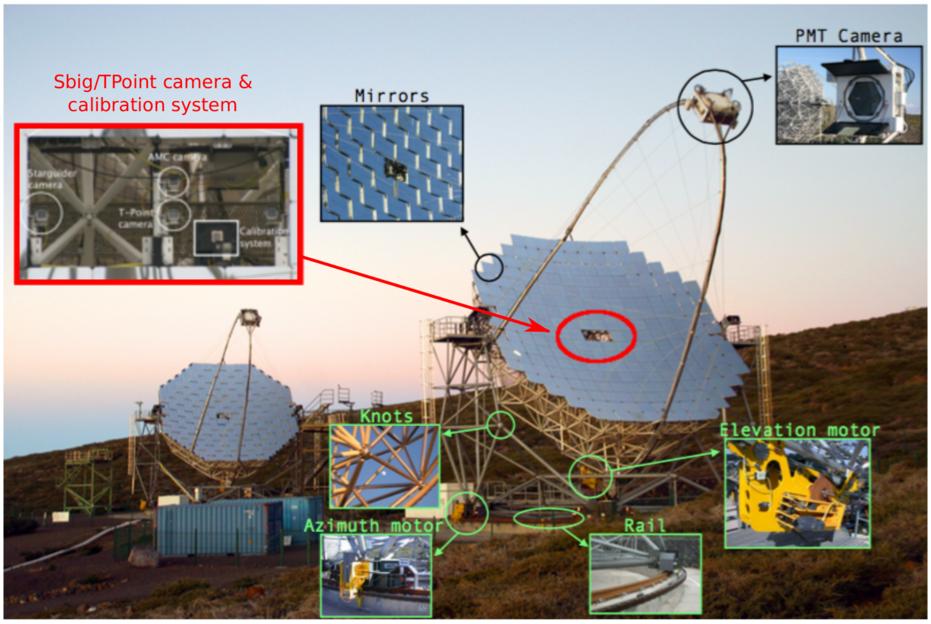

Figure 3.9 Picture of the MAGIC telescopes (MAGIC I behindm MAGIC II on the front) with some of their hardware subsystem highlighted. Image modified by [18].

telescopes (see Fig. 3.8) located in Roque de los Muchachos observatory in the Canary island of La Palma, Spain (28.8° N, 17.8° W, 2225 m a.s.l.).

MAGIC started as a stand-alone telescope, going through major upgrades during the years: in 2009 the second telescope (MAGIC II) started operation, while in 2012 the digital trigger, readout and MAGIC I camera were upgraded to the final version still in use. In this stereoscopic observational mode, the system achieved a energy threshold of 50 GeV at low zenith angles and an integral sensitivity of $0.66\pm0.03\%$ of the Crab Nebula flux in 50 hours above 220 GeV [20].

3.3.1 Hardware design

The MAGIC telescopes were designed to achieved lowest energy threshold and fast repositioning, for detecting efficiently γ ray and rapidly following transient events. Different hardware systems compose the experiment (depicted in Fig. 3.9) and are listed below:

- the structure and the drive system;
- reflector and mirror;
- camera;
- trigger and readout systems;

- atmospheric monitoring system.

3.3.1.1 Structure and drive system

The structure is identical for both telescopes. The 17 m reflector is sustained by an octagonal structure made of light carbon-epoxy tubes, held together through aluminium knots (see Fig. 3.9). The camera is held by a single aluminium tubular arc, secured to the main structure by 20 steel cables. Those materials are strong enough to sustain the weight and the tensions the telescope is exposed during the observations, while being at the same time light enough ($\sim$ 20 tons including the reflector and the camera) to allow MAGIC to be fast at reposition. In fact, MAGIC can repoint at any direction on the sky in less than 20 s.

The telescope has an alt-azimuthal mounts, which allows the telescope to move along the *Azimuth direction* (Az) and the *Zenith distance* (Zd). The structure lays on six bogies on a circular rail, where two 11 kW motors move the telescopes in Az, while a motor of the same power located behind the dish structure takes care of the Zd movement. The allowed Az range is from -90° to 318° while the telescope can moved from -70° to +105° in Zd. During the days the telescopes points through the north (Az = 0), so that the reflector are never directly exposed to the sunlight. Small bending of the structure during the telescopes movement are corrected before (and during) the data taking, through the Active Mirror Control (AMC).

The pointing of the telescope is constantly checked during the observation with the *Starguider camera*, a Charged-Coupled Device (CCD) camera located at the center of the dish. Using a set of Light-Emitting Diodes (LEDs) installed around the camera that provide a reference frame, this camera is checking the stars distribution in the FoV observed. The pointing is then corrected by the so-called bending model. This is created comparing catalogued and observed coordinates of $\sim$150 bright stars observed along the observational period (period between two consecutive full moon breaks). This allows to achieved a pointing precision of 0.01°.

3.3.1.2 Reflector dish

The reflecting surface of both MAGIC telescopes cover an area of 234 m^2, made by individual mirror panel of $\sim$ 1 m^2 each (see Fig. 3.10). The panels are arranged in a parabolic and therefore isochronous shape. This lowers the timing difference in the reflected light of less than 1 ns (Cherenkov light arrival spread time is $\sim$2 ns), thus it is possible to apply a smaller integration signal window and hence, to reduce the background (mainly NSB) contamination. The focal length (distance at which the camera is placed) is 17 m, as the diameter of the dish.

Figure 3.10 Particular of the mirror surfaces of MAGIC I (left) and MAGIC II (right).

The goodness of the reflector is controlled each night measuring the Point Spread Function (PSF) of the telescope[2], which values is typically ∼ 10 mm (whether conditions can enlarge this value). During the night the optimal focusing is maintained through the AMC system. The AMC can move the mirrors using two actuators installed on the back on each mirrors with a precision of less than 20 μm, based on a Look-up Table (LUT) binned in Az and Zd. Despite this efficiently system, after a major storm period the focusing accuracy of the instruments worsens, with an increasing of the PSF to 12-15 mm, and takes a few days to recover.

The reflectivity usually worsens during the summer months because of Calima effect, that takes the sahara sands till the MAGIC site.

3.3.1.3 Camera

The PMT cameras of the telescopes play a key role in the overall instrument. After the final upgrades in 2012 the cameras of both telescopes are identical and composed by 1039 PMTs arranged in a circle of 1 m diameter covering a FoV of 3.5° in the sky (see Fig. 3.11). The PMTs are grouped in 169 clusters of 7 pixels for an easier installation and access for maintenance. The PMTs are cylindrical with a diameter of 25.4 mm, made by the Japanese manufacturer Hamamatsu. The PMTs are composed of a hemispherical photocathode and six dynodes. Each PMT has a hexagonal Winston cone mounted on top, in order to increase the amount of collected light and to avoid gaps between the circular pixels. A DC-DC converter is mounted at the base of the PMTs, providing the bias voltages to the PMT itself and to the readout and trigger electronics. The High Voltage (HV) supplied tot he PMTs during Standard operation is of ∼900 V on average and individual values are tuned with

---

[2] The PSF is defined as the diameter at which 39% of the light from a point-like source is contained

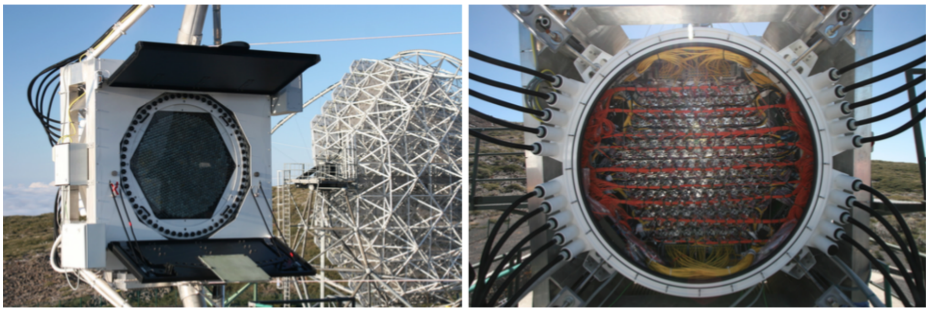

Figure 3.11 The front (left) and the back side (right) of the MAGIC cameras after 2012 upgrade.

the flat-field procedure[3]. The PMTs signal is processed by a pre-amplifier stage and then transmitted by individual optical fiber 162 m long to the *Counting House*, where the readout is performed. In order to enlarge MAGIC duty cycle, cameras can operate with different HVs values according to different NSB level, in particular during moonlight observations the PMTs operate with a relative low gain. This reduce the amount of charge that hit the last dynode (anode) during bright observation, preventing fast ageing effect. Moreover, the PMTs is automatically switched off whether the anode currents are larger than 47 μA and the telescopes are not operated if the mean current is above 15 μA. The camera is protected from environment conditions and sun light by a plexiglass window installed in front of the light collectors and a movable lid in front of it.

The camera is constantly calibrated during the observation using a Nd:YAG laser emitting at 355 nm, for homogenize the PMTs response in the whole camera. The laser is located inside the Calibration Box, which is placed at the center of the mirror near to the Starguider camera. The light intensity can be adjust by means of calibrated optical filter placed right after the laser output. To achieve an homogeneous distribution of the calibration light over all the PMTs, the laser beam is diffused through an Ulbricht sphere.

3.3.1.4 Readout and Trigger system

The optical fiber ends in the Counting House, a building placed at $\sim$ 100 m away from the telescopes, that host the readout, trigger and data-acquisition systems. The optical signals arrive in the CH and are converted back to electrical signal in the receiver boards using

---

[3] Flat-fielding is a correction technique that consist on taking a camera image with uniform illumination and divide the original images by this flat-fielded image. Flat-fielding corrects variations in the pixel-to-pixel sensitivity by compensating for different gains and dark currents in order to achieve a uniform output in the detector.

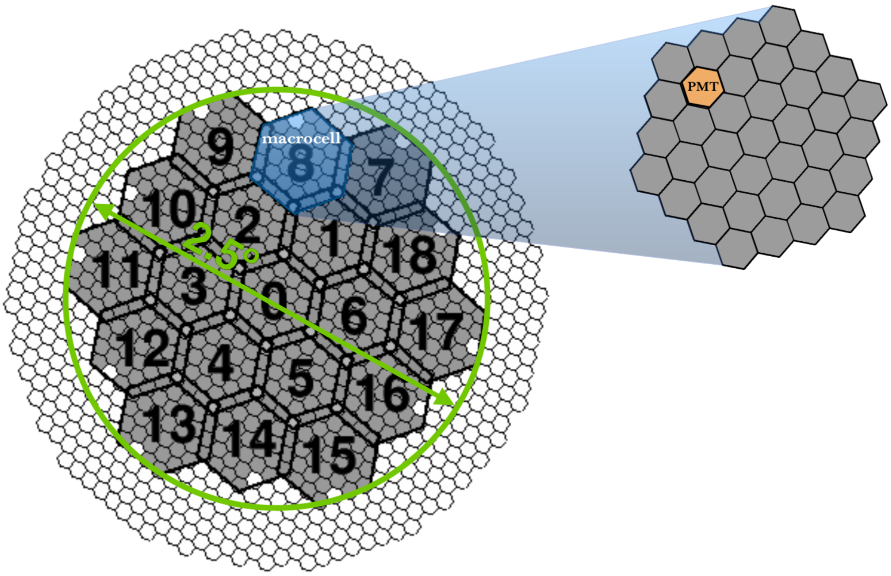

Figure 3.12 Hexagonal L1 macrocells in the current MAGIC camera version, each of which contains 37 PMTs (one blind). The numbers on the macrocells are the internal MAGIC identification. The hexagonal shape of the PMTs is given by the Winston cones. The trigger FoV is 2.5° diameter. Figure taken from [18].

photodiodes. Each signal is then split into two copies, one for the readout and one for the trigger.

Trigger system

The MAGIC trigger decision is performed using the informations carried out by the PMTs located in diameter of 2.5° in the camera (trigger region, see Fig. 3.12). The standard trigger decision is divided into three logical steps.

- **Level 0 (L0) trigger:** at this stage, an amplitude discriminator operates individually on each PMTs of the camera in the trigger area. The trigger rate depends on the Discriminator Threshold (DT) set on each PMT. During the data taking the DTs are controlled by the Individual Pixel Rate Control (IPRC) control routine, which regulates the DTs in order to keep the L0 rate into a determine interval of values. These limits are optimized to provide the lowest energy threshold while keeping the accidental rates (NSB eventS) at a level that can be handled by the DAQ, to prevent for larger dead time period. The rate intervals are adjusted according to the HV setting used.
- **Level 1 (L1) trigger:** PMTs are arranged in 19 overlapping hexagonal cells, called macrocells. The L1 searches for spatial anc coincidence between neighbour pixels

inside a macrocell. When a programmable number of *n* Next Neighbour (NN) have a L0 coincidence, the L1 trigger rises a square signal. For standard steroscopic operation, 3NN configuration is used, however n=2, 4, 5 are also used.

- **Level 3 (L3) trigger:** L3 trigger combined the informations of the L1 from both telescope, searching for timing coincidence. The amplitude of the time windows change with the pointing, since the delay of the signals from the two telescopes depends on their relative orientation. The maximum delay that can be handled is of 200 ns, which creates a forbidden region where the telescopes cannot triggered.

When an L3 trigger is issued, the signal is transmitted to the DAQ which saved the event on the disk.

There are two alternative trigger that have been installed for improving the performance at low energies, the Sum Trigger-II [100] and the Topo-Trigger [101]. The former acts by preventing the PMTs after-pulse, caused by foreign atoms ionized and backscattered inside the PMTs. The latter takes the advantage the correlation in the position of the marcocells triggered in both telescopes from a γ event, compared to the random noise produced inside the camera from NSB.

Readout system

The second copy of the PMTs signals is sent to the readout system. The MAGIC upgraded readout system is based on the Domino Ring Sampler 4 (DRS4, see Fig. 3.13) analogue memory chip [102]. The analogue signal from each receiver channel is connected to an array of 1024 capacitors. Each of the capacitor is charged by the signal for a time that is proportional to the period of the clock controlling the switching (the so-called Domino Wave). The capacitor are hence overwritten each 1024 clock cycle. When a trigger is received, the Domino wave stopped and the charge value of a few of those capacitors is digitized by an Analogue-to-Digital converter (ADC). The positions of the capacitors to be read is determine by the Az and Zd pointing, in order to cover the evolution of the arrival Cherenkov photons.

The system can perform a sampling at 1.66 Gsample/s and 50 capacitors are stored in each pixel for each event. Those capacitors are read at 33 MHz, producing a dead time of 27 μs. The signal of each pixel is then recorded as a 30 ns waveform (DAQ window) storing the raw-ADC counts, as reported in Fig. Since 50 capacitors are stored, the resolution in the DAQ window is of 0.6 ns.

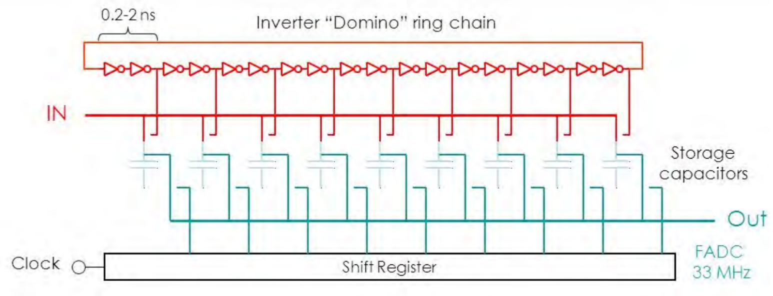

Figure 3.13 Scheme of the DRS4 chip Domino ring chain redout.

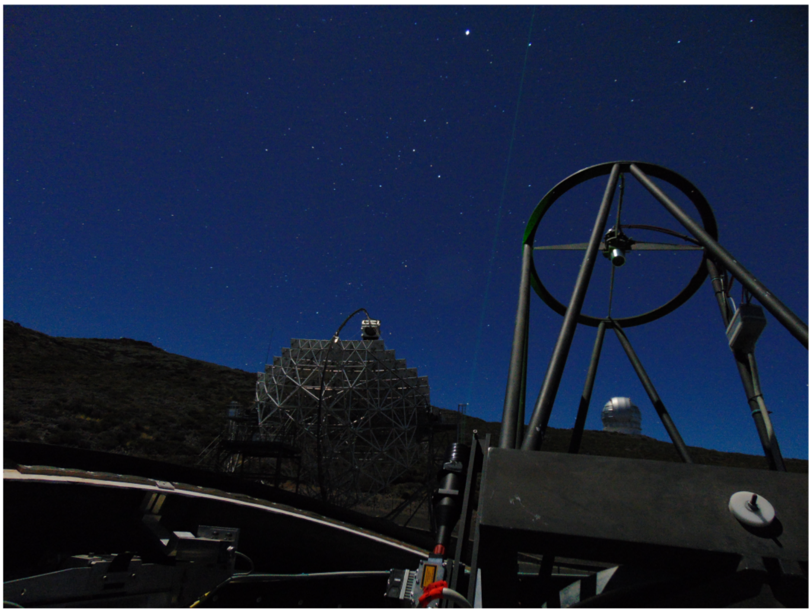

Figure 3.14 The LIDAR telescope in operation. Credit to Martin Will.

3.3.1.5 Monitoring weather system

The Cherenkov light emitted by the particle in the EAS has to pass several atmospheric layer, where the weather conditions can modify the light pool at ground level. In particularly, clouds absorb Cherenkov light, thus the resulting light density is lower than the real one. Hence, three instruments for monitoring the weather and atmospheric conditions have been installed at the MAGIC site in order to evaluate if observations can be safely performed.

- **AllSky Camera:** an camera installed on the roof provides a wide FoV optical image of the Sky over the telescopes. The shifters use it to have a qualitative estimation of the weather and clouds outside.

- **Weather station:** it is located on the root of the CH, with the aim to evaluated the main safety weather conditions, like humidity, wind speed and direction. These informations are processed by the telescopes control center to automatically evaluate whether the weather conditions satisfied the requirements for observing.

- **Pyrometer:** this instrument is installed in the center of the reflector dish (as the Starguider camera and the calibration box) pointing to the same direction of the telescopes. It measures the sky temperature and provides an atmospheric transparency estimation, through the *cloudiness* parameters:

  $$c = \frac{T_{low} - T_m}{T_{low} - T_{up}}.$$

  T_{low} and T_{up} are the temperature of the sky at its worst and best conditions respectively, which are set to $T_{low} = 250$ K and $T_{up} = 200$ K. T_m is temperature measured by the pyrometer.

- **LIDAR:** this is the most important instrument which evaluate the cloud density distribution along the line of sight (l.o.s.) of the telescope pointing [103]. Its measurements are used further in analysis to establish whether atmospheric corrections should be applied. It is located in an independent dome on the CH roof (see Fig. 3.14). The LIDAR works by flashing a pulsed laser at a position shifted by 3° from the observed source. The light is backscattered by the clouds and the aerosols on the sky. The transmissivity of the sky is measured as a function of the arrival time distribution of the backscattered light.

  LIDAR operates during MAGIC observation, providing transmission estimation at different altitudes of 3, 6, 9, 12 km. MAGIC data are classified into three Atmospheric Optical Depth (AOD) ranges. For transmission values larger than 85% the AOD is

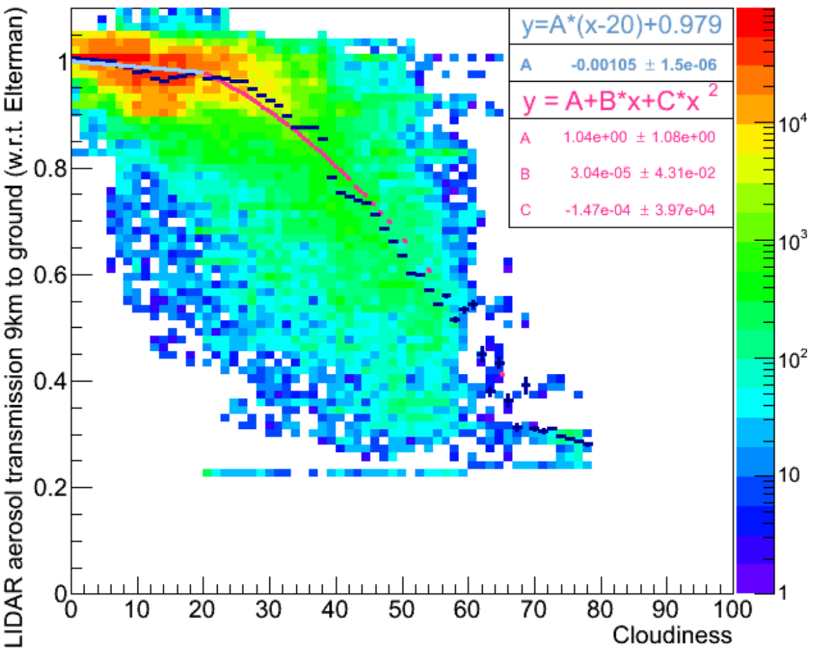

Figure 3.15 Correlation between LIDAR AOD above 9 km with cloudiness. In case LIDAR data are not available, we can rely on the Cloudiness to discrim- inate between good and bad data. In such a case, only data with very good LIDAR T_{aer} are analysed.

considered perfect and the data can be used for science with no need for correction. For transmission between 70% and 85% the data are considered to be good, but corrections are recommended, since the physical parameters estimation is bias due to the differences w.r.t. the MC simulation (where no clouds have been simulated). LIDAR corrections are instead required for transmission down to 55%, while below 55% the systematic uncertainties and bias due to the bad weather does not allow to do any science with those data.

In the case LIDAR data are not available, data correction cannot be applied. However, due to the good correlation between LIDAR transmission above 9 km and cloudiness, we can use this parameter to select data with good weather conditions (see Fig 3.15).

3.3.2 Data taking

The low gain PMTs of MAGIC camera allow the telescopes to observe under dark and moderate moonlight conditions. The maximum duty cycle in a year corresponds to a 18%, 1500 hr/year, of which ∼65% is observed and the rest is lost because of technical problems or bad weather conditions. Recently special hardware settings allow observations also during moon presence [104].

The data taking is controlled by the Central Control (CC) software, called Super-Areuchas [105], responsible fdataor all the subsystems. It receives and sends reports, monitoring each hardware subsystem and provides access to most of the functionalities of the telescopes though a LabView interface.

Usually, during a data taking run, *pedestal*, *calibration* run are taken before several *data* run. Pedestal run consists of several events (typically 2000) acquired with the camera open and trigger by an internal clock. This is needed for evaluating the background level which is lately subtracted during the data calibration process. During the calibration run, the camera triggers the pulses produced by the calibration box, which are used for calibrating the conversion from ADC counts to photoelectrons. Data run are taken pointing to the target observed using the trigger chain described in Sec. 3.3.1.4. Moreover, during the data taking, interleaved pedestal and calibration run are taken during the data taking to constantly calibrate the different channels

MAGIC can observes, during data run, using two standard observation modes: tracking (ON/OFF) mode or *wobble mode*.

- **ON/OFF mode:** in this mode, the telescopes point directly the source, maintaining the nominal position of the target at the center of each camera. In this mode, the *ON region* (i.e. the FoV where the signal from the source is expected) and the *OFF region* (i.e. where the background signal is estimated) are observed separately. The OFF should be taken under conditions as similar as possible with the ON, with no candidate source in the FoV, in order to have a reliable estimation of the background.

- **Wobble mode:** in this case, MAGIC tracks two or four different positions situated at a certain distance w.r.t the nominal position of the source. For standard observation, the offset angle is 0.4° optimized for point like sources (see Fig. 3.16). Usually each wobble position is changed every 15/20 minutes to ensure a uniform coverage in Az between the two positions and avoiding possible bias. The main advantage of this technique is that the OFF region is acquired simultaneously with the ON under the same exactly conditions, and no dedicated OFF observations are needed. In such a way, the background estimation is more robust and reliable with respect the ON/OFF mode.

  The wobble observation mode comes with two drawback: the γ-ray detection efficiency decreases due to the shift of the source, and the off-center source position can create a bias due to camera inhomogeneities (specially critical if the distribution between the different wobble is not balanced). Furthermore, stereo observations with two telescopes

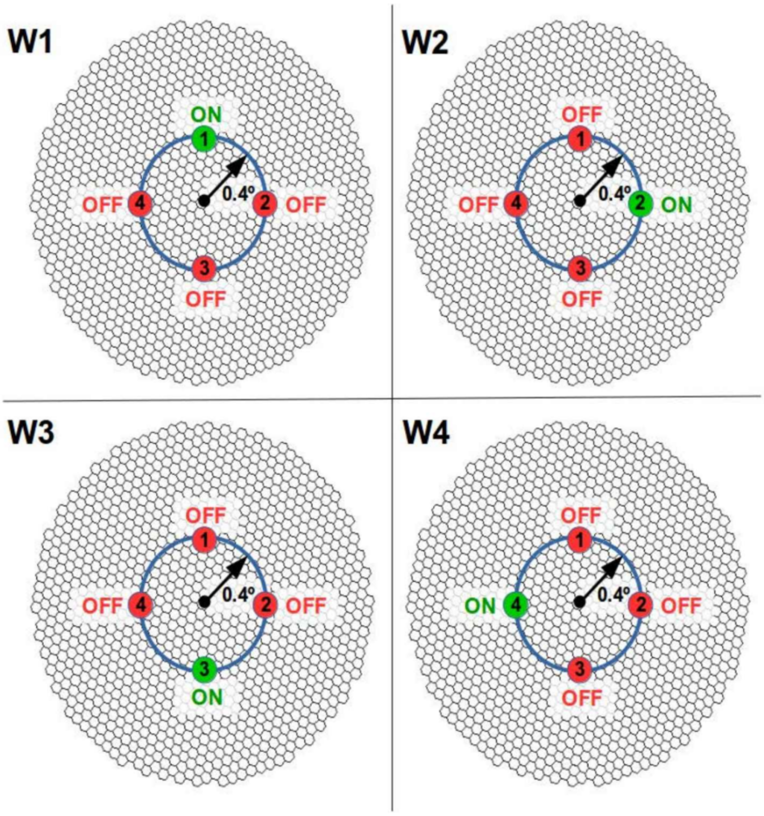

Figure 3.16 Scheme of the different wobble positions. The background region of in W2 (W4) position is used to estimate the background (OFF region) for the W1 (W3) position in order to avoid camera asymmetries and inhomogeneities. Image taken from [19].

originate an uneven acceptance along the FoV, referred to as the “stereo blob”, caused by the broken azimuthal symmetry due to the relative orientations of the telescopes.

3.3.3 Data analysis chain

The waveforms recorded at readout level are processed using the standard MAGIC Analysis & Reconstruction Software (MARS [106]). This C++ software based on the ROOT[4] libraries, converts the raw ADC counts into processed high-level data. The final goal of the analysis is to determine the characteristics of the incoming particle: the incoming direction and energy of the γ-ray candidate.

The data are processed in different stage and reduced in order to be suitable for the high level analysis.

---

[4] https://root.cern.ch

3.3.3.1 Monte Carlo simulation

IACT measurements strongly rely on MC simulations. The reason for that is that is not possible to have a controlled γ-ray source for calibrating the telescopes response, so the a MC γ-ray simulation is needed.

The MC simulations are used in two steps of the analysis: a first sample (train sample) is used to build a look-up tables and a multivariate decisions tree (random forest), which are employed for the energy and direction reconstruction and γ/hadron separation, as explained in the following sections. A second sample (test sample) is used to estimate the telescope response functions (or instrument response functions, IRF), which consist in: the *migration matrix*, that is the Probability Density Function (PDF) of the energy estimator as a function of the energy; the *effective area* (EA), the efficiency of the instrument at detecting γ rays, typically represented by an ideal surface perpendicular to the photon incoming direction.

In the analysis framework, MC simulations are produced in three different steps: first, the EAS generated by the primary particles are simulated, where all the particles composing the showers are tracked till they energy is high enough to generate Cherenkov light (CORSIKA ref); second the interaction of the Cherenkov light with the atmosphere and the reflection on the telescopes mirrors toward the camera plane are simulated (Reflector software); finally the Camera response is simulated (Camera software), taking into account among all the PMTs quantum efficiency, trigger parameters, electronic noise and the NSB. At this stage, calibration and pedestal run are simulated.

In MAGIC ringwobble MC, with source centred at 0.4° from the camera center, and diffuse MC, with events generated uniformly till a certain distance from the center of the camera, are used. MC simulations should accurately reproduce the telescopes response. Hence, each time there is a major hardware intervention or others effect that modify the telescopes response, a new version of the MC is released. In this thesis the data belong to three different periods:

- **ST0309** data took before June 2019, related to nominal conditions of the telescopes;
- **ST0310** data took between June and October 2019, where Calima phenomena reduced the reflectivity of the mirrors;
- **ST0311** data took after October 2019, when the reflectivity come back to a nominal value.

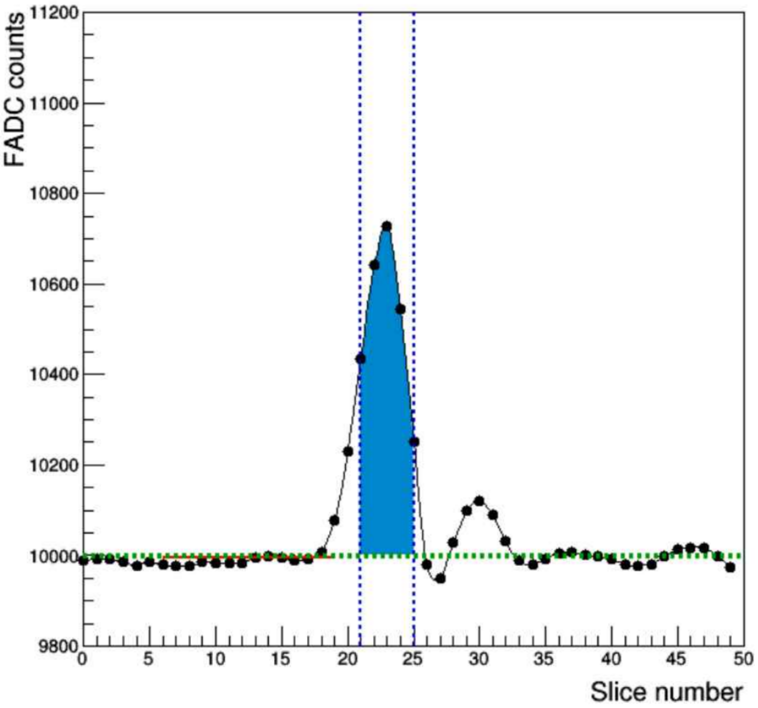

Figure 3.17 Charge extraction from a calibration events, similar to the pulse created by Cherenkov light. Dashed green area is the baseline level computed from the pedestal event. Blue dashed lines delimit the five consecutive slices that give the maximum integrated charge (filled area).

3.3.3.2 Signal extraction and Calibration

The first step in the analysis concern how to extract the signal from the DAQ window and convert the ADC counts into number of photoelectron. First of all the baseline is estimated by the mean value of a Gaussian fit to the charge distribution in the pedestal events. Then, an algorithm looks for the waveform for the largest integrated charge in a sliding window of 3 ns width (see Fig 3.17). Once the integration window is fixed the arrival time is obtained from the center of this window.

The conversion from ADC counts and phe is performed using the F-factor method over the calibration run [107]. For a calibration pulse, the number of phe follows a poissonian distribution, with mean N and standard deviation $\sqrt{N}$. If the distribution of the observed pulse in ADC counts has a charge $<Q>$ and a deviation σ_Q, both distributions are connected by an F-factor F that can be measured in lab, different for each PMTs:

$$F\frac{\sqrt{N}}{N} = \frac{\sigma_Q}{<Q>}.$$

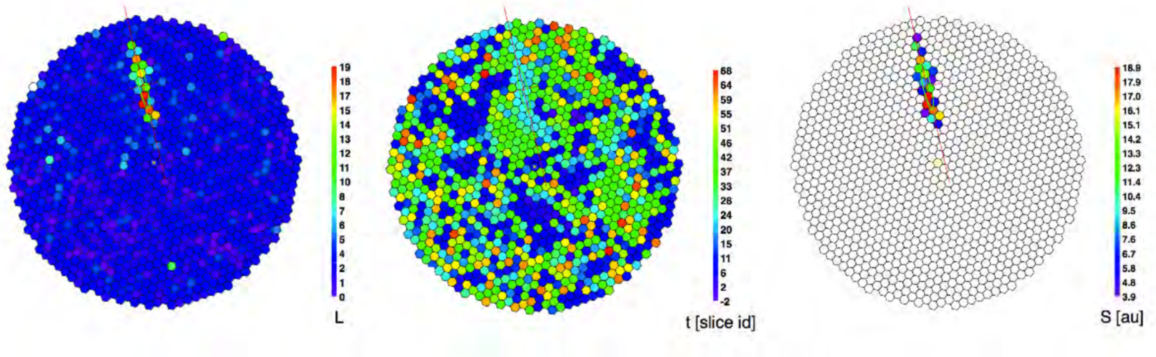

Figure 3.18 Charge distribution (left) and time distribution (center) along the camera. On the right, the final cleaned image formed by the core and boundary pixels.

Then the conversion factor C between ADC counts and number of phe is given by:

$$C = \frac{N}{<Q>} = F^2 \frac{<Q>}{\sigma_Q^2}.$$

Interleaved calibration events are needed to constantly monitoring C during data taking, since the optical transmitter gain is not constant in time.

The data after the calibration are complemented with the informations from all the other subsystems.

3.3.3.3 Image cleaning and hillas parametrization

Image cleaning aims to keep only pixels in which Cherenkov photons from the shower produced signal, discarding those pizels that do not contain useful information of the shower image [108]. This is perform by a program called *Star*, which search for group of 4, 3 or 2 neighbour pixels with a summed charged above a given threshold (Lvl1, 6 phe) and within a given time window. Once the core pixels are identified, all the neighbouring pixels with a charge larger than a given threshold (Lvl2, 3.5 phe) and within a time windows of 1.5 ns are also included in the final image (see Fig. 3.18).

The image obtained after cleaning is parametrized by an ellipse. Momenta up to the second order of the light distribution on the camera are used to parametrized the image, and called *Hillas parameters* (see Fig. 3.19). Those parameters are used later to reject background events and infer the energy and the arrival direction of the incoming particle. The most relevant are:

- *Size*: Total charge (in phe) contained in the image, closely related with the energy of the particle.

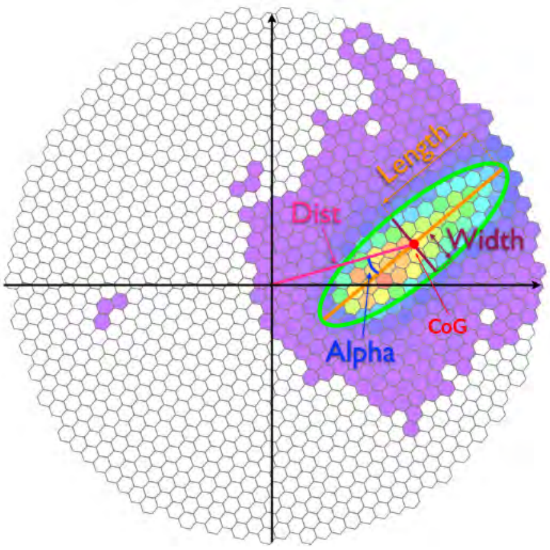

Figure 3.19 Cleaned and parametrized event image with some of the Hillas parameters indicated. Modified from [19].

- *Length*: Second moment along the major axis of the image, related with the longitudinal development of the shower.
- *Width*: Second moment along the minor axis of the image, related with the lateral development of the shower.
- *Center of Gravity (CoG)*: it is computed as the mean of the X and Y coordinates weighted mean signal along the camera.
- *Conc(N)*: fraction of the image concentrated in the N brightest pixels. It is a measurement on how compact is the image, and it is generally larger in γ-ray induced shower than in hadronic ones.
- *Number of Island*: Number of isolated groups of pixels that survived the cleaning. γ-ray shower typically produced a single island, while hadronic one may contains two or more islands.

3.3.3.4 Stereo reconstruction

MAGIC typically observes in stereo mode, thus the images of the two telescopes have to be merged in a single one. A program named *Superstar* combines the informations from both instruments to produce stereo parameters (see Fig. 3.20) that are later used for the energy and direction reconstruction. The main parameters are:

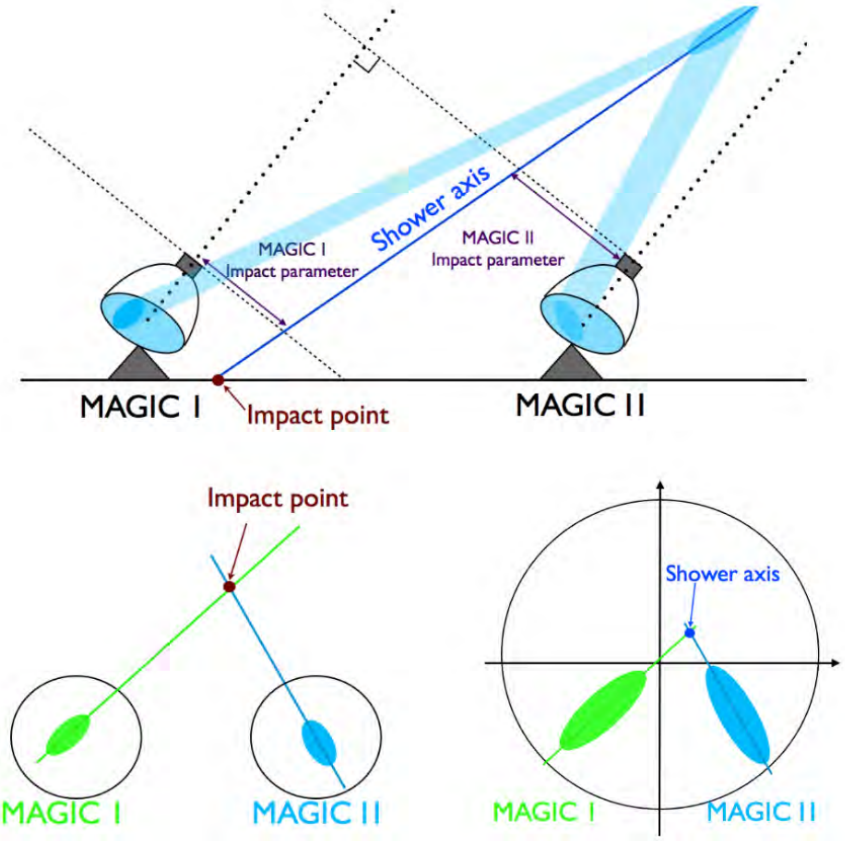

Figure 3.20 Top: Picture of the geometry of a stereo event. Below: Reconstruction of the impact point on the ground (left) and the shower axis (right) on the camera plane. Credit: Dr. R. López

- *Shower axis*: The direction of the shower is obtained by the intersection of the major axis of the two images. This information, combined with the pointing positions gives the impact point, which finally determine the shower axis.

- *Impact parameter*: Distance between the shower axis and the center of the telescope mirror (computed for each telescope).

- *Height of the shower maximum*: it is defined as the height in which the maximum of the shower occurs in terms of number of particles.

  All the steps before the stereo reconstruction are performed automatically by an On Site Analysis routine. The most of the analysis in MAGIC started by using Superstar data, whether no non-standard cleaning needed to be applied.

3.3.3.5 Data quality

Data quality cuts are necessary to guarantee a reliable results. *Quate* executable takes care of cut the events on the base of the informations from the data itself and the different subsystems monitoring the weather conditions. In standard analysis the most important cut are based on the atmospheric transmission at the time the event was recorded, measured by the LIDAR. Quality cuts can also be used in case of a miss-function of a subsystems, looking at the trigger rates or at the PMTs average currents.

3.3.3.6 γ/hadron separation

After Superstar and Quate data selection, the main background is represented by hadronic showers, which rate are order of magnitude larger than the γ-ray one. A program named *Coach* builds look-up tables and multivariate decision trees (*random forest*): the former are used for the energy reconstruction, while the latter are used to perform γ/hadron separation and reconstruct the arrival direction. Then a program named *Melibea* makes each Superstar events goes through the random forest and the look-up table, assigning a reconstructed energy E_{est} or E', an arrival direction and a tag (*hadronness, h*) indicated how likely the event has been initiated by a γ ray.

The random forest algorithm [109] uses a training sample representing γ and hadronic events. The γ-ray training sample is obtained by the MonteCarlo simulation, while the hadronic one is obtained from real data. Since the rate of hadronic shower is far large than the γ ray one, any sample containing non detected (or faint) source is suitable for this task. Both sample should be cover the same Zd angle distribution of the real data that are being analysed. The RF then “grow” a certain number of decision trees for a certain parameters useful to discriminate between γ and hadron. Finally the algorithm assign a number from 0 to 1 to each event, the hadronness, that is close to 0 for γ-like events.

3.3.3.7 Arrival direction estimation

The direction of the shower can be computed as indicated in Sec 3.3.3.4, but the method fails for parallel of small size images. The current standard MAGIC analysis chain includes an event-wise direction reconstruction performed through the *disp* parameter, representing the distance between the image CoG and the reconstructed source position. The MAGIC stereo analysis uses the *DISP RF* method, which introduces all those parameters that may influence the *disp* estimation in a dedicated RF algorithm [110]. The DISP RF is trained with a sample of simulated γ-ray events of known source position, and it grows the corresponding decision trees to evaluate the correlation between the *disp* and the input parameters. As

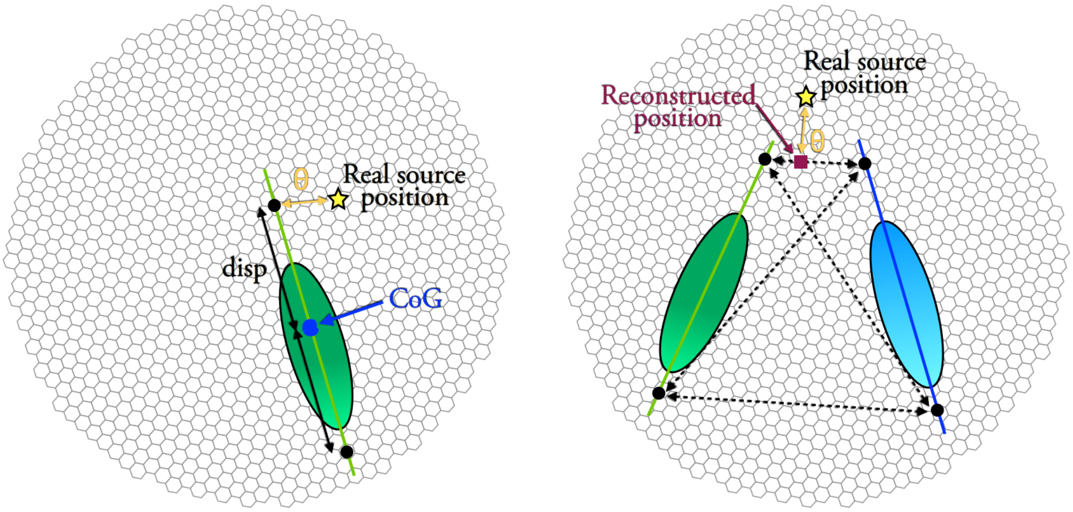

Figure 3.21 DISP method for one telescope (right) and for both telescopes (left). The possible source positions are indicated with black dots. The dotted lines indicated the distances between these possible positions. Image taken from [19].

the impact point is aligned along the the ellipse major axis, there are two possibilities or source reconstructed positions, one at each side of the CoG (indicated by the black dots in Fig. 3.21, left picture). When the events are merged, the distances of all possible combination of positions pairs are computed. The closest pair is chosen as the correct one, and the arrival direction is computed as the average of the two chosen positions plus the crossing point of the main axis of the images (Fig. 3.21, right picture). The angular distance from this point to the assumed source position is called θ, which distribution for γ rays peaked toward 0. This parameter is used to defined a circular fiducial region around the source position, from where the signal is computed.

The estimation of the DISP parameter is trained with simulated γ rays so that it usually gives inconsistent results for hadronic showers. Therefore, the DISP RF method is also used as an extra γ/hadron separation criterion and, if the none of the four pairs gives a similar arrival direction in both telescopes, the event is discarded.

3.3.3.8 Energy estimation

MAGIC standard analysis chain make use of a *Look-up Table* (LUT) method to estimate the energy of each event. The LUTs are information tables constructed using simulated gamma rays, based on a simple model for the Cherenkov light distribution on the ground based on the impact parameters, the Cherenkov radius r_C and Cherenkov density ρ_C[5]. LUTs are build for each telescope independently, by dividing the sample of simulated γ rays in bins of size and $impact/r_C$ ratio. Since the energy of the primary γ ray is proportional to the $size/\rho_C$, each bin of the table is filled with the mean of $E' \times \rho_C/size$, whereE' is the true energy of the event, with an error given by the RMS of the distribution. The final estimated energy E is the average of the energies reconstructed individually for each telescope, weighted by the inverse of their uncertainties.

3.3.4 High level analysis

At this stage, each events is determine by an arrival direction, an estimated energy and a hadronness. These informations with the one from the other stored image parameters are used to perform studies on the VHE source observed.

3.3.4.1 Collection Area

The effective collection Area can be understood as the area of an equivalent detector that would detect with en efficiency of 1 the same rate of γ rays of the real instrument. In formula, considering that from a number N_{sim} of simulated γ rays in an area A_{sim}, N_{det} events are detected, then the collection area A_{eff} depends on the the Energy E as follow:

$$A_{eff}(E) = A_{sim}\frac{N_{det}(E)}{N_{sim}(E)}. \tag{3.1}$$

The collection area increases at high energy with Zd, since the atmospheric depth is larger and the shower developing further from the telescopes creates a larger Cherenkov pool, as illustrated in Fig. 3.22. The azimuth creates an effects on the A_{eff} too, because of the variation of the telescopes distance and the effect of the geomagnetic field, which separates positive and negative charge distorting the shower and thus the associated images. These effects are smaller than the Zd dependence and can be often averaged over the whole azimuth distribution of the observation.

3.3.4.2 Angular resolution and energy reconstruction

The angular resolution is usually referred to the *point spread function* (PSF). It is defined as the as the standard deviation of the 2-dimensional Gaussian fit to the sky distribution of a

---

[5] The radius and the density of the Cherenkov light pool on the ground, computed assuming Cherenkov emission from a single electron at the height shower maximum with an energy of 86 MeV.

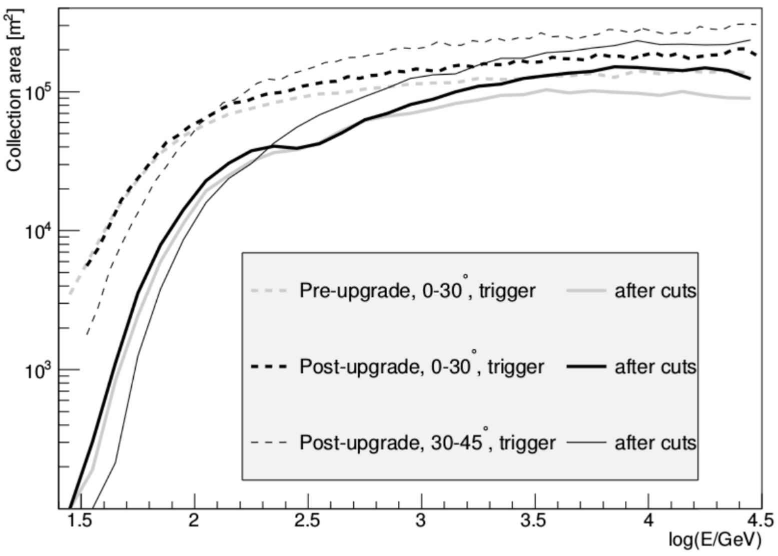

Figure 3.22 Collection area of the MAGIC telescopes after the upgrade at the trigger level (dashed lines) and after the analysis cuts (solid lines). Thick lines show the collection area for low zenith angle observations, while thin lines correspond to medium zenith angle. For comparison, the corresponding pre-upgrade collection areas are shown with gray line. Image taken from [20].

point-like source. The PSF correspond to the radius containing the 39% of the γ-ray events from the source. In Fig. 3.23 the stereo angular resolution of MAGIC is reported.

The capability of well reconstruct the energy in defined by the *energy bias* and the *energy resolution*. The resolution is defined as the width of the Gaussian distribution $E - E'/E'$, where E' and E are the true and reconstructed energy, respectively, while the mean of the fit is the relative bias. The energy reconstructed is as good as those value are close to 0. The values of energy bias and resolution for the MAGIC stereo observations are shown in Fig. 3.23.

As last, the energy threshold, E_{th} is conventionally defined as the peak of the energy distribution from a simulated γ-ray test sample, once the background rejection and the analysis cut are applied.

3.3.4.3 Signal estimation

After applying the cut in *hadronness*, further background suppression can be achieved by the use of the θ^2 parameter. As already mentioned, the θ^2 distribution peaks at 0 for γ-event from the source, while for background events whose arrival directions are isotropic, the θ^2 distribution is flat.

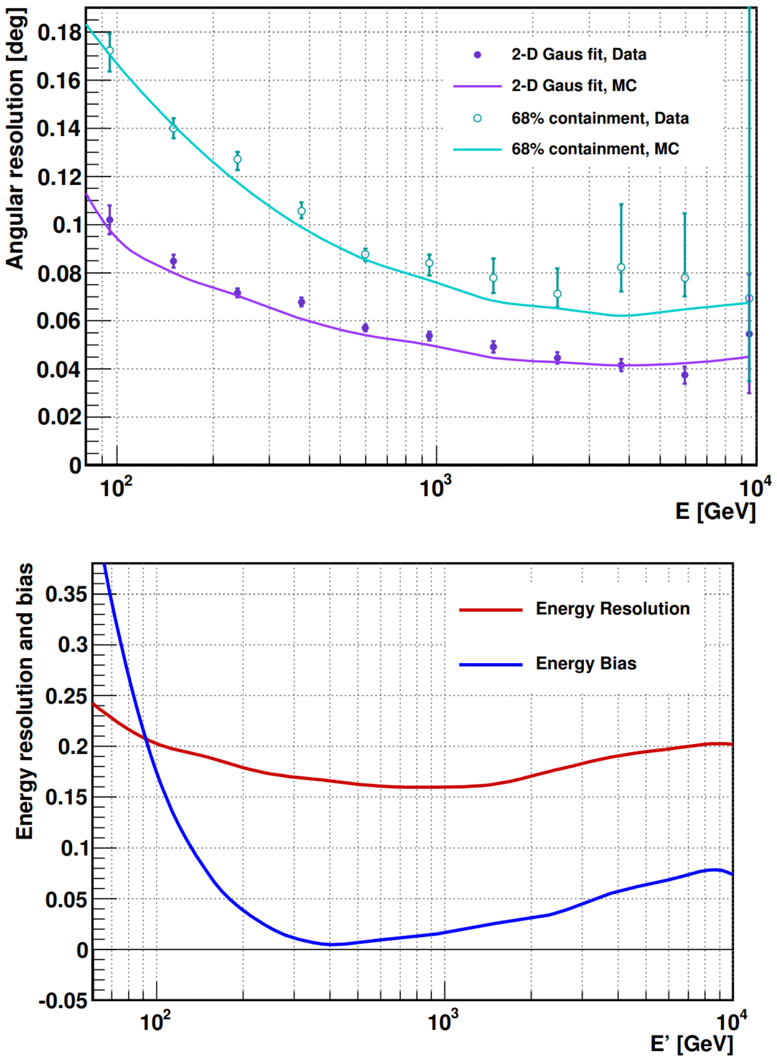

Figure 3.23 Top: MAGIC angular resolution (violet) and 68% containment radius (cyan), as computed from a MC-simulated point-like source as well from Crab Nebula sample. Bottom: MAGIC energy reconstruction parameter. Red line represents the energy resolution, the blue line the energy bias. Both image are taken from [20].

The signal region, ON, and the control background region, OFF,s are thus defined as a circle of radius θ around their nominal positions in the camera. The OFF is use to estimate the residual background in the ON region, since it does not contains γ rays, by construction. Both ON and OFF are treated in the same way, in terms of analysis method and applied cuts. From the measured number of events in the ON and OFF region, N_{ON} and N_{OFF} respectively, the number of excess events N_{ex} is calculated as:

$$N_{ex} = N_{ON} - \frac{N_{OFF}}{\kappa}, \tag{3.2}$$

where κ is the normalization factor between ON and OFF. In general, the ON and OFF are not observed for the same amount of time, thus have a different "exposure", e.g. in wobble mode for each ON, up to three OFF positions can be selected. In such a case, a rough normalization brings to scale the OFF through the inverse of the number of wobble positions considered. As both ON and OFF positions are observed simultaneously, this is in some way similar to the method used normalize exposure through the observation time, using as a scaling factor t_{OFF}/t_{ON}, where $t_{OFF/ON}$ is the observation time for OFF/ON. Such normalization method relies on the assumption that the detection rates are stable during the observations, which is not true since a small variation of rates is naturally expected due to the changing of the pointing (e.g. in wobble mode each wobble pointing has a slightly different trajectory).

A more robust approach is then to normalize the ON and OFF events distributions in a region where no signal is expected, relying on the fact that the shape of the background is the same for ON and OFF. In *Flute*, the normalization is performed considering an annulus around both ON and OFF positions. The annulus should contain only background, thus the inner radius should be large enough to not contain any excess event and the outer low enough to avoid overlapping of the normalization regions. In other words, the standard normalizations for point-like, or moderate-extended sources, is performed by using the θ^2 distributions in a region where no signal is expected, as indicated in Fig. 3.24.

Finally, the statistical significance of the excess over the background is computed the Li&Ma formula [111], typical adopted in the γ-astronomy.

3.3.4.4 High Level Output

In standard analysis, the main informations on the VHE sources are studies with the *skymap*, *θ^2-plot*, *flux* or *Spectral Energy Distribution*, *light-curves*, in which the distribution of the γ rays is shown as a function of the sky position, angular distance w.r.t. the source center, event per unit of time and surface or energy per unit of time and surface, and time.

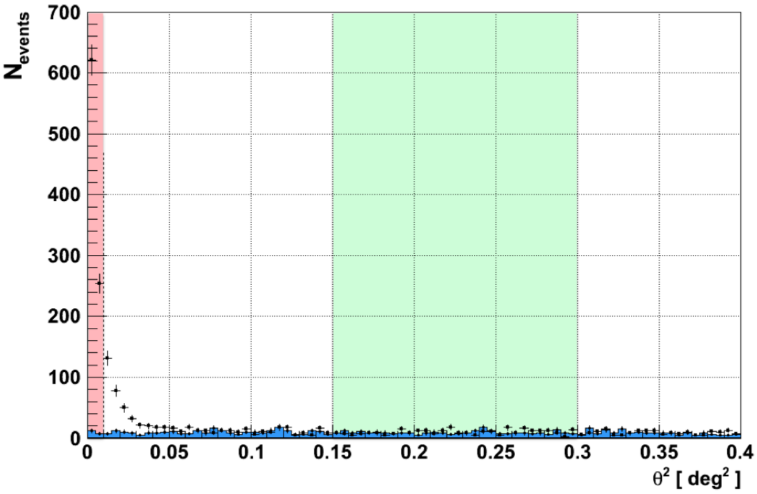

Figure 3.24 Example of a signal detection of Crab Nebula with a θ^2-plot. Excess of γ rays are given as points, while the background events are represented in blue. The red area defines the signal region, where $N_{ON,OFF}$ are computed, while the green area is the normalization region. Image taken from [20].

For a standard analysis, the θ^2 plot is built with the events survived the cuts optimized to maximize the sensitivity for Crab Nebula observations. The events are successive plotted as function of the angular distance from the source center and the reconstructed arrival direction θ, as described above. The flux is computed as:

$$\frac{d\Phi}{dE} = \frac{dN_\gamma}{dt_{eff} dA_{eff}(E) E}, \tag{3.3}$$

where t_{eff} is the effective observation time, i.e. the time during which the telescopes have recorded events, correct by the dead time of the readout system electronics.

Skymaps refers to a 2-dimensional histograms containing the arrival directions of all the γ-ray events, in equatorial coordinates. The events reported are the ones that survive the analysis cut and the background subtraction adopted to built the θ^2 histogram.

In this work, for the indirect DM searches we will use a dedicated analysis that exploits the spectral information of DM candidates, that no astrophysical counterpart could reproduce, and explained in the next sections.

3.3.5 Dark Matter analysis

As described introduce in Chapter 1, in the spot of the Universe dominated by DM, its distribution formed an almost spherical halo which extend till a certain radius. This radius

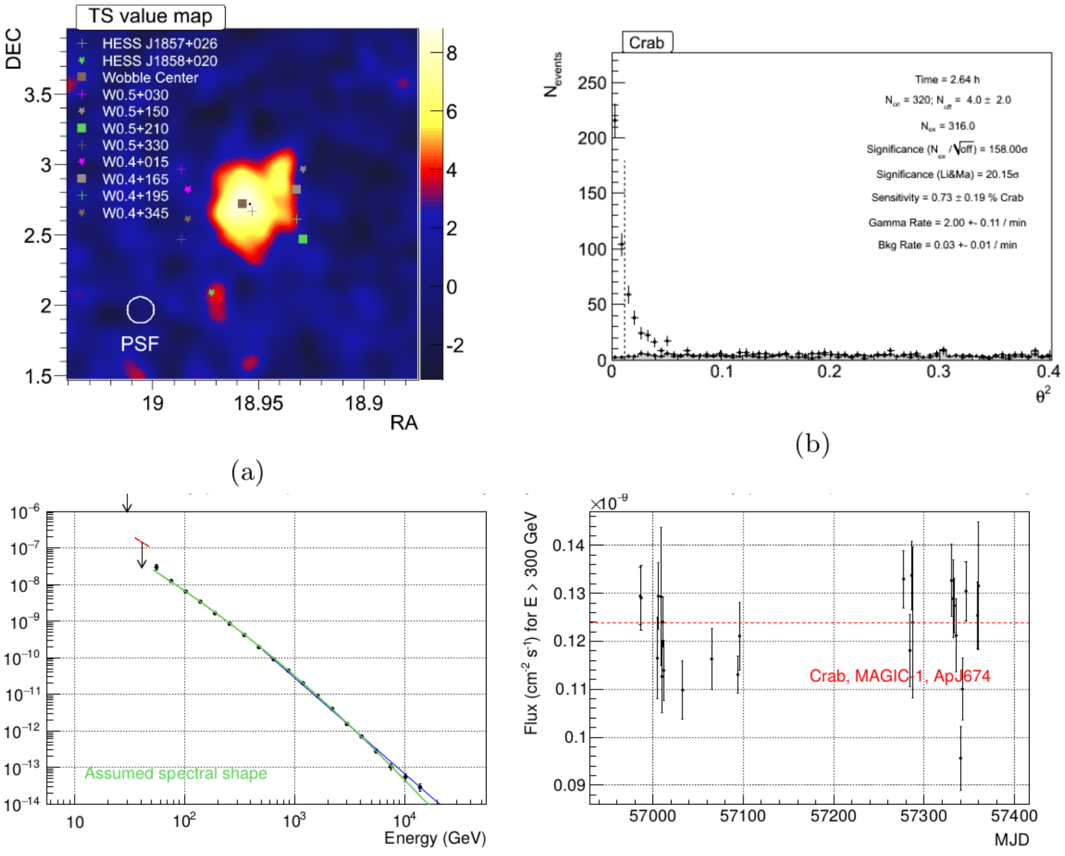

(a)

(b)

(c)

(d)

Figure 3.25 Standard analysis plot examples. (top left) shows a skyMap, the distribution of the arrival γ rays events within the observed FoV where the color-scale is associated with a test statistics of the probability of being the emission generated through background-only (the null hypothesis). (top right) shows a θ^2-plot, the distribution of reconstructed distances of γ rays events, w.r.t. to the the position of the null hypothesis source, it is typically used to claim a discovery by integrating the number of signal events up to a certain angular region, and compare it with an only-background region. In case of a positive detection spectral (bottom left) or light-curve (bottom right) analysis are performed to understand the energy and time evolution of the source.

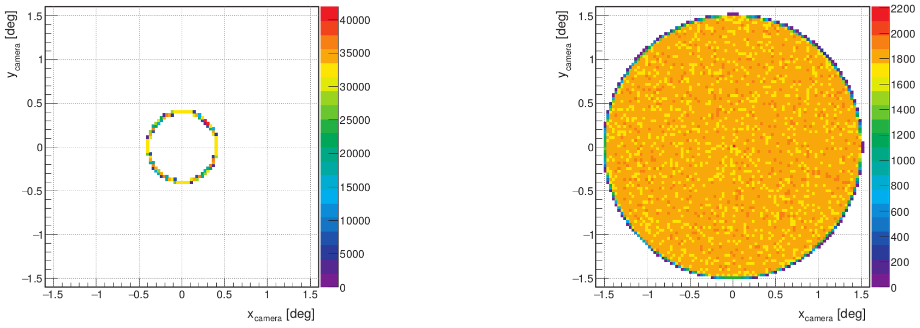

Figure 3.26 Distribution of true directions of simulated events for the point like (left) and diffuse (right) MAGIC MC productions, shown in camera coordinates. For the point-like case, this also corresponds to the distribution of the source centres.

varies depending on the target considered, but it is usually beyond the MAGIC angular resolution. Those target are considered extended source for MAGIC. Moreover, to improve the sensitivity on DM search is very important to keep the knowledge of the precise signature that DM creates in the γ-ray spectrum.

Special tools have been developed in MAGIC to take into account those aspects related to DM search.

3.3.5.1 Donut Monte Carlo method

The instrument response functions (IRFs) of IACTs are usually evaluated by means of MC simulations. For many practical purposes, it is enough to evaluate IRFs for point-like γ-ray sources. However, IRFs depend in general on the relative arrival direction of the γ rays with respect to the telescope pointing direction. This means that the evaluation of IRFs for extended sources of arbitrary sources of arbitrary shape would in principle need a simulation fo a γ-ray data sample with arrival directions distrubuted following the particular source morphology. This morphology is expected to be different from source to source. In order to compute IRF applicable to the study of any source of any arbitral morphology, while making an efficient use of the computing resources devoted to MC simulations, a method called *Donut MC* has been developed [18].

For point-like case, the IRFs are computed with a ring-wobble MC (see Fig. 3.26), where the γ rays are simulated with a true positions uniformly distributed in a ring of 0.4° centred at the telescope pointing position, to cover for all possible orientation between the pointing direction and the source position. On the other hand, extended sources do not have a well defined source position, however the pointing position of the telescope can be identify with the source center, in case we use wobble observation method. Simulating the γ rays with

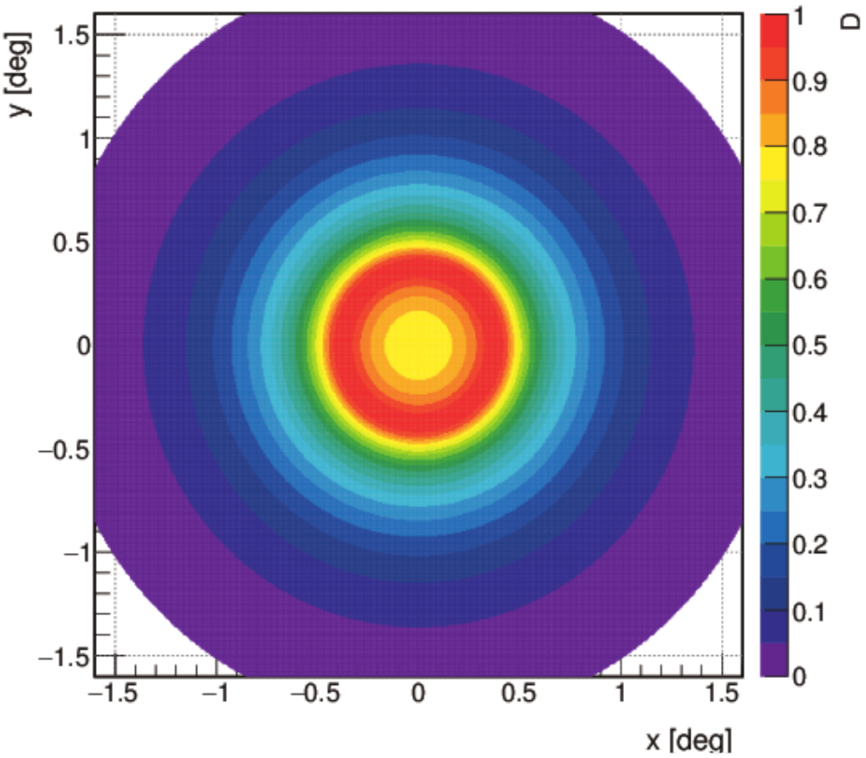

Figure 3.27 The distribution of simulated directions for a given typical radially symmetric source (wobble pointing mode), covering all possible orientations between the pointing direction and the source center position, in Cartesian coordinates (x, y) w.r.t. the FoV.

true direction following the previously mentioned source morphology around the source center would demand at least as much computer resources as the point-like production, but would only be applicable for a specific morphology. The Donut method, instead, selects events from a diffuse MC (where the γ rays are simulated with a true direction uniformly distributed uniformly in a $\sim$1.5° radius FoV, see Fig. 3.26) by adding a negligible overhead to the computing time, thus making it available for any source morphology.

Assuming a circular symmetric morphology w.r.t the source center (named *source brightness profile* of the source), a probability density function (PDF) is built by the convolution of all possible source center/pointing direction orientations, which by construction has a circular symmetry and a donut shape, from where the name of the method came from (see Fig. 3.27). The method consists in selecting the events according to this PDF and successively a source center is randomly assigned to each event, chosen from the expected ring where the pointing positions lie.

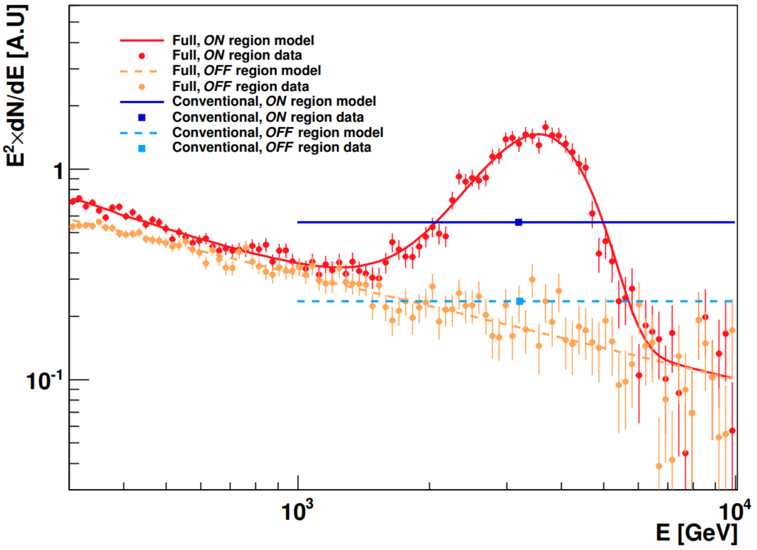

Figure 3.28 Illustration of the advantage of the full likelihood approach compared with the standard one. The red and orange line represent the spectral distribution for ON and OFF, respectively, while the points, with the same color code, represent the data (fine binning is used for demonstration purpose - the full likelihood is unbinned). The blue and cyan level correspond to the average value within the energy range considered in the conventional method. Image taken form [21].

3.3.5.2 Full likelihood method

For the case of indirect DM search, a dedicated analysis approach with IACTs has been developed. This method is called Full Likelihood (FL) [21]. The FL approach takes advantage of the distinct features expected in the γ-ray spectrum of DM origin (see Fig. 3.28), achieving better sensitivity w.r.t. the standard ON/OFF method. The method was used in [112] leading to the most stringent annihilation cross-section of DM particles masses above 1 TeV. Furthermore the method provides a framework for global, sensitivity-optimized, indirect DM search, that allows the combination of the results of all the IACT observatories of the present generation and has been applied in the first joined analysis of MAGIC and Fermi-LAT [23]. Moreover, the analysis is completely generic, and can be used to perform a global search combining present and future γ-ray detectors.

The conventional likelihood explores the existence of an astrophysical source based on Poissonian variables, i.e. number of detected events in the ON region (N_{ON}) and the number of detected events in the background region(s) (N_{OFF}). Thus, the number of γ rays (g) and background events (b) in the ON region are obtained by maximizing the likelihood function

$\mathscr{L}$:

$$\mathscr{L}(g,b|N_{\mathrm{ON}},N_{\mathrm{OFF}}) = \frac{(g+b)^{N_{\mathrm{ON}}}}{N_{\mathrm{ON}}!}e^{-(g+b)} \times \frac{(\kappa b)^{N_{\mathrm{OFF}}}}{N_{\mathrm{OFF}}!}e^{-\kappa b} \tag{3.4}$$

where κ is the normalization between the exposure of the ON and the background region, which can be computed as the ratio of the γ-like events recorded in ON/OFF within a region outside the region of interest, and equal instrument acceptance.

The FL increases the sensitivity by assuming the spectral shape of the source beforehand. The unbinned version can be written as Thus for a given model M, the likelihood form become:

$$\mathscr{L}(g,b|N_{\mathrm{ON}}) = \frac{(g+b)^{N}_{\mathrm{ON}}}{N_{\mathrm{ON!}}}e^{-(g+b)} \times \prod_{i=1}^{n}\mathscr{P}(E_i) \tag{3.5}$$

where $\mathscr{P}$ is the PDF of the event i with estimated energy E_i for signal and background.

For practical application, the binned version of the Eq 3.4, including the treatment of the uncertainty and several datasets described by different IRFs can be written as:

$$\begin{aligned}\mathscr{L}_i(\alpha;\nu|\mathscr{D}) = {} & \mathscr{J}(J|J_{\mathrm{obs}},\sigma_J) \times \mathscr{G}(\kappa_i|\kappa_{\mathrm{obs}},\sigma_{\kappa,i}) \\ & \times \prod_{j=1}^{N_{\mathrm{bins}}}\left[\frac{(g_{ij}(<\sigma v>)+b_{ij})^{N_{\mathrm{ON},ij}}}{N_{\mathrm{ON},ij}!}\cdot e^{-(g_{ij}+b_{ij})} \times \frac{(\kappa_i b_{ij})^{N_{\mathrm{OFF},ij}}}{N_{\mathrm{OFF},ij}!}\cdot e^{-\kappa_i b_{ij}}\right],\end{aligned} \tag{3.6}$$

where i runs over the different dataset considered (e.g. different wobble positions or MC periods), and j runs over the bins in energy N_{bins}. ν and $\mathscr{D}$ refer to the nuisance parameters and the dataset respectively and α is $<\sigma v>$ for DM annihilation or $1/\tau_{DM}$ for DM decay. g_{ij} and b_{ij} are the estimated number of signal and background events respectively; $\mathscr{J}$ is the likelihood for the J-factor, parametrized as a Gaussian in $\log_{10}J$; $\mathscr{G}$ is the likelihood function for the OFF/ON acceptance ratio κ_i, parametrized with a Gaussian function with mean κ_{obs} and variance $\sigma_{\kappa,i}$, which includes statistical and systematic uncertainties, with the formula

$$\sigma_\kappa^2 = \sigma_{\kappa,stat}^2 + \kappa^2 \cdot \sigma_{\kappa,syst}^2. \tag{3.7}$$

For standard operation $\sigma_{\kappa,syst} = 1.5\%$, established on the base of a dedicated performance study [20]. b_{ij}, J and κ_i are nuisance parameters, whereas g_{ij} depend on the free parameter α through:

$$g_{ij}(\alpha) = T_{obs,i}\int_{E'_{min,j}}^{E'_{max,j}} dE' \int_0^\infty dE \frac{d\phi(\alpha)}{dE}A_{eff,i}G_i(E'|E), \tag{3.8}$$

where $T_{obs,i}$ is the total observation time, E and E' are the true and estimated energy respectively. Finally G is the probability density function of the energy estimator, computed from a MC simulated γ-ray data set.

Hence, the data inputs for the likelihood are the number of events detected in the ON and OFF regions for the different bins in estimated energy (after all analysis cuts), plus the IRF computed from the tailored MC for the specific observation period (see Fig. 3.29). The null hypothesis is given by $g_{ij} = 0 \,\forall\, i,\ j$. The test hypothesis ($g_{ij} > 0$) are built considering the flux computed using Eq. 2.1 and under the hypothesis of different pure DM process. Following [113], the γ-ray DM emission and spectra are modeled using MC simluation (e.g. the PYTHIA simulation package, as in [89]). The spectra are computed by tracing all the annihilation/decay chains, including the muon radiative decay down to stable particles for each simulated event.

From Eq. 3.6 the profile likelihood ratio is defined as:

$$\lambda_P(\alpha|\mathscr{D}) = \frac{\mathscr{L}(\alpha;\hat{\hat{\nu}}|\mathscr{D})}{\mathscr{L}(\hat{\alpha};\hat{\nu}|\mathscr{D})} \tag{3.9}$$

where $\hat{\alpha}$ and $\hat{\nu}$ are the values maximizing the $\mathscr{L}$, and $\hat{\hat{\nu}}$ the value that maximizes $\mathscr{L}$ for a fixed α. Upper limits in α at 95% Confidence Level (CL) (α^{UL}) are given for:

$$-2\ln\lambda_P(\alpha^{UL}|\mathscr{D}) = 2.71. \tag{3.10}$$

The quantity $-2\ln\lambda_P$ vs α is computed for the range of α fulfilling $-2\ln\lambda_P(\alpha) \leq 2.71$.

The method allows to define the sensitivity, for a given CL, on the free parameter α, defined as the the average limit (with that CL) that would be obtained on α, under the null hypothesis. This value can be computed in two main way:

- produce as many independent Monte Carlo simulated samples as needed by the CL and compute for each the limit to g. The estimated sensitivity is the average of the obtained limits;
- take the difference between the value of g for which $-2\ln\mathscr{L}$ takes the value corresponding to the CL and the for which $-2\ln\mathscr{L}$ minimises. This approach is acceptable if it is possible to have a good description of the $-2\ln\mathscr{L}$ parabolic shape.

The first method is slower but more precise, while the second one is less accurate but way faster. In Chapter 4 and 5 this second fast simulation is used to optimize the analysis cut, which corresponds to:

$$\alpha^{svt} = (\alpha^{UL} - \hat{\alpha}). \tag{3.11}$$

Here, $\hat{\alpha}$ can assume both positive and negative values. Using this prescription, $\hat{\alpha}$ is the lowest possible value of the upper limit, irrespective of the presence of arbitrarily intense negative background fluctuations.

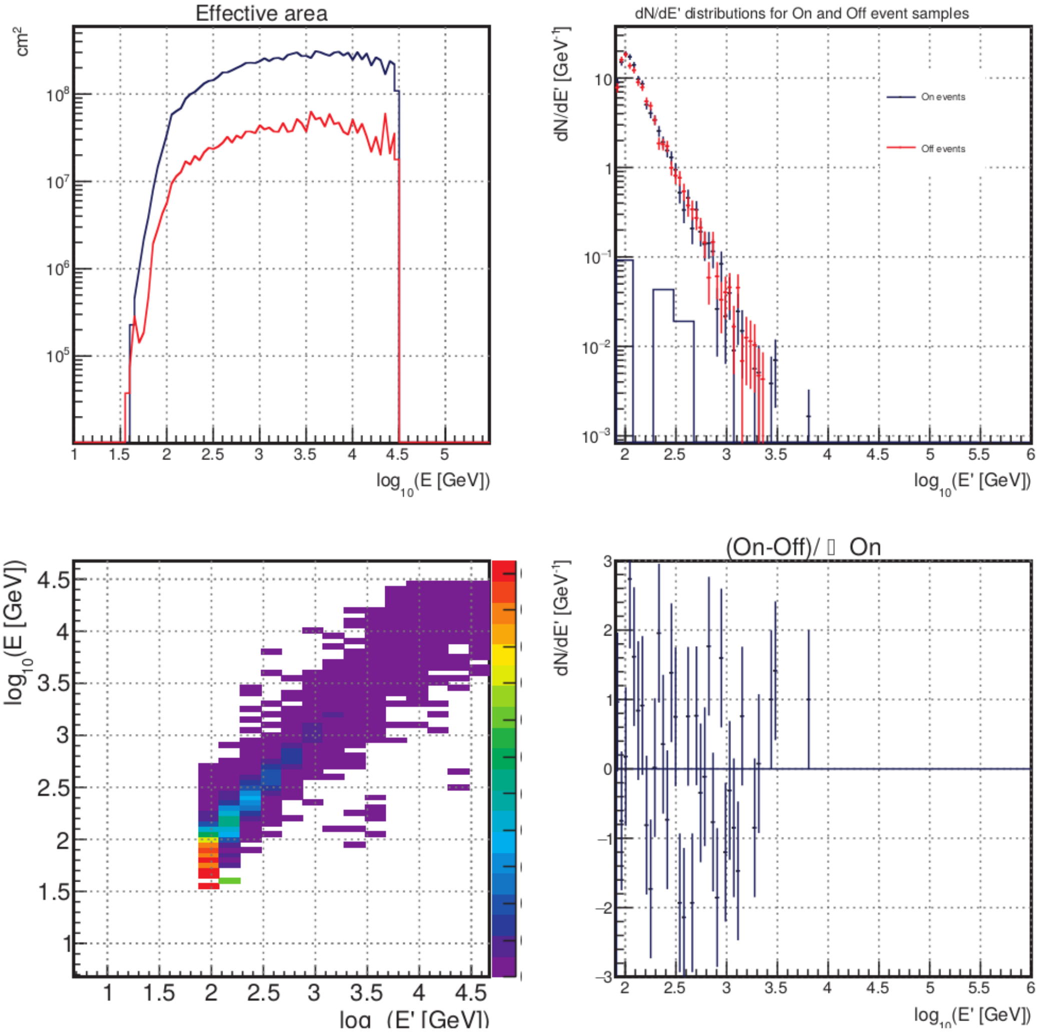

Figure 3.29 FL sample inputs: (top and bottom left) effective area for ON and OFF region (blue and red lines respectively, in unit of cm^2) and migration matrix computed from MC events, (top and bottom right) dN/dE' and relative difference of events after cuts in ON and OFF regions.

The 95% limits, is computed constraining the $\hat{\alpha} > 0$, which corresponds to the physical region. This can produce an over-coverage (i.e., the computed confidence interval contains the true value more often than the quoted confidence level) for negative background fluctuations. This effect is usually partially mitigated by showing the obtained results with its PDF for the no-DM hypothesis ($\alpha = 0$). Such PDF can be estimated using a fast simulations of the no-DM hypothesis, characterized by its median and the bounds for 68% and 95% symmetric containment quantiles. These prescriptions are adopted in the analysis reported in Chapter 4 and 5.

The whole method described is implemented in a stand-alone general-puropse ROOT-based framework, called *gLike* [114].

Chapter 4

Dark Matter Search in the Draco dwarf galaxy

4.1 The Dwarf spheroidal galaxies

In the ΛCDM model, DM is represented as a perturbation in the density distributions. DM sub-structures form by following the collapse of such over-densities. These structures act as a potential well for baryonic matter. If the structure is large enough, potential may be enough to trigger stars creation. This model is used to explain the formation of the dwarf spheroidal satellite galaxy (dSph) of the Milky Way, within the sub-structures of the Galactic DM halos [115].

In 1938, the first two dSph galaxies, Sculptor and Fornax, were discovered by Shapely [116]. Thanks to the new generation of photometric survey, such as the *Sloan Digital Sky Survey* (SDSS [5]) and the *Dark Energy Survey* (DES [117], the number of detected dSphs passes from 9 to ~ 50. This happens since the newcomer dSphs were sensibly less luminous than the previous ones. However, the number of detected dSphs is still an order of magnitude lower compared to what is predicted by N-body simulations. This discrepancy is known as *missing satellite problem* (see Sec. 1.2.3)[1] [118].

The dSphs are classified as classical dSphs, detected before the SDSS-era, and ultra-faint dSphs, detected by SDSS. The former have well established characteristics with hundreds of identified member stars, are located outside the galactic disk at a distance of $70 \div 250$ kpc from the earth, with a luminosity that ranges between $10^5 \div 10^7$ $L_\odot$, larger than any of the

---

[1] The smaller halos do may exist, but not all them may have the potential to attract enough baryonic matter to become visible, reducing the number of detected dSphs. Another possible explanation is that the smaller dwarf galaxies may tend to merge into the galaxy they orbit after the star formations, or be tidally stripped by larger galaxies [47].

newer ultra-faint dSphs. This helped in measuring the velocity of the member stars, as said velocity can be determined with a precision of a few km/s [119]. The latter have a luminosity $L \leq 10^5 L_\odot$, and only a few tens of faint-member stars, with a typical apparent magnitude of ~ 20. As a consequence, the velocity dispersion measurement, as well as the total luminosity estimation, are affected by larger uncertainty compared to the classical dSphs.

4.1.1 Dark Matter content

The measurements of the velocity of the dSphs member stars show a typical M/L of the order of $10^2 \div 10^3\ M_\odot/L_\odot$, which implies that these galaxies are the most DM-dominated objects in the Universe. Furthermore, these objects are almost γ-ray background free: the low metallic presence indicates a population of old stars with no star-formation processes expected, and the small amount of baryonic matter disfavours the presence of the typical γ-ray sources, like SuperNova remnants, Pulsars or binary systems. Moreover, their relatively close distance from the Earth and the high galactic latitude position (at least for some of them) reduce significantly the contamination due to Galactic plane background.

The proper DM density profile is estimated by measuring the velocity dispersion of the dSph member stars and fitting this distribution through the model considered. To disentangle the member stars from the foreground Milky Way stars, a membership of each star is given as a probability, through the iterative *expectation maximization* method [120]. This method provides a membership probability of each star in the FoV considered, through a likelihood analysis that takes into account the properties of the stars (velocity, luminosity, position, absorption lines) and compares to theoretical models. Stars with a membership probability larger than 0.95 are used for the measurement of the velocity dispersion distribution. Through the *Jeans* analysis [121], the velocity dispersion distribution is fitted to the DM density profile model selected. Usually, the DM density model chosen allows to explore a wide range of physically plausible DM profiles, considering both central core or cusp scenarios.

The velocity of the stars in the classical dSphs is measured with more precision compared to the ultra-faint ones, thanks to the brighter giant constituents. Still, it is not possible to determine unequivocally whether the dSphs central DM distribution is cored or cusped. Nearby classical dSphs favour DM cores over the cusps predicted by cosmological simulations, though this is under debate for at least some dSphs [2]. This uncertainty particularly affects the annihilation case, where J depends on the DM density squared and, thus, the related systematic is larger. Since these effects cannot be properly quantified, a strategy that requires

---

[2] Higher-quality photometric data from the central regions, providing a more precise measurements of the proper motion of the individual member stars, are needed for distinguishing and affirming one of the two scenario.

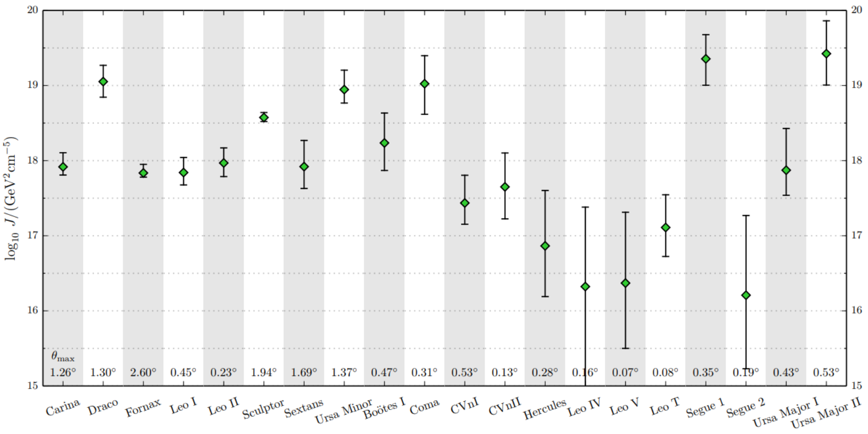

Figure 4.1 The *J*-factor for the DM annihilation process for a sample of dSphs is shown, following the results obtained in [22]. The *J*-factor has been computed using a NFW profile considering the maximum extension of the DM halo θ_{max}, which value is also reported.

the diversification of targets is usually adopted when in the search for DM signals in the annihilation channel case. Hence, the impact of the large uncertainties on J is reduced by combining the results from different targets.

Overall, dSphs represent optimal candidates for DM searches, since:

- the expected DM content is relatively high due to the very large $M/L > 100 M_\odot/L_\odot$;
- they are relatively close objects, which provide a large J-factor ($\sim 10^19$ GeV^2/cm^{-5} for annihilation case, as reported in Fig. 4.1) is important in order to detect a significant flux due to DM process;
- they are almost γ-ray background free, so any γ-ray signal can be directly related with DM processes.

Due to the relatively small size of the DM halo and the high density, they are perfect candidates for studying the DM process with IACTs. The annihilation case is the most promising for dSphs, nevertheless in this chapter both annihilation and decay case are treated, for completeness.

4.2 MAGIC DM dSphs program

DSphs represent optimal targets for DM indirect search with IACT telescopes, due to their small extension and the presence of no γ-ray background. MAGIC started observing dSphs from the Mono era citeAlbert:2007xg, but the most constraining results, in terms of the

Target	$\mathbf{log_{10}J_{ann}}(\theta_{\mathbf{max}})$ [$\mathbf{GeV^2cm^{-5}}$]	$\mathbf{log_{10}J_{dec}}(\theta_{\mathbf{max}})$ [$\mathbf{GeV^2cm^{-5}}$]	$\theta_{\mathbf{max}}$ **[deg]**	**Zd [deg]**
Segue 1	$19.36^{+0.32}_{-0.35}$	$17.61^{+0.28}_{-0.38}$	0.35	$13-37$
Ursa Major II	$19.42^{+0.44}_{-0.42}$	$18.39^{+0.25}_{-0.27}$	0.53	$35-45$
Draco	$19.05^{+0.22}_{-0.21}$	$18.97^{+0.17}_{-0.24}$	1.30	$28-45$
Coma Berenices	$19.02^{+0.37}_{-0.41}$	$17.96^{+0.17}_{-0.25}$	0.31	$11-38$

Table 4.1 List of the candidates proposed for the dSphs multi-year DM project (last two lines) and previously observed ones (first two lines). The J-factors for both DM annihilation and decay, are presented with their uncertainties, with the estimated source extension, as shown in [22]. The size of the halo, is given as the distance θ_{max} of the outermost member star used to evaluate the velocity dispersion profile, as a conservative choice of [22]. The last column presents the Zd visibility at the MAGIC site.

averagve velocity cross-section were achieved in the Stereo era, with the deep observation campaign of the ultra-faint dSphs Segue 1 [112] and Ursa Major I [113]. As ultra faint object, the error in J estimation is larger, thus MAGIC promoted in 2017 a multi-year project for enlarging the dSphs pool, applying the diversification strategy mentioned above. With reference to [22], the next-in-line dSphs to observed were selected taking into account their visibility from the MAGIC site and the J-factor value with its measured uncertainty (see Tab. 4.1). After Segue 1 and UMAII, the next-in-line targets for the observation were Draco and Coma Bernice.

In this chapter, I will focus only on the analysis of Draco dSph, observed by MAGIC during the 2018.

4.2.1 The Draco dwarf galaxy

The Draco dwarf galaxy was discovered in 1954 by the Palomar Observatory Sky Survey [122] and it belongs to the first set of discovered dSphs, thus tagged as "classical". Before the observation of Segue 1 and UMAII by SDSS, it was considered the most DM-dominated object. MAGIC observed Draco during the Mono era in 2007 [123], but it has been proposed to observe it again in the context of the multi-year campaign, since MAGIC upgraded from mono to stereo configuration, and stereo performances dominated over the mono one.

Some of the main characteristics of Draco have been reported in Tab. 4.2. As it can be seen, Draco is a very good candidate for a DM study due to its vicinity to Earth ($\sim$ 76 kpc), the large M/L ratio ($320M_{\odot}/L_{\odot}$) and the absence of background at very high energy levels caused by conventional sources. Furthermore, Draco is located well outside the Galactic

Draco	
RA(J2000)	$17^h20^m12^s$
Dec(J2000)	$+57°54'55''$
$(l,\, b)$	86.37°, 34.72°
Distance	76±6 kpc
Magnitude	-8.8±0.3
Luminosity	$2 \cdot 10^5$ $L_\odot$
M/L	$\sim$320 $M_\odot/L_\odot$
Mean[Fe/He]	-1.74
θ_{max}	1.30°
$\log_{10}[J_{ann}^{NFW}(\theta_{max})]$	$19.05^{+0.22}_{-0.21}$
$\log_{10}[J_{dec}^{NFW}(\theta_{max})]$	$18.97^{+0.17}_{-0.24}$

Table 4.2 The main characteristics of the Draco dSph.

plane in the Northern hemisphere and visible from the MAGIC site during most of the year, in a Zd range between [28°, 45°].

4.3 Observation and Data Reconstruction

MAGIC observed Draco in stereo mode between April and September 2018. Following the general strategy adopted for DM search in MAGIC (as mentioned in [113]), the observations required dark time and very good weather conditions, set with Lidar transmission at 9 km above ground level greater than 85%. Those conditions needed to be fulfilled in order to keep to a minimum the systematic effects due to bad weather conditions and the energy threshold, conditions that otherwise could degrade the sensitivity to DM process.

The observations were performed in wobble mode, using only two pointing positions in opposite directions and at 0.4° from the source, so that the distance between ON and OFF was always the maximum achievable, of 0.8°. This is particularly useful since Draco is a moderate-extended target for MAGIC, and larger distance between ON and OFF is useful to identify a proper region where to compute the OFF/ON normalization, as shown in Sec. 3. Moreover, the data acquisition was planned in order to use the *OFF from wobble partner* analysis. This method foresees to estimate, for a given ON, the background from the OFF position of the complementary wobble, thus from the same camera position where the corresponding ON is observed (see Fig. 4.2). In this way, possible inhomogeneities of the camera are cancelled out, ensuring a low systematic uncertainty in the background estimation. Comparable Az distribution for both wobble pointing positions were guaranteed

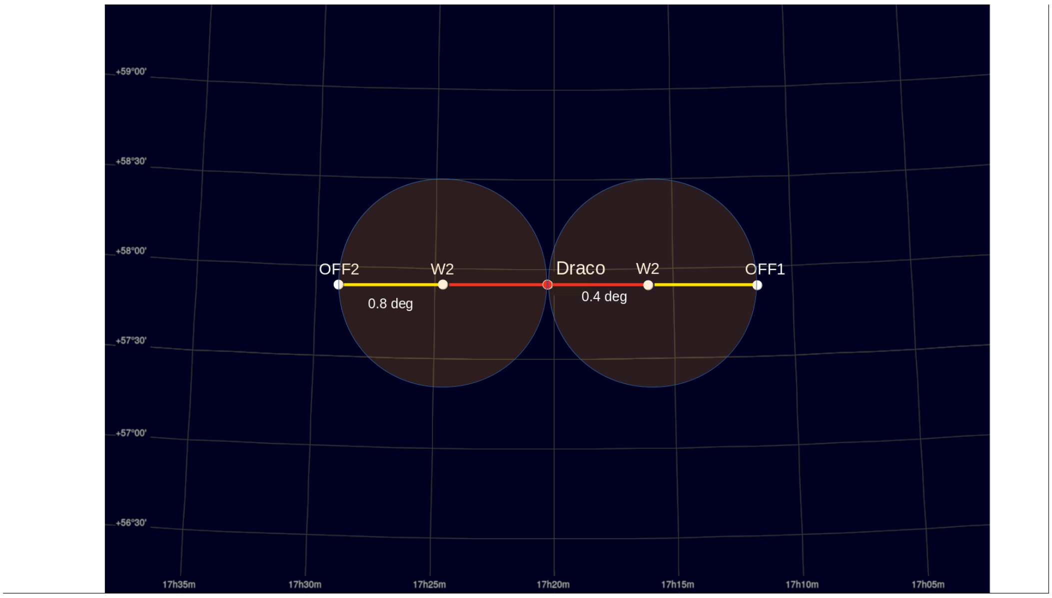

Figure 4.2 The *Off from wobble partner* scheme adopted for the dSph DM analysis, as in Draco one. The figure reports the two wobble pointing W1 and W2, where the signal (ON) and the background region (OFF) are observed at 0.4° from the center of the camera, and the OFF is at 0.8° from the target observed. In this method, the background is estimated from the OFF position of the complementary wobble. This means that at the analysis level, the ON1 is coupled with the OFF2 and vice-versa.

during the observations, in order to ensure uniform observation conditions and to avoid possible asymmetry effects due to the "stereo blob" (see Sec. 3.3.2).

The homogeneity of the Az distribution, as well the good weather conditions, were analysed reviewing the observations daily. In this way, it was possible to determine the contribution of the newcomer data in the existing Az distribution, and plan the successive observations. The Az distribution of the new data was estimated with a fast simulation of the observation based on the Astropy package [124][125], taking into account which wobble the new observation starts and the time duration of each wobble. After that, the first wobble position and the time duration of each wobble of the new observations were communicated to the data taking crew at the beginning of each observation night. In Fig. 4.3 the azimuth distributions for both analysis periods are reported.

A total amount of 66.2 hours were collected with a Zd range from 28° to 45°. During the period between June 30th - October 30th a degradation in the MAGIC mirrors reflectivity occurred, due mostly to the calima phenomena. This effect did not compromise the robustness of the data as it has been properly taken into account in the MC simulations. Thus, the data was divided into two analysis periods defined by the MC simulations used, reflecting the actual status of the instrument, named ST0309 (April - June) and ST0310 (July - September).

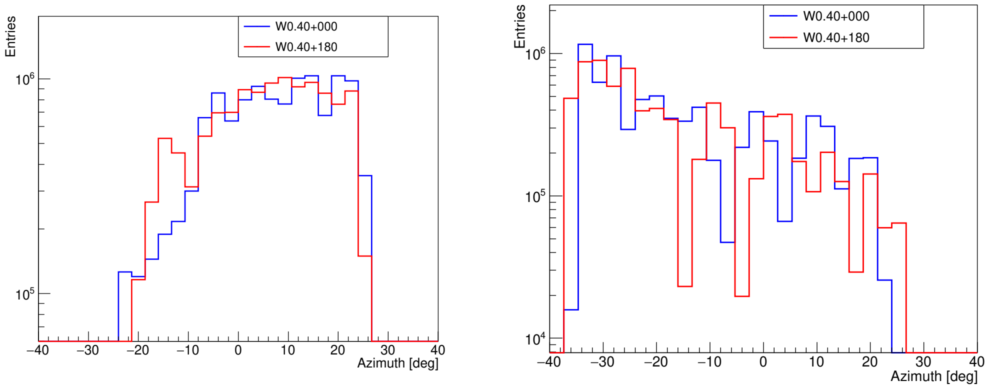

(a)

(b)

Figure 4.3 Az telescopes pointing distribution of the reconstructed events of the Draco dSph, for the two wobble positions considered. We divided the distribution into the two analysis periods considered, ST0309 (a) and ST0310 (b).

4.3.1 Quality selection

The check over the quality of the data was performed after each night of observations. The check of the Az distribution was made by an Astropy based script, while the whole quality data check was performed using the standard MARS executable *Quate*. The data were selected with an average median DC no larger than three times the NSB of a standard moonless night and an atmospheric transmission at 9km larger than 85% (Tr9km). Other data have been excluded since they were collected with incorrect wobble positions, due to a mistake during the data taking. A total of 52.3 h of good-quality data available for the analysis survives the quality checks. A summary of the quality cuts is available on Tab. 4.3.

Later, the events which pass the quality selections are processed by the *Melibea* MARS executable. With the output of the Random Forest boosted tree classified method (see Sec. 3.3.3.1, each event is assigned with an estimated energy, an estimated arrival direction and a value of the test statistic for the signal background estimation, called *hadronness* (h). Diffuse MC files, related to the different analysis, with γ rays simulated uniformly over a radius of 1.5° from the center of the camera is used, since Draco is a moderate-extended target for MAGIC (the size of the Draco DM halo is $\theta_{max} = 1.3°$).

4.3.2 The Donut Montecarlo selection

Despite that dSphs are normally compact objects, the DM halo can extend beyond the luminous part of the galaxy. In Draco, the DM halo extends till a radius of $\theta_{max} = 1.3°$, as

Period	**Obs. Time (before cut)**	**Quality cut**	**Wrong wobble**	**Obs. Time (after cut)**
ST0309	36.9 h	1.6 h	3.6 h	31.7 h
ST0310	29.3 h	7.5 h	1.2 h	20.6 h
Total	**66.2 h**	**9.1 h**	**4.8 h**	**52.3 h**

Table 4.3 Overview on the total observation time and cuts.

shown in Fig. 4.4. Due to its extension, Draco is no longer suitable for a point-like analysis, but it has to be treated as an extended source for MAGIC, since it is way larger than the MAGIC PSF.

For both the analysis periods, the IRF computation is performed using a diffuse MC simulation, providing events uniformly distributed over a circle of 1.5° of radius around the center of the camera. This flatness does not reproduce correctly the signal *probability density function* expected for the DM halo considered, of which the brightness profile curve, i.e. the $\mathrm{d}J/\mathrm{d}\Omega$ curve, is reported in Fig. 4.4b and 4.4d. Consequently, the IRFs computed with the standard diffuse MC are not the correct ones, and cannot be used for the measurements of $<\sigma_{ann}v>$ and of τ_{DM}.

Following the Donut method introduced in Sec. 4.3.2, the events from the flat diffuse MC are selected according to the Draco brightness profile, resulting in a MC that correctly takes into account the extension and the shape of the source, allowing the correct computation of the IRFs.

4.4 Analysis

4.4.1 Cut Optimization

Signals from DM processes are searched for in a Region of Interest defined in the parameter space θ cut (θ_c) and hadronness cut h_c. With MAGIC, the standard optimization procedure for θ_c and h_c is foreseen to use a sample of Crab Nebula observations, in order not to bias the significance of the tested source. In DM analysis, the Crab Nebula no longer represents a good probe, mainly because its spatial and spectral emission profile does not reproduce the one expected from a DM annihilation or decay (Crab Nebula is a point-like source for MAGIC.)

The analysis cuts are optimized by computing with the use of fast MC simulations, (see Sec. 3.3.5.2), and then by selecting the values for h_c and θ_c^2 that maximize the sensitivity to DM averaged velocity cross-section (or lifetime) in the case of no DM signal, according

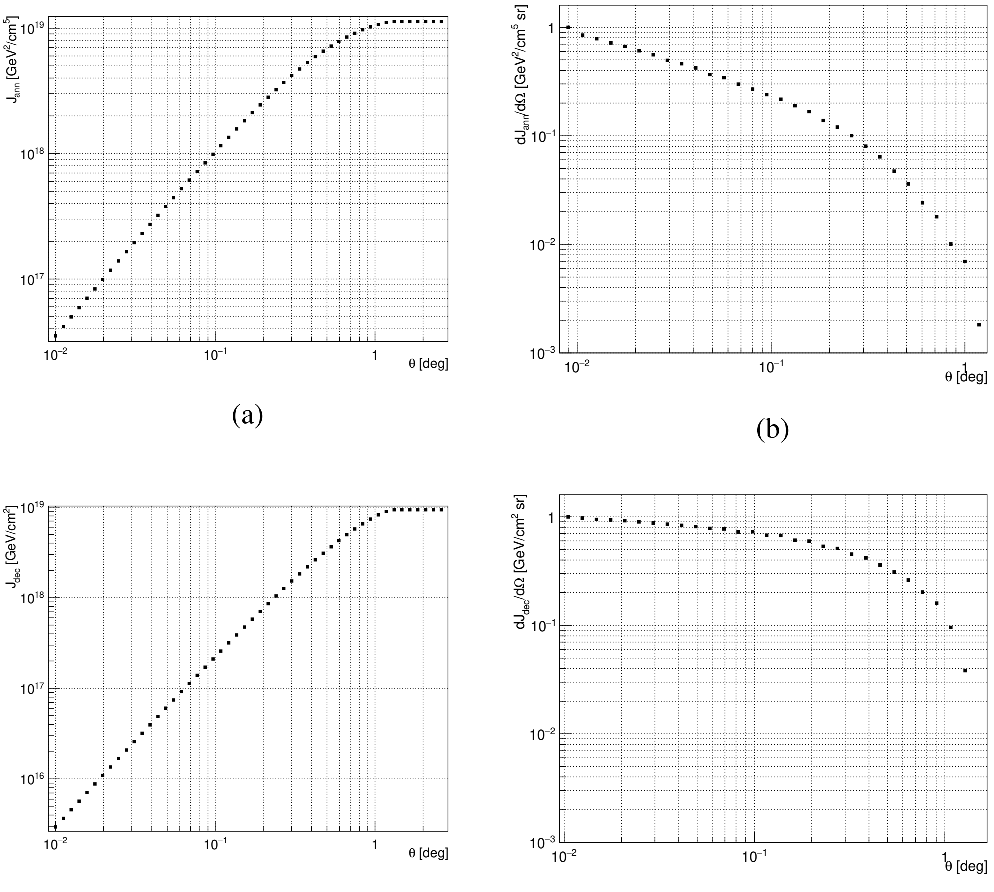

(a)

(b)

(c)

(d)

Figure 4.4 Left: the Draco integrated J-factor (a) (c) as a function of the integration angle θ, defining the distance from the center of Draco DM halo. Right: the $\frac{dJ}{d\Omega}$ (b) (d) profile as a function of the distance θ from the center of Draco DM halo for DM annihilation (above) and decay (below) are reported.

to the formula of Eq. 3.11, for a representative sample of DM masses This procedure has already been applied to other DM searches in MAGIC [113].

The cut optimization is performed in the parameters space defined by:

$$h_c \in (0,1) \ \text{ or } \ h_c(E') \in (0,1)$$

$$\theta_c^2 \in (0.01, 0.1)\ \text{deg}^2.$$

The h_c is considered both energy independent, or different for the estimated energy bins, computing the efficiency of the cut in terms of the % of MC events that survived the cut.

In Fig.4.5 left, the inverse to the thermally-averaged velocity annihilation cross-section (in $b\bar{b}$) as a function of θ_c^2 for different DM masses for a fixed value of hadronness ($h_c = 0.3$), normalized to the maximum sensitivity for each mass, is reported. In all the mass range, the best cut corresponds to $\theta_c^2 = 0.07$ deg^2. In Fig. 4.5 right, the same sensitivity ratio is reported for different cuts in hadronness. For most of the masses selected, the best cut in h is represented by energy dependent cuts with an efficiency of 60%.

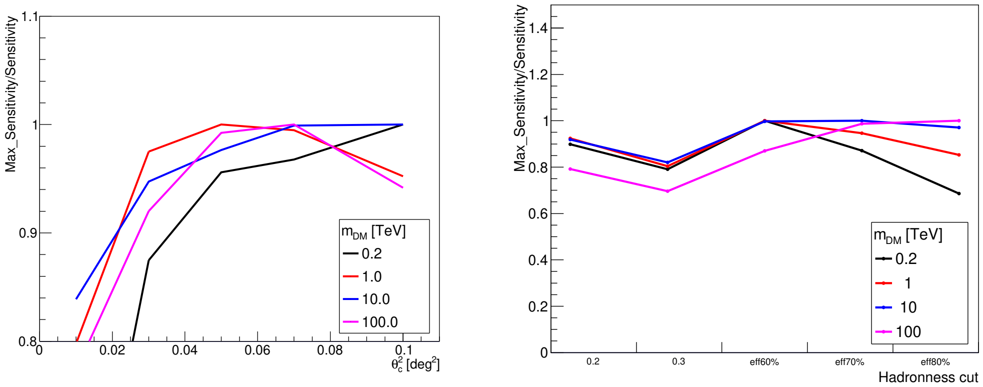

Figure 4.5 Left: relative inverse of the sensitivity to the thermally-averaged annihilation cross-section, for different values of DM masses annihilating in $b\bar{b}$ pairs, as a function of the θ_c^2, for a $h_c = 0.3$. Right: the sensitivity to the thermally-averaged annihilation cross-section for DM masses between 100 GeV and 100 TeV, for different values of h_c or $h_c(E')$ with a $\theta_c^2 = 0.07$ deg^2.

The same exactly procedure is applied for the DM decay case. Here, the optimization procedure, run considering the sensitivity to the DM lifetime, provides as the best cut $\theta_{cut}^2 = 0.07$ deg^2 and a $h_c = 60\%$, as reported in Fig. 4.6.

4.4.2 Standard Analysis Results

For completeness, the Draco data has been analysed with the MARS pipeline, with the analysis cuts described in the previous section. The θ^2 distribution (Fig. 4.7) and the sky-map (Fig. 4.8) centred on the source position are reported, as outcome of the high level analysis performed with MARS software. Both results show no evidence of γ-rays excess, with a LI&Ma significance of -0.32σ.

4.4.3 Binned Likelihood analysis results

The analysis approach optimized for DM search, called *full likelihood* method and introduced in 3.3.5.2, is applied to the Draco dataset. A energy-binned likelihood functions is adopted

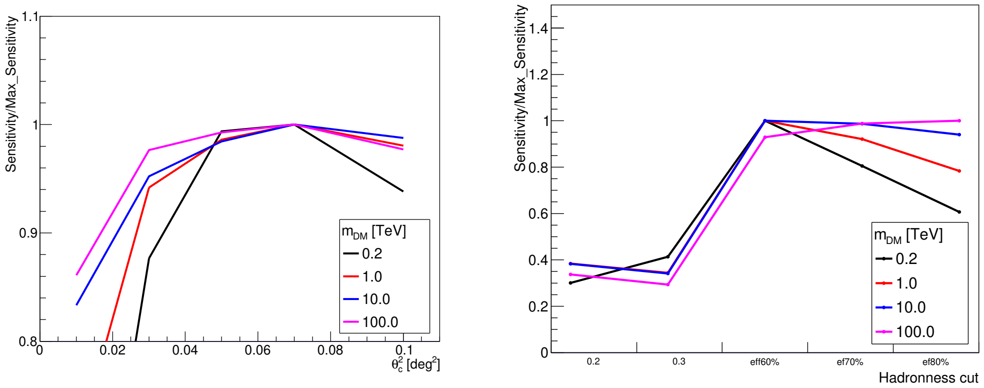

Figure 4.6 Left: relative inverse of the sensitivity to the DM lifetime, for different values of DM masses decaying in $b\bar{b}$ pairs, as a function of the θ_c^2, for a $h_c = 0.3$. Right: the sensitivity to the thermally-averaged annihilation cross-section for DM masses between 100 GeV and 100 TeV, for different values of h_c or $h_c(E')$ with a $\theta_c^2 = 0.07$ deg^2.

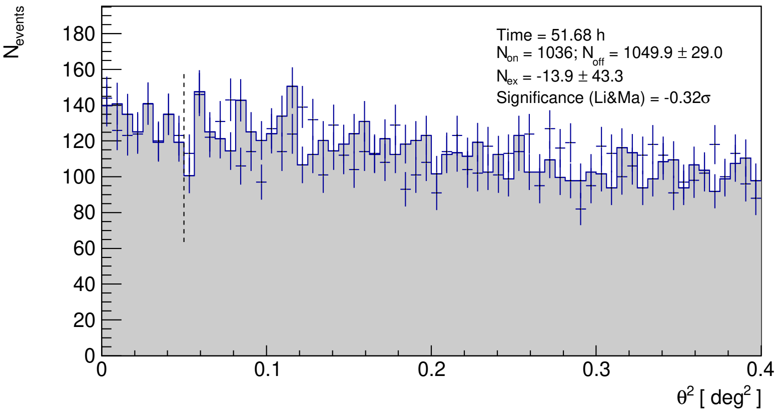

Figure 4.7 The θ^2 distribution for the Draco data sample. The signal (ON) is represented by the blue points, while the background (OFF) is the grey area. The OFF is normalised to the ON in the region where no signal is expected ($\theta^2 \in [0.15, 0.4]$ deg^2). The dashed vertical line represents the θ^2_{cut} applied, delimiting the region where the Li&Ma significance is computed.

for this analysis, with 11 energy bins equidistant in $\log_{10}E'$. The four independent data samples, which refer to the two wobble pointings of the two MC periods, as reported in Tab. 4.3, are combined together in a single likelihood function. Each term is described bythe same expected J-factor, different IRFs and different κ. The parameter κ is considered a global nuisance parameter for the sample, with no dependece on the energy, as in [113]. The uncertainty in the background estimation, parametrized as a systematic uncertainty in the parameter κ, is estimated to account for $\sigma_{\kappa,\mathrm{syst}} = 1.5\%$. The value is computed by by observing for 50 h the same FoV, so that the statistical fluctuations cancel out, and the

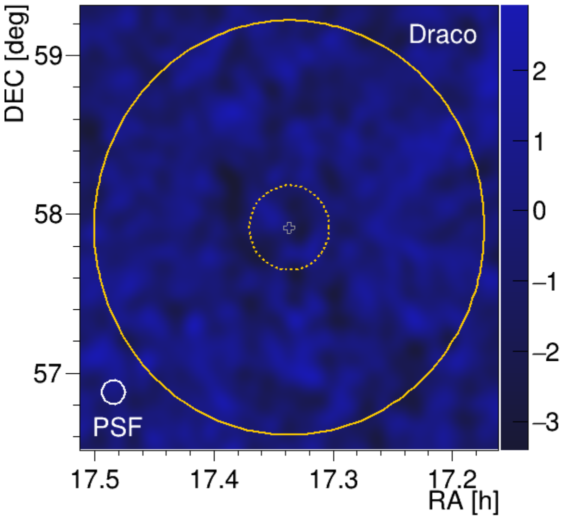

(a)

Figure 4.8 Significance skymap of Draco FoV for an extension of 2.8° in RA and Dec, from the center of the target (white cross). The orange solid line represents the DM halo extension (as defined in [22] and shown in Fig. 4.4), the dashed orange line represents the value of the cut in θ used for this work. As reference, the solid white line is the MAGIC PSF.

remaining residuals represent a measurement of $\sigma_{\kappa,\text{syst}}$. This value has been established in the performance study reported in [20] and further confirmed in [113].

The final binned likelihood, where each independent entry is described by Eq. 3.6, can be written as:

$$\mathcal{L}(\alpha_{\text{DM}}; J, \kappa|\mathcal{D}) == \prod_{i=1}^{4} \mathcal{J}(J|J_{\text{obs}}, \sigma_J) \times \mathcal{G}(\kappa_i|\kappa_{\text{obs}}, \sigma_{\kappa,i})$$
$$\times \prod_{j=1}^{N_{\text{bins}}} \left[\frac{(g_{ij}(\alpha_{\text{DM}}) + b_{ij})^{N_{\text{ON},ij}}}{N_{\text{ON},ij}!} \cdot e^{-(g_{ij}+b_{ij})} \times \frac{(\kappa_i b_{ij})^{N_{\text{OFF},ij}}}{N_{\text{OFF},ij}!} \cdot e^{-\kappa_i b_{ij}} \right], \quad (4.1)$$

where α_{DM} is the free physical parameter, identified as $\alpha =< \sigma_{ann} v >$ for annihilation and $\alpha = 1/\tau_{DM}$ for decay. The J-factor and κ are treated as nuisance parameters. $\mathcal{J}$ is the likelihood for J-factor, parametrized as a Gaussian function in $\log_{10} J$, with a mean value for $J = J_{obs}$ and width σ_J. $\mathcal{G}$ is the likelihood terms for κ_i, described by a Gaussian function with mean $\kappa_{\text{obs},i}$ and variance $\sigma_\kappa^2 = \sigma_{\kappa,\text{stat}}^2 + (\kappa \cdot \sigma_{\kappa,\text{syst}})^2$; i and j run over the data sample and the N_{bins} in energy, respectively. $N_{\text{ON},i}$, $N_{\text{OFF},i}$ are the number of observed events in the ON region and in the corresponding OFF region, respectively; $g_{i,j}$ and $b_{i,j}$ are the estimated number of signal and background events, respectively. Eq. 3.8 shows how the number of signal events is related with the physical parameter α, through the J and IRFs. For sake of completeness, the equation is reported here:

$$g_{i,j}(\alpha,J) = T_{\text{obs}} \int_{E'_{j,\text{min}}}^{E'_{j,\text{max}}} dE' \int_0^{\infty} dE \frac{d\phi}{dE} A_i(E) G_i(E,E'), \tag{4.2}$$

where T_{obs} is the total observation time, E and E' are the true and estimated energy, A is the effective Area and G is the migration matrix. Both A and G are part of the IRFs, computed trough MC simulated γ-ray dataset following the spatial distribution expected for DM-induced signals from Draco, reported in Fig 4.4.

Decay and annihilation cases are analysed with two different datasets, since J has different values, as well as the IRF computed with the proper Donut MC. For both cases, the average γ-ray spectra dN/dE are computed with the PYTHIA software, for DM particles of masses between 100 GeV and 100 TeV, as in [126], annihilating into SM final state pairs $b\bar{b}$, $\tau^+\tau^-$, $\mu^+\mu^-$, W^+W^-. For completeness, in the decay case, the spectra for a certain m_{DM} can be assumed to be the same of a DM particle with $m = m_{\text{DM}}/2$ that annihilate in one of the channel. This is true since its spectra is computed assuming that the branching ratio for that channel is 1.

The whole method is implemented in the framework *gLike* [114], which is used to produce the results of the following analysis.

4.4.3.1 Annihilation

Independent likelihood terms are defined for each wobble pointing of each MC periods considered, with $\log_{10}(J/\text{GeV}^2\text{cm}^{-5})$, merged together as Eq. 4.1 shows through the parameter $\alpha =< \sigma v >$. The null hypothesis is the case where $< \sigma v >= 0$ (no DM scenario), whereas the test hypotheses are built considering the DM flux computed according to the Eq. 2.1, with DM particles with masses spanning from 100 GeV to 100 TeV for pure annihilation channels $b\bar{b}$, $\tau^+\tau^-$, $\mu^+\mu^-$, W^+W^-. The likelihood maximization is performed constraining the annihilation cross section within the physical range, so that $< \sigma v >> 0$.

Fig. 4.9 shows the 95% CL upper limit on the $< \sigma_{\text{ann}} v >^{UL}$ obtained with the likelihood analysis as a function of the different DM masses for the different annihilation channels. The Energy bins are defined for E' ($E'_{min} =$,$E'_{max} =$), equidistant in $\log_{10}E'^3$. The two-sides 68% and 95% containment bands for the distribution of the upper limit under the null-hypothesis are also reported. The bands have been computed from the distribution of the upper limits obtained from the realization of 300 simulations of the null hypothesis ($< \sigma_{ann} v >= 0$), with the use of a toy MC simulation and assuming the same exposure as for the real data and

---

[3] Empty bins can be re-adjust and merge with neighbouring ones.

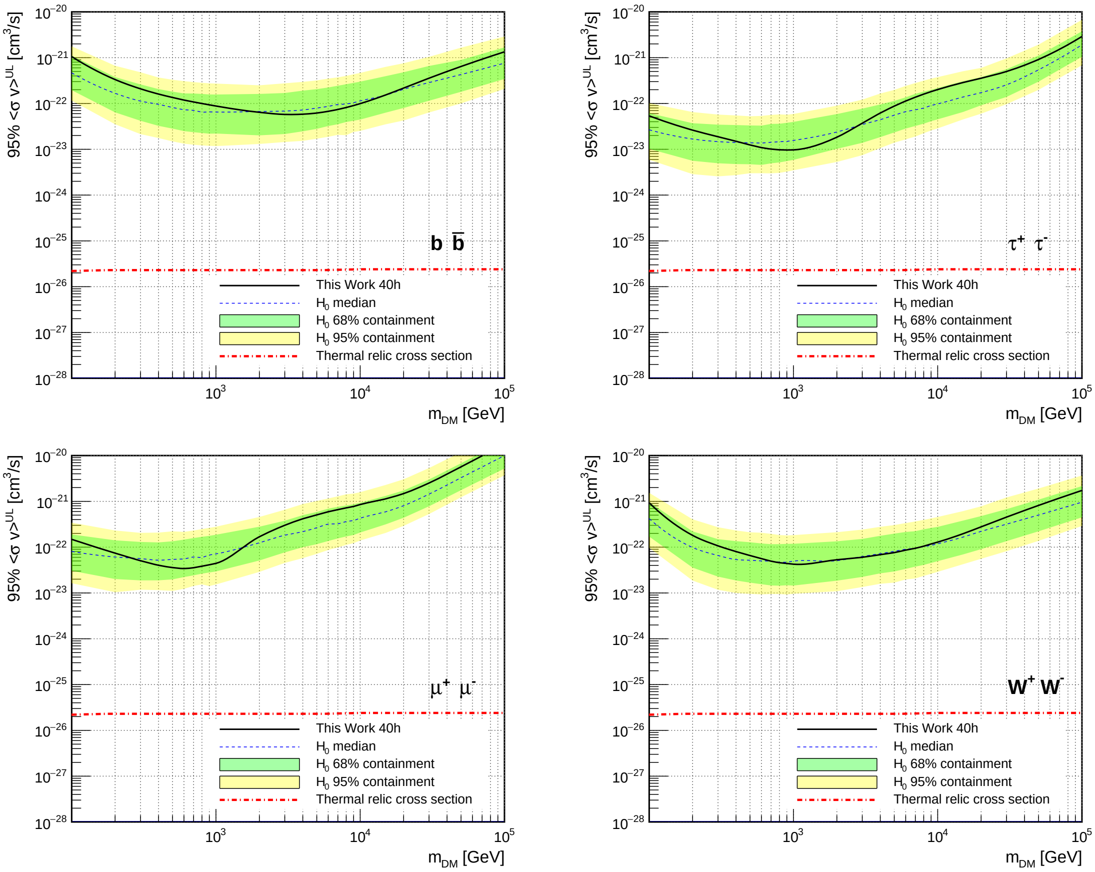

Figure 4.9 95% CL upper limit to the thermally-averaged cross-section of a DM particle annihilating into $b\bar{b}$ (top left), $\tau^+\tau^-$ (top right), $\mu^+\mu^-$ (bottom left) and W^+W^- pairs for DM masses from 100 GeV to 100 TeV obtained from the 52.3 h of good-quality observations of the Draco dSph. The green and yellow lines correspond to the 68% and 95% containment bands, respectively, of the distribution of the same estimator computed from 300 simulations of the null hypothesis ($< \sigma v >= 0$) mimicking conditions of the data sample.

with κ_i as a nuisance parameter. The relic thermal cross-section has also been reported for completeness, after considering a reference value for WIMP annihilation.

The results obtained lie within the 95% CL containment bans computed for the null hypothesis, in the entire range of DM masses. No evidence of DM annihilation is found. In each of the considered annihilation channels ($b\bar{b}$, $\tau^+\tau^-$, $\mu^+\mu^-$ and W^+W^-), $< \sigma_{ann} v >^{UL}$ is constrained at least to a value of 10^{-22} cm^3/s for DM particle mass in the TeV range.

4.4.3.2 Decay

The same analysis method is adopted for measuring the DM lifetime, considering DM particles in a mass range between 200 GeV and 200 TeV pure decaying in $b\bar{b}$, $\tau^+\tau^-$, $\mu^+\mu^-$

and W^+W^- channels. The data sample is different from the annihilation one, since the analysis cuts are different as for the J factor ($\log_{10}J = 18.97 \pm 0.17$). The null hypothesis, for which no DM contribution is expected, is described by $\alpha = 1/\tau_{\mathrm{DM}} = 0$. During the maximization of the likelihood, only the physical range is considered for the DM lifetime ($1/\tau_{\mathrm{DM}} > 0$)

Thus, the lower limits at 95% CL on the τ_{DM} are obtained with the likelihood analysis as a function of different DM masses for different decay channels ($b\bar{b}$, $\tau^+\tau^-$, $\mu^+\mu^-$ and W^+W^-) and are reported in Fig. 4.10. The two sides 68% and 95% containment bands for the distribution of the limit under the null-hypothesis are also reported. The bands have been computed from the distribution of the upper limits obtained from the realization of 300 simulations of the null hypothesis ($1/\tau_{DM} = 0$), obtained with a toy MC simulation, assuming the same exposure as for the real data and with κ_i as a nuisance parameter.

For this case too, the likelihood results are within the 95% CL containment bands, computed from the null hypothesis, for the whole DM masses range explored. Hence, no evidence of DM decay signal is found, for $b\bar{b}$, $\tau^+\tau^-$, $\mu^+\mu^-$ and W^+W^- decaying channels. The τ_{DM} is constrained up to 10^{26} s for $m_{\mathrm{DM}} > 100$ TeV, in each channel, except for $\tau^+\tau^-$ channel, where the best limit is $3{\cdot}10^{25}$ s.

4.5 Discussion and conclusions

In Fig. 4.11 the comparison of the results from this Draco analysis for DM annihilation channels with the results of the the combined Fermi-MAGIC analysis on 15 dSphs, combined analysis on dSphs from VERITAS (4 dSphs), H.E.S.S. (5 dSphs) and HAWC (15 dSphs) is shown.

The Draco results from this analysis provide ULs on $< \sigma_{ann}v >$ almost an order of magnitude less constraining than Segue 1 Fermi-MAGIC analysis, as expected from the lower J-factor value and the lesser amount of observation time used for the project. Similar arguments justified the less constraining limit compared to VERITAS and HAWC, where Segue 1 represents the most constraint result. H.E.S.S results are dominated by the 90 h observations of the Sagittarius dSph, which DM content strongly depends on the DM profile considered (the total J changes by a factor 4 considering a NFW or a Burkert profile [25]).

It must be noted that Draco was observed as part of a multi-year program, which aims to combine the limits obtained from the different dSphs in order to mitigate the systematic uncertainties linked with the J-factor estimation, thus increasing the robustness of the results achieved. Despite this, the results for a single dSph analysis are competitive w.r.t other Cherenkov experiments, thus confirming the high performances of MAGIC for DM research.

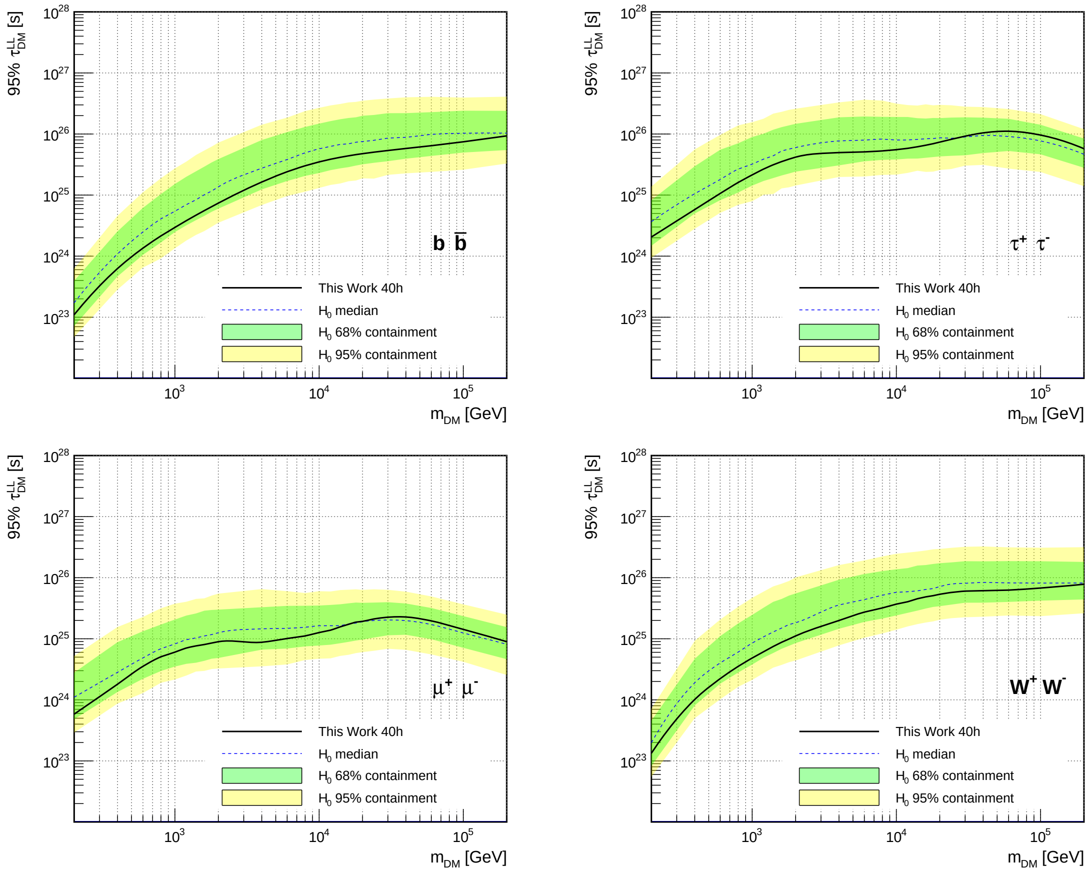

Figure 4.10 95% CL upper limit for the lifetime of a DM particle decaying into $b\bar{b}$ (top left), $\tau^{+}\tau^{-}$ (top right), $\mu^{+}\mu^{-}$ (bottom left) and $W^{+}W^{-}$ pairs for DM masses from 200 GeV to 200 TeV obtained from the 52.3h of good-quality observations of the Draco dSph. The green and yellow lines correspond to the 68% and 95% containment bands, respectively, of the distribution of the same estimator computed from 300 simulations of the null hypothesis ($1/\tau = 0$) mimicking conditions of the data sample.

In Fig. 4.12 the comparison of the DM decay channels results of this analysis on Draco data set with the analysis of 200 h of Perseus by MAGIC, the Fermi analysis on Galactic Center, the results from the analysis of Segue I by VERITAS and the combined analysis on 15 dSphs by HAWC is shown.

The extended halo and the reasonably large J-factor value of Draco provide very competitive results for the decay scenario. For small DM masses ($m_{DM} < 10(2)$ TeV for $b\bar{b}$ ($\tau^{+}\tau^{-}$)) the constraints are better than the ones achieved by Perseus analysis. For larger DM masses the limit is less stringent than the Perseus one, but it is still very competitive with the best results published so far.

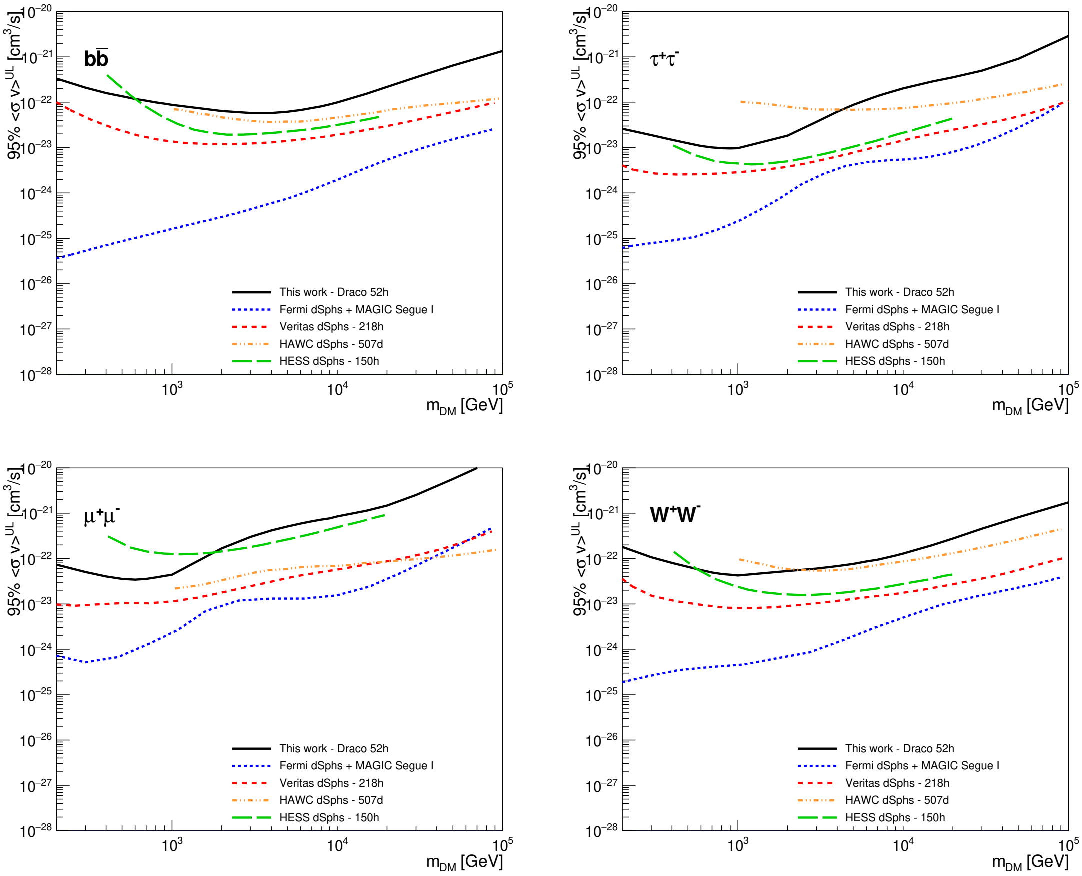

Figure 4.11 95% CL ULs on the thermally-averaged cross-section of DM particle for the $b\bar{b}$ (top left), $\tau^+\tau^-$ (top right), $\mu^+\mu^-$ (bottom left), W^+W^- (bottom right) channels, taken from the 52.3 h of good quality data from Draco dSph (this work, solid black line) compared with the limit of the joint analysis of MAGIC Segue 1 and of Fermi dSphs [23], and the limits from the combine analysis on a sample of dSphs from VERITAS [24], H.E.S.S [25] and HAWC [26]. In HAWC limits, the contribution of Triangulum II is excluded, since its DM content is not univocally defined [27].

The excellent results achieved with the Draco dSph are opening up the appealing new possibility of combining the DM lifetime constraints obtained with MAGIC into a single one. Indeed, the flexibility of the gLike framework allows to define independent likelihood terms for each of source considered, joining together results from dSphs, galaxy clusters and the Galactic Center and Halo.

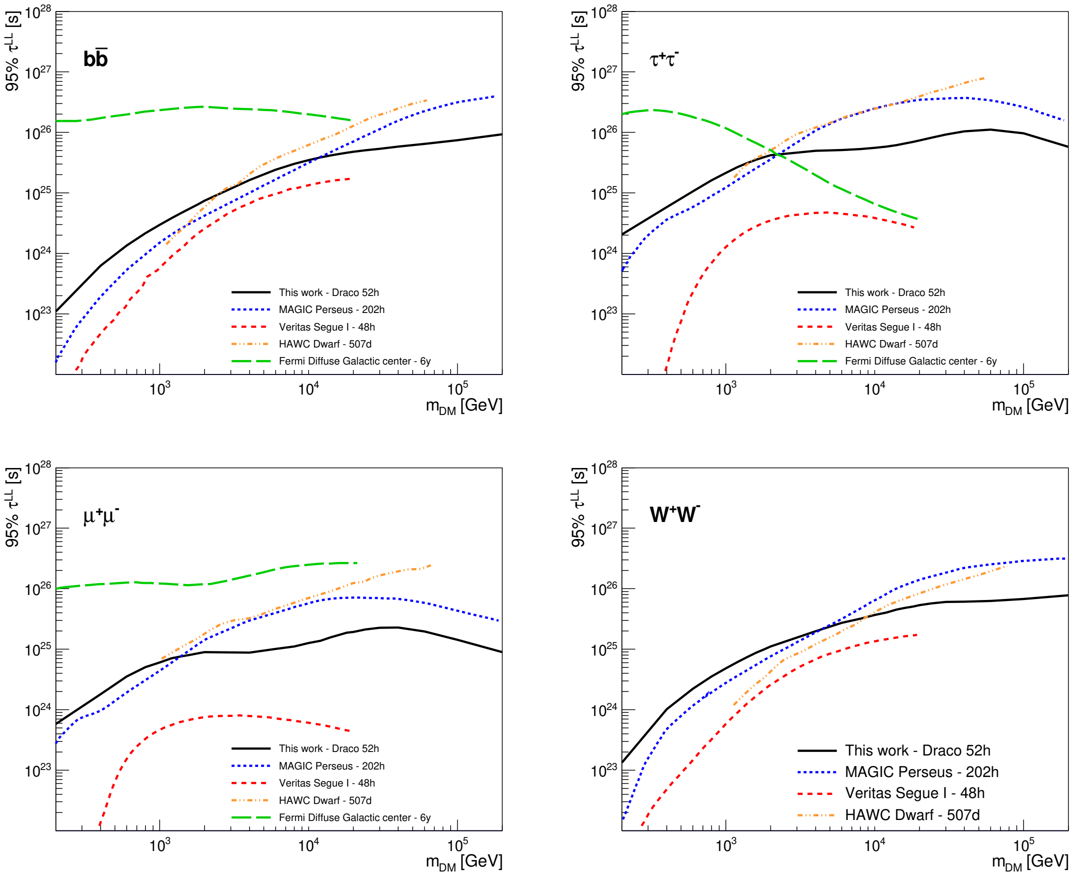

Figure 4.12 95% CL ULs on the lifetime of DM particle for the $b\bar{b}$ (top left), $\tau^+\tau^-$ (top right), $\mu^+\mu^-$ (bottom left), W^+W^- (bottom right) channels, taken from the 52.3h of good quality data from Draco dSph (this work, solid black line) compared with the previous MAGIC result on Perseus Galaxy cluster [28], the analysis of Fermi[29] on Galactic Center and of VERITAS [30] on Segue I, and the result from the combined analysis on dSphs by HAWC [26].

Chapter 5

Dark Matter search in the Galactic Halo

As introduced in Chapter 3, observations by Cherenkov telescopes are affected by the presence of a dominant (with respect to the typical gamma-ray source) and irreducible isotropic cosmic-ray background. γ-ray sources are identified as excesses of counts detected from a given region of the sky over such isotropic background. In their standard operation mode, for the estimation and subtraction of the background intensity in a given signal (or "ON") region, Cherenkov telescopes rely on the simultaneous observation of a nearby background control (or "OFF") region, with the same exposure to background events as the ON region. MAGIC has a relatively narrow field of view of $\sim$3.5° diameter, and an angular resolution of 0.1°-0.2°, depending on the energy. This allows defining convenient ON/OFF regions for the detection of point-like or slightly extended γ-ray sources, up to $\sim$0.4° radius. For larger gamma-ray sources, this method cannot be applied, and other means to estimate the residual background in the signal region must be devised.

5.1 Observation of the Galactic Halo with MAGIC

The Milky Way (MW) represents the closest and most DM-dominated object observable from the earth. The ΛCDM model predicts a DM distributions with a spherical symmetry, peaked at the center of the galaxy and decreasing towards the outer region, as shown in Fig. 5.1. As explained in Sec. 2.3.2.1, there is no a unique DM profile. N-body simulations, which aims to recreate the hierarchical formation of the CDM halos, lead to a profile with a center cusp well described by a power-law function, introduced for the first time by *Navarro-Frank-White* (NFW, see Eq. 2.8 [86]). More recent simulations, with a deeper resolution, have not shown the presence of the asymptotic slope towards the center, which best fit is represented by the Einasto profile (see Eq. 2.9 [87]). The slope of the Einasto profile function, asymptotically

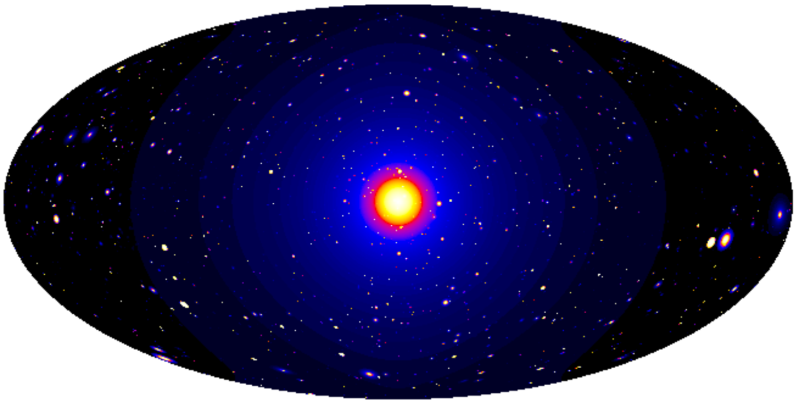

Figure 5.1 An aitof projection of a DM density profile of the Milky Way DM halo is reported. Figure adapted from [31].

approaches 0 towards the center, and consequently, providing a finite DM density value for $r = 0$. Finally, astrophysical observations show that the central cusp is not a common feature of many galaxies, which looks to be characterized by a flat core density in the innermost region. The kinematic fit to the galaxy rotation curve tends to an *isothermal* profile (see Eq. 2.10 [88]) predicts a flat core distribution, in contrast with NFW and Einasto results.

In Fig. 5.3 the three DM profiles mentioned, as a function of the galactocentric radius are reported, as well as the astrophysical or J-factor, defined in Eq. 2.4 and Eq. 2.7, for annihilation and decay case, respectively. The GC seems to be the most appealing region, according to the abundance of DM reported in Fig. 5.3a. On the other hand, the GC represents also one of the most crowded astrophysical regions. The high density of sources (also in the TeV energy range) creates a large, diffuse and non-homogeneous astrophysical background [127]. Thus, a reliable model of such emission is required, because uncontrolled background instabilities and fluctuations can mimic a possible DM signal, consequently lowering the sensitivity, or completely suppressing the faint DM signals (see also Sec. 2.3.3). Moreover, the enormous differences in the DM content foreseen by the different models in the inner part of the galaxy (see Fig. 5.3a) reflects a large disparity in the expected DM flux ϕ ($\phi^{\text{ann}}_{\text{Ein}} / \phi^{\text{ann}}_{\text{Iso}} \approx 10^2$, see Fig. 5.3b), making the measurement results highly model dependent.

On the other hand, the GH is almost background free, since it is sparsely populated and the diffuse emission of the GP and GC is not affecting this region (for an angular distance from the GC of $\varphi > 5^\circ - 10^\circ$ [128] [129] [130]). Moreover, shifting aside the GC, the DM density profiles derived from observations and simulations agree, thus J-factor and the expected flux does not depend significantly on the different models considered, as shown in Fig. 5.3. However, a drawback is that the expected flux drops off significantly with respect to the GC observations, especially for the annihilation process ($\phi(\varphi = 90)^\circ / \phi(\varphi = 0^\circ)|^{\text{NFW}}_{\text{ann}} \simeq 10^{-4}$,

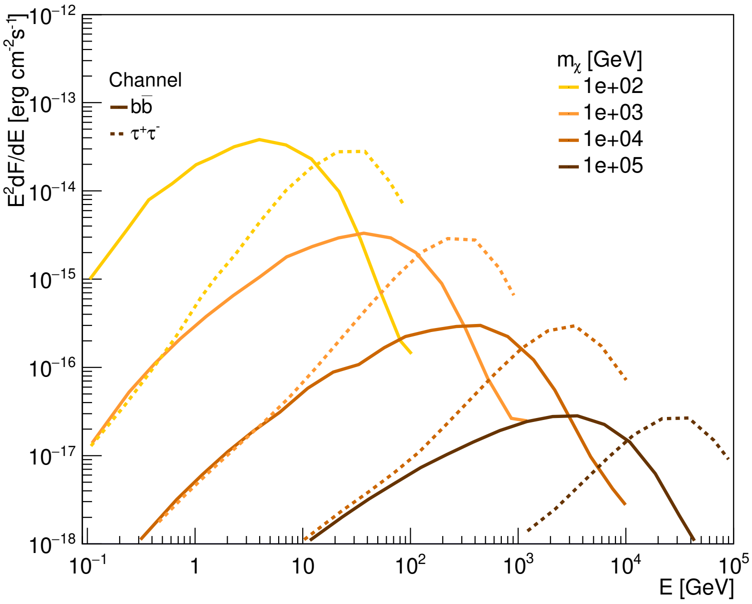

Figure 5.2 Expected γ-ray energy spectral distribution for WIMPs of masses m_χ=10^2, 10^3, 10^4, 10^5 GeV, annihilating with $<\sigma v> = 3\cdot 10^{-26}$ cm^{3}s^{-1} into $b\bar{b}$ and $\tau^+\tau^-$ pairs, for a dSph with an associated J-factor of $5\cdot 10^{21}$ GeV^{2}cm^{-5}. For decay case, a roughly estimation can be obtained by shifting the curves by a factor 2 in energy, assuming that the spectra of two DM particles annihilating corresponds to the one of a single DM particle decaying. Figure adapted from [32].

see Fig. 5.3b). That said, the expected flux from DM decay in the GH results to be comparable with the one expected from the GC (at most $\phi(\varphi = 90)^\circ/\phi(\varphi = 0^\circ)_{\text{dec}} \simeq 10^{-1}$, see Fig. 5.3b). This is the consequence of the quadratic and linear dependence of the J-factor with DM density profile ρ, as shown in Eq. 2.4 and 2.7.

Furthermore, as the GC culminates at Zd $= 57^\circ$ at the MAGIC site, the Energy threshold naturally increases because the atmospheric layer the electromagnetic cascade travels through is larger (see Sec. 3.1), the Effective Area is reduced at low Energy (hunderd GeV) and thus the sensitivity for DM process degrades. In fact, a large number of γ rays arise from DM particles annihilating or decaying have an energy around the energy threshold of MAGIC ($\sim$ 70 GeV), for WIMPs of masses up to tens of TeV, as shown in Fig. 5.2. Moving through the GH ($\varphi > 10^\circ$) MAGIC can observe regions with low Zd (Zd $< 35^\circ$), thus the Energy threshold naturally reduces and the sensitivity to DM process increases.

Because of these arguments, this chapter explores the search for DM signals in the GH, mainly through the decay channel. The key points which led to this decision are summarized:

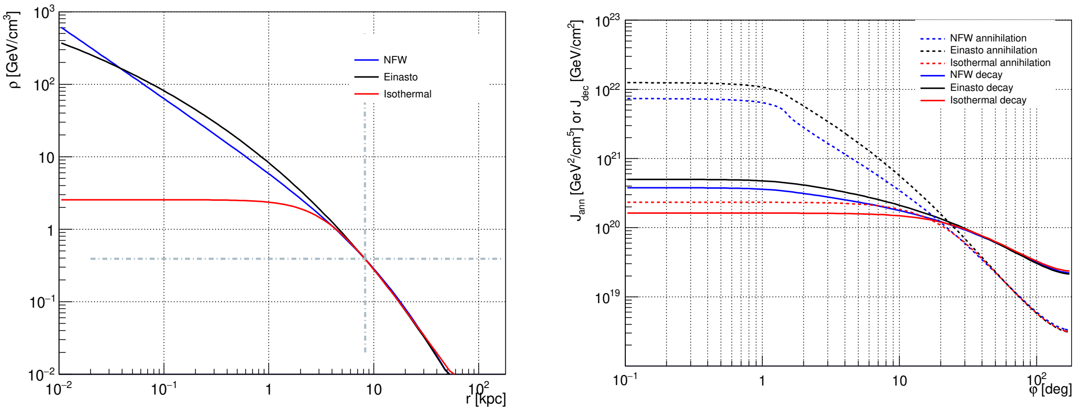

(a) (b)

Figure 5.3 The DM density profiles (a) for the MW and the respective J-factor (b), computed integrating ρ over a solid angle of radius 1.5°, for both DM annihilation and decay processes are reported in the figure. In Sec. 5.3.2 the integration angle of 1.5° is justified.

- MAGIC can observe GH at low Zd, which means low Energy threshold and large sensitivity to DM processes;
- GH background intensity is lower than the GC and GP regions and isotropic up to 10% of the sensitivity of MAGIC at 100 GeV [131];
- the expected γ-rays DM flux is consistent among the different DM density models in the GH region, increasing the robustness of the measurements;
- decay process provides an expected DM flux in the halo competitive with the one in the GC.

For sake of completeness, the results over the DM annihilation will be reported too, even though the GH will not produce competitive results compared with the best literature limits.

5.2 New method for observing very extended sources

IACTs can successfully observe point-like or moderate extended sources, benefiting from the wobble observation mode for estimating the background reliably (Sec. 3.3.2). This approach cannot be applied when performing observations of the GH, since the DM distribution covers the entire sky, as shown in Fig. 5.4.

Thus, observations of the expected signal (ON) and background region (OFF) have to be acquired in different FoVs. This observation scheme is called ON-OFF mode. When

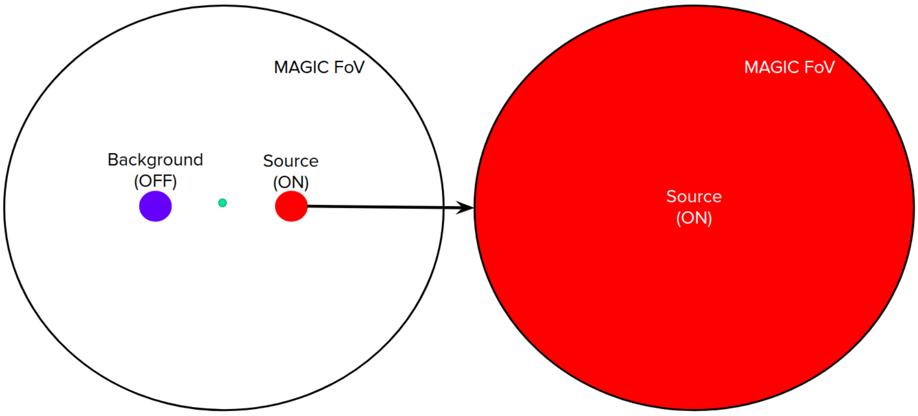

Figure 5.4 Left: qualitative illustration of a single wobble observation. The ON and the OFF are observed simultaneously with a small occupancy of the camera and therefore, by construction, under the same conditions. Right: the expected ON region of a GH observation fills completely and uniformly the camera, which forced us to use an ON/OFF observational approach. For this case, an alternative method for normalizing ON and OFF has to be investigated, as reported in Sec. 5.4.2.

observing the GH, the ON observations should be carried out with relative low φ (which corresponds to relatively high expected DM flux) and the OFF at relative high φ, (which corresponds to relatively low expected DM flux). With this configuration, in absence of systematic difference in the acceptance of the telescope's camera for different pointing, the difference of the observed number of events is proportional to the difference of DM density in the ON and OFF regions (see, Fig. 5.5).

This statement can be demonstrated by considering the expected diffuse event rate $\mathscr{R}$ detected by MAGIC (or IACTs in general) for a given observation. Its expression can be written as:

$$\mathscr{R}(l,\, b) = \mathscr{R}_{CR} + \mathscr{R}_{EG\text{-}\gamma} + \mathscr{R}_{EG\text{-}DM} + \mathscr{R}_{Gal\text{-}\gamma}(l,\, b) + \mathscr{R}_{DM}(l,\, b), \tag{5.1}$$

where:

- $(l,\, b)$ are the Galactic longitude and latitude,
- $\mathscr{R}_{CR}$ is the event rate of cosmic rays, mainly composed by H and He nuclei and e^- e^+ particle [132],
- $\mathscr{R}_{EG\text{-}\gamma}$ is the γ-rays integrated emission by the AGNs up to cosmological distances [130],
- $\mathscr{R}_{EG\text{-}DM}$ is the γ-rays events rate from the extragalactic DM sources [133],

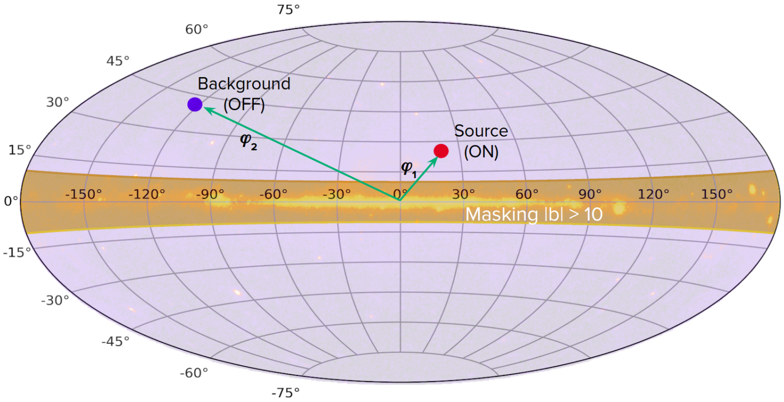

Figure 5.5 The figure shows an example of a possible ON-OFF observation pairs, as proposed for this work. The red and blue circles represent the MAGIC pointing positions for ON and OFF FoVs in galactic coordinates. The figure is superimposed to a Fermi Skymap for E >1 GeV. This shows qualitatively that with masking a region of galactic latitude $|b| < 10°$ around the galactic plane, the most of the VHE radiation are excluded. Image credit: NASA/DOE/Fermi LAT Collaboration.

- $\mathscr{R}_{Gal\text{-}\gamma}(l,\, b)$ is the γ-rays event rate from the interaction of the cosmic rays with interstellar medium and from unresolved source,
- $\mathscr{R}_{Gal\text{-}DM}(\varphi)$ is the γ-rays event rate from the DM process in the halo [134].

For observations of source-free FoVs, the first three terms are considered to be isotropic, while the last two are anisotropic, due to the Earth's location in the MW. In particular, the anisotropy of $\mathscr{R}_{Gal\text{-}DM}(l,\, b)$ is due to the non-symmetric view of the DM GH from the Earth. For observations out of the galactic region ($b > 10°$), the dominant component is $\mathscr{R}_{CR}$, which can be considered isotropic at a 0.1% level in VHE regime [135] [136]. Therefore, in an ON-OFF observation, the sensitivity to $\mathscr{R}_{Gal\text{-}DM}(\varphi)$ is limited by the statistical and the systematic uncertainties of this component.

By subtracting $\mathscr{R}$ measured in two different regions of the sky we end up with:

$$\Delta\mathscr{R}(l,\, b) = \mathscr{R}_{Gal\text{-}\gamma}(l_1,\, b_1) - \mathscr{R}_{Gal\text{-}\gamma}(l_2,\, b_2) + \mathscr{R}_{Gal\text{-}DM}(\varphi_1) - \mathscr{R}_{Gal\text{-}DM}(\varphi_2) \tag{5.2}$$

since all the isotropic components cancel out. Since $\mathscr{R}_{Gal\text{-}\gamma}$ is small and only mildly anisotropic for $b > 10°$ at TeV Energy, selecting FoVs where $\Delta\mathscr{R}_{Gal\text{-}\gamma}$ is negligible:

$$\Delta\mathscr{R} = \mathscr{R}(l_1,\, b_1) - \mathscr{R}(l_2,\, b_2) = \mathscr{R}_{Gal\text{-}DM}(\varphi_1) - \mathscr{R}_{Gal\text{-}DM}(\varphi_2). \tag{5.3}$$

This expression only depends on φ, since only the DM contribution survives. In absence of a systematic difference in the ON-OFF acceptance ratio, $\mathscr{R}_{Gal\text{-}DM}(\varphi)$ is proportional to the DM flux as Eq. 2.1 describes, therefore:

$$\Delta\mathscr{R}(\varphi_1,\varphi_2) \propto C\cdot(J(\varphi_1)-J(\varphi_2)) = C\Delta J(\varphi_1,\ \varphi_2), \tag{5.4}$$

where $C = \frac{\zeta_{\mathrm{DM}}}{4\pi}\cdot\frac{dN}{dE}$ ($\zeta^{\mathrm{ann}} = \frac{<sigma_{\mathrm{ann}}v>}{2m_{\mathrm{DM}}^2}$, $\zeta^{\mathrm{dec}} = \frac{1}{m_{\mathrm{DM}}\tau_{\mathrm{DM}}}$) and ΔJ is the difference of J-factor in the two pointings. Thus, this observation strategy strongly depends on the ON and OFF pointing positions, which have to be optimized by maximizing the ΔJ for the available positions.

5.2.1 Selection of the FoV

Eq. 5.4 states the possibility of detecting a DM signal by comparing different FoVs. The possible excess is computed using Eq. 3.2, which is reported here: $N_{\mathrm{ex}} = N_{\mathrm{ON}} - N_{\mathrm{OFF}}/\kappa$. In this case, the normalization factor κ cannot be computed as shown in Fig. 3.24. This implies that a different technique for measuring κ has to be adopted, whose systematic uncertainty $\sigma_{\kappa,\mathrm{syst}}$ have to evaluated.

Hence, the success of this ON-OFF method depends on two main factors: on one hand the ΔJ have to be as large as possible, on the other hand the σ_{syst} related to the normalization factor between ON and OFF has to be as small as possible and kept under control. These requirements can be achieved developing an appropriate pointing strategy for ON and OFF FoVs.

First of all, the observing conditions have to be as homogeneous as possible. This means that the systematic related to the pointings are kept to a minimum and possibly totally under control. In an ON mode observation this can be achieved requiring that the ON and the OFF follow exactly the same trajectory in the sky, in terms of local pointing coordinates (Zd, Az), and be acquired during the same observation night. This ensures a minimum difference in the development of the EAS, because the telescopes are observing the same identical portion of the sky with the same Earth magnetic field (see Sec. 3.1 for more details) and guarantees homogeneity and stability in both hardware and weather conditions. Furthermore, the FoVs have to be selected during dark time conditions (no moon or twilight time), avoiding the presence of bright stars and known VHE sources in the camera trigger region. Patches with stars up to a magnitude of 6 in blue light are dismissed. Stars and VHE energy sources positions are taken from in the NOMAD [137] and 3FHL [138] catalogues, respectively. All those requests limit the possibility to have a large NSB level and inhomogeneities between the FoVs, which could consequently increase the σ_{syst} level.

In order to maximize the performance related to the DM search, the observations are foreseen to occur with a Zd < 35° (see Sec. 5.1). Constraining the trajectory of the ON and

OFF limits the available values of ΔJ during a night of observation. In fact, during each night, the sky performs an apparent rotation around the Polaris, i.e. each point in the sky moves following a circular arc, as can be seen in Fig. 5.6. Thus, ON and OFF are constrained to follow the same arc too, limiting the ΔJ to the value accessible over such trajectory. Therefore, each pointing positions, i.e. each trajectory followed, need to be optimized in order to achieve the best value of ΔJ.

The best pointing is computed as follow. For each ON/OFF couple, the associated ΔJ is given by computing φ of each pointing and reading the corresponding value of J from the plot in Fig. 5.3b. The largest value of ΔJ is selected for each night and for each possible pointing position, over one Cycle of MAGIC observation (approximately one year). Then, the means of the ΔJ values over the period considered and for the different pointing positions (or trajectories) are computed and shown in Fig. 5.7. As result, pointing positions around (Zd, Az) $= (30°, 180°)$ maximize the ΔJ for ON and OFF that follow the same trajectory. This result was foreseen since this pointing is orthogonal w.r.t. the Polaris position and gives access to the closest points to the GC fulfilling the required conditions. Consequently, the sky rotation occurs faster, the distance achievable between ON and OFF is larger and, hence, the ΔJ results the maximum.

Figure 5.6 The figure shows the apparent rotation of the sky through a long time exposure photo, where the tracks of the stars are visible. All the sky positions rotate around a spot where the Polaris is. The length of each track clearly depends on its distance from the rotation center.

Therefore, the a-priori requirements to fulfil when selecting the pointing positions for both ON and OFF are:

- following the same trajectory in local coordinates during the same night,

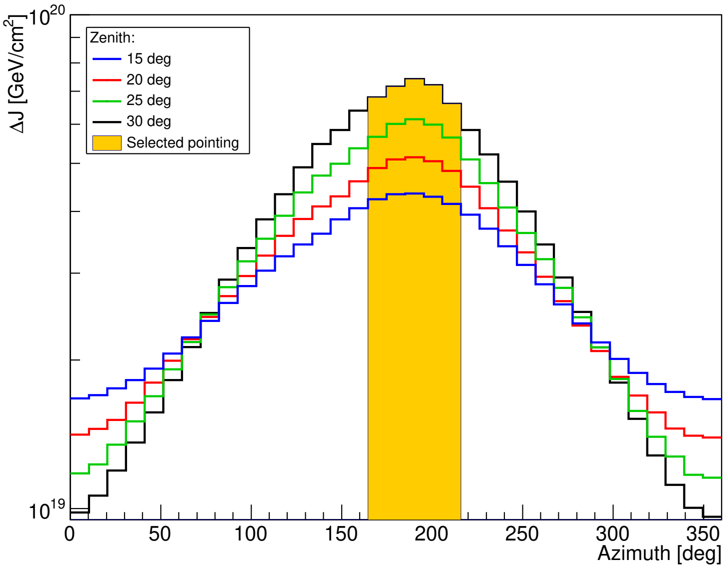

Figure 5.7 The maximum ΔJ values computed over one year of observation of the GH at the MAGIC site as a function of the Az pointing, for different Zd pointing are reported in the figure. The entire dataset has an Az starting pointing aligned within the orange band.

- Zd $< 35^\circ$,
- $b > 10^\circ$,
- maximizing the ΔJ,
- using dark FoV, containing neither bright stars nor known γ-ray sources inside the trigger region,
- dark observation time.

In order to guarantee the homogeneity between ON and OFF FoVs, the atmospheric conditions have to be carefully monitored during the data taking, using the LIDAR. To limit the bias on the energy estimation to a 10%, a lower limit of 0.9 on the atmospheric transmission at 9 km is set, as suggested in [103]. This constraint ensures the energy bias be lower than the nominal MAGIC energy bias of $\sim$ 15% [20].

A remarkable point is that in our region of search ($\varphi > 10^\circ$ in Fig. 5.3b, since $\varphi^2 = b^2 + l^2$) the three models considered agree on the GH DM content, making our results more robust. In the next sections, the term J-factor is referred to the value obtained from the einasto profile, which is anyway similar to the values obtained from the the others profiles within 10% of its value (see also A.1).

5.2.2 Scheduling of the observation

The GH observations have been planned such that they include one-hour-long ON/OFF pairs during the same night with the highest ΔJ as possible, while respecting the constraints presented above. The duration of the slots is long enough to guarantee a good statistic even in the case part of the observational slot is lost due to external causes (e.g. bad weather).

Thus, the possible ON-OFF couples are selected among all the available dark time slots for the MAGIC observation nights, fulfilling the constraints mentioned above (see Fig. 5.9) and ranked according to the maximum ΔJ available (the J factor is computed on a FoV of 1.5°, corresponding to the MC radius, as explained in Sec. 5.3.1). The minimum ΔJ accepted is computed by a fast MC simulation, ensuring a sensitivity on τ_{DM} of 10^{26}s for 40 h of observation, resulting in a limit of 85 % of the largest ΔJ available during the year. With this requirement, about 50 days (i.e. 100 h) have been considered suitable for GH observations.

When a time slot is assigned to a GH observation, a second optimization of the initial (Zd, Az) pointing, together with an adjustment of the slot timing position is performed. When these two parameters are optimized the largest ΔJ for that night, fulfilling all the requirements requested, is obtained.

As mentioned, the above requirements are meant to minimize the systematic uncertainties σ_{syst} between the acceptance ratio of ON-OFF slots. Their evaluation required dedicated observations where the contamination of possible DM signal is minimum, i.e. with a ΔJ as lower as possible. All the other constraints have to be applied to these observations, too. A sample of 18 nights is identified, with a $\Delta J \approx 25$ lower w.r.t. the night with high ΔJ. This sample has to be equally representative of the whole sample in terms of time distance between ON and OFF. Fig. 5.8 (left panel) shows that the low ΔJ sample typical time distance is a factor 2 lower than the one relative to the observations with high ΔJ, approximately 3 h. This time is enough to observe FoVs belonging to different patches of the sky, as Fig. 5.8 (right panel) shows, making the low ΔJ sample representative of the entire GH observations.

Finally the scheduling procedure has been fine-tuned even further to obtain compatible trajectories in observations scheduled over consecutive days. So, expecting a σ_{syst} value, in this case, compatible with the one referring to the same night, a "faulty" slot can be replaced by the one belonging to the following night without wasting observation time. In this work, those observations are used for evaluating the σ_{syst} in consecutive days observations, as described in Sec. 5.4.4.

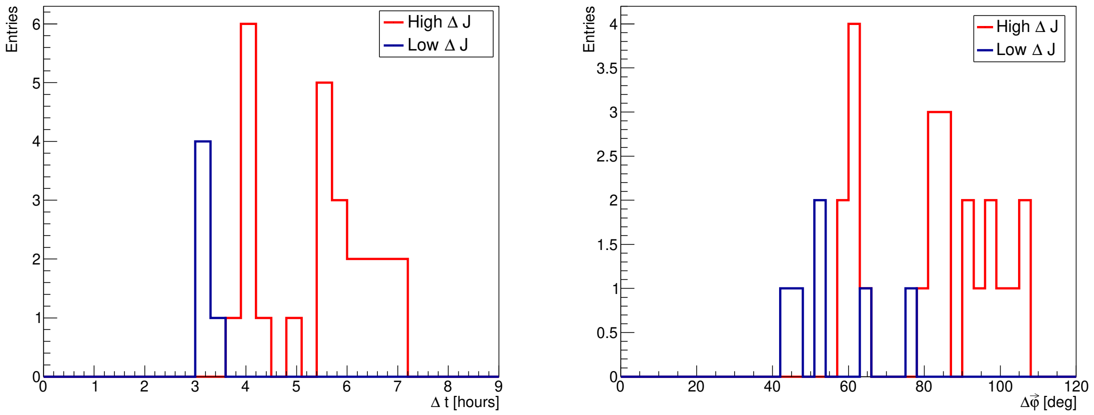

Figure 5.8 Left: the time distance between the ON and OFF slots for the entire dateset of GH observations. Right: the angular distance of ON-OFF slots for the GH data sample. For both panels, the high ΔJ sample is in red, while the low ΔJ one is in blue.

5.2.2.1 GH scheduling and observing process

The scheduling process of a GH observation requires a good synergy between different parts of the MAGIC collaboration. First of all, a scheduling team is in charge of planning the observation of the whole night at the begin of each period. Each observation has a different priority, ranked on its scientific value. Transient phenomena, like GRB or gravitational waves events, as well as Target of Opportunities (ToO) sources have always the priority and the scheduling can be changed also during the observation, whether is needed.

The scheduling of the GH observations needs to fit inside this not so predictable mechanism, with the disadvantage that the time slots are fixed once the trajectories are defined. For big delays in the time slot or changes in the schedule, new GH slots have to scheduled in order to guarantee the largest ΔJ available. To ensure a fast computation, a python script based on *astropy* class computes the J-factors for the time slots and the pointing positions requested, and sorts them. For each J, the corresponding FoVs are selected if they fulfil the constraints required. This fast computation allows to promptly react to scheduling issues.

5.3 Description of the dataset

GH was observed by MAGIC during 2018-2019. The dataset consists of a small data sample with low ΔJ for evaluating the σ_{syst} and a larger one with high ΔJ for measuring τ_{DM}. MAGIC collaboration granted 10 hours of observation time (5 h for the ON(OFF) slots) with low ΔJ

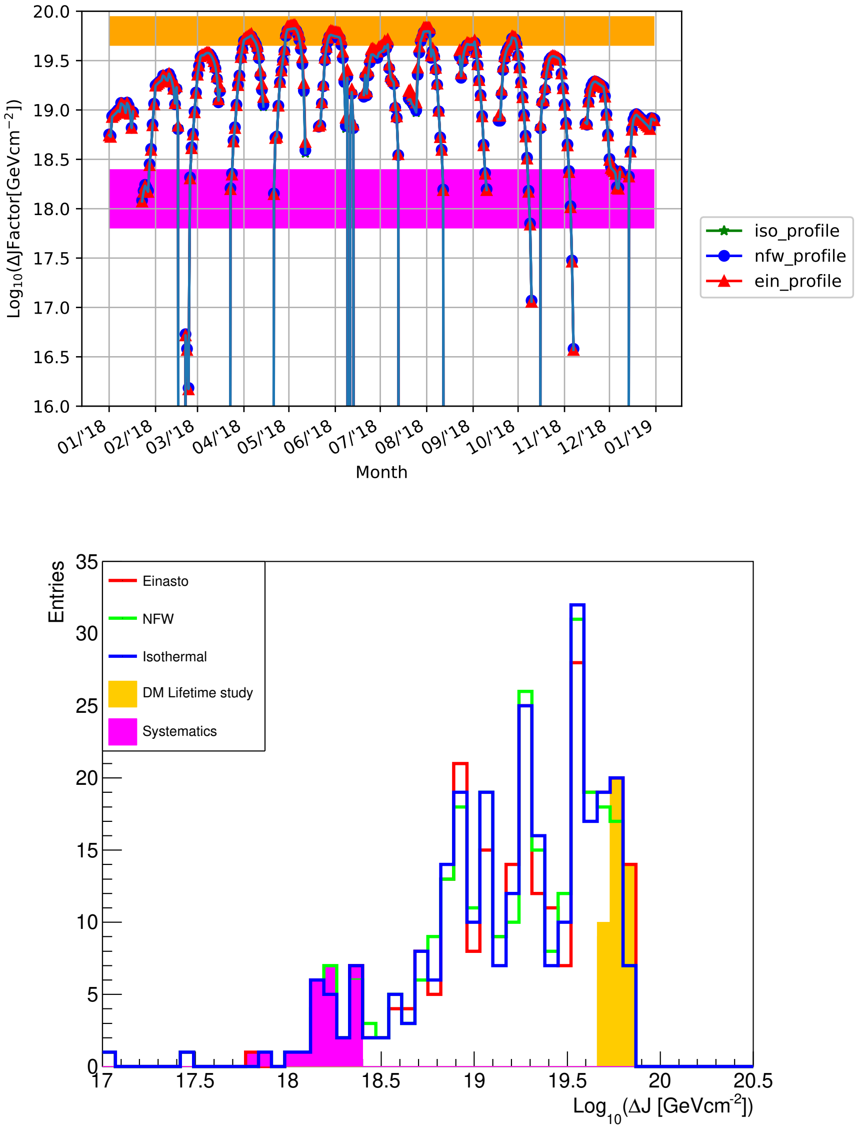

Figure 5.9 Top: $\mathrm{Log}_{10}(\Delta J_{\mathrm{dec}})$ computed for all the available nights of one year of observation, with a starting pointing of (Zd, Az) = (30°, 180°). The plot refers to the observations for 2018, which has a shape fully compatible for 2019. Bottom: distribution of the $\log_{10}\Delta J_{\mathrm{dec}}$ from the left panel. The orange and magenta histograms represent the J-factor values for the selected observation nights used for the DM lifetime study and systematic evaluation, respectively. For the systematic study we did not consider the lowest J-factor available (10^{16} GeV/cm^{-2}), because the time separation between ON and OFF slots was not the typical one used during the nights dedicated to the lifetime study.

Period	Setup	Validity date
ST0309	Normal operation	20180101−20180630
ST0310	Low mirrors reflectivity due to strong Calima	20180630−20180831
ST0311	Mirrors reflectivity come back to nominal value	20180831−20190831

Table 5.1 Summary of the analysis periods during which GH observations have been performed.

for studying and characterizing σ_{syst}, while 40 hours (20 h for the ON(OFF) slots) with high ΔJ for the measurement of the DM lifetime.

During the two years of observation, MAGIC acquired a total of ∼63 hours of GH observations among three different analysis periods, defined by a change in the telescopes' performance, as mentioned in Sec. 3.3.3 and Tab. 5.1. Those different conditions are taken into account in different MC production.

The entire dataset of 63 hours is presented in Tab. A.1 in Appendix 1. The data are grouped into the analysis period defined by the different MC simulations. For each observation, the pointing information, as well as the total J-factor and ΔJ for each night have been reported.

A summary of the pointing positions in terms of galactic coordinates are presented in Fig. 5.10. The pointing positions are shown in Aitoff-projection, where the galactic latitude and longitude are reported. Each point represents the FoV tracked for each of the slots observed. The ON-OFF couples with high ΔJ are represent by the red-blue markers, while the light red-cyan diamonds are the couples with low ΔJ. The red line represents the (Zd, Az) = (30°, 180°) pointing, and the observations lie around this line, as expected. Moreover, the ONs are observed over this trajectory in positions closer to the galactic center w.r.t. the OFFs and the FoV with low ΔJ.

5.3.1 Quality cuts and data reduction

To ensure an excellent quality of the data, the observations were reviewed daily, interacting with the data taking crew when needed. The standard MAGIC data quality check was run for each night individually, selecting events with DC lower than 3000 mA and a 9km atmospheric transmission > 0.9. In parallel, the ON/OFF pointing requirements were checked, in terms of trajectories overlap and distance from the galactic plane.

From the entire dataset of observations, 13 hours have been discarded, as reported in Tab. 5.2. Mainly, those nights were discarded due to a worsening of the weather conditions, meaning that one of the slots could not be observed. In other cases, a last minute ToO requested during one of the slots assigned to GH made it impossible to rearrange the schedule

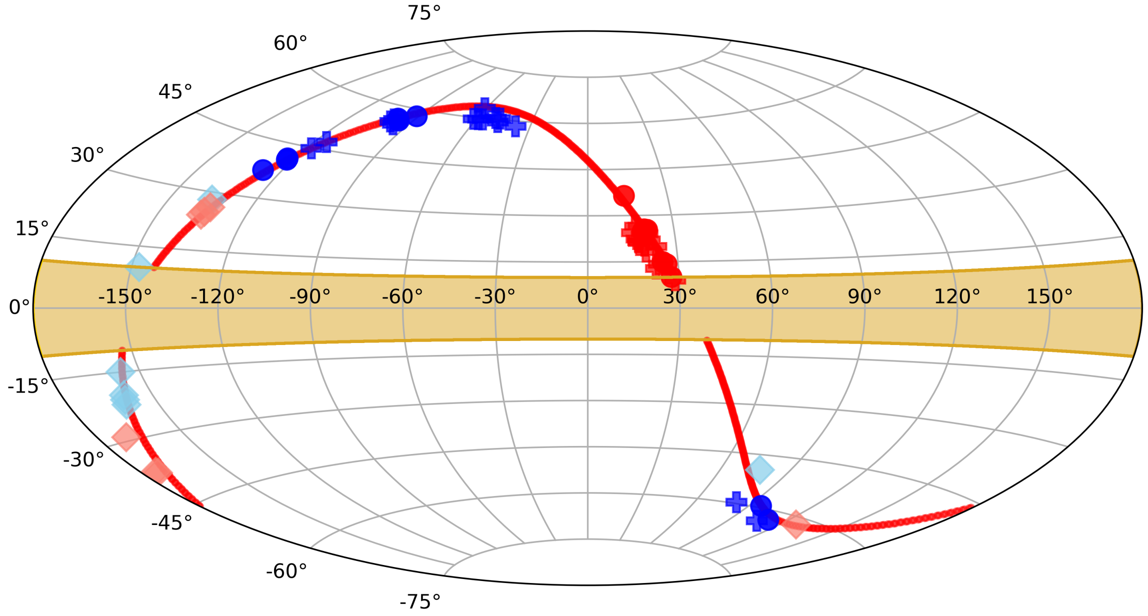

Figure 5.10 The figure shows the Aitoff-projection of the dataset, with the exclusion the 10° exclusion region around GP (light orange) are reported. The red and the blue points are the ON and OFF FoVs for the nights with larger ΔJ, respectively (circle and cross for 2018 and 2019 data). The light red/light blue diamonds refer to the observations with low ΔJ. The red solid line refers to a typical pointing of (Zd, Az) = (30°, 180°) from the MAGIC site. The observations lies around this line, as expected, since this is the pointing that maximize the ΔJ .

Period	**Obs. Time (hh) (before cut)**	**Quality cut (hh)**	**Scheduling cut (hh)**	**Az Overlap cut (hh)**	**Obs. Time (hh) (after cut)**
			low ΔJ data		
ST0309	12	2	-	2.1	7.9
			high ΔJ data		
ST0309	12	-	4	0.2	7.8
ST0310	6	2	-	-	4
ST0311	33	3	2	-	28
Total	**63**	**7**	**6**	**2.3**	**47.7**

Table 5.2 Overview on the data selection cuts. The total observation time dedicated to the project, the time cut by the data checking and the total time after cuts were reported. Here, the quality cut refers to the areosol Tr9km > 0.9 condition, the scheduling cut refers to the problem related with scheduling issues, while the Az refers to the trajectories overlap.

for that night, with the result that the slot was lost. Two cases of an overestimation of the online lidar transmission at 9 km during calima were spoiled, so that the transmission value computed offline was lower than expected. Finally, the difficult scheduling of the source created misunderstandings that sometimes ended in a wrong schedule for the source. Through the experience gained, we have learned how to avoid these problems and we have increased the duty cycle of the observations: during 2018, the observation duty cycle was 71%, whereas in 2019 it was 88%. A summary of all the problems affecting the dataset is presented in Tab. 5.3.

The events which pass the quality selection are processed by the *Melibea* executable, and are assigned an estimated energy, an estimated direction and a hadronness value (h), computed by a RF boosted decision tree. The RF has been computed using the *coach* executable, for three different analysis periods, as reported in Tab 5.1. The three periods are defined according to different mirrors' reflectance, taken into account in the MC data.

The training of the RF algorithm, as well as the computation of the IRF, are performed using a sample of Monte Carlo simulations of a diffuse gamma-ray emission, with events uniformly distributed in a radius r_{MC} of 1.5°. In particular, the IRFs are computed by scaling the total MC generation area by the ratio of the events passing all the analysis cuts, $N^{\theta<\theta_{max}}$, (quality, hadronness and θ) over the total generated events within a radius of 1.5°, $N^{1.5^\circ}$. Consequently, the J-factor values of Fig. 5.3b are computed over the same radius of 1.5°. Further, a scaled effective J-factor is adopted during the analysis[1].

The IRFs are computed considering an uniform distribution of J into the FoVs, whereas it is present a J-factor gradient in the direction towards the GC. The maximum difference is

---

[1] The effective J-factor in the analysis is scaled by $N^{\theta<\theta_{max}}/N^{1.5^\circ}$, the same scaling factor of the IRF.

Night	Issue
20180114	Humidity > 90 % during the OFF slots$^{(1)}$
20180216	Tr9km < 0.9 during the OFF slots$^{(1)}$
20180412	Wrong time slots assignation$^{(2)}$
20180511	Wrong coordinates scheduled$^{(2)}$
20190602	Strong wind during one of the slot$^{(1)}$
20190604 20180712	Calima made the onsite LIDAR analysis overestimated the Tr9km$^{(1)}$
20190503 20190801	Last Minute ToO requested in the GH time slots$^{(3)}$

Table 5.3 Summary of the issues encountered during the GH observations. Bad atmospheric conditions $^{(1)}$ cannot be well predicted, because the forecast at the observatory can change rapidly. Scheduling issues are divided in two categories, the $^{(2)}$ concerns the telescope scheduling operation, avoided with an extensive cross-checking of the schedule by the whole observation team, while the $^{(3)}$ refers to the case when observations with higher priority that during the GH slots.

of between the values of J in the camera goes from 7% for FoVs close to the GC ($\varphi = 10^\circ$) to 1% for $\varphi = 90^\circ$. This effect creates a inhomogeneity in the events distribution inside the camera, that are not taken into account in the diffuse MC, thus the IRFs may be affected. The gradient affects the Zd distribution, increasing systematically the events for certain Zd. Hence, it is possible to evaluate this effect by computing the IRF (e.g. EAs) for two pointing positions distant at least $\sim 2^\circ$. In Fig. 5.11 the EAs of two GH OFF observations, distant $\sim 2^\circ$ in local coordinates, are reported, as well as the their relative difference (applying the analysis cuts, presented in the next section). In the plateau region, the relative difference between the two EAs is at most 5%. This value can be considered as an upper limits of the effect of the gradient on the IRF computation. Since it affects only the ON slots (they are closer to GC $\varphi \approx 30^\circ$), the 5% can be considered as an extra uncertainty to be added in squared to the statistical uncertainty of the ON EAs.

5.3.2 Cut otpimization

In MAGIC, the signal region is defined in terms of θ_c and h_c and it is optimized using a sample of Crab Nebula observations. In this case the Crab Nebula is no longer a good probe, since it does not match the characteristics of our source emission (the Crab is a point-like source for MAGIC). Thus, the analysis cuts have been optimized in terms of θ and hadronness (h) using fast MC simulations and maximizing the sensitivity on $\tau_{\rm DM}$ for the case of no DM signal, according to the Eq. 3.11, for a representative sample of DM masses.

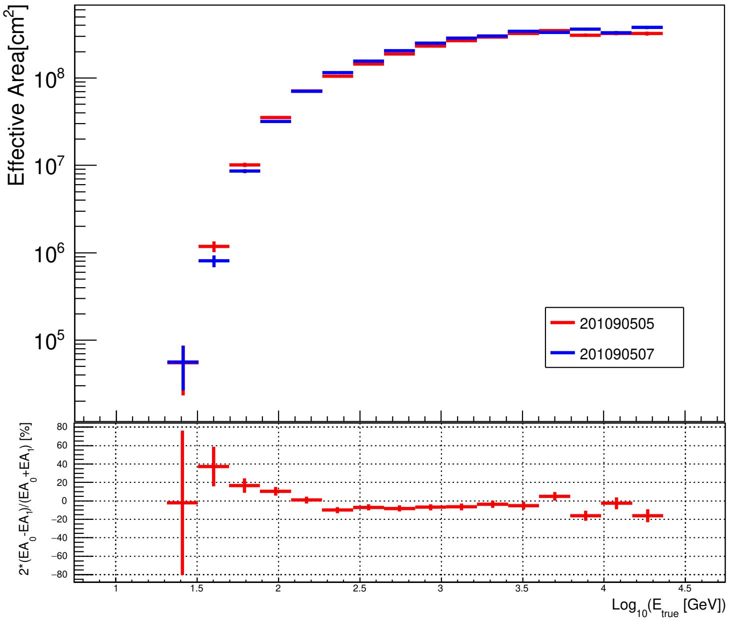

Figure 5.11 Top: the Effective Area for the OFF slots of the observations carried out in 20190505 and 20190507 are shown. Bottom: the relative difference between the two Effective Area is reported.

In Fig. 5.12 the sensitivity for different cut values over the maximum sensitivity to the DM lifetime for a given DM masses, is reported. Left panel shows the dependence of the sensitivity ratio as a function of θ_c, for a fix value of $h = 0.3$. The best θ_c choice is driven by two main factors. The GH signal is considered flat into the entire FoV, hence a larger angular cut corresponds to more signal integration, i.e. the sensitivity increases. In some cases, it can happen that some events with θ close to 1.5° (limit of the simulated MC events) would actually have a reconstructed $\theta > 1.5°$, due to the angular resolution of the camera. These events are not included in the reconstructed MC events, then, the IRFs for a $\theta_c = 1.5°$ would not be correct. As shown in the left panel of Fig. 5.12, going beyond the MC radius of 1.5° results in a wrong computation of the IRF, since the MC events with $r > r_{MC}$ are missing. A θ_c lower than the r_{MC} is a conservative and safer choice. Hence, for these reasons a θ_c selected is 1.2° is selected, where the acceptance is expected to decrease at most by a 10% for DM mass of 100 TeV

Right panel of Fig 5.12 reports the sensitivity ratio for different h_c, with $\theta_c = 1.2°$. Both energy dependent and independent h_c are considered. The former are computed considering the fraction of MC events that survives the analysis cuts (70%, 80%, 90%), while the latter is a constant cut for the all energy bins. The largest sensitivity for most of the DM masses scanned is obtained for $h_c = 0.3$.

Hence, our signal region is defined as $\theta_c < 1.2°$ and $h_c < 0.3$.

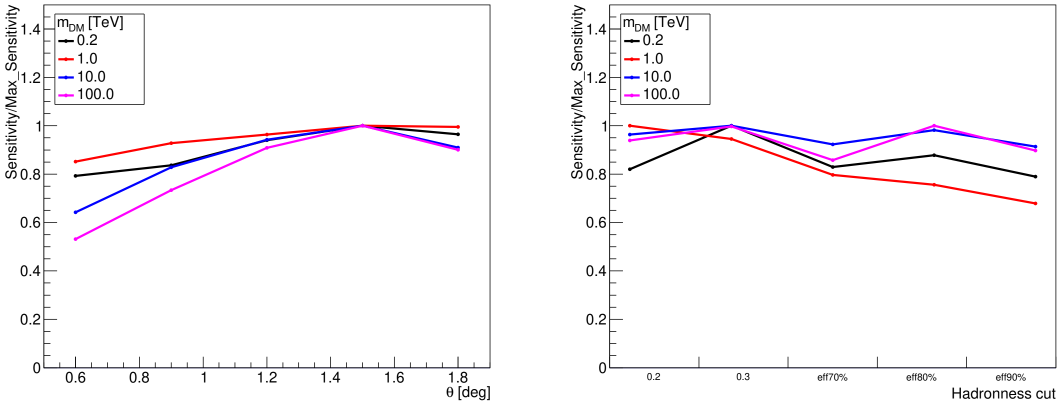

(a) (b)

Figure 5.12 Sensitivity over the maximum sensitivity values to DM lifetime for different DM masses, computed as explained in the text, as a function of θ_c (left) and of h_c (right).

5.4 Systematic uncertainties on the GH measurement

In this section the evaluation of the σ_{syst}, the systematic uncertainty of the telescope acceptance within the ON and OFF FoVs, is described.In particular:

- first, the problems related to the evaluation of the σ_{syst} for the observation method adopted in this work are presented. Later, the non-standard methodology developed for evaluating σ_{syst} with ON-OFF observations is described in detail, and applied to the low ΔJ data. The value found represents the σ_{syst} that is used in the DM lifetime measurements.

- A second approach concerns the evaluation of σ_{syst} in the case of consecutive observation days. As mentioned in Sec. 5.2.1, the dataset contains compatible observations in terms of the (Zd, Az) trajectory carried out during consecutive days. In the case the systematic uncertainties maintain the same properties as the one computed with the low ΔJ sample, observations from consecutive nights can also be combined in the likelihood analysis.

- The systematic uncertainties are then studied with a different approach. Using the dataset and combined ON-OFF observations with low ΔJ it is possible to study both the variation of the systematic value for different periods of the year.

- Finally, a future prospective concerning the application of this method to archival data is presented. A first proof of concept on a sample of Draco data is presented, computing the value of σ_{syst} in this case. Further studies are needed to properly evaluate which observations would be suitable for this project.

5.4.1 Introduction

The ON-OFF observation mode is not considered the optimal method for MAGIC, and it should be only adopted in special cases, when the wobble mode cannot be used. In general, the ON and the OFF have the same acceptance for the background events only up to a certain level of precision, which needs to be estimated. This effect is quantified in the systematic uncertainties related to the ON/OFF normalization factor, $\sigma_{\kappa,\text{syst}}$. The value of $\sigma_{\kappa,\text{syst}}$ cannot be computed a priori, and need a specific analysis for evaluating it properly. Moreover, its impact in the analysis is clearly identified, since the normalization factor κ enter in the likelihood as a nuisance parameter, described by a Gaussian function with a width σ_{κ}^2=$\sigma_{\kappa,\text{stat}}^2 + \kappa^2\sigma_{\kappa,\text{syst}}^2$.

In general, the systematic sources in the ON/OFF acceptance ratio can be related to weather conditions, to the instrument itself and to the FoV. Atmospheric phenomena can change rapidly at the Roque observatory, with weather conditions highly variable even during a single night. Phenomena like dense clouds, calima and humidity can modify the quantity of Cherenkov light reaching the telescopes, lowering the number of photons detected. Atmospheric monitoring is mandatory to ensure the good quality of the data acquired. Moreover, the accurate LIDAR measurement of the atmospheric transmission can later be used to correct the energy of the EAS detected and the shape of collection area, even though a certain systematic in energy estimation is introduced [103]. The instrumentation can also alter the level of the systematic, due to problems with the mirror, trigger inefficiencies or camera inefficiencies. Usually, when those problems occur during the observations, the data collection is halted. In cases where those effects do not prevent the collection of quality data, a new MC production takes into account the different conditions of the instrumentation, as mentioned in Sec. 3.3.3.1. The pointing can also introduce some systematics, because the development of the electromagnetic shower is influenced by the thickness of the atmospheric layer (Zd pointing) and the Earth's magnetic field (Az pointing) [139]. How these effects could influence the background acceptance is taken into account in the value of σ_{syst}, which is studied in details in the next Section.

A fundamental aspect is whether the κ depends or not on the energy, and in case of energy dependence whether or not the values at different energy bins are correlated. In the case κ changes independently in each energy bin, this behaviour can, in principle, mimic any possible spectral shape, thus also a possible DM signal. In this case the DM spectral information is completely ruined, loosing the advantage of using the full likelihood approach, with the consequence of worsening the sensitivity as the value of σ_{syst} is larger. On the other hand, the variation of κ in each energy bin can be not independent, or, even better, completely correlated. In such case, is possible to disentangle the information of the DM spectra with the effects of the background normalization. The sensitivity to DM process is preserved, indeed.

These scenario are reported in Fig. 5.13, where the background normalized is reported together with a possible DM spectra. It is clear that how κ depends in the energy bins, has a large impact in the overall sensitivity of the measurement. In Fig. 5.14 the sensitivity values computed with a fast MC simulation of the null hypothesis (no DM) as a function of σ_{syst} over the value of sensitivity for $\sigma_{\mathrm{syst}} = 0$, are reported. In terms of likelihood functions, the two cases are represent by one single nuisance parameter valid for the all bins in energy ($\mathscr{L} = \mathscr{G}(\kappa)\prod_i^{N_{\mathrm{bins}}} \mathscr{P}(g_i)\mathscr{P}(b_i)$, where $\mathscr{P}$ is the poissonian likelihood for both signal and background events), or one per energy bin ($\mathscr{L}(g,b) = \prod_i^{N_{\mathrm{bins}}} \mathscr{G}(\kappa_i)\mathscr{P}(g_i)\mathscr{P}(b_i)$) The two canvases show the effect of the κ that varies independently (E dependence) or not (No E dependence) in each energy bin for an observation time of 5 h and 20 h.

For both scenario (E dependence or not), the use of an energy binned likelihood limits the sensitivity loss. The sensitivity tends to reach a plateau when the κ is constant for each energy bin, while is worsening if an energy dependence appears. This effect is larger for the 20 h case, since the systematic dominates over the statistical uncertainty for long exposure. In the optimistic case of no energy dependence, the sensitivity loss is at most a factor 2.

5.4.2 Evaluation method

I have introduced the observation methodology adopted for the GH data in Sec. 5.2.1, aiming to control and keep to a minimum the systematic uncertainties in the ON-OFF acceptance ratio. The study and the analysis developed for evaluating the σ_{syst} is performed over the data collected during winter 2018. These data, observed following the procedure described in the Sec. 5.2.1, have an average $\Delta J_{\mathrm{syst}} \approx 4\%$ of the average ΔJ used for the DM search, as shown in Fig. 5.9 and reported in Tab A.1. This means that even if the presence of DM affected our computation of systematics, it would only contribute for a 4% of the signal, i.e. it would not reduce significantly our sensitivity for detecting the DM signal.

5.4.2.1 Normalization procedure

In general, the ON and OFF are not observed for the same amount of time, thus they have a different “exposure”, e.g. in wobble mode for each ON, up to three OFF positions can

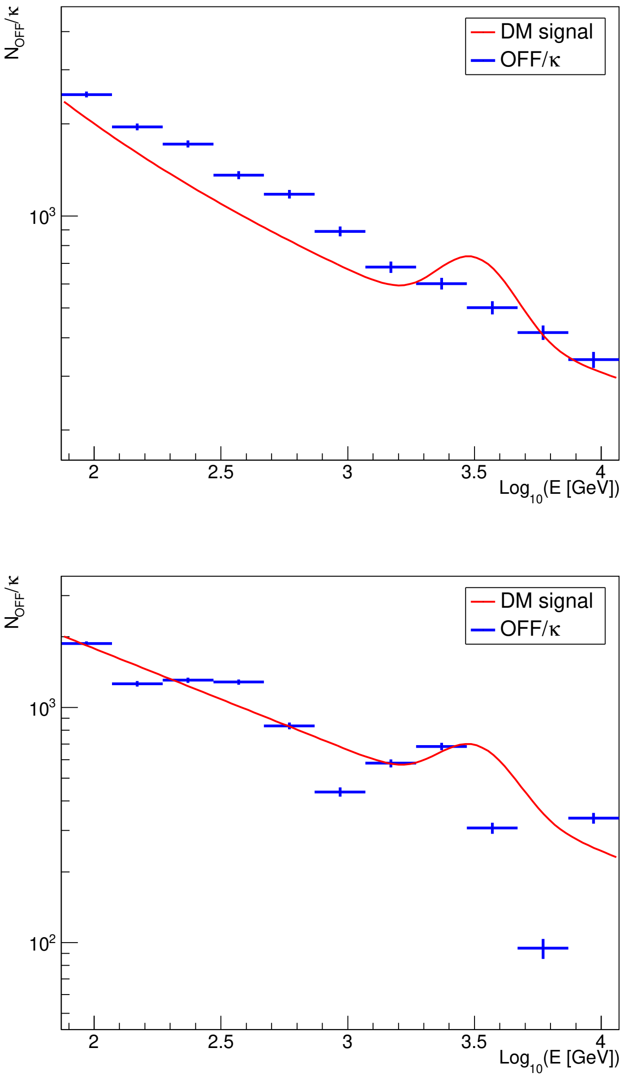

Figure 5.13 Illustration of how the energy dependence of the ON/OFF normalization (κ) can affect the sensitivity to DM signals. Top: κ has the same value for all energy bins. Bottom: the value of κ depends on the energy, in which case the normalized background can mimic the DM signal, degrading the sensitivity to those signals. The point are simulated according to different background model assumed, and the red line is a possible DM spectra. The energy bins are naturally defined by the size of the energy resolution.

be selected. The normalization between ON and OFF is needed to compute the number of γ-ray excess, as reported in Eq. 3.2. In general, the normalization is performed looking at a parameter space where is possible to define regions containing only background events, for both ON and OFF FoVs. The standard approach adopted in MAGIC makes use of the θ^2 distribution. In the case of a point-like target, in the region with $\theta^2 \in [0.1, 0.4]$ ON and OFF

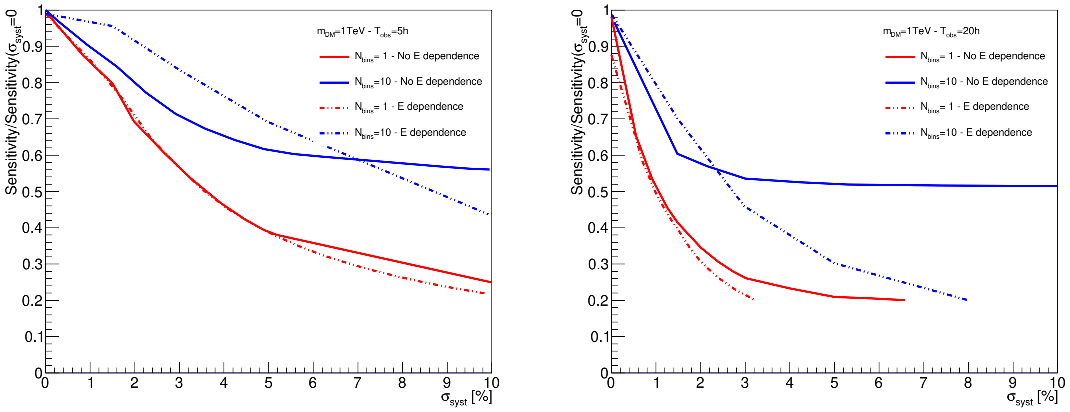

Figure 5.14 Sensitivity curves for DM search as a function of the systematic uncertainty in the ON/OFF acceptance ratio σ_{syst}, normalized with the sensitivity for $\sigma_{\text{syst}} = 0$. The curves have been computed for 5 (left) and 20 (right) hours of observation time and a DM particle mass of 1 TeV, according to the theoretical model (continuum of energy) and using a binned likelihood function in estimated energy. This solid blue line in the left canvas is representative for the GH observation reported in this thesis.

contains only background events (see Fig. 3.24), and thus, it is possible to compute κ in such θ^2 range.

This approach is no longer suitable for GH observations. The DM distribution extends over the FoV of MAGIC, and therefore, there are no regions in the camera containing only background events. As result, the θ^2 distribution is not the right instrument to normalize ON and OFF. As an alternative, the hadronness distribution can be used to perform the normalization. In fact, the hadronness distribution is built such that the events with low value of hadronness, h, identify possible γ-ray candidates, while at high h the background dominates. As for the standard approach, the background shape in the normalization region should be the same for both ON and OFF, so the hardonness curves should be as close as possible for normalization purposes. For h in [0.4, 0.75], the hadronness shape is normally flat and stable. This interval is hence the new normalization region for computing κ in GH observation, as shown in Fig. 5.17.

In the case of identical telescope performances and weather conditions, the pointing can modify the shape of the hadronness curves, as shown in Fig. 5.16. This is a further reason why the GH observations strongly require that ON and OFF follow the same trajectory. The perfect overlap is later ensured by precisely selecting Az bins where there is a simultaneous ON and OFF coverage. Moreover, each Az interval is divided into three bins to ensure an even more precise overlap and thus make the normalization procedure more robust. The

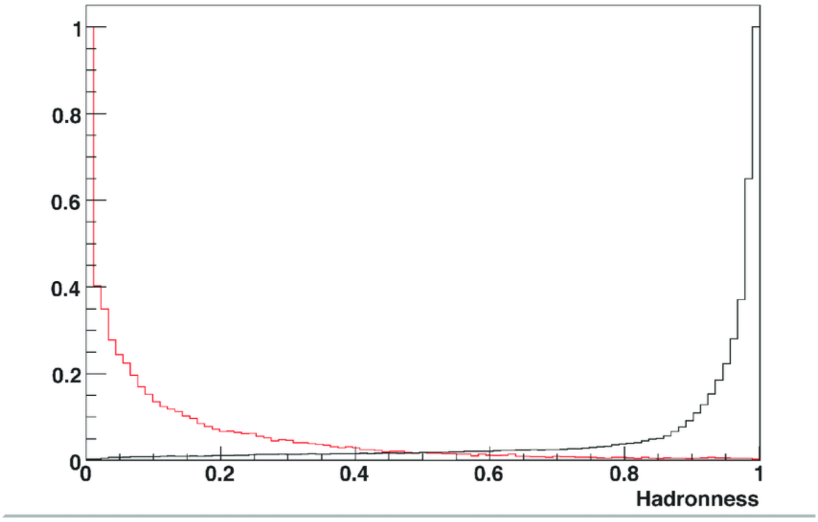

Figure 5.15 Normalized Hadronness distributions for MC generated γ events (red line) and OFF data (black line). Image taken from [33].

three Az bins are equidistant, since the Az distribution is in first approximation flat and thus each bin has approximately the same exposure (see Fig. 5.18).

Finally, with reference to the the Fig. 5.17 the normalization factor κ_i is computed for each Az bin of each observation night as:

$$\kappa_i = \frac{N^{\kappa}_{\mathrm{OFF},i}}{N^{\kappa}_{\mathrm{ON},i}}, \tag{5.5}$$

where $N^{\kappa}_{ON/OFF,i}$ is the number of events passing the quality and the analysis cuts with $h \in [0.4,\ 0.75]$ for ON and OFF observations respectively. The statistical uncertainty on κ_i, $\sigma_{\kappa_i,\mathrm{stat}}$, is computed too as:

$$\sigma_{\kappa_i,\mathrm{stat}} = \kappa_i \cdot \sqrt{\frac{N^{k}_{\mathrm{OFF},i} + N^{k}_{\mathrm{ON},i}}{N^{k}_{\mathrm{OFF},i} N^{k}_{\mathrm{ON},i}}}. \tag{5.6}$$

5.4.2.2 Systematic evaluation

The main quantity computed for evaluating the systematic is the normalized residual, defined as:

$$R_i = 2 \cdot \frac{N^{h}_{\mathrm{ON},i} - N^{h}_{\mathrm{OFF},i}/\kappa_i}{N^{h}_{\mathrm{ON},i} + N^{h}_{\mathrm{OFF},i}/\kappa_i}, \tag{5.7}$$

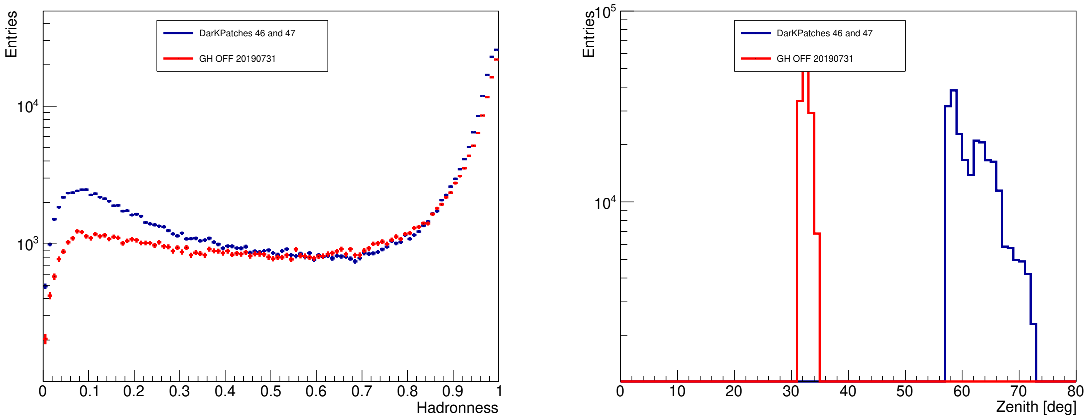

Figure 5.16 On left: comparison of hadronness curves for the OFF slot of one GH night (20190731) and observations of Dark Patches 46 and 47. On right: the Zd distributions for the same observations. Dark Patches observations and GH OFF should contain only background events by definition, since they are selected for this purpose. However, due to the different pointing, with a relevant different in Zd, the shape of the residual background in the signal region (i.e. low h) is different and totally not compatible.

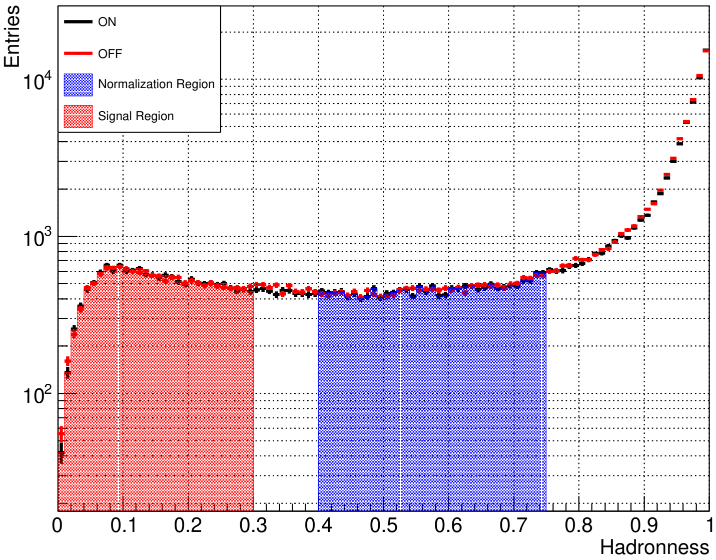

Figure 5.17 Hadronness curves for ON and OFF data: for each azimuth bin i of each observation night, the normalization factor κ_i is computed as the ratio of the hadronness curves in the blue region, while R_i (Eq. 5.7) is computed as the normalized residual from the red region of the curves. The limits of each region have been computed by the minimization of the variance of the distribution of R, as described in the text.

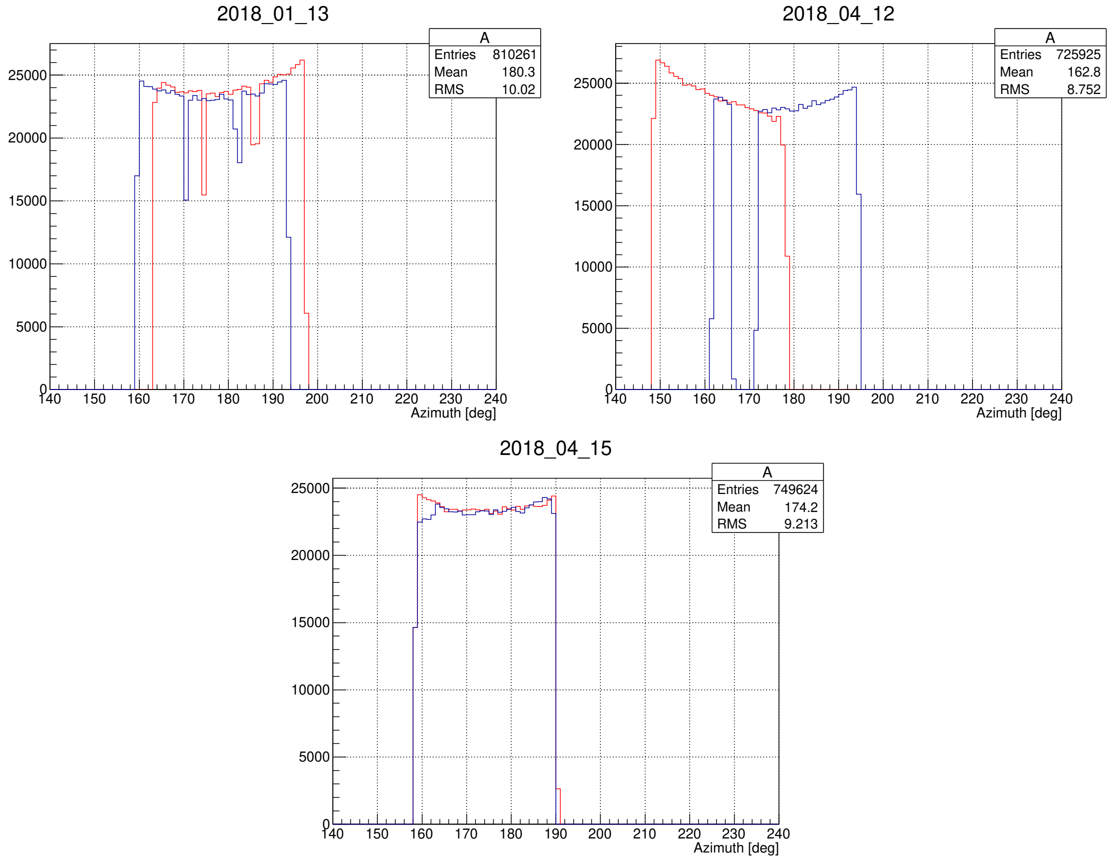

Figure 5.18 Example of Az distribution for three night observed in the GH campaign. Red line is ON, blue the OFF. In the top left the 20 min run division is visible. Top Right show an example of incomplete overlap of the trajectory, in this case due to schedule issue. Bottom figure is representative of a normal observation.

where $N^h_{ON/OFF,i}$ is the number of ON (OFF) events passing quality and the analysis cuts with $h < 0.3$ (see Fig. 5.17), and i is referred to the Az bin in each observation night. This quantity, computed with data with low ΔJ, represents the residual fluctuations of the background in the signal region. In the absence of a systematic difference of acceptance between ON and OFF regions, R_i should distribute around 0, with a dispersion corresponding to its statistical uncertainty. Any additional dispersion will be attributed to the systematic uncertainty $\sigma_{\rm syst}$, that can be assigned to κ_i using error propagation formulae. In fact, the statistical error on R_i can be written as:

$$\sigma^2_{R_i} = \left(\frac{\partial R_i}{\partial N^h_{\mathrm{ON},i}}\right)^2 \sigma^2_{N^h_{\mathrm{ON},i}} + \left(\frac{\partial R_i}{\partial N^h_{\mathrm{OFF},i}}\right)^2 \sigma^2_{N^h_{\mathrm{OFF},i}} + \left(\frac{\partial R_i}{\partial \kappa_i}\right)^2 \sigma^2_{\kappa_i} \tag{5.8}$$

where $\sigma_{N_{\mathrm{ON},i}}$ and $\sigma_{N_{\mathrm{OFF},i}}$ are the statistical poissonian fluctuation of the number of events detected in the ON and OFF, respectively. Substituting σ_{κ_i} with the Eq. 3.7, σ_{R_i} becomes:

$$\sigma_{R_i}^2 = \left(\frac{\partial R_i}{\partial N_{\mathrm{ON},i}^h}\right)^2 \sigma_{N_{\mathrm{ON},i}^h}^2 + \left(\frac{\partial R_i}{\partial N_{\mathrm{OFF},i}^h}\right)^2 \sigma_{N_{\mathrm{OFF},i}^h}^2 + \left(\frac{\partial R_i}{\partial \kappa_i}\right)^2 (\sigma_{\kappa_i,\mathrm{stat}}^2 + \kappa^2 \sigma_{\kappa_i,\mathrm{syst}}^2). \tag{5.9}$$

The first three terms of this equation describe the statistical fluctuation due to the random variable N_{ON}^h, N_{OFF}^h and κ, while the last terms refers to the systematic uncertainties in the background estimation. It is hence possible to rewrite Eq. 5.9 as:

$$\sigma_{R_i}^2 = \sigma_{\mathrm{stat},i}^2 + \sigma_{\mathrm{syst},i}^2, \tag{5.10}$$

with:

$$\begin{cases} \sigma_{\mathrm{stat},i}^2 = \left(\frac{\partial R_i}{\partial N_{\mathrm{ON},i}^h}\right)^2 \sigma_{N_{\mathrm{ON},i}^h}^2 + \left(\frac{\partial R_i}{\partial N_{\mathrm{OFF},i}^h}\right)^2 \sigma_{N_{\mathrm{OFF},i}^h}^2 + \left(\frac{\partial R_i}{\partial \kappa_i}\right)^2 \sigma_{\kappa_i,\mathrm{stat}}^2, \\ \sigma_{\mathrm{syst},i}^2 = \left(\frac{\partial R_i}{\partial \kappa_i}\right)^2 \kappa_i^2 \sigma_{\kappa_i,\mathrm{syst}}^2, \end{cases} \tag{5.11}$$

In the hypothesis that $N_{\mathrm{ON},i}^h \sim N_{\mathrm{OFF},i}^h / \kappa_i$, can be demonstrated that $\partial R / \partial \kappa_i \approx 1/\kappa_i$, and thus the term related with systematic in Eq. 5.11 is exactly the relative systematic uncertainty $\sigma_{\kappa_i,\mathrm{syst}}$.

Let's consider the distribution $\mathscr{R}$ formed with the whole R_i values, computed for each Az bins in each observation night, for a total of N_{set} entries. If each entry has approximately the same exposure, the statistical uncertainty σ_{R_i} is almost constant for each R_i. As consequence, the standard deviation of $\mathscr{R}$, σ_{R}, has to be $\approx \sigma_{R_i}$. Calling σ_{stat} the statistical uncertainty contribution in σ_{R}, it is possible to extract the systematic value by inverting the Eq. 5.10, as:

$$\sigma_{\mathrm{syst}} = \sqrt{\sigma_{\mathsf{R}}^2 - \sigma_{\mathrm{stat}}^2}. \tag{5.12}$$

This is a very simple equation, that can be solved once the value of σ_{R} and σ_{stat} are known

- The quantity σ_{R} can be estimated through the sample variance s_{R} of $\mathscr{R}$, as:

$$s_{\mathsf{R}}^2 = \frac{1}{N_{\mathrm{set}} - 1} \sum_{i=1}^{N_{\mathrm{set}}} (R_i - < R >)^2, \tag{5.13}$$

where $< R >$ is the sample mean of $\mathscr{R}$. The statistical error on s_{R}^2 is the variance of the sample variance, $\Delta[s_{\mathrm{R}}^2$, computed as,

$$Var[s_{\mathrm{R}}^2] = \frac{1}{N_{\mathrm{set}}}\left(\mu_4 - \frac{N_{\mathrm{set}}-3}{N_{\mathrm{set}}-1}s_{\mathrm{R}}^4\right), \quad \mu_4 = \frac{1}{N_{\mathrm{set}}-1}\sum_{i=1}^{N_{\mathrm{set}}}(R_i - < R >)^4, \tag{5.14}$$

- σ_{stat} can be evaluated as the sample mean $< \sigma_{\mathrm{stat},i} >$ of the distribution of $\sigma_{\mathrm{stat},i}$ (Eq. 5.11). The error on the sample mean is evaluated as

$$\Delta[< \sigma_{\mathrm{stat},i} >] = \sqrt{\frac{s_{\mathrm{stat}}^2}{N_{\mathrm{set}}}}, \tag{5.15}$$

  where $s_{\mathrm{stat},i}^2$ is the sample variance of the distribution of $\sigma_{\mathrm{stat},i}$.

Using the standard propagation of the statistical uncertainty and substituting the estimators in Eq. 5.12, the systematic uncertainty and its statistical error $\Delta[\sigma_{\mathrm{syst}}]$ are:

$$\sigma_{\mathrm{syst}} = \sqrt{s_{\mathrm{R}}^2 - < \sigma_{\mathrm{stat},i} >^2}, \tag{5.16}$$

$$\Delta[\sigma_{\mathrm{syst}}] = \sqrt{\frac{\Delta[s_{\mathrm{R}}^2] + (2\Delta[< \sigma_{\mathrm{stat},i} >] < \sigma_{\mathrm{stat},i} >)^2}{4\sigma_{\mathrm{syst}}^2}}. \tag{5.17}$$

The assumption of similar exposure between each entry is guarantee in the GH dataset, since, by construction, GH observations are performed considering the same observation time for ON and OFF slots. Furthermore, the use of a binning in Az guarantees an even more similar exposure between each bin. An adaptable Az bins size, that takes into, can account the proper observation time (or the number of events) can produce an even more narrow distribution of $\sigma_{\mathrm{stat},i}$, makes equality exposure sample more robust. Nevertheless this hypothesis is verified within a ∼7% level with the approach used, which is enough to validate the method.

5.4.3 Application to the dataset with low ΔJ

The systematic uncertainties in the ON-OFF acceptance for the GH observations can now be computed following the procedure described in Sec. 5.4.2. The observations with low ΔJ are the ones suitable for this task. Tab. 5.4 summarizes the observations used for evaluating σ_{syst}. The overlapping time is measured after the quality and Az cuts.

Then, two independent sub-samples are created out of the low ΔJ dataset, the first used for optimizing the entire set of analysis cuts (odd-numbered events or training sample) and the

Date	Overlapping Time (h)
20180113	0.84
20180121	0.70
20180215	0.77
20180217	0.84
20180218	0.89
Tot. overlap. time	**4.4**

Table 5.4 The subsample of the observations with low ΔJ used for the evaluation of the $\sigma_{\rm syst}$ for the GH observation. The overlapping time between ON and OFF is reported.

second one for evaluating $\sigma_{\rm syst}$ (even-numbered events or testing sample). The analysis cut optimization is performed by minimizing the variance of distribution of R. The final values of the analysis cuts used later in the $\sigma_{\rm syst}$ analysis and in the DM lifetime measurements are:

- $\mathrm{E}_{\rm est} > 65$ GeV,
- Size > 50,
- $h < 0.3$,
- $\theta < 1.2^\circ$.

The systematic uncertaintiy value $\sigma_{\rm syst}$ is computed from the complementary sample (test sample). For each bin, the R_i (Eq. 5.7) and $\sigma_{{\rm stat},i}$ (Eq. 5.11) are computed, and the distributions are shown in Fig. 5.19. The total variance $\sigma_{\rm R}$ and the statistical part of the variance $\sigma_{\rm stat}$ are estimated as the sample variance and the sample mean of the R_i and $\sigma_{{\rm stat},i}$ distribution respectively, which values are reported in Tab. 5.5. According to Eq. 5.16, the value of $\sigma_{\rm syst}$ for GH observations, computed with the low ΔJ dataset is $\sigma_{\rm syst} = 3.71 \pm 1.42$ %.

$\sigma_{\rm R}$ (%)	$\sigma_{\rm stat}$ (%)	$\sigma_{\rm syst}$ (%)
5.80±0.91	4.45±0.06	3.71±1.42

Table 5.5 The values for $\sigma_{\rm tot}$, $\sigma_{\rm stat}$ and $\sigma_{\rm syst}$ are reported for the study of the systematic uncertainties with the data described in Tab 5.4.

This value is larger than the 1.5% computed for a standard MAGIC operation [113]. Eventually, two different ways of measuring systematic uncertainties in OFF/ON acceptance are considered: for standard operations, the value of $\sigma_{\rm syst}$ is computed using a long observation of the *same* FoV ($\sim$ 50 h in wobble mode), in such a way that the statistic fluctuations tend to cancel out, averaging around zero, and the only remaining contribution is indeed

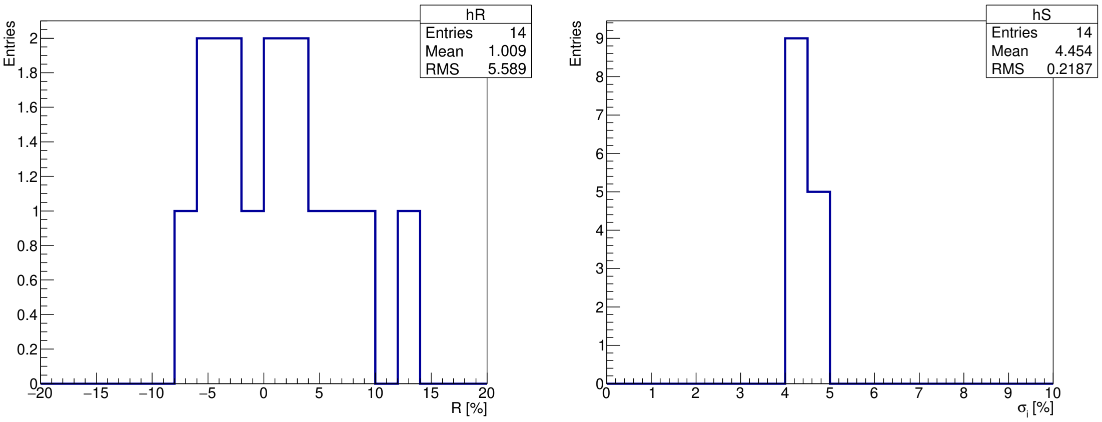

Figure 5.19 The distributions of R_i (left) and its statistical error $\sigma_{\text{stat},i}$ (right) are reported.

the systematic uncertainty (see [20]). Thus, the value found cannot be properly compared with the 1.5% of the standard analysis, because they refers to different quantity: while for standard operation the interest is in measuring the different among the same FoV, for GH observation the systematics are referred to the comparison of ON/OFF couples, each one related to different FoVs.

5.4.3.1 Energy dependence

The large impact σ_{syst} has on the measurement concerns whether κ can vary independently or not in the energy bins. Fig. 5.14 shows that in the case where κ assumes uncorrelated values for each energy bin, the worsening of the sensitivity is larger and does not reach a stable plateau. This mainly happens because the systematic (in this case) can mimic a DM signal modifying the spectral shape of the background, thus the sensitivity would worsen with the increasing of the the systematic magnitude. This is not happening in the case κ results equal in each energy bin, since the systematic cannot modify the spectral shape of the background.

The behaviour of κ can be studied looking how the R_i varies in the energy bin, since $\sigma_R \approx \sigma_\kappa/\kappa$ for $N^h_{\text{ON}} \sim N^h_{\text{OFF}}/\kappa$. For 11 energy bins equally spaced in $\log_{10}(E[\text{GeV}])$, from 65 GeV to ~10 TeV (same binning adopted also in the likelihood analysis), the number of events in the signal region, overlapping in Az and passing the analysis cut (see Fig. 5.17), is computed for ON and OFF, respectively, and normalized with the κ computed for in the whole energy range. Later, R_j is computed for each j^{th}-bin in energy as Eq. 5.7 shows.

Fig. 5.20 shows that, within statistical errors, the values of R_j are compatible with being independent of the energy, for all examined datasets. This hypothesis is confirmed by the χ^2

test, which results are reported in the bottom right table of Fig. 5.20. This is a very relevant result for the DM lifetime measurement, since the the worsening of the sensitivity almost independent by the value of σ_{syst}, since it reaches a plateau, mitigating the effects of possible over/under-estimation of the σ_{syst} (shown by the solid blue lines in Fig. 5.14.

5.4.4 Systematic uncertainties over consecutive days

The GH data-collecting method ensures that the ON-OFF trajectories overlap as much as possible. This result is achieved through a precise schedule of the ON-OFF slots and the effort of the crew responsible for data collection at La Palma. The high weather variability, especially during the winter time, and unforeseen technical problems can force La Palma crew to interrupt observations to prevent telescopes from being damaged. Usually, these events are related to strong gusts of wind, high humidity, subsystem crashes during telescope operation, or even last-minute ToO access. In such cases, the affected observation slot is delayed or, in the worst case, cancelled. Thus, when those unexpected events happened during a GH time slot, the trajectory overlap is compromised and the slots cannot be combined for our purpose.

In order to not completely lose the slots acquired, an observation with a compatible trajectory with the proper ΔJ value, can be scheduled in the following days, making the method more flexible when faced with unexpected events.

The sub-sample of consecutive-night observations with compatible trajectories is used for studying how the σ_{syst} behaved under this hypothesis, and whether it was compatible with the value found for same-night observations. Tab. 5.6 reports the consecutive-days data set with the ΔJ of each pair of observations as well as the overlapping time of the trajectories. The slots are paired as ON-ON and OFF-OFF slots, so that the J is comparable within the two FoVs with a final ΔJ comparable w.r.t the observations with low ΔJ, or even lower. Some entries are missing since one of the two slots was not observed, as reported in Tab. 5.3. Finally, the overlapping time is computed after the quality and Az cuts.

Then, the equations described in Sec. 5.4.2 are applied to the data sample considered. In the first two entries the time overlap is very low, since the trajectories overlapping is half of the total Az interval. In this case, single Az bin is considered to ensure comparable statistic with the rest of the sample. For the other entries, three Az bins are adopted. In Tab 5.7 the values for σ_{R}, σ_{stat} and σ_{syst} are reported, computed from the distribution of R_i and $\sigma_{\text{stat},i}$ of Fig. 5.21. The σ_{syst} has a value compatible with the results found in Tab. 5.5. The dependence of σ_{syst} from energy has also been checked, and no evidence from dependence is found in this case either. For completeness, in Tab. 5.8 the χ^2 values for the constant fit to residuals of the energy distribution (as shown in Fig. 5.20) are reported. As conclusion, ON-OFF couples belonging to consecutive-days and following the remaining constraints on

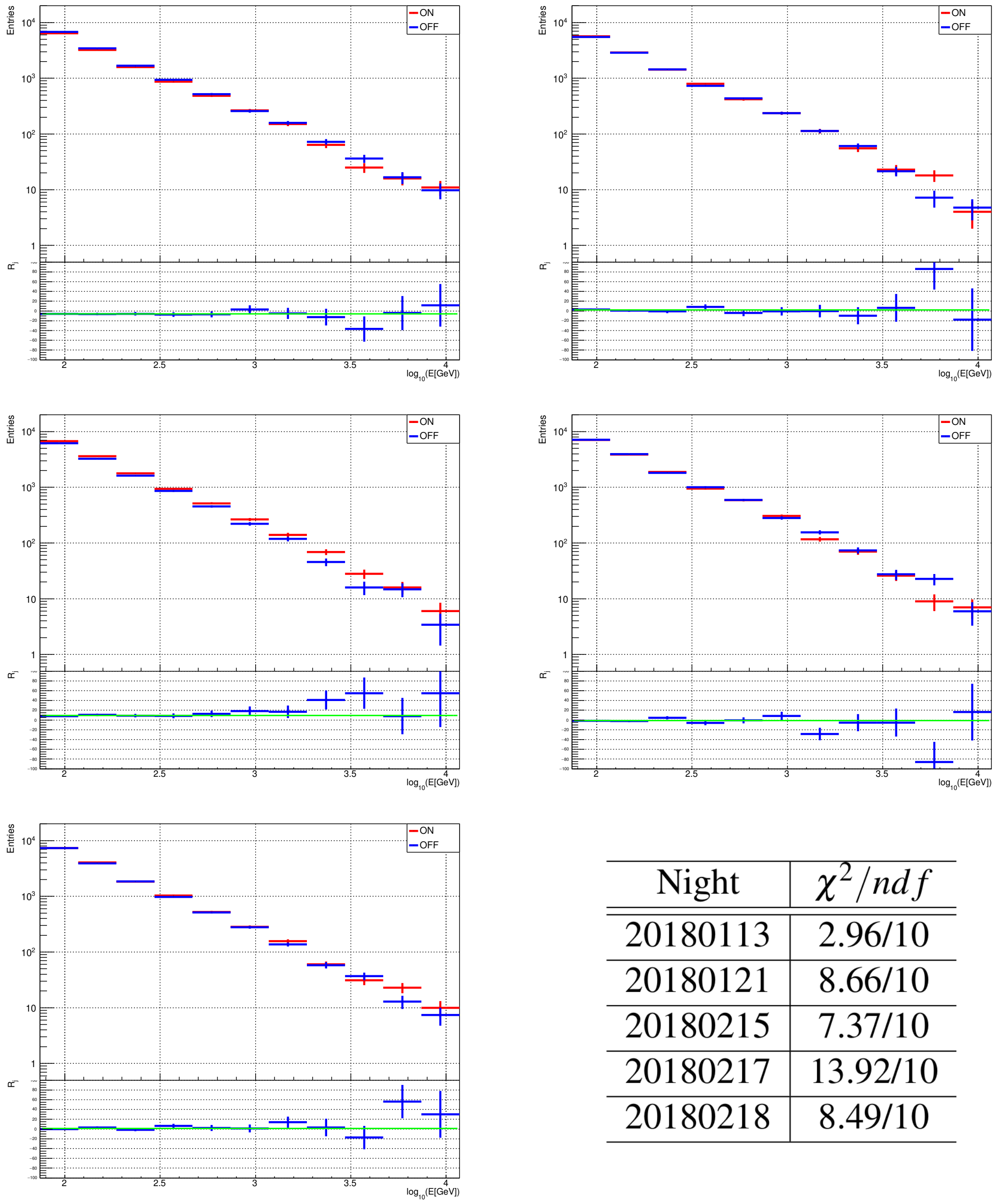

Night	χ^2/ndf
20180113	2.96/10
20180121	8.66/10
20180215	7.37/10
20180217	13.92/10
20180218	8.49/10

Figure 5.20 The number of events passing the analysis cut in the signal region ($h < 0.3$) as a function of the estimated Energy E_{est} for the nights used for evaluating σ_{syst} are reported together with the values of R_j. The energy binning used is identical to the one adopted in the likelihood analysis to evaluate the DM lifetime, in order to reproduce bin by bin possible energy dependences of the κ. The plots show no energy dependence and a clearly flat trend, compatible with the hypothesis of constant κ, tested with a χ^2 test which results are reported in the bottom right Table.

trajectory and weather, result compatible in terms of systematic and thus suitable for the DM lifetime measurement.

Date	$\Delta J^{(\text{ON-ON})}$ [GeV/cm^2]	Overlapping Time (h)	$\Delta J^{(\text{OFF-OFF})}$ [GeV/cm^2]	Overlapping Time (h)
		Winter 2018		
20180215 20180216	–	–	$2.11 \cdot 10^{16}$	0.40
20180216 20180217	–	–	$2.08 \cdot 10^{16}$	0.48
20180217 20180218	$1.56 \cdot 10^{17}$	0.89	$0.55 \cdot 10^{17}$	0.86
		Spring 2019		
20190528 20190529	$3.98 \cdot 10^{18}$	0.84	$0.595 \cdot 10^{18}$	0.94
20190529 20190530	$1.25 \cdot 10^{18}$	0.84	$0.613 \cdot 10^{18}$	0.96
20190531 20190601	0	1.00	$0.67 \cdot 10^{18}$	1.12
20190602 20190603	–	–	$2.669 \cdot 10^{18}$	1.03

Table 5.6 Summary of the observation nights used for evaluating the stability of σ_{syst} throughout the year. Slots of the same type are analysed in the consecutive nights context, to check the feasibility of coupling consecutive-days observations. Some entries are missing since from certain nights only one slot is present, as explained in Tab.5.3.

Period	σ_{R} (%)	σ_{stat} (%)	σ_{syst} (%)
2018+2019	4.10 ± 0.51	3.48 ± 0.05	2.16 ± 0.96

Table 5.7 The values of σ_{R}, σ_{stat} and σ_{syst} for the entire sample presented in Tab. 5.6.

5.4.4.1 Stability of the systematic in different period of the year

The data sample for the analysis of σ_{syst} during consecutive days can be used to verify whether the systematic uncertainties are stable over time, since no other low ΔJ data with compatible trajectory can be extracted from the entire dataset. It is possible to define two data sub-samples, belonging to a winter period (February 2018) and a spring period (May

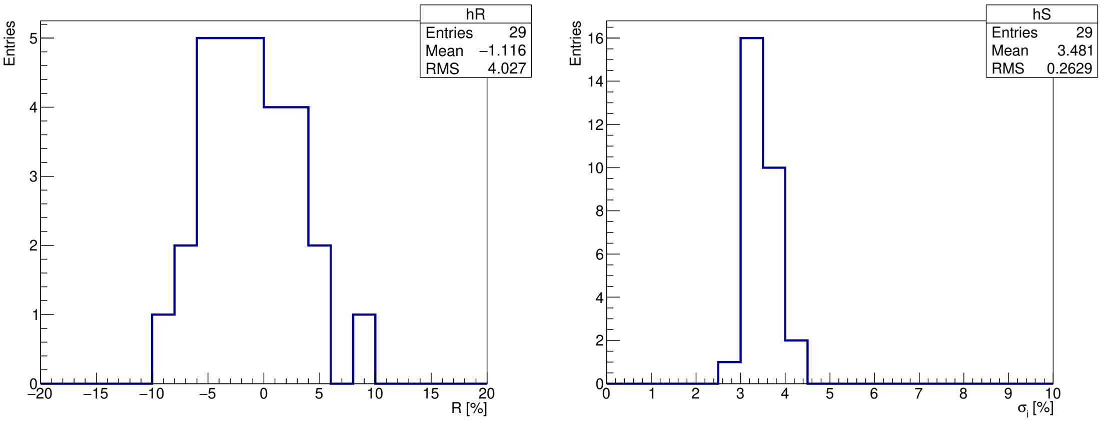

Figure 5.21 The distribution of R (left) and $\sigma_{\text{stat},i}$ (right) for the entire sample presented in Tab. 5.6.

Date	χ^2**/ndf**	
	ON-ON	**OFF-OFF**
20180215-20180216	–	10.87/10
20180216-20180217	–	22.40/10
20180217-20180218	24.67/10	14.86/10
20190528-20190519	4.96/10	4.50/10
20190529-20190530	5.04/10	5.77/10
20190531-20190601	16.12/10	10.81/10
20190602-20190603	–	8.27/10

Table 5.8 The χ^2/ndf values from the constant fit of the residuals of the energy distribution, as done in 5.20. The larger χ^2 values are created by the fluctuations in the high energy bins, where there is a lack of statistics.

2019), as reported in Tab. 5.6. This represents a test also for the stability of the telescope's performances, thus is expected that the value does not change significantly.

The R_i and $\sigma_{\text{stat},i}$ distributions are carried out on data for the two selected periods and reported in Fig. 5.22. Then, after the evaluations of σ_{R} and σ_{stat}, the σ_{syst} for the two periods is found to be in perfect agreement (see Tab 5.7 and Tab. 5.5). This indicates that the method is robust enough to ensure a stable level of systematics for different observation periods.

5.4.4.2 Standard archival data

The observation method described shows a level of systematic uncertainties within the 4% for the background acceptance, with no evidence for independent variation of that value with the energy bin. That is important because the treatment of a constant systematic value is easier in

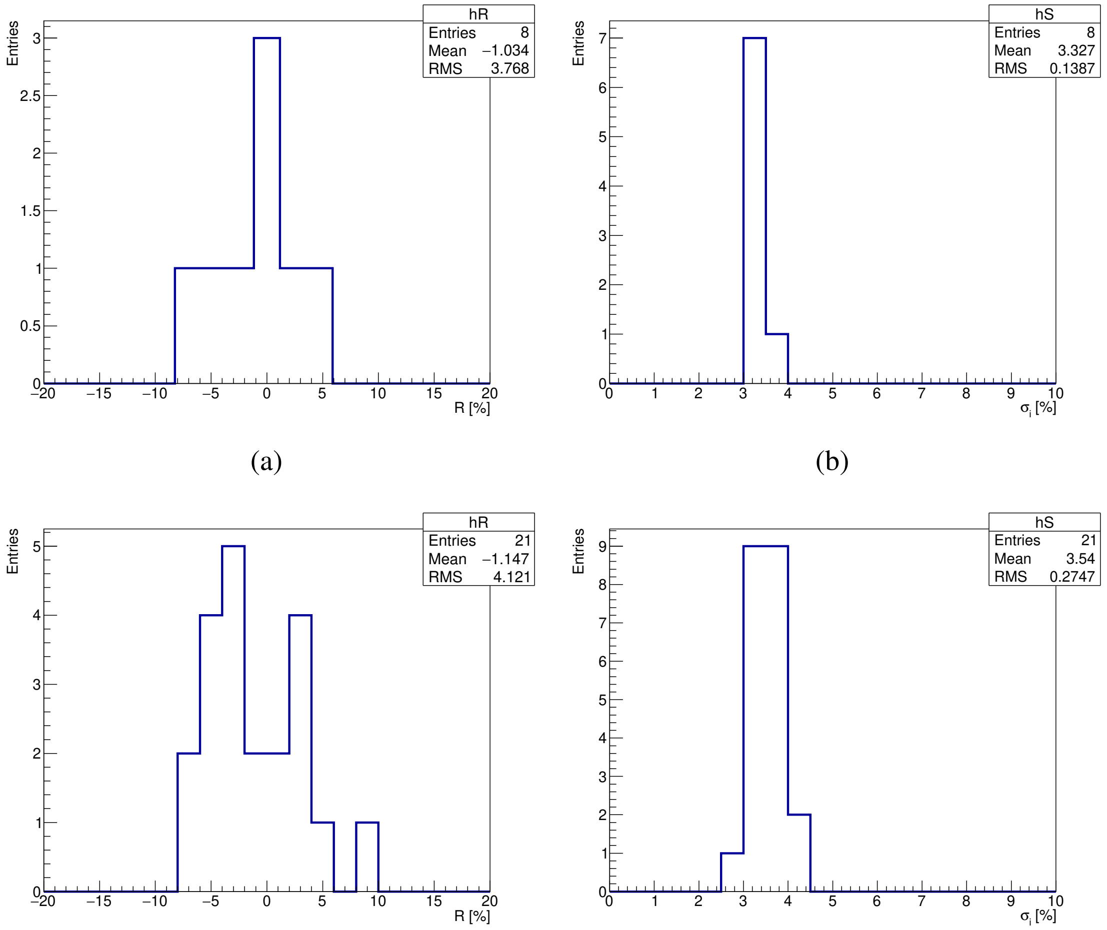

(a) (b)

(c) (d)

Figure 5.22 The distribution of R_i and $\sigma_{\mathrm{stat},i}$ for the periods *winter2018* (Figs. a and b respectively) and *spring2019* (Figs. c and d respectively).

Period	σ_{R} (%)	σ_{stat} (%)	σ_{syst} (%)
Winter2018	4.03 ± 0.92	3.33 ± 0.05	2.27 ± 1.63
Spring2019	4.22 ± 0.61	3.54 ± 0.06	2.30 ± 1.12

Table 5.9 The values of σ_{R}, σ_{stat} and σ_{syst} for the two sub-periods Winter 2018 and Spring 2019 presented in Tab. 5.6.

the likelihood analysis, and the results appear robust against possible σ_{syst} underestimation, since the the worsening of the sensitivity is almost constant for larger values of σ_{syst} (see Fig. 5.14).

The weakness of the method concern the observation time. GH data collection requires twice the number of hours w.r.t a wobble mode observation, where the ON-OFF are acquired

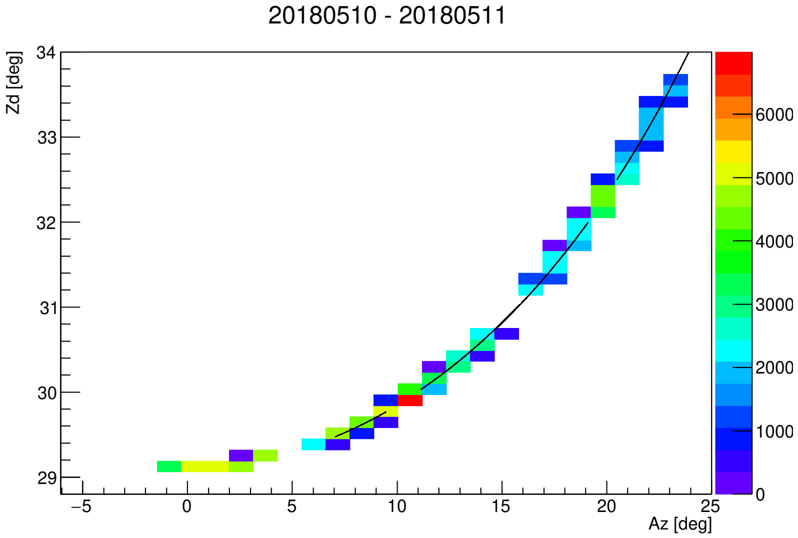

Figure 5.23 Superimposition of the trajectories for a couple of Draco observations used for evaluate $\sigma_{\rm syst}$. On Z-axis the entries for each Zd-Az bin is reported. The visible holes are the moment in which the wobble changing happen.

simultaneously. Furthermore, the scheduling of the targets is not a trivial task and requires a good synergy among the entire team responsible for the observations. The possibility of performing observations on consecutive nights makes managing the observations easier, which results in a easier scheduling and, possibly, a larger duty-cycle.

For this reason, the use of archival data to enlarge the dataset of GH observations appears very appealing, since observation time is added without wasting any minutes of the MAGIC observation time. I am presenting here the first example of a systematic study as presented in Sec. 5.4.2 applied to archival data, using FoV not selected ad *ad hoc* for this task. In this case, for simplicity, the ON and OFF slots are selected from observations of the same source during consecutive nights. All the required constraints (presented in Sec. 5.2.1) are applied to this case, too. Since most of the MAGIC observations are in wobble mode, the trajectories will not be perfectly superimposed due to the wobbling (see Fig. 5.23), however, this effect is not expected to largely affect the value of $\sigma_{\rm syst}$. In case the FoV considered does not contain any γ-ray sources or bright stars, the method is perfectly suitable for measuring the systematics, since by construction the $\Delta J \approx 0$ disentangles the measurement completely from possible residual DM signals.

For simplicity, the method has been applied to the Draco dSph FoV, since the data complies with the constraints required: Zd < 35°, Tr9km > 0.9, $b > 10^{\circ}$ and was observed during consecutive days. Moreover, this FoV is empty of any luminous spot and of VHE energy, as the results of the Chapter 4 show. This source is observed with an Az between [-

Date	**Az [deg]**	**Overlapping time (h)**
20180510-20180511	7.07−23.28	1.25
20180512-20180513	-4.33−12.55	0.77
20180516-20180517	1.51−25.36	1.62
20180618-20180619	-18.21−3.40	1.94
20180713-20180714	-23.59−11.52	0.66

Table 5.10 Draco dataset used for the evaluation of $\sigma_{\rm syst}$. The Az interval and the overlapping time in such intervals are reported too. The Az bin has been selected in order to equalize the number of entries.

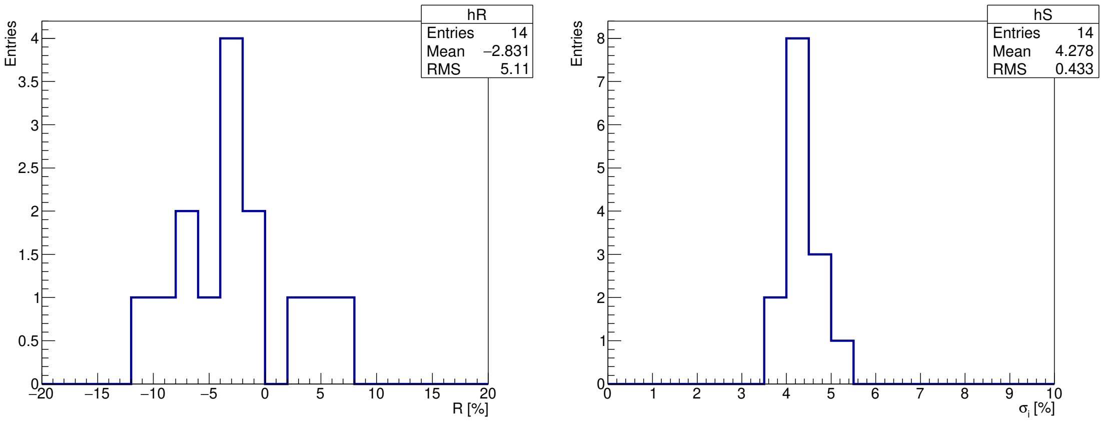

Figure 5.24 The distribution of R_i and σ_i for the FoV of Draco are shown.

40°, 30°], which can reveal if the systematic level share any dependence with the Az pointing. In Tab. 5.10 the dataset used for this measurement is reported. The strategy of performing an Az binning is adopted, too, with different bin sizes, since Az distribution is usually shorter when pointing closer to the Polaris. Thus, applying the formulas described in Sec. 5.4, from the distributions of R_i and $\sigma_{{\rm stat},i}$ (Fig. 5.24), can be obtained $\sigma_{\rm syst} = 3.13 \pm 1.37\%$ from Eq. 5.16.

Also, for this case, no evidence of energy dependence of $\sigma_{\rm syst}$ has been found, as Tab. 5.11.

Perfect agreement and compatibility with the previous estimation of the systematics is found. This test, hence, confirms that selecting data from consecutive days, both from an archive or a new operation, is completely safe and, moreover, can improve significantly the GH observation time.

$\sigma_{\rm R}$ (%)	$\sigma_{\rm stat}$ (%)	$\sigma_{\rm syst}$ (%)
5.30 ± 0.80	4.28 ± 0.12	3.13 ± 1.37

Date	χ^2/ndf
20180510-20180511	14.01/10
20180512-20180513	16.78/10
20180516-20180517	7.04/10
20190618-20190619	11.40/10
20190713-20190714	19.14/10

Table 5.11 The χ^2/ndf values from the constant fit of the residuals of the energy distribution for consecutive observation days of Draco FoV, as done in 5.20. The larger $\chi 2$ values are created by the fluctuations in the high energy bins, where there is a lack of statistics.

5.4.4.3 More than consecutive

While the sample of GH observation can be enlarged relatively easily, with archival data or new observations, the maximum ΔJ available within the observation scheme proposed, is strictly limited by the required made.

Larger ΔJ could be explored by relaxing the requirements referring to the trajectory followed by ON and OFF. Thus:

- the Zd can be limited to larger values, e.g. Zd$< 50°$, which makes region closer to the GC accessible, then larger J for the ON slots. This choice makes the sensitivity to γ rays from DM process lower, thus not much appealing;
- the distance in terms of days between the observation can be enlarge for more than consecutive days, keeping the trajectories limited to region with Zd$< 35°$;
- allowing slightly different trajectories. As seen, the hadronness shape depends on the pointing, thus this can potentially lead to an OFF that do not provide a compatible background estimation and, therefore, makes the data unusable. Moreover the difference in terms of trajectory would need to be precisely quantify, which requires more observation times for completing this task.

The second option could provide successfully results, while the other two approaches failed in some parts. Moreover, as the consecutive days approach works, the natural consequence is to see which is the limit on time distance allowing a systematic level under control and a normalization constant in energy. Then, a subsample of days with compatible trajectories and a time distance ≥ 2 days with low ΔJ is selected out of the total data set and reported in Tab. 5.12.

The search is limited to the available data, limiting the search for observations occurred at most in one month. The majority of observations couples have a time distance from 2 day to

Date	$\Delta J^{(\text{ON-ON})}$ [GeV/cm^2]	Overlapping Time (h)	$\Delta J^{(\text{OFF-OFF})}$ [GeV/cm^2]	Overlapping Time (h)
20180215 20180218	$9.5 \cdot 10^{16}$	0.95	$9.7 \cdot 10^{16}$	0.54
20180416 20180511	–	–	$2.08 \cdot 10^{16}$	0.86
20180511 20180514	$6.115 \cdot 10^{18}$	0.74	–	–
20190506 20190508	$5.21 \cdot 10^{17}$	0.0.97	$7.49 \cdot 10^{18}$	0.96
20190529 20190603	$3.67 \cdot 10^{18}$	0.99	$3.54 \cdot 10^{18}$	0.96
20190530 20190603	$3.1 \cdot 10^{17}$	0.96	$2.94 \cdot 10^{18}$	0.98

Table 5.12 Summary of the observation nights used for evaluating the σ_{syst} in the long distance observations. From each coupled nights, OFF-OFF and ON-ON combinations are considered, in order to keep the ΔJ to low values. Some entries are missing since from certain nights only one slot is present, as explained in Tab.5.3.

1 week. Applying the algorithm described in this section, computing the distribution related to R_i (see Fig. 5.25), a $\sigma_{\text{syst}} = 4.32 \pm 1.79\%$ is found (see Tab. 5.13). Such value is larger compared to the previous analysis, which is expected since the time distance is larger and thus the homogeneity in the observation conditions are not ensured to be as homogeneous as possible. However, the value found is still compatible with the results found in the other approaches.

σ_{R} (%)	σ_{stat} (%)	σ_{syst} (%)
5.69 ± 0.65	3.70 ± 0.06	4.32 ± 1.79

Table 5.13 The values of σ_{R}, σ_{stat} and σ_{syst} for observations of in Tab. 5.6 are reported.

Finally, as in the others analysis, the variation of the ON/OFF normalization factor in each energy bins is computed. Most of the observations does not show any deviation from the hypothesis of a global κ for the entire bins within the statistical uncertainty (see Tab. 5.14), except for one observation (OFF slots of 20190506-08). The larger χ^2 value appears as an outlier for the $\chi 2$ distribution over the entire outcomes. However, no changes in transmission neither other problems related to the instrumentation seems justify a larger $\chi 2$ value. A possible explanation can be related to the presence of a star with B magnitude of 2.9 close to

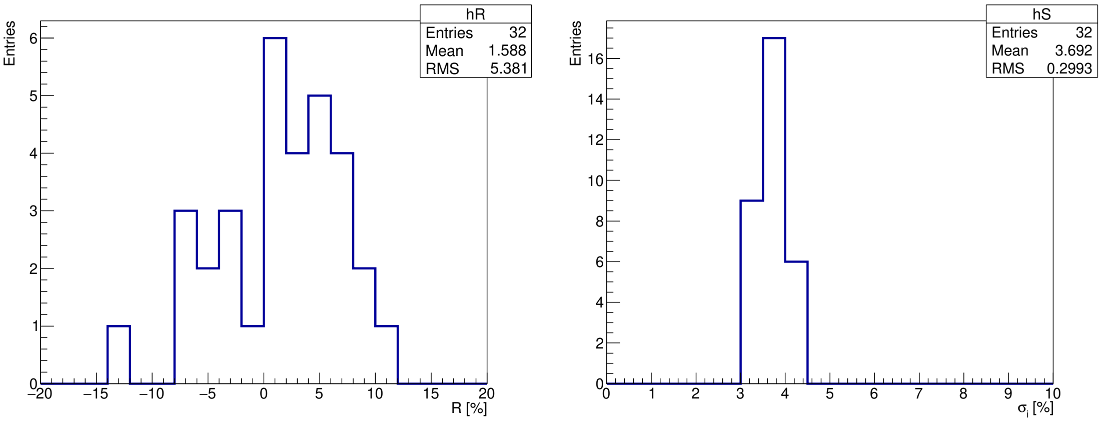

Figure 5.25 The distribution of R_i and $\sigma_{\mathrm{stat},i}$ for the observations reported in Tab 5.12 are shown.

Date	χ^2/ndf **ON-ON**	 **OFF-OFF**
20180215-20180218	16.90/10	6.23/10
20180416-20180511	–	13.55/10
20180511-20180514	11.13/10	–
20190506-20190508	11.43/10	68.78/10
20190529-20190503	10.55/10	8.79/10
20190530-20190603	16.18/10	12.78/10
20190531-20190603	–	14.89/10

Table 5.14 The χ^2/ndf values from the constant fit of the residuals of the energy distribution, as done in 5.20. The larger χ^2 values are created by the fluctuations in the high energy bins, where there is a lack of statistics.

the border of the trigger region (1.7° distant from the center of the FoV), but its contribution as a possible cause have to be deeper investigated.

5.4.5 Conclusions and remarks

Fig. 5.26 summarises the results obtained with the systematic uncertainties study, showing that the dispersion of the different values of σ_{syst} computed in the different conditions. The constraints required for the observations allow us to maintain control over the systematic effects, resulting in systematic uncertainties values consistent and homogeneous within the statistical error. In all the scenario analysed, no significant variation of the ON/OFF normalization factor κ with the energy within the statistical uncertainty is reported, which makes the worsening of the sensitivity constant for larger values of σ_{syst}. Only one case over

Data sample	σ_{stat} **Standard Deviation (%)**
GH low ΔJ - Tab. 5.4	5.05
2018+2019 - Tab. 5.6	7.74
Winter 2018 - Tab. 5.6	4.25
Spring 2019 - Tab. 5.6	7.77
Draco - Tab. 5.10	10.5
Large slot distance - Tab. 5.12	9.17

Table 5.15 The table reports the relative standard deviation of the distribution of σ_{stat}, which indicates till which precision the exposure in each ON-OFF couples differs within each data sample. As reported, the fluctuation is lower than 10%.

the 32 nights analysed show a possible variation of κ in the energy bins. This happened for the long time distant case, and needs to be further investigated. The possibility of using data from consecutive days, or even more distant in time, is very appealing both for new observation projects and for the use of archival data, which could significantly enlarge the dataset. As next step, a study on how the systematics change by comparing dataset with different Az, but comparable Zd, has to be carried out, since this would led to a easier selection of the FoVs (both for new observations or archival search) with considerable larger ΔJ.

All the analysis done are valid in the hypothesis that the exposure between each entry is as similar as possible, so that R_i distribute with a variance similar to its standard deviation (as in Sec. 5.4.2). In Tab. 5.15, is reported the relative value of the standard deviation of the $\sigma_{\mathrm{stat},i}$ distribution, for the different sub-sample analysed. The relative uncertainty is $< 7\%$ for GH data with a time distance of 1 day, at most. Draco dataset has the largest deviation, still below the 10%. This is expected since the Az distribution overlaps between the two azimuth and its not as flat as the one expected for GH. A finer selection of the Az binning, allowing different size of the bins in each observation night, would reduce the deviations measured, making the systematic measurements more robust.

Moreover, the ON-OFF method presented in this thesis produces couples of observations of different FoVs uncorrelated with the rest of the sample. This makes the method suitable for measuring possible anisotropies in the flux of the detected events, correlated with the residual galactic background, being either γ rays, e^+e^- pairs or CRs. This solution can results successful compared to other approaches [140], because possible pointing dependences are naturally cancelled out.

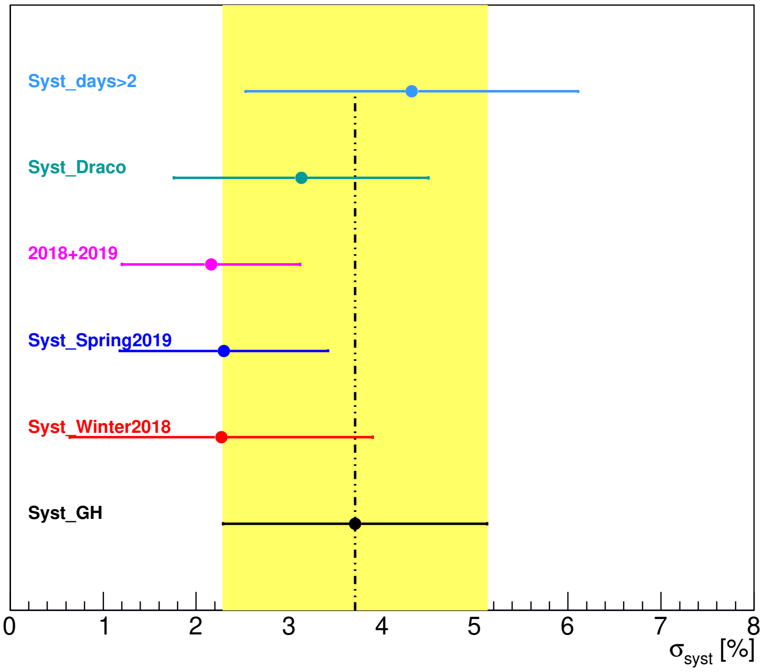

Figure 5.26 The values of σ_{syst} computed with the low ΔJ data (black point and dashed black line), the consecutive day sample from winter 2018 (blue) and spring 2019 (pink), the combination of the consecutive day samples (red), the draco sample (green) and with the long-time distance sample (Tab. 5.12, azure) are reported. The yellow band represents the statistical error on the low ΔJ σ_{syst} analysis.

5.5 Analysis

A total amount of 39.8 hours of good quality data, with the highest ΔJ, the ON-OFF following the same trajectory and observed during the same night, is analysed to search for DM decay signals. The same cuts and the same OFF normalization adopted for the evaluation of the systematic described in Sec. 5.4 is applied, with a $\theta_c = 1.2^\circ$, $h_c < 0.3$ and three equidistant Az bins. Each terms of the sample represents an entry of the likelihood analysis, and are described by different IRF, computed according to the proper MC period reported in Tab. 5.1. The DM analysis has been performed using the *full likelihood* approach described in the Sec. 3.3.5.2. The normalization factor κ is treated as a global nuisance parameter for each likelihood term, constant in each energy bin, as proved in Sec. 5.4.3.1. No uncertainty on ΔJ are considered in this thesis, and it is left for subsequent work, as it is out of the scope of this thesis. An energy binned likelihood formula is adopted for the analysis of the data samples, with the benefit shown in Fig. 5.14, and can be written as:

$$\mathscr{L}(1/\tau_{DM};\nu|\mathscr{D}) = \prod_{i=0}^{N_{\text{samples}}} \Bigg[\mathscr{G}(\kappa_i|\kappa_{\text{obs}},\sigma_{\kappa,i}) \times \prod_{j=0}^{N_{\text{bins}}} \left(\frac{(g_{ij}(1/\tau_{DM})+b_{ij})^{N_{\text{ON},ij}}}{N_{\text{ON},ij}!} \cdot e^{-(g_{ij}+b_{ij})} \times \frac{(\kappa_i b_{ij})^{N_{\text{OFF},ij}}}{N_{\text{OFF},ij}!} \cdot e^{-\kappa_i b_{ij}} \right)\Bigg], \quad (5.18)$$

where ν and $\mathscr{D}$ represent the nuisance parameters and the dataset respectively; i runs over the number of samples, $N_{samples}$, defined as the product between the number of Az bins per nights and the number of observation nights used for this analysis. The index j runs over the total number of bins in estimated energy, N_{bins}; g_{ij}, b_{ij} are respectively the estimated number of signal and background events; g_{ij} depends on τ_{DM}, J and IRFs through the Eq. 3.8, which is reported here for sake of completeness:

$$g_{ij}(1/\tau_{\text{DM}}, J) = T_{\text{obs},i} \int_{E'_{\text{min},j}}^{E'_{\text{max},j}} dE' \int dE \frac{d\phi}{dE}(1/\tau_{\text{DM}}, J) A_i(E) G_i(E, E'), \quad (5.19)$$

where E and E' are the true and estimated energies, $A(E)$ is the effective area and $G(E, E')$ is the migration matrix. $N_{\text{ON},ij}$ and $N_{\text{OFF},ij}$ are the number of observed events in the ON region and in the corresponding OFF region, respectively; $\mathscr{G}$ is the likelihood for κ_i, parametrized by a Gaussian function with mean $\kappa_{obs,i}$ and variance $\sigma_{\kappa,i}$. The σ_{syst} is taken into account in our likelihood as an additional term to the uncertainty on κ, following the formula 3.7 $\sigma_\kappa = \sqrt{\sigma^2_{\kappa,stat} + (\kappa^2 \cdot \sigma^2_{\text{syst}})}$, where $\sigma_{\kappa,stat}$ is the statistical error on κ.

5.5.1 Decay results

Independent likelihood terms are defined for each Az bin of each observation night considered, merged together as Eq. 5.18 shows through the parameter $1/\tau_{DM}$. The null hypothesis refers to the case $1/\tau_{DM} = 0$, while the test hypotheses are built considering the DM flux computed according to the Eq. 2.1, under the hypothesis of different DM particles with masses spanning from 200 GeV and 200 TeV for pure decays in $b\bar{b}$, $\tau^+\tau^-$, $\mu^+\mu^-$, W^+W^-. During the maximization of the likelihood function the value of DM lifetime is constrained within the physical range defined by $1/\tau_{DM} \geq 0$.

In Fig. 5.27 the 95% C.L. lower limit on the decay lifetime for DM particles (τ_{DM}^{LL}) is reported, obtained with the binned likelihood analysis, using 11 energy bins (N_{bins}) equidistant in $\log E'$ (E'[GeV] $\in$ [0.65, 20]). The two-sided 68% and 95% containment bands for the distribution of the lower limits are obtained from the analysis of 300 realizations of the null hypothesis ($1/\tau_{DM} = 0$), consisting of toy MC simulations generated from pure background PDF, assuming similar exposures as for the real data, and assumed κ_i as a nuisance parameter in the likelihood function.

Our results are within the 95% CL containment band expected for null hypothesis, for the full range of DM masses explored, thus no evidence in the GH of DM decaying into $b\bar{b}$, $\tau^+\tau^-$, $\mu^+\mu^-$, W^+W^- channels has been found. Constraints on τ_{DM} larger than 10^{26} s are achieved in all the channels, except for $\mu^+\mu^-$, where the DM lifetime is constrained up to 3×10^{25} s.

5.5.1.1 Discussion

The results presented in Fig. 5.27 are obtained considering a DM density profile following the Einasto model. As shown in Fig. A.1, an average different of 10% in J computation is present when a NFW or isothermal profile is considered. As consequence, the constraints on τ_{DM} change depending on the DM profile considered, as reported in Fig. 5.28. However, the small variation in J limits the spread of the 95% CL lower limits on τ_{DM} to a 10% in all the channels considered, at most. This confirms that the GH observation method presented in this thesis is robust and weakly dependent on the DM profile model considered.

In Fig. 5.29 is reported the comparison of our results with the previous MAGIC analysis on 202 h of Perseus galaxy cluster [28]. The limits from other experiments, VERITAS, FERMI and HAWC are reported too. Compared to Fermi, MAGIC limits do not depend on any model of the Galactic γ-ray emission. Compared to Perseus, VERITAS and HAWC results, this is obtained from a DM source subject to completely different uncertainties, and in particular, this measurement, has a negligible dependence on the chosen DM distribution

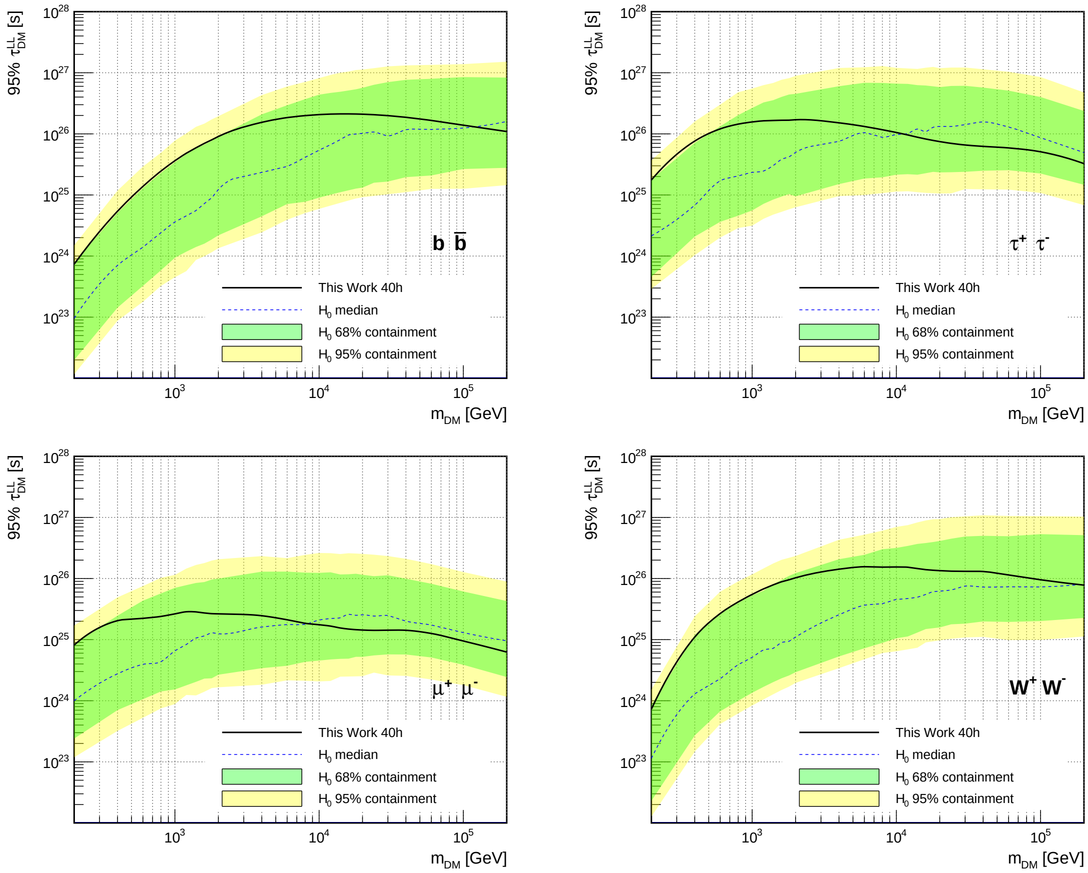

Figure 5.27 95% CL lower limit to the life-time of DM particles decaying into $b\bar{b}$ (top left), $\tau^+\tau^-$ (top right), $\mu^+\mu^-$ (bottom left) and W^+W^- pairs for DM masses from 200 GeV to 200 TeV obtained for the 40 h of good quality observation of the Milky Way GH. Green and yellow lines correspond to the 68% and 95% containment bands, respectively, of the distribution of the same estimator computed from 300 simulations of the null hypothesis (i.e. $1/\tau_{DM} = 0$) mimicking conditions of the data sample.

profile. At low DM masses Fermi provides the most stringent constraints, having a larger sensitivity in the MeV-GeV range. HAWC instead can provide stronger constraints with the advantage of its large FoV, to larger DM masses. HAWC's GH constraints reported in Fig. 5.29 are obtained with an Einasto profile, as in this work. Nevertheless, the use of a core DM profile (e.g. Burket one) lead to a limit on DM lifetime 50% less constraining compared to Einasto, thus a not-negligible dependence on DM distribution profile is present. At the moment MAGIC covers a wide energy range, spanning through Fermi and HAWC mass ranges. GH results provide better limits for low DM masses w.r.t. MAGIC Perseus cluster analysis, and the better constraints expect in $\mu^+\mu^-$ channel for DM masses around 10 TeV.

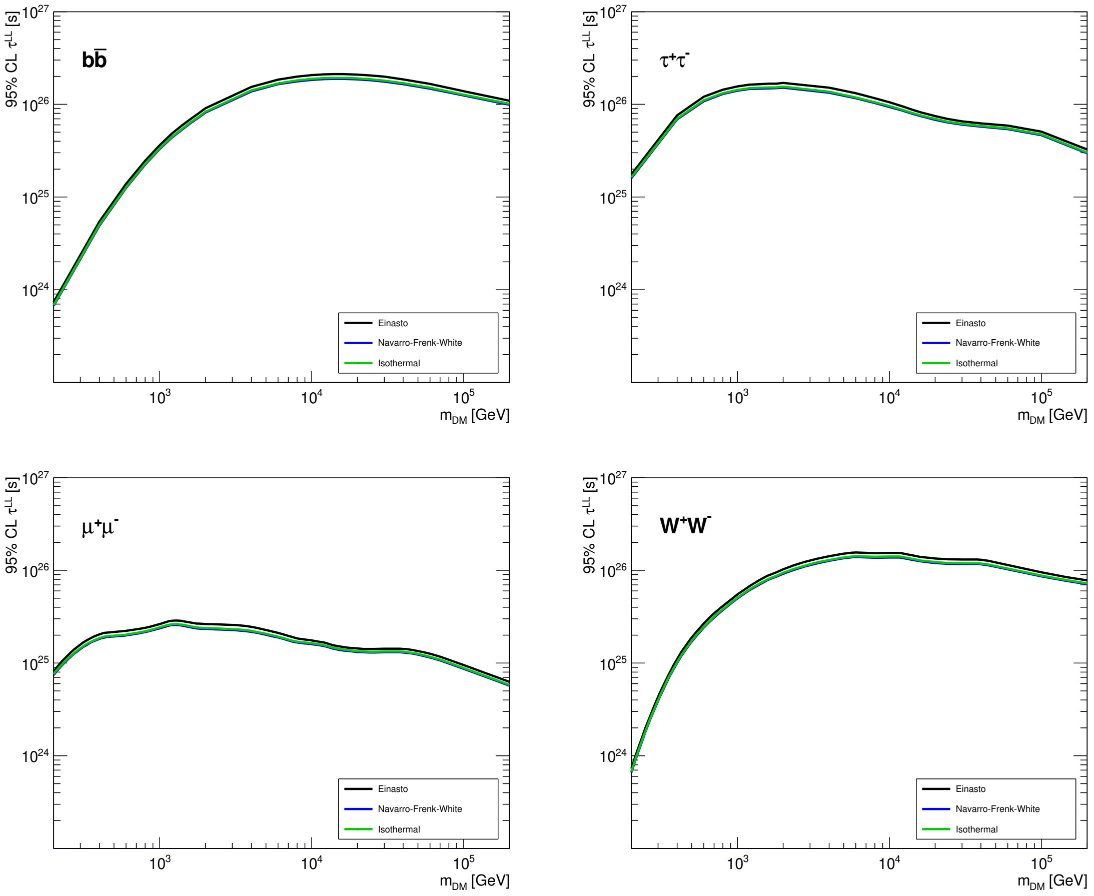

Figure 5.28 Comparison of the 95% CL lower limits on τ_{DM} for a DM particle decaying into pairs of $b\bar{b}$ (top left), $\tau^+\tau^-$ (top right), $\mu^+\mu^-$ (bottom left), W^+W^- (bottom right) for DM masses from 200 GeV to 200 TeV, inferred from the Einasto, NFW and Isothermal DM distribution profiles. As described in the text, the curves differs for at most a 10% in all the channels. This confirms the negligible results of our results with the chosen DM distribution profile.

Hence, the method adopted is very powerful since those limits are produced using a fraction of the total observation time used by the other method.

Decaying DM scenarios have been studied deeply and are currently being investigated with several classes of instruments. Some studies provide very constraining limits, making use of the integrated cosmological decaying DM contribution to the extragalactic diffuse light [141] made up of prompt and secondary emission. It must be said that those studies adopted an approach that strongly depends on the models describing secondary emission, which boosts the expected DM flux considerably and thus the DM constraints. Those works are weaker than the GH analysis presented here, since the method relies only on the DM

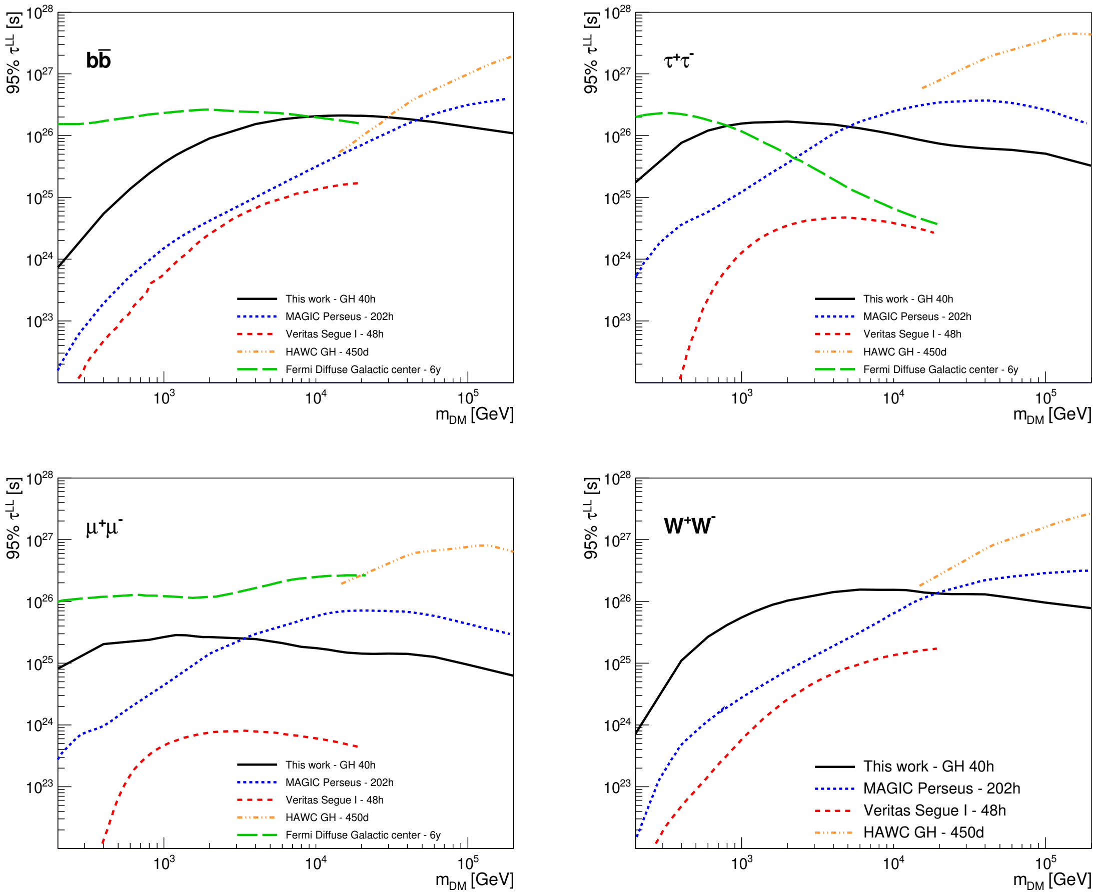

Figure 5.29 The black solid line reports the 95% CL lower limit on decay lifetime for a DM particle decaying into pairs of $b\bar{b}$ (top left), $\tau^+\tau^-$ (top right), $\mu^+\mu^-$ (bottom left) and W^+W^- (bottom right) for DM masses from 200 GeV to 200 TeV from 40 h of good quality data from the GH observations. We compared the limit obtained with the previous MAGIC results on 202 h of Perseus galaxy cluster [28], the limit from 48 h on Segue 1 from VERITAS [30], limit GH from HAWC [34], and the results from the Fermi search in the diffuse Galactic Center [29].

profile models in the region of search considered. Finally, at larger DM masses (>100 TeV) the most stringent constraints can be obtained by considering the heavy-WIMP scenario in HAWC [34] or neutrinos in IceCube [142].

5.5.2 Annihilation results

For completeness, in this section the results for DM annihilation is reported. The same procedure adopted for DM decay is used here, as well as the analysis cuts. Since the MC used is the same in both case, there is no reason that justify different cut in θ^2 and h for the

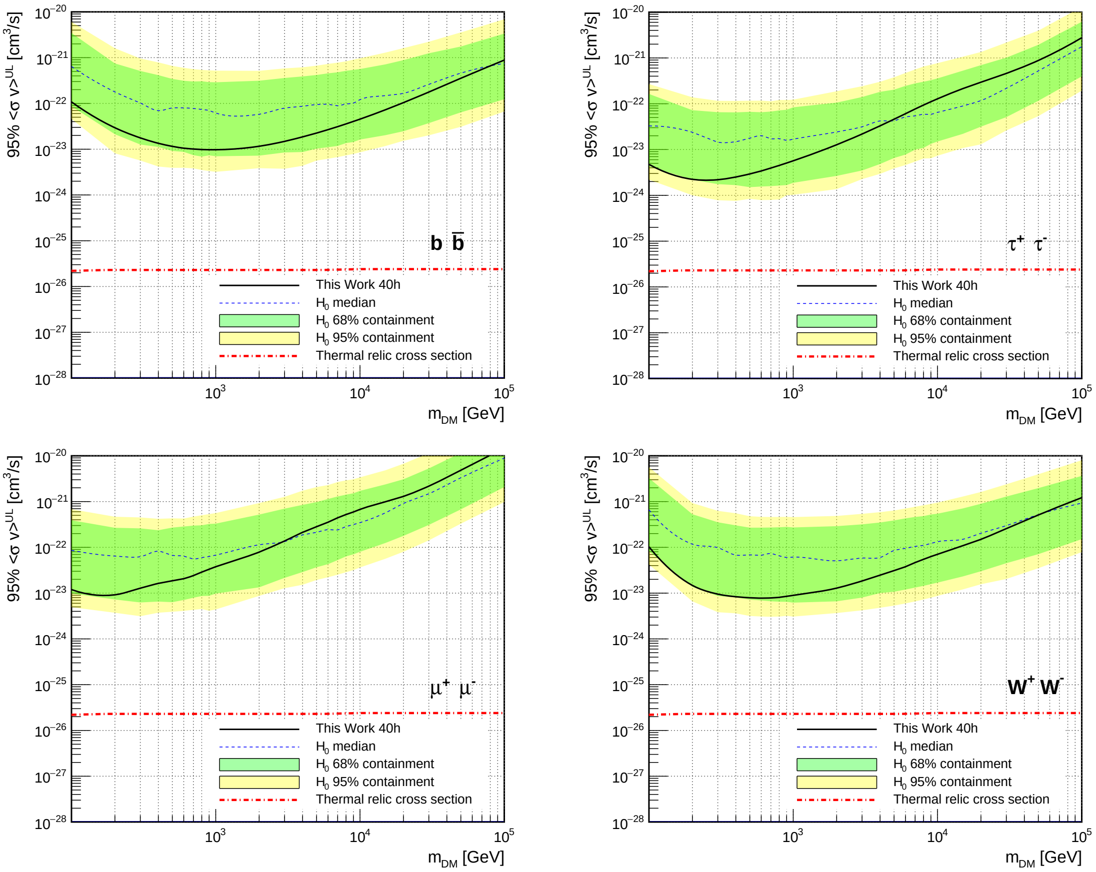

Figure 5.30 95% CL lower limit to the thermally averaged cross-section of DM particle annihilating into $b\bar{b}$ (top left), $\tau^+\tau^-$ (top right), $\mu^+\mu^-$ (bottom left) and W^+W^- pairs for DM masses from 100 GeV to 100 TeV obtained for the 40 h of good quality observation of the Milky Way GH. Green and yellow lines correspond to the 68% and 95% containment bands, respectively, of the distribution of the same estimator computed from 300 simulations of the null hypothesis ($<\sigma v>= 0$) mimicking conditions of the data sample.

annihilation case. The data sample is the same, except for the value of ΔJ computed from the curves of Fig. 5.3b.

In Fig. 5.30 the 95% C.L. upper limit on the thermally averaged velocity cross-section for DM particles ($<\sigma v>^{UL}$) is reported, obtained with the binned likelihood analysis. The two-sided 68% and 95% containment bands for the distribution of the upper limits are obtained from the analysis of 300 realizations of the null hypothesis ($<\sigma v>= 0$), consisting of toy MC simulations generated from pure background PDF, assuming similar exposures as for the real data, and assumed κ_i as a nuisance parameter in the likelihood function. In all the channel considered, the $<\sigma v>$ is constrained down to a value of 10^{-23} cm^{3}s^{-1}

In Fig. 5.31, is reported the comparison of our results with Fermi+MAGIC combined analysis on dSphs [23], the combined analysis on dSphs by VERITAS [30], the GH results from HAWC analysis [34] and the limit computed by the observation of the GC by HESS [35]. Despite the limits are not as constraining as the best ones provided by Fermi+MAGIC and HESS, the results achieved by GH are very competitive, being on the same level of the results from VERITAS and HAWC.

It should be mentioned that the results from HESS are busted by the observations of the inner region of the Milky Way, where the uncertainty in the DM density profile foreseen by the various model is the largest. Their results are strongly model dependent, in contrast with our that does not depend on the DM profile assumed.

5.5.3 Conclusions and remarks

This work represents a new method to search for DM signals with IACT instruments in very extended sources like the GH. The method benefits from the integration of a large FoV, that allows us to increase the sensitivity to DM decay with a relatively low amount of observation time. The systematic uncertainty level turns out to be well controlled under different scenarios where we removed some of the constraints required and the dependence on energy, so that fluctuations in the systematics would not compromise the sensitivity.

The value and the properties of the systematic uncertainties have been used as input for the likelihood analysis, letting us to constrain a DM lifetime to 10^{26} s, one of the most constrained results for IACTs, achieved with 20% of the effective time used for previous MAGIC work on the Perseus galaxy cluster. DM annihilation search constrains $< \sigma v >$ down to 10^{-23} cm^{3}s^{-1}, resulting anyway competitive with the limits reported in literature. It is remarkable that the strong constraints achieved with GH data, are obtained with a fraction of the observation time used for the other experiments. Moreover, our results are totally model-independent hence more robust compared to Galactic center observations (HESS and HAWC).

Furthermore, the method shows that archival data complying with the constraints required are consistent in terms of systematic uncertainties, thus can be added as additional terms to the likelihood function, improving the sensitivity, and thus, the constraint for DM lifetime.

Finally, the methodology can naturally be applied to CTA observations, where the sensitivity can significantly improve thanks to the the larger FoV available.

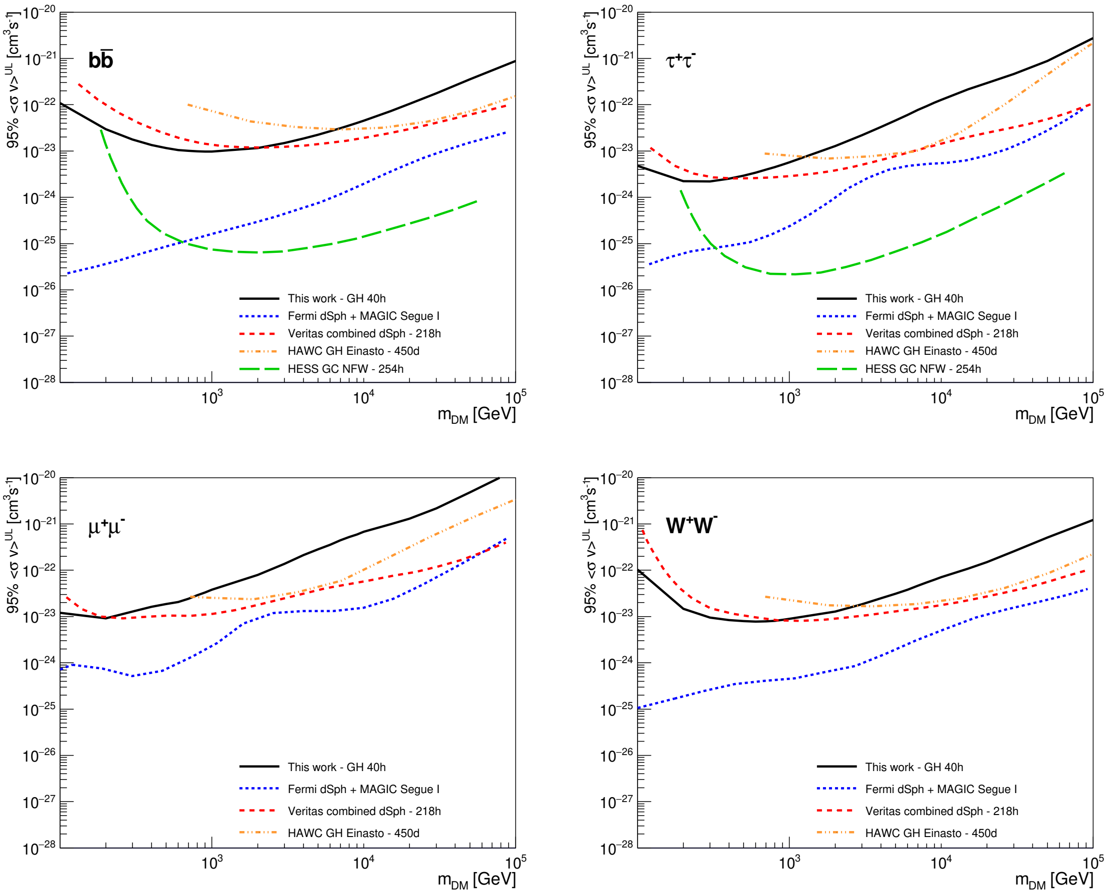

Figure 5.31 The solid black line shows the 95% CL lower limit on the thermally averaged cross-section for a DM particle annihilating into pairs of $b\bar{b}$ (top left), $\tau^+\tau^-$ (top right), $\mu^+\mu^-$ (bottom left) and W^+W^- (bottom right) for DM masses from 100 GeV to 100 TeV from 40 h of good quality data from the GH observations. We compared the limit obtained with the result of the combined analysis by Fermi (dSph) and MAGIC (Segue I) [23], the limit from 48 h on Segue 1 from VERITAS [30], limit on GH from HAWC [34], and the results from the H.E.S.S search in Galactic Center [35].

Conclusions

Albeit the large efforts in search for DM with different experimental approaches, no experimental detection of this mysterious kind of matter has been found, so far.

In this thesis I reported the study of the search for DM signals in both annihilation and decay through the indirect detection of the γ rays produced by two different types of targets, the Draco dSph and the Milky Way GH. The observations were carried out with the MAGIC telescopes, located at the La Palma canary island observatory, during the 2018.

As a dSph, Draco is a DM dominated object, with almost no γ-ray background, with a DM halo that extends till a radius of 1.3° from the center of its halo. This object was observed in a multi-year campaign promoted by MAGIC, with the aim of combining the data of all the dSphs observed so far, into a single more constraining limit. Special requirements in terms of equally Az coverage between the wobble positions and good quality of the weather conditions, have been guaranteed by a daily check of the data taken. The correct computation of the IRF is achieved with the use of the Donut Monte Carlo method, that rescales the MC events according to the morphology of the expected γ rays in the Draco halo.

The GH region represents a challenge for MAGIC, because its extension prevents the use of wobble mode observation, forcing us to use the ON/OFF mode. ON and OFF have to be selected in order to ensure the largest ΔJ, and keep the systematic in the background estimation controlled and down to a minimum. Special requirements have been adopted from the data taking level, constraining both ON and OFF to follow the same trajectory in terms of local coordinates pointing. Moreover, dark conditions of the sky, no presence of bright objects (no stars neither known VHE sources) and excellent weather conditions were required to keep the systematics under control. These results have been achieved thanks to the efforts of the GH analyser (me), the MAGIC scheduling team and the observers at the MAGIC site. Moreover, a different normalization method based on the hadronness curve has been successfully developed.

Successively, the systematic were estimated measuring the residual background in the signal region, for a set of data observed ad-hoc, where the expected contribution of DM was the lowest as possible. The stability of systematic was tested with different dataset in different conditions. These observations belong to archival data or happened in consecutive days, during different periods of the year, in long distance in time and were. All these tests showed that the systematic level is consistent within the statistical error, confirming the validity of the approach used. Further studies are needed for checking whether the constraints required can be relaxed, in order to enlarge the data sample with the introduction of archival data, and increasing the ΔJ that can be explored. Moreover, the normalization procedure can be optimized too, depending on the type of sample used.

Both the Draco and GH dataset were analysed by using the *full likelihood* method, that takes into account the spectral features contained in the γ-ray DM spectra. No significant excess was found above the background, thus the observations were used to set constraints on the DM particle properties. In particular, limits on thermally averaged velocity cross-section and lifetime were computed for SM final states $b\bar{b}$, $\tau^+\tau^-$, $mu^+\mu^-$, W^+W. The calculation did not assume any dependence from models, assuming a branching ratio of 100% for each channel. The 95% confidence level limits were obtained for DM masses in the interval from 100 GeV to 100 TeV.

The Draco best limits for annihilation are reached in $\tau^+\tau^-$ channel, constraining $< \sigma v >$ down to 10^{-23} cm^{3}s^{-1}. This value is less constrained compared to the previous results carried out by MAGIC, due to the lower J-factor of the target. As mentioned, Draco was observed as part of a multi-year program and not as a stand-alone observation. Surprisingly, more competitive results were achieved for DM decay, constraining the DM lifetime to 10^{26} s in $b\bar{b}$, $\tau^+\tau^-$ and W^+W channels. Moreover, the results are comparable for $m_{\mathrm{DM}} < 20$ TeV with ones obtained with the deep observation campaign of Perseus by MAGIC.

GH constraints result very competitive in the decay scenario, since the expected ΔJ is comparable with the values obtained by observations of the Galactic center. DM lifetime is constrained up to $2{\cdot}10^{26}$ s in $b\bar{b}$, $\tau^+\tau^-$ and W^+W channels, resulting the most constraining limits for MAGIC in $b\bar{b}$ for $m_{\mathrm{DM}} < 60$ TeV, in $\tau^+\tau^-$ for $m_{\mathrm{DM}} < 5$ TeV and the achieving the best limit in W^+W^- for $m_{\mathrm{DM}} < 20$ TeV so far. Moreover, these results confirm the power of the method, that provides limits competitive with the other experiments, using a fraction of the total time, and being totally independent from the DM profile considered. As a drawback, since it consumes the double of observation time w.r.t. a wobble observation, the possibility of adding archival data to the sample would provide more constraining limits without wasting any observation time.

Appendix A

Galactic Halo Data sample

In the following tables, the entire GH dataset is presented. The values of J and $DeltaJ$ is given in unit of $\log_{10}\mathrm{J}[\mathrm{GeVcm}^{-2}]$, for the DM profiles considered in the text and presented in Chapter 5.

Moreover, in Fig. A.1, the relative difference $\mathfrak{D}$ of the ΔJ^{NFW} and ΔJ^{iso} w.r.t. the ΔJ^{ein} is reported, and computed as:

$$\mathfrak{D}^X = 2\frac{\Delta J^{\mathrm{ein}} - \Delta J^X}{\Delta J^{\mathrm{ein}} + \Delta J^X}\%, \tag{A.1}$$

where X is iso or NFW. The average of D is $\sim$10% for NFW case and $\sim$8% for isothermal case.

Table A.1 The GH dataset, observed during 2018 and 2019 is presented in this table. The pointing in terms of the local Az coordinate, the right ascension and declination, the J-factor (for each DM-profile considered, as in Fig. 5.3b) for each slot and the ΔJ for each observation night is reported. The data are divided into observations with low ΔJ used for the evaluation of σ_{syst}, and the one with high ΔJ for the DM lifetime measurement, and in MAGIC analysis period.

Date	**Slot**	**Az [deg]**	**(RA, Dec) ([ha], [deg])**	$\mathbf{log_{10}J^{ein}}$ **[GeVcm^{-2}]**	$\mathbf{log_{10}\Delta J^{ein}}$ **[GeVcm^{-2}]**	$\mathbf{log_{10}J^{NFW}}$ **[GeVcm^{-2}]**	$\mathbf{log_{10}\Delta J^{NFW}}$ **[GeVcm^{-2}]**	$\mathbf{log_{10}J^{iso}}$ **[GeVcm^{-2}]**	$\mathbf{log_{10}\Delta J^{iso}}$ **[GeVcm^{-2}]**
σ_{syst} study - ST0309									
20180113	ON	163.1 – 197.2	3.853, 3.228	19.362	18.201	19.377	18.212	19.402	18.203
	OFF	159.3 – 193.5	8.867, 3.228	19.391		19.406		19.429	
20180114	ON	160.8 – 194.6	3.849, 2.829	19.362	–	19.378	–	19.402	–
	OFF	–	–	–		–		–	
20180121	ON	189.2 – 220.4	4.429, 4.978	19.351	17.415	19.366	17.427	19.392	17.417
	OFF	190.2 – 221.3	7.437, 4.978	19.356		19.371		19.396	
20180215	ON	165.4 – 197.5	8.631, 1.262	19.387	18.312	19.402	18.324	19.425	18.314
	OFF	172.0 – 200.8	5.121, 1.262	19.349		19.364		19.390	
20180216	ON	–	–	–	–	–	–	–	–
	OFF	171.5 – 190.8	5.204, 1.262	19.348		19.364		19.390	
20180217	ON	161.7 – 195.4	8.796, 1.265	19.392	18.372	19.407	18.383	19.429	18.374
	OFF	168.5 – 200.1	5.286, 1.265	19.348		19.363		19.389	
20180218	ON	167.4 – 199.9	8.694, 1.263	19.389	18.351	19.404	18.362	19.427	18.352
	OFF	159.7 – 195.9	5.686, 1.263	19.347		19.362		19.388	
DM lifetime study - ST0309									
20180412	ON	148.2 – 178.5	16.151, 1.964	19.892	19.714	19.882	19.691	19.896	19.701
	OFF	161.8 – 194.6	9.633, 1.964	19.419		19.434		19.455	
20180415	ON	158.4 – 190.5	16.994, 1.406	19.961	19.808	19.943	19.776	19.956	19.785
	OFF	158.4 – 189.9	9.974, 1.406	19.434		19.448		19.468	
20180416	ON	172.3 – 203.4	16.983, 0.981	19.966	19.815	19.947	19.782	19.960	19.791
	OFF	172.7 – 204.0	9.964, 0.981	19.434		19.448		19.468	
20180419	ON	165.5 – 196.6	16.953, 0.619	19.968	19.783	19.949	19.747	19.962	19.757
	OFF	166.2 – 197.3	11.438, 0.619	19.509		19.522		19.538	

Table A.2 Continue of Tab. A.1.

Date	**Slot**	**Az** [deg]	**(RA, Dec)** ([ha], [deg])	$\mathbf{log_{10}J^{ein}}$ [GeVcm^{-2}]	$\mathbf{log_{10}\Delta J^{ein}}$ [GeVcm^{-2}]	$\mathbf{log_{10}J^{NFW}}$ [GeVcm^{-2}]	$\mathbf{log_{10}\Delta J^{NFW}}$ [GeVcm^{-2}]	$\mathbf{log_{10}J^{iso}}$ [GeVcm^{-2}]	$\mathbf{log_{10}\Delta J^{iso}}$ [GeVcm^{-2}]
DM lifetime study - ST0309									
20180511	ON	178.0 – 209.4	16.978, -0.178	19.978	19.796	19.958	19.758	19.970	19.768
	OFF	176.1 – 208.2	11.463, -0.178	19.512		19.525		19.541	
20180514	ON	166.5 – 199.7	17.727, -0.198	20.005	19.829	19.981	19.787	19.992	19.795
	OFF	177.2 – 207.1	11.711, -0.198	19.527		19.539		19.555	
ST0310									
20180809	ON	165.9 – 197.5	17.811, 0.593	19.995	19.820	19.973	19.779	19.984	19.788
	OFF	165.4 – 202.7	23.961, 0.593	19.516		19.529		19.545	
20180811	ON	160.4 – 204.9	18.097, -0.244	20.000	19.840	19.977	19.800	19.988	19.808
	OFF	159.3 – 203.9	0.464, -0.244	19.489		19.502		19.519	
ST0311									
20190408	ON	192.5 – 160.1	16.983, 0.962	19.966	19.808	19.947	19.775	19.960	19.785
	OFF	187.9 – 156.9	10.298, 1.0	19.449		19.463		19.482	
20190502	ON	184.5 – 213.3	17.385, 0.837	19.985	19.832	19.964	19.795	19.976	19.804
	OFF	184.1 – 213.3	10.499, 0.837	19.458		19.472		19.491	
20190503	ON	–	–	–	–	–	–	–	–
	OFF	158.1 – 198.5	11.633, 0.837	19.520		19.532		19.548	
20190505	ON	[164.5, 196.1]	17.066, 0.731	19.973	19.792	19.954	19.755	19.966	19.765
	OFF	161.8 – 195.5	11.384, 0.731	19.505		19.518		19.535	
20190506	ON	170.6 – 199.9	17.005, 0.322	19.974	19.795	19.955	19.758	19.967	19.768
	OFF	167.1 – 199.3	11.340, 0.322	19.503		19.516		19.533	
20190507	ON	177.0 – 205.4	16.802, -1.144	19.977	19.795	19.957	19.757	19.969	19.767
	OFF	176.3 – 204.5	11.404, -1.144	19.510		19.523		19.540	
20190508	ON	167.7 – 199.5	18.190, 0.289	19.990	19.766	19.968	19.721	19.980	19.731
	OFF	168.0 – 199.3	12.741, 0.289	19.596		19.606		19.620	

Table A.3 Continue of Tab. A.1.

Date	**Slot**	**Az** [deg]	**(RA, Dec)** ([ha], [deg])	$\log_{10}J^{\mathrm{ein}}$ [GeVcm^{-2}]	$\log_{10}\Delta J^{\mathrm{ein}}$ [GeVcm^{-2}]	$\log_{10}J^{\mathrm{NFW}}$ [GeVcm^{-2}]	$\log_{10}\Delta J^{\mathrm{NFW}}$ [GeVcm^{-2}]	$\log_{10}J^{\mathrm{iso}}$ [GeVcm^{-2}]	$\log_{10}\Delta J^{\mathrm{iso}}$ [GeVcm^{-2}]
DM - ST0311									
20190528	ON	178.4 – 208.1	16.878, -3.208	20.006	19.788	19.983	19.741	19.993	19.749
	OFF	178.9 – 208.5	12.701, -3.208	19.602		19.612		19.626	
20190529	ON	178.2 – 207.9	17.128, -3.214	20.023	19.811	19.997	19.762	20.006	19.768
	OFF	177.9 – 207.3	12.783, -3.214	19.609		19.619		19.632	
20190530	ON	175.2 – 204.2	17.043, -3.212	20.018	19.799	19.993	19.750	20.002	19.756
	OFF	176.4 – 207.6	12.865, -3.212	19.615		19.624		19.638	
20190531	ON	171.8 – 202.0	17.246, -2.154	20.016	19.788	19.991	19.738	20.001	19.745
	OFF	172.6 – 205.7	13.068, -2.154	19.628		19.637		19.650	
20190601	ON	172.2 – 201.0	17.245, -2.154	20.016	19.784	19.991	19.733	20.001	19.740
	OFF	173.2 – 204.9	13.151, -2.154	19.634		19.643		19.656	
20190602	ON	–	–	–	–	–	–	–	–
	OFF	175.7 – 207.0	13.096, -2.154	19.630		19.639		19.652	
20190603	ON	176.1 – 205.4	17.105, -3.214	20.022	19.789	19.996	19.738	20.005	19.744
	OFF	176.3 – 206.5	13.161, -3.214	19.639		19.647		19.660	
20190604	ON	168.8 – 200.3	17.370, -2.962	20.032	19.786	20.005	19.731	20.013	19.735
	OFF	170.6 – 199.7	13.526, -2.962	19.669		19.676		19.689	
20190731	ON	176.9 – 204.0	17.782, -3.169	20.043	19.874	20.014	19.825	20.021	19.828
	OFF	176.1 – 203.7	23.548, -3.169	19.550		19.562		19.577	
20190801	ON	–	–	–	–	–	–	–	–
	OFF	170.0 – 198.1	23.878, -3.169	19.529		19.542		19.557	
20190803	ON	159.2 – 189.7	17.732, -1.626	20.023	19.868	19.997	19.825	20.006	19.830
	OFF	159.6 – 190.4	0.334, -1.626	19.499		19.512		19.529	
20190804	ON	180.5 – 207.8	18.572, -2.256	20.000	19.815	19.977	19.772	19.988	19.780
	OFF	179.6 – 209.2	23.670, -2.256	19.540		19.553		19.568	

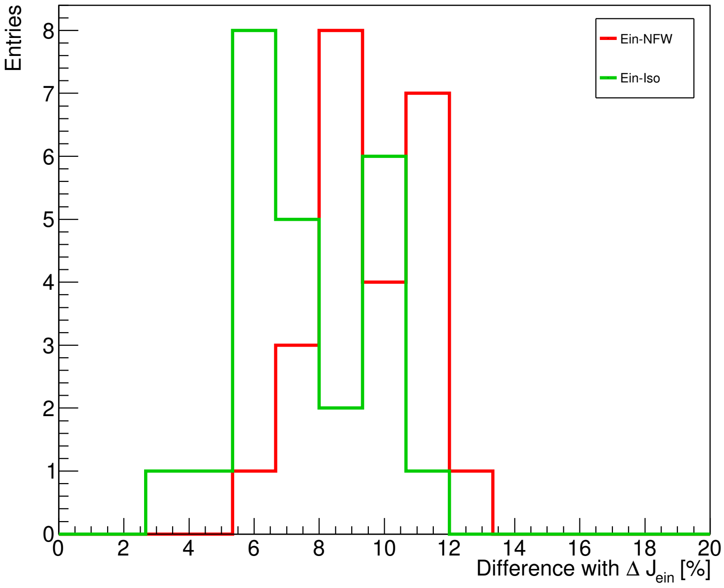

Figure A.1 The relative difference of the NFW and Isothermal ΔJ and the ΔJ_{ein} computed with Einasto profile, is reported. The mean values of such difference for NFW case is $\sim 10\%$ and for isothermal case if $\sim 8\%$.

Bibliography

[1] K. G. Begeman, A. H. Broeils, and R. H. Sanders. Extended rotation curves of spiral galaxies : dark haloes and modified dynamics. *mnras*, 249:523, April 1991.

[2] P.A.R. Ade et al. Planck 2013 results. I. Overview of products and scientific results. *Astron. Astrophys.*, 571:A1, 2014.

[3] P.A.R. Ade et al. Planck 2015 results. XIII. Cosmological parameters. *Astron. Astrophys.*, 594:A13, 2016.

[4] The 2dF Galaxy Redshift Survey collaboration. The 2df galaxy redshift survey hompage, 2020.

[5] The Sloan Digital Sky Survey collaboration. Sloan digital sky survey hompage, 2019.

[6] J. Huchra, M. Davis, D. Latham, and J. Tonry. A survey of galaxy redshifts: 4. The data. *Astrophys. J. Suppl.*, 52:L89–L119, 1983.

[7] The Virgo consortium. The millennium simulation project hompage, 2020.

[8] Jonathan L. Feng. Dark Matter Candidates from Particle Physics and Methods of Detection. *Ann. Rev. Astron. Astrophys.*, 48:495–545, 2010.

[9] Howard Baer, Ki-Young Choi, Jihn E. Kim, and Leszek Roszkowski. Dark matter production in the early universe: Beyond the thermal wimp paradigm. *Physics Reports*, 555:1 – 60, 2015. Dark matter production in the early Universe: Beyond the thermal WIMP paradigm.

[10] B. Abbott, Jasmin Abdallah, O. Abdinov, B. Abeloos, R. Aben, M. Abolins, O. AbouZeid, H. Abramowicz, Heather Abreu, Ricardo Abreu, Y. Abulaiti, B. Acharya, L. Adamczyk, D. Adams, J. Adelman, S. Adomeit, T. Adye, A. Affolder, and L. Zwalinski. Search for supersymmetry at

$$\sqrt{s} = 13$$

s = 13 tev in final states with jets and two same-sign leptons or three leptons with the atlas detector. *The European Physical Journal C*, 76, 05 2016.

[11] E. Aprile, J. Aalbers, Francesca Agostini, Matteo Alfonsi, F. Amaro, Mouliere Anthony, F. Arneodo, P. Barrow, Laura Baudis, B. Bauermeister, M.L Benabderrahmane, T. Berger, P.A Breur, Andrew Brown, Ethan Brown, S. Bruenner, Gianmarco Bruno, R. Budnik, L. Butikofer, and T. Zhu. First dark matter search results from the xenon1t experiment. *Physical Review Letters*, 119, 10 2017.

[12] E. Aprile et al. First Dark Matter Search Results from the XENON1T Experiment. *Phys. Rev. Lett.*, 119(18):181301, 2017.

[13] Andi Tan et al. Dark Matter Results from First 98.7 Days of Data from the PandaX-II Experiment. *Phys. Rev. Lett.*, 117(12):121303, 2016.

[14] E. Aprile et al. XENON100 Dark Matter Results from a Combination of 477 Live Days. *Phys. Rev. D*, 94(12):122001, 2016.

[15] E. Aprile et al. Observation of Excess Electronic Recoil Events in XENON1T. 6 2020.

[16] Ulrich R. M. E. Geppert. S. Longair,high energy astrophysics, vol. 1,particles photons and their detection, Cambridge University Press, Cambridge, 1992. *Astrophysics and Space Science*, 201, 1992.

[17] Robert Marcus Wagner. *Measurement of Very High Energy Gamma-Ray Emission from Four Blazars Using the MAGIC Telescope and a Comparative Blazar Study*. PhD thesis, Munich, Tech. U., 2006.

[18] Joaquim Palacio Navarro. *Indirect dark matter search on the Triangulum-II dwarf spheroidal galaxy and the Perseus galaxy cluster with the MAGIC telescopes.* PhD thesis, UAB, 2018.

[19] Daniel Alberto Guberman. *MAGIC observation with bright moon and their application to measuring the VHE gamma-ray spectral cut-off of the PeVatron candidate Cassiopea A*. PhD thesis, UAB, 2018.

[20] J. Aleksić et al. The major upgrade of the magic telescopes, part ii: A performance study using observations of the crab nebula. *Astroparticle Physics*, 72:76 – 94, 2016.

[21] J. Aleksić. Optimized analysis method for indirect dark matter searches with Imaging Air Cherenkov Telescopes. In *33rd International Cosmic Ray Conference*, page 0088, 1 2016.

[22] Alex Geringer-Sameth, Savvas M. Koushiappas, and Matthew Walker. Dwarf galaxy annihilation and decay emission profiles for dark matter experiments. *Astrophys. J.*, 801(2):74, 2015.

[23] M.L. Ahnen et al. Limits to Dark Matter Annihilation Cross-Section from a Combined Analysis of MAGIC and Fermi-LAT Observations of Dwarf Satellite Galaxies. *JCAP*, 02:039, 2016.

[24] S. Archambault et al. Dark Matter Constraints from a Joint Analysis of Dwarf Spheroidal Galaxy Observations with VERITAS. *Phys. Rev. D*, 95(8):082001, 2017.

[25] A. Abramowski et al. Search for dark matter annihilation signatures in h.e.s.s. observations of dwarf spheroidal galaxies. *Phys. Rev. D*, 90:112012, Dec 2014.

[26] A. Albert et al. Dark Matter Limits From Dwarf Spheroidal Galaxies with The HAWC Gamma-Ray Observatory. *Astrophys. J.*, 853(2):154, 2018.

[27] Evan N. Kirby, Judith G. Cohen, Joshua D. Simon, Puragra Guhathakurta, Anders O. Thygesen, and Gina E. Duggan. Triangulum ii. not especially dense after all. *The Astrophysical Journal*, 838(2):83, Mar 2017.

[28] V.A. Acciari et al. Constraining Dark Matter lifetime with a deep gamma-ray survey of the Perseus Galaxy Cluster with MAGIC. *Phys. Dark Univ.*, 22:38–47, 2018.

[29] M. Ajello, W. Atwood, L. Baldini, Guido Barbiellini, Denis Bastieri, Keith Bechtol, Ronaldo Bellazzini, R. Blandford, E. Bloom, Emanuele Bonamente, A. Borgland, E. Bottacini, T. Brandt, J. Bregeon, M. Brigida, P. Bruel, R. Buehler, Stefano Buson, G. Caliandro, and Stephan Zimmer. Constraints on the galactic halo dark matter from fermi-lat diffuse measurements. *The Astrophysical Journal*, 761, 05 2012.

[30] E. Aliu et al. VERITAS Deep Observations of the Dwarf Spheroidal Galaxy Segue 1. *Phys. Rev. D*, 85:062001, 2012. [Erratum: Phys.Rev.D 91, 129903 (2015)].

[31] Lidia Pieri, Julien Lavalle, Gianfranco Bertone, and Enzo Branchini. Implications of high-resolution simulations on indirect dark matter searches. *Physical Review D*, 83(2), Jan 2011.

[32] Javier Rico. Gamma-ray dark matter searches in milky way satellites—a comparative review of data analysis methods and current results. *Galaxies*, 8(1):25, Mar 2020.

[33] Konstancja Satalecka. *Multimessenger studies of point-sources using the IceCube neutrino telescope and the MAGIC gamma-ray telescope*. PhD thesis, 10 2010.

[34] A.U. Abeysekara et al. A Search for Dark Matter in the Galactic Halo with HAWC. *JCAP*, 02:049, 2018.

[35] Lucia Rinchiuso and Emmanuel Moulin. Dark matter searches toward the Galactic Centre halo with H.E.S.S. In *52nd Rencontres de Moriond on Very High Energy Phenomena in the Universe*, pages 255–262, 2017.

[36] F. Zwicky. Die Rotverschiebung von extragalaktischen Nebeln. *Helv. Phys. Acta*, 6:110–127, 1933. [Gen. Rel. Grav.41,207(2009)].

[37] E. Opik. An estimate of the distance of the Andromeda Nebula. *apj*, 55:406–410, June 1922.

[38] J. H. Oort. The force exerted by the stellar system in the direction perpendicular to the galactic plane and some related problems. *bain*, 6:249, August 1932.

[39] P. Shnider, J. Ehlers, and E. Falco. *Gravitational Lenses*. Springer, 2010.

[40] Steven Weinberg. *Cosmology*. 9 2008.

[41] Scott Dodelson. *Modern Cosmology*. Academic Press, Amsterdam, 2003.

[42] Joel R. Primack. Whatever happened to hot dark matter? *SLAC Beam Line*, 31N3:50–57, 2001.

[43] Volker Springel, Carlos S. Frenk, and Simon D.M. White. The large-scale structure of the Universe. *Nature*, 440:1137, 2006.

[44] Pedro Colin, Vladimir Avila-Reese, and Octavio Valenzuela. Substructure and halo density profiles in a warm dark matter cosmology. *Astrophys. J.*, 542:622–630, 2000.

[45] W.J.G. de Blok. The Core-Cusp Problem. *Adv. Astron.*, 2010:789293, 2010.

[46] James Bullock. Notes on the missing satellites problem. *Local Group Cosmology*, 09 2010.

[47] Joshua D. Simon and Marla Geha. The kinematics of the ultra-faint milky way satellites: Solving the missing satellite problem. *The Astrophysical Journal*, 670(1):313–331, Nov 2007.

[48] Stacy McGaugh. The Baryonic Tully-Fisher Relation of Gas Rich Galaxies as a Test of LCDM and MOND. *Astron. J.*, 143:40, 2012.

[49] M. Milgrom. A Modification of the Newtonian dynamics as a possible alternative to the hidden mass hypothesis. *Astrophys. J.*, 270:365–370, 1983.

[50] Jacob D. Bekenstein. Relativistic gravitation theory for the MOND paradigm. *Phys. Rev. D*, 70:083509, 2004. [Erratum: Phys.Rev.D 71, 069901 (2005)].

[51] Gianfranco Bertone, Dan Hooper, and Joseph Silk. Particle dark matter: Evidence, candidates and constraints. *Phys. Rept.*, 405:279–390, 2005.

[52] Edward Witten. Mass hierarchies in supersymmetric theories. *Physics Letters B*, 105(4):267 – 271, 1981.

[53] John R. Ellis, S. Kelley, and Dimitri V. Nanopoulos. Constraints from gauge coupling unification on the scale of supersymmetry breaking. *Phys. Lett. B*, 287:95–100, 1992.

[54] John Ellis, J.S. Hagelin, D.V. Nanopoulos, K. Olive, and M. Srednicki. Supersymmetric relics from the big bang. *Nuclear Physics B*, 238(2):453 – 476, 1984.

[55] Supersymmetry and weak, electromagnetic and strong interactions. *Physics Letters B*, 64(2):159 – 162, 1976.

[56] J. Wess. SUPERSYMMETRY AND SUPERGRAVITY. In *22nd International Conference on High-Energy Physics*, page II.84, 7 1984.

[57] A. H. Chamseddine, R. Arnowitt, and Pran Nath. Locally supersymmetric grand unification. *Phys. Rev. Lett.*, 49:970–974, Oct 1982.

[58] John Ellis, Toby Falk, Keith A. Olive, and Yudi Santoso. Exploration of the mssm with non-universal higgs masses. *Nuclear Physics B*, 652:259 – 347, 2003.

[59] Gianfranco Bertone and M.P. Tait, Tim. A new era in the search for dark matter. *Nature*, 562(7725):51–56, 2018.

[60] Takehiko Asaka and Mikhail Shaposhnikov. The νmsm, dark matter and baryon asymmetry of the universe. *Physics Letters B*, 620(1):17 – 26, 2005.

[61] Martin Goetz and Jesper Sommer-Larsen. Galaxy formation: warm dark matter, missing satellites, and the angular momentum problem. *Astrophys. Space Sci.*, 284:341–344, 2003.

[62] Jonathan L. Feng, Arvind Rajaraman, and Fumihiro Takayama. SuperWIMP dark matter signals from the early universe. *Phys. Rev. D*, 68:063504, 2003.

[63] R.D. Peccei and Helen R. Quinn. Cp conservation in the presence of pseudoparticles**work supported in part by national science foundation grants no. phy 75-18444 and no. phy 75-20427. In L. WOLFENSTEIN, editor, *CP Violation*, pages 328 – 331. Elsevier, Amsterdam, 1989.

[64] R. Bernabei et al. Further results on the WIMP annual modulation signature by DAMA/NaI. *Nucl. Phys. B Proc. Suppl.*, 138:45–47, 2005.

[65] Rita Bernabei et al. The Annual Modulation Signature for Dark Matter: DAMA/LIBRA-Phase1 Results and Perspectives. *Adv. High Energy Phys.*, 2014:605659, 2014.

[66] C. E. Aalseth, P. S. Barbeau, J. Colaresi, J. I. Collar, J. Diaz Leon, J. E. Fast, N. E. Fields, T. W. Hossbach, A. Knecht, M. S. Kos, M. G. Marino, H. S. Miley, M. L. Miller, J. L. Orrell, and K. M. Yocum. Search for an annual modulation in three years of cogent dark matter detector data, 2014.

[67] D.S. Akerib, S. Alsum, H.M. Araujo, X. Bai, A.J. Bailey, J. Balajthy, P. Beltrame, E.P. Bernard, A. Bernstein, T.P. Biesiadzinski, and et al. Limits on spin-dependent wimp-nucleon cross section obtained from the complete lux exposure. *Physical Review Letters*, 118(25), Jun 2017.

[68] H. Kraus and F.A. Danevich, editors. *Proceedings, 1st International Workshop 'Radiopure Scintillators for EURECA' (RPScint'2008): Kiev, Ukraine, September 9-10, 2008*, Kiev, 2009. INR.

[69] J. Aalbers et al. DARWIN: towards the ultimate dark matter detector. *JCAP*, 11:017, 2016.

[70] C. E. Aalseth, F. Acerbi, P. Agnes, I. F. M. Albuquerque, T. Alexander, A. Alici, A. K. Alton, P. Antonioli, S. Arcelli, R. Ardito, and et al. Darkside-20k: A 20 tonne two-phase lar tpc for direct dark matter detection at lngs. *The European Physical Journal Plus*, 133(3), Mar 2018.

[71] Corey Reed. Measuring neutrinos with the ANTARES telescope. *AIP Conf. Proc.*, 1182(1):60–63, 2009.

[72] M. G. Aartsen et al. The IceCube Neutrino Observatory: Instrumentation and Online Systems. *JINST*, 12(03):P03012, 2017.

[73] M.G. Aartsen et al. Search for Neutrinos from Dark Matter Self-Annihilations in the center of the Milky Way with 3 years of IceCube/DeepCore. *Eur. Phys. J. C*, 77(9):627, 2017.

[74] R. Abbasi et al. Search for Neutrinos from Annihilating Dark Matter in the Direction of the Galactic Center with the 40-String IceCube Neutrino Observatory. 10 2012.

[75] G. Ambrosi et al. Direct detection of a break in the teraelectronvolt cosmic-ray spectrum of electrons and positrons. *Nature*, 552:63–66, 2017.

[76] Mattia Di Mauro and Andrea Vittino. AMS-02 electrons and positrons: astrophysical interpretation and Dark Matter constraints. *PoS*, ICRC2015:1177, 2016.

[77] S. Abdollahi et al. Cosmic-ray electron-positron spectrum from 7 GeV to 2 TeV with the Fermi Large Area Telescope. *Phys. Rev. D*, 95(8):082007, 2017.

[78] Oscar Adriani et al. An anomalous positron abundance in cosmic rays with energies 1.5-100 GeV. *Nature*, 458:607–609, 2009.

[79] I. V. Moskalenko and A. W. Strong. Production and propagation of cosmic-ray positrons and electrons. *The Astrophysical Journal*, 493(2):694–707, feb 1998.

[80] Nasa Goddard Space Flight Center. The femri gamma-ray space telescope, 2013.

[81] Aous A. Abdo et al. Measurement of the Cosmic Ray e+ plus e- spectrum from 20 GeV to 1 TeV with the Fermi Large Area Telescope. *Phys. Rev. Lett.*, 102:181101, 2009.

[82] M. Aguilar, G. Alberti, Behcet Alpat, Antonio Alvino, Giovanni Ambrosi, Karen Andeen, H. Anderhub, Luisa Arruda, Philipp Azzarello, A Bachlechner, Fernando Barao, B. Baret, Aurelien Barrau, L. Barrin, Alessandro Bartoloni, L. Basara, A. Basili, L. Batalha, J. Bates, and C. Zurbach. First result from the alpha magnetic spectrometer on the international space station: Precision measurement of the positron fraction in primary cosmic rays of 0.5-350 gev. *Phys. Rev. Lett.*, 110:141102, 04 2013.

[83] Marco Cirelli, Mario Kadastik, Martti Raidal, and Alessandro Strumia. Model-independent implications of the e+-, anti-proton cosmic ray spectra on properties of Dark Matter. *Nucl. Phys. B*, 813:1–21, 2009. [Addendum: Nucl.Phys.B 873, 530–533 (2013)].

[84] Dan Hooper, Pasquale Blasi, and Pasquale Dario Serpico. Pulsars as the Sources of High Energy Cosmic Ray Positrons. *JCAP*, 01:025, 2009.

[85] M. Aguilar et al. Antiproton Flux, Antiproton-to-Proton Flux Ratio, and Properties of Elementary Particle Fluxes in Primary Cosmic Rays Measured with the Alpha Magnetic Spectrometer on the International Space Station. *Phys. Rev. Lett.*, 117(9):091103, 2016.

[86] Julio F. Navarro, Carlos S. Frenk, and Simon D. M. White. The Structure of cold dark matter halos. *Astrophys. J.*, 462:563–575, 1996.

[87] Alister W. Graham, David Merritt, Ben Moore, Juerg Diemand, and Balsa Terzic. Empirical models for Dark Matter Halos. I. Nonparametric Construction of Density Profiles and Comparison with Parametric Models. *Astron. J.*, 132:2685–2700, 2006.

[88] Raul Jimenez, Licia Verde, and S. Peng Oh. Dark halo properties from rotation curves. *Mon. Not. Roy. Astron. Soc.*, 339:243, 2003.

[89] Marco Cirelli, Gennaro Corcella, Andi Hektor, Gert Hutsi, Mario Kadastik, Paolo Panci, Martti Raidal, Filippo Sala, and Alessandro Strumia. PPPC 4 DM ID: A Poor Particle Physicist Cookbook for Dark Matter Indirect Detection. *JCAP*, 1103:051, 2011. [Erratum: JCAP1210,E01(2012)].

[90] Edward Kolb and Michael Turner. The early universe. *Front. Phys., Vol. 69,*, -1, 02 1983.

[91] Gianfranco Bertone, Wilfried Buchmuller, Laura Covi, and Alejandro Ibarra. Gamma-Rays from Decaying Dark Matter. *JCAP*, 11:003, 2007.

[92] David Merritt, Milos Milosavljevic, Licia Verde, and Raul Jimenez. Dark matter spikes and annihilation radiation from the galactic center. *Phys. Rev. Lett.*, 88:191301, 2002.

[93] M. Ackermann, M. Ajello, A. Albert, W. B. Atwood, L. Baldini, J. Ballet, G. Barbiellini, D. Bastieri, R. Bellazzini, E. Bissaldi, and et al. Thefermigalactic center gev excess and implications for dark matter. *The Astrophysical Journal*, 840(1):43, May 2017.

[94] Qiang Yuan and Bing Zhang. Millisecond pulsar interpretation of the galactic center gamma-ray excess. *Journal of High Energy Astrophysics*, 3-4, 04 2014.

[95] D.Y. Nieto, Jelena Aleksić, Juan Abel Barrio, José Contreras González, Michele Doro, S. Lombardi, N. Mirabal, A. Moralejo, Silvia Pardo, Javier Rico, and F. Zandanel. The search for galactic dark matter clump candidates with fermi and magic. *Proceedings of the 32nd International Cosmic Ray Conference, ICRC 2011*, 5, 09 2011.

[96] Louis E. Strigari, Savvas Michael Koushiappas, James S. Bullock, Manoj Kaplinghat, Joshua D. Simon, Marla Geha, and Beth Willman. The Most Dark Matter Dominated Galaxies: Predicted Gamma-ray Signals from the Faintest Milky Way Dwarfs. *Astrophys. J.*, 678:614, 2008.

[97] The Fermi-LAT Collaboration. Constraints on dark matter annihilation in clusters of galaxies with the fermi large area telescope. 2010.

[98] Alexey Boyarsky, A. Neronov, Oleg Ruchayskiy, and Mikhail Shaposhnikov. Restrictions on parameters of sterile neutrino dark matter from observations of galaxy clusters. *Phys. Rev. D*, 74:103506, 2006.

[99] P.A. Cherenkov. Visible luminescence of pure liquids under the influence of γ-radiation. *Dokl. Akad. Nauk SSSR*, 2(8):451–454, 1934.

[100] J.R. García, F. Dazzi, D. Häfner, D. Herranz, M. López, M. Mariotti, R. Mirzoyan, D. Nakajima, T. Schweizer, and M. Teshima. Status of the new Sum-Trigger system for the MAGIC telescopes. In *33rd International Cosmic Ray Conference*, page 0666, 2013.

[101] R. López-Coto, D. Mazin, R. Paoletti, O. Blanch Bigas, and J. Cortina. The topo-trigger: a new concept of stereo trigger system for imaging atmospheric cherenkov telescopes. *Journal of Instrumentation*, 11(04):P04005–P04005, Apr 2016.

[102] Julian Sitarek, Markus Gaug, Daniel Mazin, Riccardo Paoletti, and Diego Tescaro. Analysis techniques and performance of the domino ring sampler version 4 based readout for the magic telescopes. *Nuclear Instruments and Methods in Physics Research Section A: Accelerators, Spectrometers, Detectors and Associated Equipment*, 723:109 – 120, 2013.

[103] Christian Fruck, Markus Gaug, Roberta Zanin, Daniela Dorner, Daniel Garrido, Razmik Mirzoyan, and Lluis Font. A novel LIDAR-based Atmospheric Calibration Method for Improving the Data Analysis of MAGIC. In *33rd International Cosmic Ray Conference*, page 1054, 3 2014.

[104] Daniel Guberman, P. Colin, and for collaboration. Performance of the magic telescopes under moonlight. 09 2017.

[105] R. Zanin and J. Cortina. The Central Control of the MAGIC telescopes. 7 2009.

[106] Roberta Zanin, Emiliano Carmona, Julian Sitarek, Pierre Colin, Katharina Frantzen, Markus Gaug, Saverio Lombardi, Marcos Lopez, Abelardo Moralejo, Konstancja Satalecka, Valeria Scapin, and Victor Stamatescu. MARS, the MAGIC analysis and reconstruction software. In *Proceedings of the 33rd International Cosmic Ray Conference (ICRC2013): Rio de Janeiro, Brazil, July 2-9, 2013*, page 0773, 2013.

[107] R. Mirzoian, E. Lorenz, D. Petry, and C. Prosch. On the influence of afterpulsing in PMTs on the trigger threshold of multichannel light detectors in selftrigger mode. *Nucl. Instrum. Meth. A*, 387:74–78, 1997.

[108] Saverio Lombardi, Karsten Berger, Pierre Colin, Alicia Diago Ortega, and S. Klepser. Advanced stereoscopic gamma-ray shower analysis with the MAGIC telescopes. In *32nd International Cosmic Ray Conference*, volume 3, pages 266–269, 9 2011.

[109] J. Albert et al. Implementation of the Random Forest Method for the Imaging Atmospheric Cherenkov Telescope MAGIC. *Nucl. Instrum. Meth. A*, 588:424–432, 2008.

[110] J. Aleksić, L. A. Antonelli, P. Antoranz, M. Backes, C. Baixeras, J. A. Barrio, D. Bastieri, J. Becerra González, W. Bednarek, A. Berdyugin, and et al. Search for an extended vhe-ray emission from mrk 421 and mrk 501 with the magic telescope. *Astronomy Astrophysics*, 524:A77, Nov 2010.

[111] T. P. Li and Y. Q. Ma. Analysis methods for results in gamma-ray astronomy. *apj*, 272:317–324, September 1983.

[112] J. Aleksić et al. Optimized dark matter searches in deep observations of Segue 1 with MAGIC. *JCAP*, 02:008, 2014.

[113] M.L. Ahnen et al. Indirect dark matter searches in the dwarf satellite galaxy Ursa Major II with the MAGIC Telescopes. *JCAP*, 03:009, 2018.

[114] Javier Rico and Cosimo Nigro and Daniel Kerszberg and Tjark Miener and Jelena Aleksić. gLike: numerical maximization of heterogeneous joint likelihood functions of a common free parameter plus nuisance parameters, sep 2020.

[115] Gerard Gilmore, Mark I. Wilkinson, Rosemary F.G. Wyse, Jan T. Kleyna, Andreas Koch, N.Wyn Evans, and Eva K. Grebel. The Observed properties of Dark Matter on small spatial scales. *Astrophys. J.*, 663:948–959, 2007.

[116] H. Shapley. Two stellar systema of a new kind. *Nature*, 142, 1938.

[117] The Dark Energy Survey collaboration. Dark energy survey hompage, 2020.

[118] Anatoly Klypin, Andrey V. Kravtsov, Octavio Valenzuela, and Francisco Prada. Where Are the Missing Galactic Satellites? , 522(1):82–92, September 1999.

[119] Matthew G. Walker, Mario Mateo, and Edward Olszewski. Stellar Velocities in the Carina, Fornax, Sculptor and Sextans dSph Galaxies: Data from the Magellan/MMFS Survey. *Astron. J.*, 137:3100, 2009.

[120] Matthew G. Walker, Mario Mateo, Edward W. Olszewski, Bodhisattva Sen, and Michael Woodroofe. Clean kinematic samples in dwarf spheroidals: An algorithm for evaluating membership and estimating distribution parameters when contamination is present. *The Astronomical Journal*, 137(2):3109–3138, Jan 2009.

[121] James Binney and Scott Tremaine. Galactic dynamics: Second edition. *Galactic Dynamics: Second Edition*, 01 2008.

[122] A. G. Wilson. Sculptor-Type Systems in the Local Group of Galaxies. *PASP*, 67(394):27–29, February 1955.

[123] J. Albert et al. Upper limit for gamma-ray emission above 140-GeV from the dwarf spheroidal galaxy Draco. *Astrophys. J.*, 679:428–431, 2008.

[124] Astropy Collaboration, T. P. Robitaille, E. J. Tollerud, P. Greenfield, M. Droettboom, E. Bray, T. Aldcroft, M. Davis, A. Ginsburg, A. M. Price-Whelan, W. E. Kerzendorf, A. Conley, N. Crighton, K. Barbary, D. Muna, H. Ferguson, F. Grollier, M. M. Parikh, P. H. Nair, H. M. Unther, C. Deil, J. Woillez, S. Conseil, R. Kramer, J. E. H. Turner, L. Singer, R. Fox, B. A. Weaver, V. Zabalza, Z. I. Edwards, K. Azalee Bostroem, D. J. Burke, A. R. Casey, S. M. Crawford, N. Dencheva, J. Ely, T. Jenness, K. Labrie, P. L. Lim, F. Pierfederici, A. Pontzen, A. Ptak, B. Refsdal, M. Servillat, and O. Streicher. Astropy: A community Python package for astronomy. , 558:A33, October 2013.

[125] Astropy Collaboration, A. M. Price-Whelan, B. M. SipHocz, H. M. G"unther, P. L. Lim, S. M. Crawford, S. Conseil, D. L. Shupe, M. W. Craig, N. Dencheva, A. Ginsburg, J. T. Vand erPlas, L. D. Bradley, D. P'erez-Su'arez, M. de Val-Borro, T. L. Aldcroft, K. L. Cruz, T. P. Robitaille, E. J. Tollerud, C. Ardelean, T. Babej, Y. P. Bach, M. Bachetti, A. V. Bakanov, S. P. Bamford, G. Barentsen, P. Barmby, A. Baumbach, K. L. Berry, F. Biscani, M. Boquien, K. A. Bostroem, L. G. Bouma, G. B. Brammer, E. M. Bray, H. Breytenbach, H. Buddelmeijer, D. J. Burke, G. Calderone, J. L. Cano Rodr'iguez, M. Cara, J. V. M. Cardoso, S. Cheedella, Y. Copin, L. Corrales, D. Crichton, D. D'Avella, C. Deil, 'E. Depagne, J. P. Dietrich, A. Donath, M. Droettboom,

N. Earl, T. Erben, S. Fabbro, L. A. Ferreira, T. Finethy, R. T. Fox, L. H. Garrison, S. L. J. Gibbons, D. A. Goldstein, R. Gommers, J. P. Greco, P. Greenfield, A. M. Groener, F. Grollier, A. Hagen, P. Hirst, D. Homeier, A. J. Horton, G. Hosseinzadeh, L. Hu, J. S. Hunkeler, Z. Ivezi'c, A. Jain, T. Jenness, G. Kanarek, S. Kendrew, N. S. Kern, W. E. Kerzendorf, A. Khvalko, J. King, D. Kirkby, A. M. Kulkarni, A. Kumar, A. Lee, D. Lenz, S. P. Littlefair, Z. Ma, D. M. Macleod, M. Mastropietro, C. McCully, S. Montagnac, B. M. Morris, M. Mueller, S. J. Mumford, D. Muna, N. A. Murphy, S. Nelson, G. H. Nguyen, J. P. Ninan, M. N"othe, S. Ogaz, S. Oh, J. K. Parejko, N. Parley, S. Pascual, R. Patil, A. A. Patil, A. L. Plunkett, J. X. Prochaska, T. Rastogi, V. Reddy Janga, J. Sabater, P. Sakurikar, M. Seifert, L. E. Sherbert, H. Sherwood-Taylor, A. Y. Shih, J. Sick, M. T. Silbiger, S. Singanamalla, L. P. Singer, P. H. Sladen, K. A. Sooley, S. Sornarajah, O. Streicher, P. Teuben, S. W. Thomas, G. R. Tremblay, J. E. H. Turner, V. Terr'on, M. H. van Kerkwijk, A. de la Vega, L. L. Watkins, B. A. Weaver, J. B. Whitmore, J. Woillez, V. Zabalza, and Astropy Contributors. The Astropy Project: Building an Open-science Project and Status of the v2.0 Core Package. *aj*, 156(3):123, September 2018.

[126] Marco Cirelli, Gennaro Corcella, Andi Hektor, Gert Hutsi, Mario Kadastik, Paolo Panci, Martti Raidal, Filippo Sala, and Alessandro Strumia. PPPC 4 DM ID: A Poor Particle Physicist Cookbook for Dark Matter Indirect Detection. *JCAP*, 03:051, 2011. [Erratum: JCAP 10, E01 (2012)].

[127] H. Abdalla et al. The H.E.S.S. Galactic plane survey. *Astron. Astrophys.*, 612:A1, 2018.

[128] S. Carrigan, F. Brun, R. C. G. Chaves, C. Deil, H. Gast, and V. Marandon. Charting the TeV Milky Way: H.E.S.S. Galactic plane survey maps, catalog and source populations. In *Proceedings, 48th Rencontres de Moriond on Very High Energy Phenomena in the Universe: La Thuile, Italy, March 9-16, 2013*, pages 95–102, 2013.

[129] Christoph Deil. The H.E.S.S. view of the Milky Way in TeV light. In Richard J. Tuffs and Cristina C. Popescu, editors, *The Spectral Energy Distribution of Galaxies - SED 2011*, volume 284 of *IAU Symposium*, pages 365–370, August 2012.

[130] M. Ackermann, M. Ajello, A. Albert, W. B. Atwood, L. Baldini, J. Ballet, G. Barbiellini, D. Bastieri, K. Bechtol, R. Bellazzini, and et al. The spectrum of isotropic diffuse gamma-ray emission between 100 mev and 820 gev. *The Astrophysical Journal*, 799(1):86, Jan 2015.

[131] A. Neronov and D. Semikoz. Galactic diffuse gamma-ray emission at tev energy. *Astronomy Astrophysics*, 633:A94, Jan 2020.

[132] Jean-Paul Mayer, Luke OC Drury, and Donald C Ellision. Galactic Cosmic Rays from Supernova Remnants. I. A Cosmic-Ray Composition Controlled by Volatility and Mass-to-Charge Ratio. *Apj*, 487:182, 1997.

[133] M. Ackermann et al. Fermi-LAT Observations of the Diffuse gamma-Ray Emission: Implications for Cosmic Rays and the Interstellar Medium. *Astrophys. J.*, 750(3):88, 2012.

[134] Alejandro Ibarra, David Tran, and Christoph Weniger. Detecting Gamma-Ray Anisotropies from Decaying Dark Matter: Prospects for Fermi LAT. *Phys. Rev. D*, 81:023529, 2010.

[135] D. Borla Tridon, P. Colin, L. Cossio, M. Doro, and V. Scalzotto. Measurement of the cosmic electron spectrum with the MAGIC telescopes. In *Proceedings, 32nd International Cosmic Ray Conference (ICRC 2011): Beijing, China, August 11-18, 2011*, volume 6, pages 47–50, 2011.

[136] G. Di Sciascio and R. Iuppa. On the observation of the cosmic ray anisotropy below 10^{15} ev, 2014.

[137] U.S Naval Observatory. Nomad catalogue, 2008.

[138] M. Ajello et al. 3FHL: The Third Catalog of Hard Fermi-LAT Sources. *Astrophys. J. Suppl.*, 232(2):18, 2017.

[139] S.C. Commichau, A. Biland, J.L. Contreras, R. de los Reyes, A. Moralejo, J. Sitarek, and D. Sobczyńska. Monte carlo studies of geomagnetic field effects on the imaging air cherenkov technique for the magic telescope site. *Nuclear Instruments and Methods in Physics Research Section A: Accelerators, Spectrometers, Detectors and Associated Equipment*, 595(3):572 – 586, 2008.

[140] Ann Kathrin Mallot. *The energy spectrum of cosmic electrons measured with the MAGIC telescopes*. PhD thesis, Humboldt U., Berlin, 2017.

[141] Timothy Cohen, Kohta Murase, Nicholas L. Rodd, Benjamin R. Safdi, and Yotam Soreq. γ-ray Constraints on Decaying Dark Matter and Implications for IceCube. *Phys. Rev. Lett.*, 119(2):021102, 2017.

[142] Arman Esmaili, Sin Kyu Kang, and Pasquale Dario Serpico. IceCube events and decaying dark matter: hints and constraints. *JCAP*, 12:054, 2014.